EXTRACTION OF INPUT PARAMETERS FOR THE THEORY OF RADIATIVE ENERGY TRANSFER USING DECONVOLUTION

HUAJIAN CUI

PhD 2009

UNIVERSITY OF GLAMORGAN

EXTRACTION OF INPUT PARAMETERS FOR THE THEORY OF RADIATIVE ENERGY TRANSFER USING DECONVOLUTION

HUAJIAN CUI

A thesis submitted in partial fulfilment of the requirements of the

University of Glamorgan for the degree of Doctor of Philosophy

March 2009

UNIVERSITY OF GLAMORGAN

DECLARATION

I declare that this thesis has not been, nor currently being, submitted for award of any other degree or similar qualification.

signed _____

Huajian Cui

DEDICATION

This thesis is dedicated to my parents, wife and sister

ACKNOWLEDGEMENTS

It is a pleasure to thank the many people who made this thesis possible.

I wish to express my gratitude to my Director of Studies, Dr. Jürgen Richter for his thorough guidance, continuous supports and many fruitful discussions throughout the four years of study and research. I owe him more than any words can describe. With gratitude I would especially acknowledge my two supervisors, Professor Miqdad Al-Nuaimi and Dr. Rafael Caldeirinha who never failed me when I need their advice.

I am especially indebted to my colleagues Dr. Telmo Fernandes who helped on initial data analysis and computer programming. I would also like to thank Mr. John Williams who gave all kinds of helps whenever I need.

The financial support of the University of Glamorgan is gratefully acknowledged.

I wish to express my special thanks to my wife Yuanyuan Zhou for her constantly encouragement and love, and being with me through my PhD period. Finally I sincerely thank my parents and my sister for their understanding and supports.

ABSTRACT

The ever growing application of wireless communication systems requires accurate models for characterising radiowave propagation when affected by the presence of a variety of obstacles. In particular if the obstacles take the shape of vegetation volumes, like single trees or groups of trees and are present in the radio path, they give rise to absorption and scattering of radio signals. This thesis presents a literature review of common models for radiowave propagation through vegetation, the theory of Radiative Energy Transfer (RET) is one of these models and provides an accurate analysis of radiowave propagation through a vegetation media.

Extensive measurements have been designed and conducted in a controlled indoor environment to provide valuable measurement data for later development of deconvolution approaches. It can be shown that the measured directional spectra are convolution products of the phase function pattern and the receiver antenna radiation patterns, which impacts determination of the RET input parameters. Consequently, in order to achieve more accurate determination of the RET input parameters, the adverse influence caused by receiver antenna radiation patterns have to be removed from measured directional spectra by implementing a process of deconvolution.

This thesis provides successful implementation of two iterative based deconvolution techniques on the measurement directional spectra. To the author's knowledge, this is its first kind of application to eliminate distortion caused by the receiver antenna radiation pattern during measurements. This thesis reports a number of novel approaches. These include the further development and extension of deconvolution techniques such as combining the Bennia-Riad criterion and an error function to determine optimal parameters, as well as using pre-filtering techniques to improve the deconvolution results. Development of clearly defined criteria based on the knowledge of the central-limit theorem and discussion of loss of information avoidance during convolution is another novel contribution. Further novelty lies in the modification of the two methods to suit implementation on the measurement data from radiowaves impacting on vegetation volumes. As a result of these refinements,

extracted RET input parameters from the restored patterns after applying the deconvolution processes show evident improvements compared to those extracted from directly measured patterns.

Early stage results of this project are published in the IEEE Proceedings on Next Generation Applications, Services and Technologies.

Contents

List of Figures

List of Tables

Chapter 1

Introduction

1.1 Background of the study

In 1873, James Clerk Maxwell proposed the four Maxwell equations which describe the behaviour of both the electric and magnetic field as well as their interactions with matter [1]. In 1901, Guglielmo Marconi conducted the first transatlantic radio communication between a transmitting station in Poldhu, Cornwall (UK) and St John's Newfoundland (Canada) [2]. Its success demonstrated to the world the possibility of transmitting information by radiowaves over long distances. With the invention of the transistor and integrated circuits in the 20th century [3], personal mobile communications became reality. The first cellular mobile communication network was pioneered in the mid 1980's [4]. The second generation (2G) and the third generation (3G) have been introduced recently in 1992 and 2004 respectively [5].

Despite the novelty of the 3G Universal Mobile Telecommunications System (UMTS), its 384 kbit/s of maximum usable downlink data rate soon proved to be insufficient, and consequently wireless communication systems recently evolved to faster communication protocols such as the High-Speed Downlink Packet Access (HSDPA) [6]. Further development is expected through the deployment of fourth generation (4G) networks between 2010 and 2015 [7], which will be based on packet switching only and provide high quality video services such as video chat, mobile TV and Digital Video Broadcasting [8]. In the next few years, the development of new technologies will bring together the convergence of several mobile multimedia

broadband services and applications such as in the Worldwide Interoperability for Microwave Access system (WiMAX) [5].

Future communication systems will be characterised by their high flexibility, spectral efficiency and high data communication rates. These services are also expected to integrate terrestrial and satellite links providing worldwide roaming and global coverage. The need for widespread network coverage, especially in remote areas, further increases the interest for reliable propagation models and consequently justifies the need for further research in these areas.

The ever growing demand for bandwidth, speed and coverage urges radio communication system developers to employ higher carrier frequencies while maintaining acceptable levels of interference. According to the Ofcom, the 20 GHz frequency band has a possible use for wireless video links to fixed cabled access points for the 2012 London Olympic Games [9] and a current employment in the satellite transmissions. The measurements of satellite systems are underway at 20.7 GHz carried on the US Department of Defense (DoD) satellite UFO-9. Three receivers are utilised two of which are located in the South of England with a 7.5 km separation and the third in Dundee in Scotland, allowing long distance site diversity [10]. The Broadband Fixed Wireless Access (BFWA) uses different frequency bands between 20 and 40 GHz. The 40.5-43.5 GHz band is a key resource for developing the next generation of broadband services, such as Multimedia Wireless Systems (MWS) in Europe. The band has the capacity to deliver very high bandwidths sufficient to support a number of broadcast services as well as high capacity two-way telecommunication links such as video on demands, video communications and other peer-to-peer applications [11[.

At these frequencies there is still a considerable need for accurate planning and design of wireless links and networks. This requires accurate models underpinned by good quality experimental results. Predictions are required for appropriate coverage planning, the determination of propagation modes as well as co-channel interference to and from existing radio links. These form the basis for the planning process of high-level networks. Therefore, design, implementation and deployment of future

communication services rely on radiowave propagation simulation models, which accurately describe the interaction of radiowaves with various obstacles in the radio path [12]. Amongst these possible obstacles such as the terrain profile, buildings and cars, vegetation is known to have a major influence on the performance of radio communications [13]. As a large variety of different types of vegetation is likely to be present in urban, suburban and rural environments, it is desirable to seek propagation models capable of representing the vegetation effects on the communication systems.

1.2 Radiowave propagation through vegetation

Due to the unguided nature of radiowave propagation, wireless communication systems are predisposed to be affected by the interaction of radiowaves and obstacles present within or in the vicinity of the radio path. Although obstacles usually lead to excess losses and reduce the radio system coverage, they can be used to reduce system co-channel interference, for example employing site shielding as an interference reduction technique [14].

In fixed radio communication systems, the transmitter and the receiver are normally positioned so that the environment causes a limited degradation of the radio signal. The degradation is limited by ensuring the radio path is unobstructed and consequently the transmitter and receiver antennas are in a Line of Sight (LOS) configuration. Even when this desirable LOS situation is possible, the surrounding environment might be a useful ally blocking the radio signal propagation in selected directions, thus increasing the immunity of the system to destructive interference. Whenever LOS geometries are impossible, the losses associated with the obstacles present in the radio path must be accurately accounted for using appropriate simulation models. In mobile radio communications, the uncertainty in the mobile station location seldom allows a permanent LOS communication. Thus, the reliability of the mobile communication systems completely relies on the accurate characterisation of the losses caused by all types of obstacles [14].

Radiowave propagation in an urban radio environment suffers from different interaction modes arising from objects found in the vicinity of the radio path. These modes include specular reflections from flat surfaces such as buildings, diffraction caused by edges such as building roofs and corners, absorption from walls, floors and vegetation screens, and also diffuse scattering caused by rough surfaces or more complex structures such as vegetation [15[. In remote areas like suburban and rural propagation environments, the interaction with hilltops and vegetation commonly occurs. In the absence of buildings and other man-made structures, radiowave propagation effects caused by the interaction with natural structures represent a significant influence in the prediction of the communication system performance.

Experimental results reported in [12[show that single trees or groups of trees present in the radio path significantly influence the amount of received signal level in point-to-point links. The principal propagation mechanisms responsible for this are:

- Diffraction around the vegetation edges;
- Reflection by the ground underneath the vegetation canopy;
- Absorption and multiple scattering inside the vegetation volume.

At millimetre and microwave frequencies, the most complex propagation component is due to the scattered signal within the foliage structure [16[. The effects arising mainly involve absorption and scattering of radiowaves [13, 16[. The theory of Radiative Energy Transfer (RET) has provided a means of modelling the effects of absorption and multiple scattering occurring inside the vegetation volume in terms of re-radiated energy. The RET theory is capable of describing the relationship between absorption and scatter, even directional spreading of radiowaves, using a set of 4 parameters. These parameters can be extracted from the measurements like those conducted in this research project.

1.3 Objective of the research project

The RET theory is an analytical model initially established by [16–18] *etc.*, and further verified through experiments in the research unit of radiowave propagation and system design [13, 19–26] at the University of Glamorgan. Throughout this research project, the RET theory has been utilised to predict the excess loss caused by the presence of vegetation media in the radio path. A set of 4 input parameters in this theory is used to describe the behaviour of radiowave propagation through vegetation. Methods to extract these RET input parameters from measurements conducted in this project have been demonstrated.

The RET theory can provide a sufficiently accurate analysis of the mechanism involved in the radiowave propagation through vegetation. Nevertheless, analysis found that accuracy of the RET predictability is adversely affected by the receiver antenna radiation pattern. Measured signal patterns at the receiver side are not precisely incident signal patterns which are represented by the phase function inside a vegetation medium [16[, but a convolution product between incident signal patterns and the receiver antenna radiation pattern. The modelling accuracy relies heavily on the accuracy of the input parameter determination. In the measurements carried out to determine these parameters, the radiation pattern of the receiver antenna influences the measurement results strongly. Countermeasures need to be developed to eliminate the influence of the receiver antenna radiation pattern.

A method to eliminate the influence of the receiver antenna radiation pattern *i.e.* to inverse its measurement process or convolution product is called deconvolution. In this research project, deconvolution methods are introduced and exercised to separate the phase function pattern from the receiver antenna radiation pattern. Restored patterns after the deconvolution process are closer representing the presumed shape of the phase function pattern, consequently the accuracy of determining the RET input parameters is expected to be improved by extracting the 4 parameter values from those restored patterns rather than the directly measured patterns.

Deconvolution techniques have been studied for many years in various fields such as Astronomy, Spectrology and Image Processing [27–29]. Many well established super-resolution techniques such as MUltiple SIgnal Classification (MUSIC) [30[and Estimation of Signal Parameters via Rotational Invariance Techniques (ESPRIT) [31] and the maximum likelihood (ML) based optimisation algorithms, Expectation Maximisation (EM) [32] and Space-Alternating Generalised Expectation maximisation (SAGE) [33] have been used successfully in many radiowave propagation applications and do often perform some form of deconvolution or operations of a similar nature.

However it was found for a number of reasons they are less suitable to the RET input parameter extraction optimisation. Often these algorithms perform best for high Signal-to-Noise Ratio (SNR) signals and require very good estimates for the initial iteration for good convergence [32[. They can also be extremely demanding on computational effort [33[. They also usually require complex input data, whereas the data available in this project only contains amplitude values lacking any phase information. Furthermore that data points are sampled sequentially for each location at a time in this project, which is different again to the requirement of some of the algorithms of spacially separated sampling at the same time instance.

Although many measurements and investigations had been undertaken previously in this research unit, none of them focused on deconvolution, *i.e.* removing the influence of the receiver antenna radiation pattern to obtain the precise knowledge of the phase function inside the vegetation medium. This thesis gives a targeted overview of deconvolution techniques considered for the intended purpose of compensation for the influence of the receiver antenna radiation on measured signal level distribution inside the vegetation medium. The difficulties normally associated with the deconvolution process are illustrated and two successfully implemented techniques overcoming these difficulties are presented. The improvements are demonstrated graphically from the restored patterns by deconvolution techniques and quantitatively through the extracted values of the RET parameters.

The principal aim of this research project is to develop effective deconvoluiton

techniques, which can be implemented successfully on the measured data in a vegetation medium. The main objectives of this thesis are:

1. Literature review of previous, current and possible future simulating models on predicting radiowave propagation through vegetation at frequencies above 1 GHz, with particular emphasis on the theory of Radiative Energy Transfer.

2. Numerical evaluation of the RET theory via computer programming.

3. Design and conduct measurements to investigate: (i) the re-scattering effect of a single tree; (ii) directional spectrum of measured signal patterns inside a downsized homogeneous forest; (iii) excess loss in the boresight of transmitter and receiver.

4. Review of existing deconvolution techniques leading to an investigation of the deconvolution process and related problems with ill-posedness.

5. Introduce deconvolution techniques into the field of radiowave propagation and implement these techniques on measured data, and then tailor them to suit the kind of measured data encountered inside a vegetation medium.

6. Apply the chosen deconvolution techniques on the sets of measured data to remove the receiver antenna's distortion, then extract the input parameters of the RET theory based on the deconvolved patterns.

1.4 Outline of the thesis

The contents of this thesis can in principle be divided into 3 classifications, namely simulation modelling, measurements and deconvolution techniques. Chapter 1 is an introduction into the background of the study and outlines the whole thesis.

The first part of the thesis consisting of chapters 2 and 3 focuses on established models of predicting excess loss incurred in radiowave propagating through vegetation. Chapter 2 gives a summary review of existing models. These are divided into three types according to their prediction means, *i.e.* empirical, semi-empirical

and theoretical. Chapter 3 concentrates on the RET in more detail. Modelling outcomes such as directional spectra as a function of rotation angle and excess loss as a function of vegetation depth are detailed by both theoretical analysis and graphical illustration. Feasible methods of extracting the input parameters for the RET theory are explained. Preliminary results for the extraction of input parameters from straightforward measured data are shown. The convolution relationship of the phase function and the receiver antenna radiation pattern leading to the measured signal pattern is also given.

The second part consisting of chapters 4 and 5 concentrates on the measurements conducted during this research project. Chapter 4 introduces the measurement systems at 20 and 40 GHz including the transmitter section, the receiver section and the characteristics of the antennas used. The chosen measurement environment in the form of an anechoic chamber is also introduced. Measurement error analysis completes chapter 4. Chapter 5 presents three types of measurements and their corresponding results. These measurements are particularly designed to study (i) the re-scattering effects, (ii) the directional spectrum as a function of rotation angle, and (iii) excess loss as a function of vegetation depth. This chapter fully describes the chosen measurement scenarios and geometries and presents some of the many results obtained.

The last part consisting of chapters 6, 7 and 8 is concerned with the application of deconvolution techniques. To the author's knowledge, it is the first time this kind of deconvolution methods have been applied in the field of radiowave propagation through vegetation. Chapter 6 studies various deconvolution methods and highlights the ill-posedness problems. Chapter 7 demonstrates successful implementation of two deconvolution techniques. Their derivation, principle and criteria of assessing their performance are comprehensively explained. Chapter 8 demonstrates the application of these two deconvolution methods onto realistic measurement data and evaluates their performance. The concept of using pre-filtering to further improve the performance of the deconvolution is introduced and explained and finally demonstrated on measurement data.

Chapter 9 completes this thesis with concluding remarks, outlines the contribution made and shows avenues for further studies based on the findings presented here.

Chapter 2

Literature review of radiowave propagation through vegetation

2.1 Introduction

Influences of vegetation on propagation of the radiowave have been a topic of research for a few decades, a representative, but by no means comprehensive cross-section of literature describing this research is given by references [12–14, 16–18, 34–37]. Initially, many research programmes have been carried out for military purposes for developing new digital communication techniques and radar systems [12, 34, 35]. However results from those earlier investigations found popular applications in more widespread non-military fields and are becoming increasingly important to provide radio system planners with accurate models for the predicting of radio wave propagation through the vegetation [38–41].

When vegetation is present in the propagation channel in the form of a forest, individual trees or even bushes or shrubs, two main effects can be attributed. Firstly there are the direct effects like absorption, reflection and diffraction. Secondly lateral contributions are introduced through scattering of radiowaves. Early models typically take the form of curve fitting to the measured data. These are the so-called empirical models. Later analytical models were developed, which allow radiowave propagation inside and near the vegetation to be predicted effectively and

accurately.

The influence of the vegetation medium in the form of single trees or groups of trees on the quality of the transmitted signal is part of the research work presented here. In this chapter different model types, empirical, semi-empirical and analytical, are summarised briefly. Their prediction performances in terms of advantages and disadvantages are also summarised. The quantities modelled usually include the excess loss caused by absorption and scattering, and the collateral contributions by re-scattering while radiowave propagating through vegetation.

The review of the various types of models is kept brief here and takes the form of an overview summary. More comprehensive reviews have been conducted in [12–14[. The Vector Radiative Transfer theory, which was not included in those previous reviews, offers the inclusion of phase information into the scalar RET model. This may prove valuable for future studies, but because of its complexity will not be pursued any further here.

2.2 Empirical prediction models

The main advantage of empirical prediction models is their relatively simple mathematical representation. Their expressions are usually established through curve fitting to the measured data. This is achieved by adjusting one or more parameter in the mathematical formulation. However, the weakness of this type of modelling is that formulated models are strictly related to a specific measured data and fail to give any indication as to the physical processes involved in the propagation within the channel [42[. The empirical prediction models could be categorised as exponential models and semi-empirical models.

2.2.1 Exponential models

The exponential law is commonly used to express the decaying rate while radiowave propagates through vegetation media [43[. The two most commonly used exponential models are summarised as following [12, 13, 43[:

2.2.1.1 The Modified Exponential Decay Model

The Modified Exponential Decay (MED) model uses exponential equations to characterise the excess attenuation when radiowaves propagate inside the vegetation. Weissberger developed the MED model [43] after reviewing several exponential decay models, which were based on the specific attenuation in terms of dB per meter of path length, and compared them with several sets of available measured data carried out in different environments in the United States at frequencies from 230 MHz to 96 GHz [12,13]. The model is given by

$$L = 0.45f^{0.284}d \qquad 0m \leq d \leq 14m \tag{2.1}$$

$$L = 1.33f^{0.284}d^{0.588} \qquad 14m \leq d \leq 400m \tag{2.2}$$

where L represents loss in dB, f represents the frequency in GHz, and d represents the vegetation depth in metres. The difference in path loss for trees with and without leaves reported in [43] is 3 to 5 dB in the frequency range of 450-950 MHz [12,13].

2.2.1.2 The ITU-R model and its derivatives

To improve the limited accuracies of the MED model, the Consultative Committee for International Radio (CCIR) developed a new model, ITU-R, named after the International Telecommunications Union - Radiocommunications Section [21,22,24]. The ITU-R model and its derivatives documented in [44] have been optimised for different geometries and types of vegetation, providing quick and general estimates of the amount of excess attenuation caused by a particular vegetation medium [12,13].

The model proposed in European Cooperation in the field of Scientific and Technical Research (COST) 235 considered the various states of foliation, *e.g.* in-leaf and out-of-leaf. Its mathematical expressions are given by [45]:

$$L = 15.6f^{-0.009}d^{0.26}\ [dB] \qquad In\ leaf \tag{2.3}$$

$$L = 26.6f^{-0.2}d^{0.5}\ [dB] \qquad Out\ of\ leaf \tag{2.4}$$

where L represents loss in dB, f represents the frequency in MHz, and d represents the vegetation depth in metres.

Further optimisation was carried out using measurement data at 11.2 GHz and 20 GHz for each of the foliation states. This resulted in the modification of the three numerical coefficients in Eqs. 2.3 and 2.4. The modified ITU-R model has been reported in [46], named as the Fitted ITU-R (FITU-R) model and given by:

$$L = 0.39 f^{0.39} d^{0.25} \; [dB] \qquad In\ leaf \tag{2.5}$$

$$L = 0.37 f^{0.18} d^{0.59} \; [dB] \qquad Out\ of\ leaf \tag{2.6}$$

where L represents loss in dB, f represents the frequency in MHz, and d represents the vegetation depth in metres.

The excess attenuation is shown to be higher for trees with leaves due to higher absorption per unit volume, and at higher frequencies at which the wavelength becomes comparable to the dimensions of the leaves and small branches [12,13]. The COST235 and FITU-R models indicate that the signal decays considerably faster within small vegetation depth while relatively slow in the region of large vegetation depth. This is in good agreement with the predictions obtained from the theoretical model of Radiative Energy Transfer [16, 24]. It can be explained by the interaction between the coherent (direct path) component, which dominates at short distances into the vegetation depth but is strongly attenuated, and the incoherent (multipath scattered) component, which is less attenuated and takes over at large vegetation depths [12, 13].

2.2.2 Semi-empirical models

The semi-empirical models are the developed version of the exponential models. To overcome the problem of prediction inaccuracies caused by two distinct attenuation rates at various vegetation depths, the concept of initial and final specific attenuation rates were introduced. The improved model was developed by researchers at Rutherford Appleton Laboratory (RAL) and is called as semi-empirical model,

the Non-Zero Gradient (NZG) model [23].

2.2.2.1 The Non-Zero Gradient model

The NZG model is given by:

$$L = R_\infty d + k\left[1 - e^{\frac{(R_0 - R_\infty)d}{k}}\right] \tag{2.7}$$

Where L is the excess attenuation caused by vegetation in dB, and R_0 and R_∞ are the initial and final specific attenuation rates in dB/m respectively, d is the vegetation depth in metre and k the final attenuation offset of the final asymptotic attenuation rate in dB. The best known estimate for the three parameters was reported in [22,44] and presented in Table 2.1 based on measurements at 11.2 and 20 GHz systems.

NZG parameter	In-leaf	Out-of-leaf
$R_0\,(^{dB}/_m)$	19.82	6.25
$R_\infty\,(^{dB}/_m)$	0.33	0.24
$k\,(dB)$	37.87	6.45

Table 2.1: NZG model parameters at 11.2 and 20 GHz

2.2.2.2 The Dual Gradient model

Although this provides a more accurate description of the changing attenuation rates with increasing vegetation depth, the NZG model neither considers the geometry of vegetation volume nor the influences of the antenna radiation patterns. Further development by researchers at RAL [45,47] yields the Dual Gradient (DG) model to accommodate the effects of site specific geometry and various beamwidths of the transmitter and the receiver. This is illustrated in Fig. 2.1.

DG parameters	In-leaf	Out-of-leaf
a	0.7	0.64
b	0.81	0.43
c	0.37	0.97
k	68.8	114.7
R_0	16.7	6.59
R_∞	8.77	3.89

Table 2.2: Dual Gradient model parameters

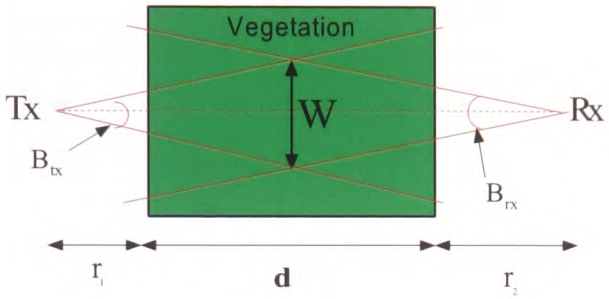

Figure 2.1: Dual Gradient model vegetation measurement geometry

where W is the maximum effective coupling width between the transmitter and receiver antennas, and is given by:

$$W = \begin{bmatrix} \frac{(r_1+d+r_2)tan(B_{tx})tan(B_{rx})}{tan(B_{tx})+tan(B_{rx})} \\ (r_1+d)tan(B_{tx}) \\ (d+r_2)tan(B_{rx}) \\ \omega \end{bmatrix} \tag{2.8}$$

where B_{tx} and B_{rx} represent the transmitter and receiver 3 dB beamwidths respectively; ω is the width of the vegetation volume, d is the vegetation depth; and r_1 and r_2 represent the distances of the transmitter to vegetation and the receiver to vegetation respectively. The DG model also includes the frequency of propagation and is given by:

$$L = \frac{R_\infty}{f^a W^b} d + \frac{k}{W^c}\left[1 - e^{\frac{(R_0 - R_\infty)W}{k}}\right] \tag{2.9}$$

where L represents the excess attenuation in dB; f is given in GHz; and parameters

a, b, c, k, R_0 and R_∞ are constants presented in Table 2.2.

2.3 Generic vegetation model development

Radiowave propagation with vegetation in the path mainly involves three modes of propagation mechanism: reflection from the ground, diffraction from the edge and top of the vegetation volume, and scattering when radiowave passes through the vegetation [48–50]. This could be illustrated as in Fig. 2.2. To establish a generic model, which is capable of predicting the three types of effects effectively and accurately, each mode is better to be resolved independently, and then later grouped together.

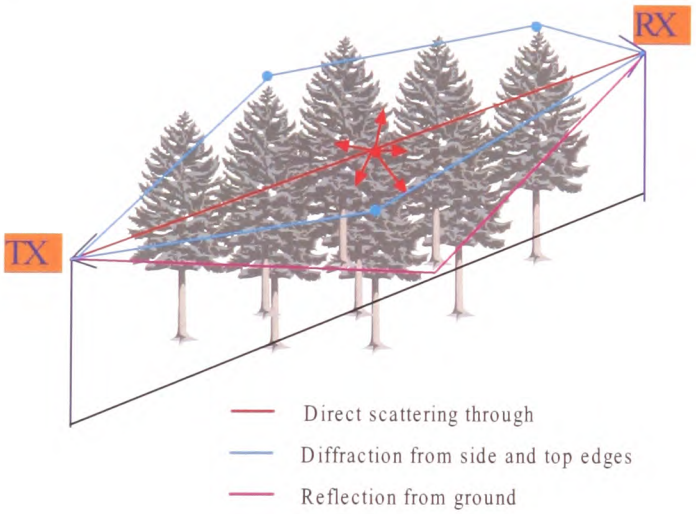

Figure 2.2: Three modes of propagation of through and around the vegetation

A generic 1-60 GHz propagation model [13, 19, 20] was developed under a consortium formed by University of Glamorgan, University of Portsmouth, Rutherford Appleton Laboratory and QinetiQ. The aim of this research project was to study the effects of microwave and millimetre wavelength radiowave propagating through vegetation and to develop a generic model of signal attenuation for narrowband systems. This was achieved through a combination of an extensive measurement campaign and deterministic modelling [13].

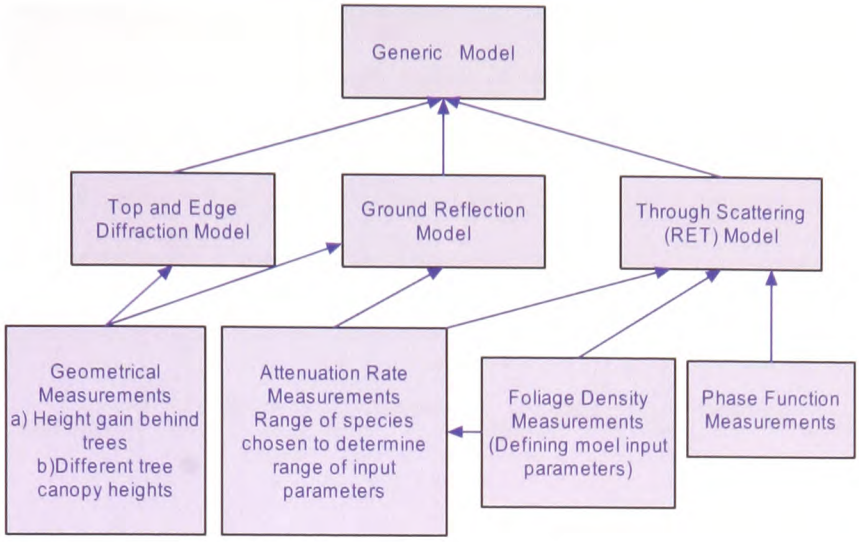

Figure 2.3: Generic vegetation model propagation

The general rationale for the development of the generic vegetation model is demonstrated in Fig. 2.3 [13]. The authors state that measurements of the top-diffracted and ground-reflected components were made by varying the receiver height for various vegetation depths. Comparisons were then made between predictions of the diffracted and ground reflected components for a given measurement geometry and the actual attenuation measured. The predicted edge diffracted attenuation was also compared with the measured attenuation, in order to determine in which locations the measured signal was limited by an edge-diffracted component. A series of measurements were conducted for parameter fitting the scattering and re-scattering components, which are: (a) as a function of depth through the vegetation and (b) phase function measurements to determine the nature of the scatter function of the vegetation.

The diffracted received signal, including two-side and one-top diffracted components, was obtained using the ITU-R Rec. 526-7 model. The ground reflected signal also consists of two distinct phenomena: the ground reflected component and the partially scattered component. This is explained as the partial scattering happens when a portion or portions of the reflected path are intercepted by the vegetation

volume. The complex reflection coefficient was obtained using the formulae given in the CCIR report 1008-1 [51] with values of the permittivity and conductance as plotted in ITU-R Rec. 527-3 [52[. The scattering and re-scattering components occurred when radiowave passing through the inside of the vegetation media were calculated using the RET model]16[. The total loss, L_{total}, experienced by a signal propagating through trees is then given by the combination of the loss terms:

$$L_{total} = -10\log_{10}\left\{10^{\left(\frac{-L_{sidea}}{10}\right)} + 10^{\left(\frac{-L_{sideb}}{10}\right)} + 10^{\left(\frac{-L_{top}}{10}\right)} + 10^{\left(\frac{-L_{ground}}{10}\right)} + 10^{\left(\frac{-L_{scatter}}{10}\right)}\right\} \tag{2.10}$$

2.4 The general Radiative Transfer theory

Radiative Transfer (RT) is an important method to treat multiple scattering in media consisting of random discrete scatterers [18]. RT has been described in numerous reports and books over many years [13, 16–18, 36, 37, 53–55[. Although diffraction and interference effects can be included in the consideration of scattering from and absorption by single particles, RT theory does not consider diffraction effects [55[. The most widely adapted and most thoroughly developed theory is the scalar form of the Radiative Energy Transfer (RET) theory. This approach concentrates on establishing signal amplitudes inside a vegetation medium, that is considered to be homogeneous. Two notable extensions exist for the RET:

- The discrete RET is capable of modelling an inhomogeneous vegetation medium by using a discrete volume of vegetation.
- The Vector Radiative Transfer theory models amplitude and phase effects throughout.

The scalar RET is described in section 2.4.1, the extension to discrete RET in 2.4.2 and the vector RET in 2.4.3.

2.4.1 The scalar Radiative Energy Transfer theory

The Scalar Radiative Transfer (SRT) equation is an integro-differential equation governing the propagation of specific intensity. A vegetation medium is considered to be consisting of a large number of random particles such as twigs and branches, $I(\bar{r}, \hat{s})$ represents the specific intensity at $\bar{r}$ and for all directions $\hat{s}$ due to multiple scattering. Considering a small volume element, Fig. 2.4, $dV = dA \cdot dL$, where dA represents the cross section area of the small volume element, dL is the length along the direction $\hat{s}$, and $d\omega$ denotes the differential of the solid angle. The small volume element is centered at $\bar{r}$. The differential change in specific intensity $I(\hat{s})$ as it passes through dV is given by:

$$dP = -I_{in}(\hat{s})dAd\omega + I_{out}(\hat{s})dAd\omega = -I(\bar{r}, \hat{s})dAd\omega + I(\bar{r} + \hat{s}ds, \hat{s})dAd\omega \quad (2.11)$$

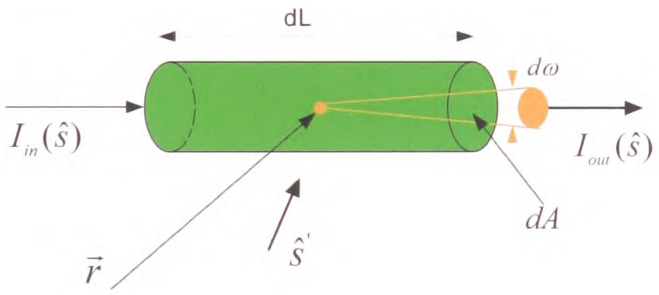

Figure 2.4: Specific intensity $I(\hat{s})$ in direction $\hat{s}$ in and out of elemental volume

The volume dV is much bigger than λ^3 at microwave and millimeter waves so the random phase prevails [16]. There are three types of changes affecting the specific intensity $I(\hat{s})$ during the propagation progress [18]:

- Extinction which contributes a negative change. k_e denotes the extinction coefficient, *i.e.* the extinction cross section per unit volume, the differential

change of power from extinction is given by

$$dP_1 = -k_e dV I(\bar{r},\hat{s})\, d\omega \tag{2.12}$$

- Emission by the particles inside the volume dV, which contributes a positive change. Let $\varepsilon(\bar{r},\hat{s})$ represent the emission power per unit volume of medium per unit solid angle per unit angular frequency, then

$$dP_2 = \varepsilon(\bar{r},\hat{s}) dV d\omega \tag{2.13}$$

- Bistatic scattering (re-scattering) from direction $\hat{s}'$ into direction $\hat{s}$ which contributes a positive change. $I(\bar{r},\hat{s}')$ denotes the specific intensity in direction $\hat{s}'$, and $p(\hat{s},\hat{s}')$ be the bistatic scattering cross section per unit volume, then

$$dP_3 = \int_{4\pi} I(\bar{r},\hat{s}')\, d\omega' \cdot p(\hat{s},\hat{s}')\, dV d\omega \tag{2.14}$$

where integration on $d\omega'$ is over 4π space, *i.e.* 3-dimensional.

Substituting Eqs. 2.12, 2.13, and 2.14 into 2.11, and $\frac{dI}{ds}$ denoting the rate of change of $I(\bar{r},\hat{s})$ per unit distance in direction $\hat{s}$, it follows that:

$$\frac{dI(\hat{r},\bar{s})}{ds} = -k_e I(\bar{r},\hat{s}) + \varepsilon(\bar{r},\hat{s}) + \int_{4\pi} d\omega' p(\hat{s},\hat{s}')\, I(\bar{r},\hat{s}') \tag{2.15}$$

Equation 2.15 is known as the radiative transfer equation. The definitions of the scattering coefficient and absorption coefficient are given by

$$k_s = \int_{4\pi} d\omega p(\hat{s},\hat{s}') \tag{2.16}$$

$$k_a = k_e - k_s \tag{2.17}$$

For the case of thermal emission [18],

$$I = \frac{hf^3}{c^2} \frac{1}{exp\left(\frac{hf}{KT}\right) - 1} \tag{2.18}$$

where f is the frequency, and c is the velocity, h is Planck's constant, equal to 6.634×10^{-34} $^{joule}/_{sec}$ [17], T is the temperature and K is Boltzmann's constant. For microwave frequencies, $hf \ll KT$, so that with $exp\left(\frac{hf}{KT}\right) - 1 \approx \frac{hf}{KT}$, Eq. 2.18 becomes

$$I = \frac{KT}{\lambda^2} \tag{2.19}$$

The Radiative Transfer theory, or the Radiative Energy Transfer (RET) theory [16], can then be further simplified by considering the absorption and scattering events only and no emission. Consequently, the radiative transfer equation becomes

$$\hat{s} \cdot \nabla I(\bar{r}, \hat{s}) = -k_e I(\bar{r}, \hat{s}) + \int d\omega' p(\hat{s}, \hat{s}') I(\bar{r}, \hat{s}') \tag{2.20}$$

where $\hat{s} \cdot \nabla I(\bar{r}, \hat{s})$ also denotes the rate of change of $I(\bar{r}, \hat{s})$ in direction $\hat{s}$, $\frac{dI}{ds}$. Solution of Eq. 2.20 and methods to extract the input parameters of the scalar RET theory will be presented in chapter 3.

2.4.2 The discrete Radiative Energy Transfer (dRET) theory

The discrete RET (dRET) model was originally proposed in [56] and further developed in [14, 25, 26] to overcome some limitations inherent in the scalar RET theory. These limitations include the assumptions of the forest as a homogeneous medium, uniform illumination at the air-to-vegetation interface, infinite air-to-vegetation interface and semi-infinite vegetation volume. The dRET model focus on the inhomogeneity of the vegetation medium and its limited physical dimensions of vegetation volume, which is distinct from the original RET model.

The dRET technique divides the vegetation medium into several non overlapping vegetation cells having the same propagation characteristics as illustrated in Fig. 2.5. Then a modifled version of the RET model is applied to determine the overall interactions between the cells inside the whole vegetation medium.

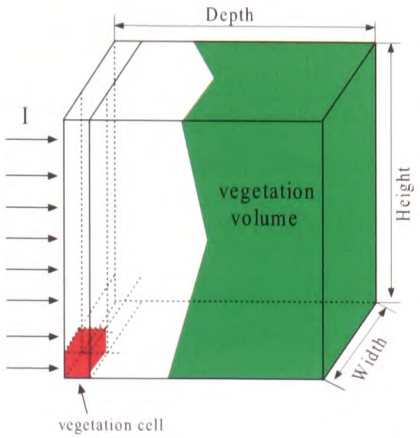

Figure 2.5: Discrete vegetation cell structure

The output intensities are calculated for each individual vegetation cell as a function of the input intensities. The process starts at the first layer of cells (air-to-vegetation interface) where the input intensity, I, is known. The algorithm proceeds throughout the overall vegetation volume in a way that can be explained as a step-by-step marching technique [14]. Following this process the intensities of all vegetation cells can be obtained.

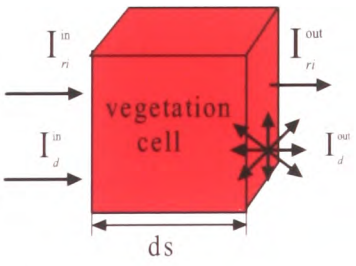

Figure 2.6: Demonstration of the input and output intensities of a cubic vegetation cell in the dRET model

The relationship of the input and output intensity in a cubic discrete vegetation cell is depicted in Fig. 2.6 and given by:

$$I_{ri}^{out}(\gamma_o) = I_{ri}^{in}(\gamma_o) - k_e I_{ri}^{in}(\gamma_o) \cdot ds \tag{2.21}$$

$$I_d^{out}(\gamma) = I_d^{in}(\gamma) + \left[-k_e I_d^{in}(\gamma)\right] \cdot ds + \left[k_s \sum_{1}^{26} P(\gamma, \gamma') I_d^{in}(\gamma') + k_s P(\gamma, \gamma_o) I_{ri}^{in}(\gamma_o)\right] \cdot ds \tag{2.22}$$

where k_e and k_s represent the extinction and the scattering coefficients respectively; I_{ri}^{in} and I_{ri}^{out} represent the input and output coherent intensity components respectively, while I_d^{in} and I_d^{out} denote the input and output diffuse intensity components respectively. P denotes the discrete version of the phase function. γ_o represents the wave propagation direction, and γ represents the direction between the cell under consideration and one of its neighbour cells. In the 3-dimensional structure shown in Fig. 2.5, each cell is surrounded by 26 direct neighbouring cells]14[. Consequently, there will be 26 distinct contributions of the diffuse intensity components from its neighbour cells.

Eqs. 2.21 and 2.22 are used to describe every vegetation cell and its effect on the neighbouring cells. The entire vegetation body is described by considering all the mutual effects of the cells on each other in the manner described below]56[:

1. The impinging intensity, I, at the air-to-vegetation interface is used as I_{ri}^{in} ($I_d^{in} = 0$) to calculate the coherent and incoherent intensities emanating from each of the illuminated elementary vegetation cells in layer 1, *e.g.* the air-to-vegetation interface.

2. The output intensities, coherent and incoherent, from the previous layer of the vegetation cells are utilised as the input intensities for the current layer of vegetation cells. That is the coherent output component from the $k-1$th layer cell is used as the coherent input component for the kth cell. So are the incoherent components.

3. The emanating intensities, I_{ri}^{out} and I_d^{out}, from each cell in the kth layer are determined for all directions γ using the discrete RET equations.

4. Repeat steps 2 and 3 for all the layers of the vegetation volume.

The iterative process is applied until the decay rate of the signal strength reaches a steady state as proceeding further into the vegetation, meaning no significant

variation of the signal strength has been observed between several successive iterations [14]. The comparison between the intensity of the vegetation cell under consideration and that of at the air-to-vegetation interface can be used to estimate the excess attenuation caused by the vegetation medium.

The dRET model therefore applies the assumption of vegetation as a homogeneous medium at a smaller scale via considering the same propagation characteristics in a specific vegetation cell, and demonstrates the inhomogeneity of forest by representing the mutual interactions of the input and output intensities amid overall vegetation cells. The dRET model has been further developed and a demonstration of its application is given in more detail in [14[.

2.4.3 The Vector Radiative Transfer (VRT) theory

The radiative transfer equation, which is used to describe the characteristics of discrete particles, consists of three terms: extinction matrix, phase matrix and emission vector. The extinction matrix describes the attenuation of specific intensity due to absorption and scattering. The phase matrix characterises the coupling of intensities in two different directions due to scattering. The emission vector gives the thermal emission source of the specific intensity [18[. Since the specific intensity is a four-element Stokes vector [16[, the extinction and phase matrices are 4×4 matrices and the emission vector is a 4×1 column matrix. The resultant equations are called vector radiative transfer equations to distinguish them from the scalar transfer equation. The vector radiative transfer equation for specific intensity is given by:

$$\begin{aligned} \frac{d\bar{I}(\bar{r},\hat{s})}{ds} &= -\bar{\bar{k}}_e(\bar{r},\hat{s})\,\bar{I}(\bar{r},\hat{s}) - k_{ag}(\bar{r},\hat{s})\,\bar{I}(\bar{r},\hat{s}) + \bar{J}_e \\ &\quad + \int_{4\pi} d\Omega' \bar{\bar{P}}(\bar{r},\hat{s},\hat{s}') \cdot \bar{I}(\bar{r},\hat{s}) \end{aligned} \tag{2.23}$$

where $\bar{\bar{P}}(\bar{r},\hat{s},\hat{s}')$ is the phase matrix giving the contribution from direction $\hat{s}'$ into the direction $\hat{s}$. $\bar{\bar{k}}_e$ is the extinction matrix for Stokes parameters due to the scatterers, $\bar{J}_e$ is the emission vector, and k_{ag} is the absorption coefficient for the background

medium which is assumed to be isotropic. In general, extinction is a summation of absorption and scattering [18].

- Phase matrix of independent scattering

For example, an expression of the phase matrix for ellipsoids with axes a, b, c and orientation Eulerian angles α, β, γ, with respective to the principal frame is given by:

$$\bar{\bar{P}}(\bar{r},\hat{s},\hat{s}') = n_0 \int da \int db \int dc \int d\alpha \int d\beta \int d\gamma \cdot p(a,b,c,\alpha,\beta,\gamma)\, \bar{\bar{L}}(\bar{r},\hat{s},\hat{s}') \quad (2.24)$$

where $p(a,b,c,\alpha,\beta,\gamma)$ represents the probability density function for the quantities a, b, c, α, β and γ; and n_0 is a constant dependent on the scattering particle. $\bar{\bar{L}}(\bar{r},\hat{s},\hat{s}')$ is the Stokes matrix. The Stokes matrix describes the relation between the incident wave and the scattered wave for a single particle [18]. Thus,

$$\bar{I}_s = \bar{\bar{L}}\left(\hat{k}_s,\hat{k}_i\right)\bar{I}_i \quad (2.25)$$

where $\bar{I}_s$ and $\bar{I}_i$ are the 4×1 Stokes vectors, respectively, for the scattered wave and the incident wave, and $\bar{\bar{L}}\left(\hat{k}_s,\hat{k}_i\right)$ is a the 4×4 Stokes matrix for a single particle. The mathematical formulations for the Stokes vectors and the Stokes matrix are usually complex, and vary with different shapes of particles, such as small spheres, ellipsoids, and random media. These mathematical formulations are documented in Tsang's books [18, 36]. They all consist of four elementary Stokes parameters given by:

$$I_v = \frac{|E_v|^2}{\eta} \quad (2.26)$$

$$I_h = \frac{|E_h|^2}{\eta} \quad (2.27)$$

$$U = \frac{2}{\eta} Re\left(E_v E_h^*\right) \quad (2.28)$$

$$V = \frac{2}{\eta} Im\left(E_v E_h^*\right) \tag{2.29}$$

where $\hat{v}$ and $\hat{h}$ denote the two orthogonal polarisation direction, $\hat{k}$, $\hat{v}$ and $\hat{h}$ following the right-hand rule, $\hat{k}$ represents the wave propagation direction. E represents the complex electric field. $*$ denotes complex conjugate; Re and Im represent the real part and the imaginary part, respectively. $\eta = \sqrt{\mu/\epsilon}$ denotes the wave impedance; μ and ϵ are the permeability and permittivity, respectively.

- Extinction matrix

For spherical particles the extinction matrix is diagonal and is a constant times the unit matrix, given by:

$$\bar{\bar{k}}_e = \begin{bmatrix} k_e & 0 & 0 & 0 \\ 0 & k_e & 0 & 0 \\ 0 & 0 & k_e & 0 \\ 0 & 0 & 0 & k_e \end{bmatrix} \tag{2.30}$$

For non-spherical particles, the extinction matrix is generally nondiagonal and given by:

$$\bar{\bar{k}}_e = \begin{bmatrix} -2Re\left(M_{vv}\right) & 0 & -Re\left(M_{vh}\right) & -Im\left(M_{vh}\right) \\ 0 & -2Re\left(M_{hh}\right) & -Re\left(M_{hv}\right) & Im\left(M_{hv}\right) \\ -2Re\left(M_{hv}\right) & -2Re\left(M_{vh}\right) & -\left(Re\left(M_{vv}\right) + Re\left(M_{hh}\right)\right) & \left(Im\left(M_{vv}\right) - Im\left(M_{hh}\right)\right) \\ 2Im\left(M_{hv}\right) & -2Im\left(M_{vh}\right) & -\left(Im\left(M_{vv}\right) - Im\left(M_{hh}\right)\right) & -\left(Re\left(M_{vv}\right) + Re\left(M_{hh}\right)\right) \end{bmatrix} \tag{2.31}$$

$$M_{jl} = \frac{i2\pi n_0}{k} \left\langle f_{jl}\left(\theta, \phi\right)\right\rangle \qquad j, l = v, h \tag{2.32}$$

where the angular bracket $\langle\rangle$ denotes average to be taken over the orientation and size distribution of the particles. f_{jl} constitutes the 2×2 scattering amplitude matrix

which obeys the relation:

$$\begin{bmatrix} E_{vs} \\ E_{hs} \end{bmatrix} = \begin{bmatrix} f_{vv} & f_{vh} \\ f_{hv} & f_{hh} \end{bmatrix} \begin{bmatrix} E_{vi} \\ E_{hi} \end{bmatrix} \tag{2.33}$$

where v, h represent vertical, horizontal polarisation, respectively; s and i denote the scattering and incident directions, respectively. (θ, ϕ) is given by representing the propagation direction $\hat{s}$ with $\hat{s}(\theta, \phi) = \sin\theta\cos\phi\hat{x} + \sin\theta\sin\phi\hat{y} + \cos\theta\hat{z}$.

- Emission vector

The emission vector $\bar{J}_e$ is given by:

$$\bar{J}_e = \bar{F}T\frac{K}{\lambda^2} \tag{2.34}$$

where K is Boltzmann's constant, T the temperature of the particle, and λ denotes the wavelength. The 4×1 vector $\bar{F}$ is given by:

$$\bar{F}(\hat{s}) = \begin{bmatrix} k_{a1}(\hat{s}_b) \\ k_{a2}(\hat{s}_b) \\ -k_{a3}(\hat{s}_b) \\ -k_{a4}(\hat{s}_b) \end{bmatrix} \tag{2.35}$$

where $\hat{s}_b$ represents the opposite direction of $\hat{s}$.

$$k_{a1}(\hat{s}) = k_{e11}(\hat{s}) - \int d\Omega' \left[P_{11}(\hat{s}', \hat{s}) + P_{21}(\hat{s}', \hat{s})\right] \tag{2.36}$$

$$k_{a2}(\hat{s}) = k_{e22}(\hat{s}) - \int d\Omega' \left[P_{12}(\hat{s}', \hat{s}) + P_{22}(\hat{s}', \hat{s})\right] \tag{2.37}$$

$$k_{a3}(\hat{s}) = 2k_{e13}(\hat{s}) + 2k_{e23}(\hat{s}) - 2\int d\Omega' \left[P_{13}(\hat{s}', \hat{s}) + P_{23}(\hat{s}', \hat{s})\right] \tag{2.38}$$

$$k_{a4}(\hat{s}) = -2k_{e14}(\hat{s}) - 2k_{e24}(\hat{s}) + 2\int d\Omega' \left[P_{14}(\hat{s}', \hat{s}) + P_{24}(\hat{s}', \hat{s})\right] \tag{2.39}$$

where k_{eij} and P_{ij} are the ith and jth element of $\bar{\bar{k}}_e$ and $\bar{\bar{P}}$, respectively, with $i, j = 1, 2, 3, 4$.

With Eqs. 2.24 to 2.39, the specific intensity in the VRT Eq. 2.23 can be calculated. However, it is obviously computational expensive. The VRT theory using four coupled integro-differential equations provides a more accurate and complete description of the physical electromagnetic phenomena involved at the expense of more complex formulation as well as computational expense. The simplified version, the scalar radiative transfer, has been developed and adapted to be used in practice [13, 16–18, 78[.

It is worth mentioning that unlike the classical definition in which only the single-particle scattering characteristics are included in the phase matrix definition, Leung Tsang *etc.* [18[give a new definition to the phase matrix as the averaged scattering cross section per unit volume of space where the volume is larger than many wavelengths and also large enough to include many particles, in order to include the coherent wave interactions among particles within wavelength scales, and the collective scattering effects of particles in the neighbourhood of each other. Similarly, the extinction coefficient is defined as the average extinction cross section per unit volume of space, and the absorption coefficient is average absorption cross section per unit volume of space.

2.5 Other analytical (theoretical) models

Analytical models utilise mathematical expressions to describe physical mechanisms involved during the propagation progress through and near the vegetation. These models generally require an appropriate description of the geometry of the vegetation media, including trunks, branches, twigs, and leaves. Due to the inherent high complexity, analytical models often use numerical approximations and simplified geometrical models to provide valuable solutions [14[.

The Lindenmayer systems [36, 57–59] provide a possibility of simulating the growth stages of a plant by controlling their rewriting rules in the generation process of plant structure, and consequently realistic plant structures can be generated by

adding variation to the rewriting rules [60–64]. An example of a three-dimensional bush-like tree structure generated by a bracketed Lindenmayer system is illustrated in Fig. 2.7.

Figure 2.7: A 3D bush-like tree structure generated by the Lindenmayer system [58]

The Lindenmayer systems may be used to generate accurate computer representation of vegetation bodies for modelling radiowave propagation and offer an interesting alternative to the RET. However at the stage of conducting this research project the RET is far more established as a readily available tool, provided the aspects investigated in this program are included in its application. Lindenmayer systems are therefore presented as an interesting future alternative but not investigated further.

A layered structure of modelling the forest volume has been proposed in [65–68] according to various densities. This is shown in Fig. 2.8, in which the forest was partitioned into four distinct dielectric layers: the semi-infinite free space above the forest, *e.g.* the air layer, the canopy layer, the trunk layer and the semi-infinite

ground layer beneath the forest volume. In the stratified models, vegetation media in individual layers are assumed to be isotropic and homogeneous [12–14,68], consequently the propagation characteristics of each layer are considered to be constant.

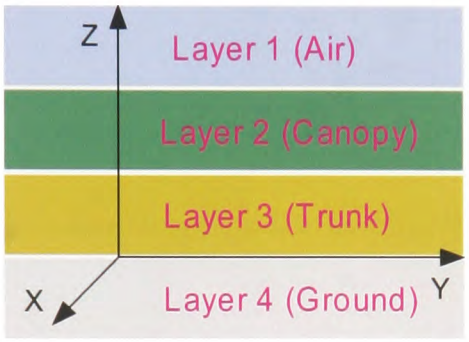

Figure 2.8: Model of a four-layered forest structure

In contrast to modelling the vegetation volume as homogeneous media, other approaches consider the forest to be inhomogeneous, typically such as the Physical Optics (PO) method [69,70] and the Discrete Radiative Energy Transfer (dRET) model [25,26]. In addition to the aforementioned theoretical models, other popular models include: Physical Optics (PO) [69, 70], General Theory of Diffraction/Uniform Theory of Diffraction (GTD/UTD) [67,71], Michigan Microwave Canopy Scattering Model (MIMICS) [72–74], Method of Moments (MoM) [75], Finite Difference Time Domain (FDTD) [12, 76] , Green Function [18] and Parabolic Equation [77].

The Physical Optics (PO) method [69, 70] uses simple geometrical shapes to model the forest elements, typically cylinders for trunks, and flat circles or ellipses for leaves. In this model, the properties of a tree are characterised by the mean field, the attenuation, and phase delay. The PO theory and multiple Kirchhoff-Huygens integration are then used to evaluate the diffracted field at each of the successive absorbing/phase half-screens up to the mobile receiver [12–14]. Trees are represented as an ensemble of leaves and branches having prescribed location and orientation statistics, as shown in Fig. 2.9.

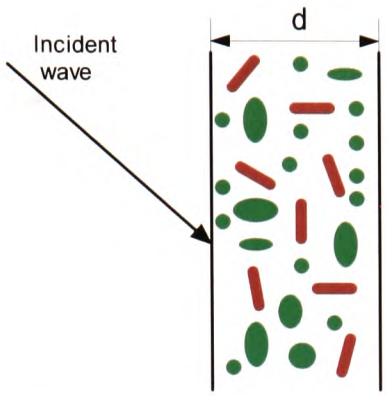

Figure 2.9: Incident plane wave on slab with thin disc and cylinders [13]

The General Theory of Diffraction/Uniform Theory of Diffraction (GTD/UTD) models are ray-based models [67, 71], and are applicable at relative high-frequency bands, which means that the object dimensions are usually more than a few wavelengths. The GTD/UTD provides a mathematical description of the interactions of rays with specific geometries. The definition of ray-tracing interactions indicates that the illuminated object must be placed in the far-field region of the source [12,13].

The Michigan Microwave Canopy Scattering (MIMICS) model is also based on the theory of RET, and considers both co- and cross-polarised scattering within the vegetation canopy [72,73]. In the MIMICS model, the forest is treated as a structure of three-layer corresponding to canopy, trunk, and ground. Characteristics such as the average height and diameter of the canopy size are counted in the first layer, the canopy-layer modelling; the trunk's height, diameter, and density are included in the second layer, the trunk-layer modelling; and the ground-layer modelling considers factors such as dielectric properties and roughness of the soil surface. A later version of the MIMICS model was developed to accommodate the case of nonuniform forest canopy modelling, called Multi-MIMICS [74].

The Method of Moments (MoM) transforms a complex integral equation into a set of linear equations, which can be solved using numerical techniques [1]. In [75], a numerical solution combined the MoM with Monte Carlo simulations is utilised to evaluate the scattering effect in sparsely distributed tree trunks. The canopy of the

forest was assumed to be homogeneous and the scattering inside the forest could be ignored. This method only counts the components from the direct transmitting in the boresight, the reflected from the upper and lower interfaces, and the diffracted or lateral waves along the air-to-vegetation interface [14].

The Finite Difference Time Domain (FDTD) is one of the widest applied techniques in the field of electromagnetic computation [12]. The FDTD approach allows near and far-field analysis, and visualisation of the interactions of the individual scatterers inside the canopy with the incident plane wave. The Radar Cross Section (RCS) of a single leaf can be calculated using the FDTD method, and furthermore a complex tree structure can be modelled. Using FDTD methods to model vegetation especially at millimetre wave frequencies with realistic vegetation sizes requires large computational effort and may lead to very long run times [12]. Detailed applications and simulations based on the FDTD methods can be found in literature [12, 76].

The Green Function and Parabolic Equation (PE) are two important full wave methods. Applications of such methods require the full geometric knowledge of the propagation medium, consequently are relatively complex and computational expensive. More literature regarding the two approaches can be found in [18, 67, 68, 77].

2.6 Summary and interim conclusion

It is important for radio planners and service suppliers to predict excess attenuation of radiowave propagating through vegetation. Models which are capable of predicting accurately and effectively have been reported in [13, 34, 43]. Initially, empirical and semi-empirical models offer simple mathematical formulation for the prediction results. These models, however, lack the ability to describe electromagnetic propagation mechanisms involved during the prediction process. Consequently, theoretical analysis models such as the Radiative Energy Transfer were developed, which provide in-depth insight of the propagation process at the expensive of more complex mathematical computation.

The fundamental model covered in this research project is the scalar Radiative Energy Transfer, which assumes the vegetation volume as a homogeneous medium with semi-infinite physical size. This chapter summarises popular prediction models. Comments are given by the author as to their applicability for the studies presented in this work. In the next chapter, emphasis will be given to the RET theory. The RET theory will be present with comprehensive mathematical explanation and graphical demonstration. The sensitivity of the RET results to variations of the input parameters will be demonstrated. Furthermore, methods to extract the essential input parameters of the RET theory will also be introduced. Further literature reviews on the topic of various deconvolution studies are described in chapter 6.

Chapter 3

The RET theory and input parameter extraction

3.1 Introduction

This chapter first provides a detailed enough description for an understanding of the general working and the mathematical formulation of the RET. Particular care has been taken to present the RET model in a clearly structured manner, often not found in this way in the literature, *e.g.* [16[. As part of this research project a MATLAB code has been developed and rigorously verified to produce all the RET modelling results in this thesis. The later part of this chapter then details the importance of the input parameter accuracy as well as the methods of extracting these parameters from measurements.

The analytical solutions based on the transport theory were developed in order to address complex multiple scattering phenomena [17]. Based on Maxwell's differential equations, the analytical theory is capable of describing thoroughly the electromagnetic phenomena taking place inside almost any medium. However, this capability depends on comprehensive knowledge of the medium's structure and geometry. Accurate description of position and orientation of each individual element becomes essential to attain mathematical rigour for describing the scattering and re-scattering phenomena occurring when radiowaves propagate through vegetation. In

reality, such detailed description of the propagation media is rarely available since it is usually impractical to obtain information of such complexity [13]. Instead of utilising the elementary wave equations, the transport theory, alternatively, concentrates directly on the transport of the energy throughout a medium consisting of randomly distributed particles. Although this theory is heuristic and lacks the mathematical rigour of the analytical theory, the Radiative Energy Transfer theory is a widely used method to model radiowave propagation through random media [17].

It is worth mentioning that only absorption and scattering events, no emission, are considered in scalar RET theory. The Radiative Energy Transfer approach is a heuristic treatment of multiple scattering of radiation, which assumes that no correlation between fields exists, resulting in the addition of power terms, rather than the addition of fields [55]. The RET theory provides an evident description of energy distribution, for radiowave propagation around and through vegetation. This research project aims to improve the method of input parameter extraction for the RET theory. The principle formulation of the RET with its application for radiowave propagation through vegetation is summarised in the following sections. Section 3.5 illustrates the sensitivity of the RET modelling results to variations in the input parameters. Section 3.7 concentrates on methods to extract the RET input parameters.

3.2 Brief RET theory description

At microwave and millimetre frequencies, the signal wavelengths become comparable to or smaller than the physical dimensions of the scattering particles including trunks, branches, twigs, leaves or needles, and fruits, in a forest. As a consequence, the forest medium yields strong forward scattering and its scatter characteristic, known as the phase function, can be represented by a pronounced forward lobe with an isotropic background [16, 78]. With the existence of this phase function, the medium is characterised by four parameters: the absorption cross section per volume k_a, the scatter cross section per volume k_s, the beamwidth β of the forward

scatter lobe, and the ratio α of the forward scattered power over the total scattered power.

In a vegetation medium containing random particles, the electromagnetic field can be divided into two parts [13, 14, 16, 17, 53, 78]:

- The **coherent component** is the average field and has a well-defined direction of propagation and a predominantly well-defined polarisation at any point in the vegetation medium. It suffers from mainly absorption and some scattering, and hence has a comparatively high attenuation rate.

- The **incoherent component** is the zero-mean field and consists of many wave trains propagating in various directions. It does not have a unique direction of propagation but is characterised by a directional spectrum at any point in the vegetation medium. It is generated by scattering and decreased by absorption, consequently has a lower attenuation rate.

While the radiowave is propagating through the vegetation, the coherent component, initially, enters at the air-to-vegetation interface, dominates at short distances and decreases with a relatively high attenuation rate. At large vegetation depth, the incoherent component takes over with a reduced attenuation rate, and consequently leads to significant beam broadening and depolarisation. In the RET theory the fundamental quantity, the specific intensity $I(\bar{r}, \hat{s})$, is defined as the power per unit area and per unit solid angle propagating at point $\bar{r}$ into the direction $\bar{s}$. Therefore, $I(\bar{r}, \hat{s})$ is given by:

$$I(\bar{r}, \bar{s}) = \frac{dP(\bar{r}, \hat{s})}{da d\omega} \tag{3.1}$$

where $P(\bar{r}, \hat{s})$ represents the power at point $\bar{r}$ with the direction $\hat{s}$; da is the area of the surface element normal to the unit vector $\hat{s}$, and $d\omega$ is the differential of the solid angle Ω centred about $\bar{r}$, shown as in Fig. 3.1.

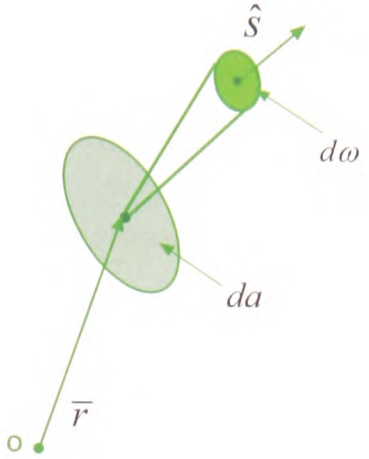

Figure 3.1: Schematic definition of specific intensity $I(\bar{r}, \bar{s})$

The fundamental equation of the RET theory is the transport equation, which can be represented in terms of the specific intensity $I(\bar{r}, \hat{s})$ according to the energy conservation theorem [16, 17]. Consider a cylinder-shape scatter with volume $dV = da \cdot dL$, shown as in Fig. 3.2, which is centred at point $\bar{r}$ and whose axis has the direction of the unit vector $\bar{s}$.

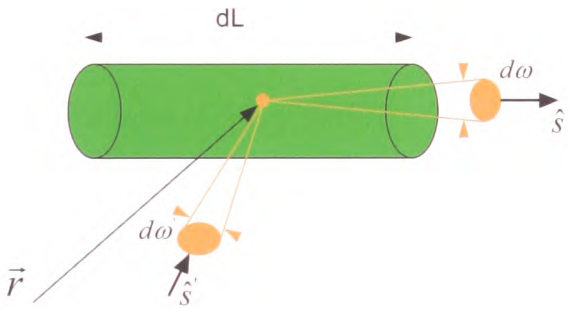

Figure 3.2: A cylinder-shape scatterer in the RET theory

Two independent effects will occur as a consequence of energy conversion as radiowave propagates through a particular scatter:

- Reduction of the power in the direction of propagation due to absorption and

scattering. The amount of variation of the specific intensity is given by

$$dI_1 = -(k_a + k_s)\, I(\bar{r}, \hat{s})\, dL \tag{3.2}$$

where k_a and k_s denote the absorption and scattering cross section per unit volume of the vegetation medium; dL is length of the scatterer. $I(\bar{r}, \hat{s})$ represents the specific intensity at location $\bar{r}$ and in the direction $\hat{s}$.

- A fraction of the power propagating in a random direction $\hat{s}'$ will be redirected into the direction $\hat{s}$ by scattering within the scatterer. This effect will collaterally contribute a positive increase to $I(\bar{r}, \hat{s})$. The amount of increment is represented as

$$dI_2 = \frac{1}{4\pi} k_s \iint_{4\pi} p(\hat{s}, \hat{s}')\, I(\bar{r}, \hat{s}')\, d\omega' dL \tag{3.3}$$

where the integration is performed over all spatial directions $\hat{s}'$. The $p(\hat{s}, \hat{s}')$ is the phase function and represents the scatter characteristic of the vegetation medium. $p(\hat{s}, \hat{s}')$ is usually assumed normalised such that

$$\frac{1}{4\pi} \iint_{4\pi} p(\hat{s}, \hat{s}')\, d\omega' = 1 \tag{3.4}$$

Consequently, the total variation of the specific intensity $I(\bar{r}, \hat{s})$ over the length dL of the volume element dV is the sum of dI_1 and dI_2:

$$dI = dI_1 + dI_2 \tag{3.5}$$

Substituting Eqs. 3.2 and 3.3 into Eq. 3.5:

$$\frac{dI(\bar{r}, \hat{s})}{dL} = -(k_a + k_s)\, I(\bar{r}, \hat{s}) + \frac{k_s}{4\pi} \iint p(\hat{s}, \hat{s}')\, I(\bar{r}, \hat{s}')\, d\omega' \tag{3.6}$$

Eq. 3.6 is the scalar formulation of the RET transport equation. A forcing term may appear on the right side of the Eq. 3.6 if emission is considered or a source is located inside the medium. Eq. 3.6 holds on the assumption that all signal sources

are located outside the vegetation medium [16, 17]. More precisely, the transmitter antenna is placed outside the forest at a certain distance, which is far enough away from the air-to-vegetation interface to guarantee far-field radiation characteristics, while the receiver antenna is situated within the forest volume.

3.3 Mathematical formulation of the RET theory

The geometry model illustrated in Fig. 3.3 is utilised to describe microwave and millimeter wave propagation in the vegetation medium. In this geometry model the vegetation halfspace is separated from the air halfspace by an infinite planar interface, the air-to-vegetation interface. The vegetation volume is characterised as a statistically homogeneous medium consisting of random scattering particles. The absorption and scatter coefficients, k_a and k_s, are considered independent of location $\bar{r}$, that is, k_a and k_s do not vary with $\bar{r}$. Moreover the phase function $p(\hat{s}, \hat{s}')$ is assumed to depend only on the scatter angle $\gamma = \cos^{-1}(\hat{s}, \hat{s}')$ subtended by the directions $\hat{s}$ and $\hat{s}'$.

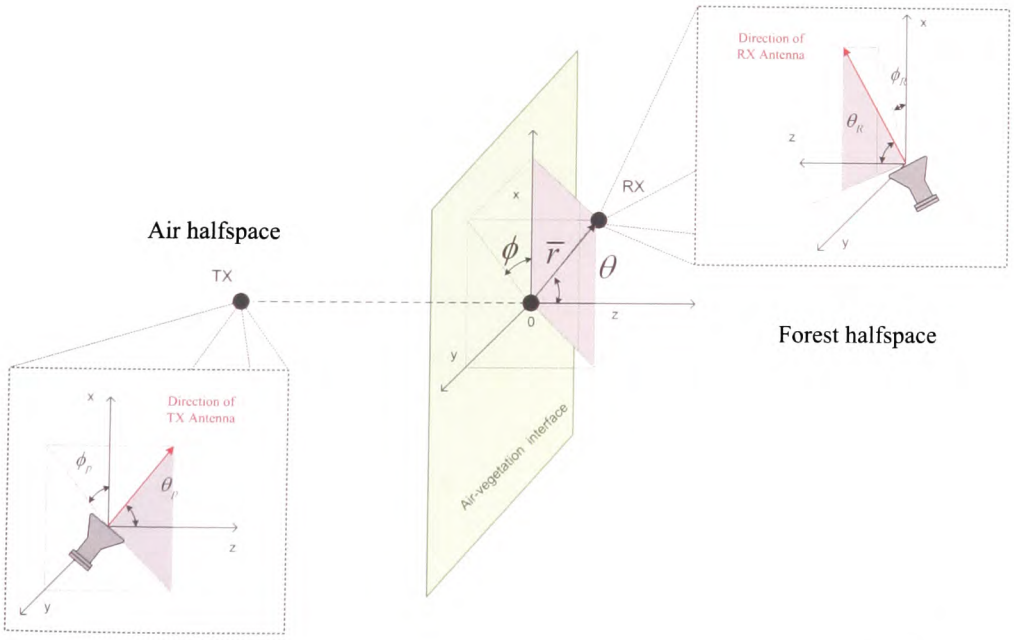

Figure 3.3: Geometry model of the vegetation medium and its coordinates used in the RET theory [14]

Furthermore, the field incident upon the air-to-vegetation interface can be described as a plane wave because the transmitter antenna is placed far away from the interface in the air halfspace [16[. The incidence of the plane wave can be perpendicular to the air-to-vegetation interface or oblique at an angle. The geometry of the incident wave may be described by the coordinate system illustrated in Fig. 3.3. In this particular coordinate system, the Z axis is normal to the interface, and the interface is set to coincide with the plane $Z = 0$. θ is the angle counted from the positive Z axis; and ϕ represents the projected angle in the plane Z = constant. With the assumptions above, it is evident that the specific intensity I exclusively relies on the Z coordinate and angles θ and ϕ, but is independent of the cross-sectional coordinates X and Y. The transport equation 3.6 is then simplified to

$$\cos\theta \frac{\partial I(Z,\theta,\phi)}{\partial Z} = -(k_a + k_s) I(Z,\theta,\phi) + \frac{k_s}{4\pi} \int_0^{2\pi} \int_0^{\pi} p(\gamma) I(Z,\theta',\phi') \sin\theta' d\theta' d\phi' \tag{3.7}$$

where γ represents the scatter angle, given by $\cos\gamma = \cos(\phi - \phi')\sin\theta\sin\theta' + \cos\theta\cos\theta'$.

3.3.1 The boundary condition

The characteristics of the incident wave at the boundary are used to solve Eq. 3.7. At the air-to-vegetation interface, $Z = 0$, the specific intensity I is determined by the incident wave for all forward directions, *i.e.* $0 \leq \theta \leq \frac{\pi}{2}$. Hence, the specific intensity I starting to enter the vegetation medium is given by [16[:

$$I(Z = 0,\theta,\phi) = S_p \frac{\delta(\theta - \theta_p)}{\sin\theta} \delta(\phi - \phi_p) \tag{3.8}$$

where δ denotes the delta function; S_p is the Poynting vector; θ_p and ϕ_p represent the propagation angles of the incident wave, respectively.

Since the vegetation is a dissipative medium, it indicates that the specific inten-

sity I finally must vanish at infinity. This leads to

$$I(Z \rightarrow +\infty, \theta, \phi) \rightarrow 0 \tag{3.9}$$

Further physical insight of radiowave propagation through vegetation can be gained by splitting the specific intensity I into two parts:

$$I(Z, \theta, \phi) = I_{ri}(Z, \theta, \phi) + I_d(Z, \theta, \phi) \tag{3.10}$$

where I_{ri} represents the reduced incident intensity or the coherent components; and I_d denotes the diffused intensity or the incoherent components. At $Z = 0$, the incident wave is just impinging upon the air-to-vegetation interface, which indicates that the scattering effect has not taken place yet. The specific intensity $I = I_{ri}$ leads to the scattering term in Eq. 3.7 being suppressed. Hence,

$$I_{ri}(0, \theta, \phi) = S_p \frac{\delta(\theta - \theta_p)}{\sin\theta} \delta(\phi - \phi_p) \quad 0 \leq \theta \leq \frac{\pi}{2} \tag{3.11}$$

$$\cos\theta \frac{\partial I_{ri}}{\partial Z} + (k_a + k_s) I_{ri} = 0 \quad Z \geq 0 \tag{3.12}$$

Eq. 3.12 is a first order linear differential equation and Eq. 3.11 represents one of its solutions, consequently Eq. 3.12 can be solved in closed form:

$$I_{ri}(Z, \theta, \phi) = \left(S_p \frac{\delta(\theta - \theta_p)}{\sin\theta_p} \delta(\phi - \phi_p) \right) e^{-\frac{k_a + k_s}{\cos\theta_p} Z} \quad Z \geq 0 \tag{3.13}$$

Eq. 3.13 shows that I_{ri} decays exponentially with the vegetation depth, and its attenuation rate is determined by the extinction coefficient $k_e = k_a + k_s$. The diffused intensity I_d is equivalent to zero at the air-to-vegetation interface as the scattering effect happens only inside the vegetation medium, and will eventually reduce to zero due to the dissipative characteristic of the vegetation medium. Hence,

$$I_d(Z, \theta, \phi) = \begin{cases} 0 & Z = 0 \; and \; 0 \leq \theta \leq \frac{\pi}{2} \\ 0 & Z \rightarrow +\infty \end{cases} \tag{3.14}$$

Using Eq. 3.10 and considering the diffused intensity only, the transport equation 3.7 is transformed into:

$$\begin{aligned}\cos\theta\frac{\partial I_d}{\partial Z}+(k_a+k_s)\,I_d &= \frac{k_s}{4\pi}\int_0^{2\pi}\int_0^{\pi} p(\gamma)\,I_d(Z,\theta',\phi')\sin\theta' d\theta' d\phi' \\ &+ \frac{k_s}{4\pi}S_p e^{-\frac{k_a+k_s}{\cos\theta_p}Z}p(\gamma_p)\end{aligned} \tag{3.15}$$

where γ_p is the angle subtended by the directions of I_{ri} and I_d. The second term on the right hand side of Eq. 3.15 represents the transformation from the coherent component I_{ri} into the incoherent component I_d due to the scattering effect. The problem of depolarisation due to the scattering effect is well documented in literature [16–18[and thus has not been addressed in this research programme.

3.3.2 The characteristics of the scattering effect

Since, in a vegetation medium, all scatter elements are usually large compared to the microwave and millimeter wavelengths, strong forward scattering will occur and the phase function P is assumed to consist of a narrow Gaussian forward lobe superimposed over an isotropic background [16], and given by mathematical expressions as:

$$p(\gamma)=\alpha q(\gamma)+(1-\alpha) \tag{3.16}$$

where

$$q(\gamma)=\left(\frac{2}{\beta}\right)^2 e^{-\left(\frac{\gamma}{\beta}\right)^2} \tag{3.17}$$

is the Gaussian forward lobe of the phase function p and $(1-\alpha)$ represents the isotropic background. Separating the diffused intensity term I_d into two parts:

$$I_d(Z,\theta,\phi)=I_1(Z,\theta,\phi)+I_2(Z,\theta,\phi) \tag{3.18}$$

where I_1 is determined primarily by the forward lobe $q(\gamma)$ of the phase function and I_2 is the remainder of I_d which depends mainly on the isotropic background [16[.

Thus, Eq. 3.15 is separated into two equations:

$$\cos\theta\frac{\partial I_1}{\partial Z} + (k_a + k_s)\, I_1 = \alpha\frac{k_s}{4\pi}\int_0^{2\pi}\int_0^{\pi} q(\gamma)\, I_1(Z,\theta',\phi')\sin\theta' d\theta' d\phi' + \alpha\frac{k_s}{4\pi} q(\gamma)\, S_p e^{-\frac{k_a+k_s}{\cos\theta_p}Z} \tag{3.19}$$

$$\begin{aligned}\cos\theta\frac{\partial I_2}{\partial Z} + (k_a + k_s)\, I_2 &= \alpha\frac{k_s}{4\pi}\int_0^{2\pi}\int_0^{\pi} q(\gamma)\, I_2(Z,\theta')\sin\theta' d\theta' d\phi' \\ &+ (1-\alpha)\frac{k_s}{4\pi}\int_0^{2\pi}\int_0^{\pi}\left[I_1(Z,\theta',\phi') + I_2(Z,\theta')\right]\sin\theta' d\theta' d\phi' \\ &+ (1-\alpha)\frac{k_s}{4\pi} S_p e^{-\frac{k_a+k_s}{\cos\theta_p}Z}\end{aligned} \tag{3.20}$$

In [16], approximations regarding the specific intensity I_1 and I_2 are made to simplify the process of finding the solutions for Eqs. 3.19 and 3.20. The following normalisations are introduced in order to provide explicit formulation for the solutions, I_1 and I_2.

$$\tau = (k_a + k_s)\, Z \tag{3.21}$$

$$\hat{\tau} = [k_a + (1-\alpha)\, k_s]\, Z \tag{3.22}$$

where τ in Eq. 3.21 denotes the optical density, and $\hat{\tau}$ in Eq. 3.22 denotes the reduced optical density, Z is the vegetation depth in metres. Consequently, the optical density τ is a normalised distance related to the propagation characteristics of the vegetation medium, while in the equation of the reduced optical density $\hat{\tau}$, the scattering coefficient k_s has been conveniently weighted by the amount of $(1-\alpha)$ in accordance with the level of the isotropic background.

$$\mu = \cos\theta \tag{3.23}$$

$$\mu_p = \cos\theta_p \tag{3.24}$$

$$W = \frac{k_s}{k_a + k_s} \tag{3.25}$$

$$\hat{W} = \frac{(1-\alpha)\, k_s}{k_a + (1-\alpha)\, k_s} = \frac{(1-\alpha)\, W}{1-\alpha W} \tag{3.26}$$

where Eqs. 3.23 and 3.24 use symbols μ, μ_p to represent the direction of propagation angle θ; μ, μ_p are within the range of $0 \sim 1$. Eq. 3.25 gives the definition of the parameter, albedo W, the ratio of the scattered power over the total extinguished power inside the vegetation medium. Eq. 3.26 defines the reduced albedo, in which the scattering coefficient k_s is weighted according to the level of the isotropic background.

3.3.3 Solutions of the diffused specific intensity

I_1 in Eq. 3.19 could be solved using the method of undetermined coefficients [16], and is represented as:

$$\begin{aligned} I_1(\tau,\mu,\phi) &= \frac{S_p}{4\pi}\left(e^{-\frac{\tau}{\mu_p}} - e^{-\frac{\tau}{\mu_p}} q_M(\gamma_p)\right) \\ &+ \frac{S_p}{4\pi}\left\{e^{-\frac{\tau}{\mu_p}} \sum_{m=1}^{M} \frac{1}{m!}\left(\frac{\alpha W}{\mu_p}\tau\right)^m \left[q_m(\gamma_p) - q_M(\gamma_p)\right]\right\} \end{aligned} \tag{3.27}$$

where γ_p and $q_m(\gamma_p)$ are given by:

$$\gamma_p = \cos(\phi - \phi_p)\sqrt{(1-\mu^2)\left(1-\mu_p^2\right)} + \mu\mu_p \tag{3.28}$$

$$q_m(\gamma_p) = \frac{4}{m\beta^2} e^{-\frac{1}{m}\left(\frac{\gamma_p}{\beta}\right)^2} \tag{3.29}$$

The upper limit, M, in Eq. 3.27 is chosen to be sufficiently large so that the value of I_1 no longer changes when M is increased.

An approach using the method of moments is introduced to obtain the solution for I_2 in Eq. 3.20 [16]. This technique expands the μ dependence of I_2 into a series of overlapping triangle basis functions. These triangle functions, $F_n(\mu)$, are define as illustrated in Fig. 3.4 within the range of $-1 \leq \mu \leq +1$ subdivided into N evenly spaced intervals

$$\mu_{n-1} \leq \mu \leq \mu_n \qquad n = 1, 2, \cdots N \tag{3.30}$$

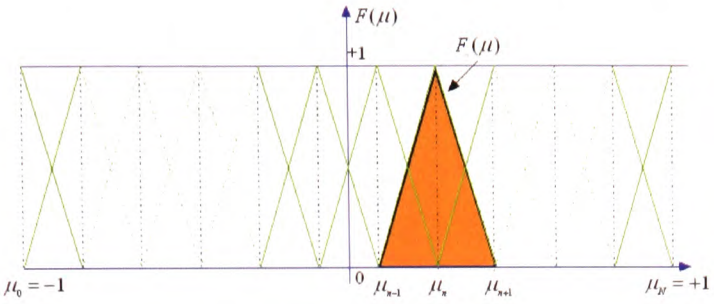

Figure 3.4: Overlapping triangular basis functions

where N is set to be odd and u_n is given by

$$\mu_n = \cos\left(1 - \frac{n}{N}\right)\pi = -\cos\left(\frac{n}{N}\pi\right) \tag{3.31}$$

Thus:

$$F_n(\mu) = \begin{cases} 0 & -1 \le \mu \le \mu_{n-1} \\ \frac{\mu-\mu_{n-1}}{\mu_n-\mu_{n-1}} & \mu_{n-1} \le \mu \le \mu_n \\ \frac{\mu_{n+1}-\mu}{\mu_{n+1}-\mu_n} & \mu_n \le \mu \le \mu_{n-1} \\ 0 & \mu_{n+1} \le \mu \le 1 \end{cases} \qquad n = 1, 2, \cdots N-1 \tag{3.32}$$

The "boundary" functions $F_0(x)$ and $F_N(x)$ have the shape of half-triangles and are given by

$$F_0(\mu) = \begin{cases} \frac{\mu_1-\mu}{\mu_1+\mu} & -1 \le \mu \le \mu_1 \\ 0 & \mu_1 \le \mu \le +1 \end{cases} \tag{3.33}$$

$$F_N(\mu) = \begin{cases} \frac{\mu-\mu_{N-1}}{1-\mu_{N-1}} & \mu_{N-1} \le \mu \le +1 \\ 0 & -1 \le \mu \le \mu_{N-1} \end{cases} \tag{3.34}$$

The final form for the solution I_2 in Eq. 3.20 is given by

$$I_2(\tau, \mu) = \frac{S_p}{2\pi}\left\{-e^{\frac{\tau}{\mu_j}}\frac{F_j(\mu)}{P_j} + \sum_{k=\frac{N+1}{2}}^{N}\left[A_k e^{-\frac{\tau}{S_k}}\frac{F_n(\mu)}{1-\frac{\mu_n}{S_k}}\right]\right\} \tag{3.35}$$

where

$$\mu_j = \mu_p = \cos(\theta_p) \tag{3.36}$$

$$P_k = \int_{-1}^{1} F_k(\mu)\, d\mu = \begin{cases} \sin\left(\frac{\pi}{N}\right)\sin\left(\frac{\pi k}{N}\right) & k = 1, 2, \cdots N-1 \\ \sin^2\left(\frac{\pi}{2N}\right) & k = 0, N \end{cases} \tag{3.37}$$

$$\frac{\hat{W}}{2}\sum_{n=0}^{N}\frac{P_n}{1-\frac{\mu_n}{S}} = 1 \tag{3.38}$$

$$\sum_{k=\frac{N+1}{2}}^{N}\frac{A_k}{1-\frac{\mu_n}{S_k}} = \frac{\delta_{jn}}{P_j} \tag{3.39}$$

where S_k denotes the attenuation coefficients which is determined numerically by the characteristic equation 3.38. Note that only positive solutions of S_k with magnitudes less than unity have physical meanings [13, 14, 16]. The amplitude factors A_k are obtained by a system of linear equations given by Eq. 3.39. This system of linear equations can be solved by either Gauss elimination or matrix inversion by rewriting Eq. 3.39 into the matrix form $A \cdot B = C$

$$\begin{bmatrix} A_{\frac{N+1}{2}} \\ \vdots \\ A_N \end{bmatrix} \cdot \begin{bmatrix} b_{\frac{N+1}{2},\frac{N+1}{2}} & \cdots & b_{\frac{N+1}{2},N} \\ \vdots & & \vdots \\ b_{N,\frac{N+1}{2}} & \cdots & b_{N,N} \end{bmatrix} = \begin{bmatrix} \frac{\delta_{1,j}}{P_j} \\ \vdots \\ \frac{\delta_{N,j}}{P_j} \end{bmatrix} \tag{3.40}$$

where

$$b_{n,k} = \frac{1}{1+\frac{\mu_n}{S_k}} \tag{3.41}$$

$$\delta_{n,m} = \begin{cases} 0 & n \neq m \\ 1 & n = m \end{cases} \tag{3.42}$$

Notice that the process of finding solutions for I_1 and I_2 follows closely the work of Johnson and Schwering [16]. Some other methods of attaining solutions for the transport equation are available in the literature [17].

3.4 Received power by the receiver antenna

The Radiative Energy Transfer theory assumes that the vegetation halfspace is illuminated by a plane wave incident from the air halfspace [16]. This assumption indicates that the transmitter antenna is placed at considerably large distance from the air-to-vegetation interface, while the receiver antenna is located inside the vegetation medium. The received power at a point in the vegetation volume is contributed by two parts: the specific intensity $I(\bar{r}, \hat{s})$ of the signal and the power radiation pattern $G_R(\gamma_R)$ of the receiver antenna:

$$P_R(\tau, \mu_R, \phi_R) = \frac{\lambda^2}{4\pi} \int_0^{2\pi} \int_{-1}^{+1} G_R(\gamma_R)\, I(\tau, \mu, \phi)\, d\mu d\phi \tag{3.43}$$

where λ denotes the wavelength; $\mu = \cos\theta$ and $\mu_R = \cos\theta_R$; θ, ϕ represent the propagation angle of the incident wave, and θ_R, ϕ_R represent the orientation of the mainbeam of the receiver antenna in accordance with Fig. 3.3. The angle γ_R is given by

$$\cos\gamma_R = \cos(\phi - \phi_R)\sin\theta\sin\theta_R + \cos\theta\cos\theta_R \tag{3.44}$$

The received power P_R depends on the location and orientation of the receiver antenna. Eq. 3.43 indicates that P_R is the integration of the specific intensity I of the signal and the power radiation pattern G_R of the receiver antenna. It is, as explained in chapter 6, a convolution process between the two components.

A highly directive antenna with narrow beamwidth, more precisely, with a Gaussian radiation pattern was chosen as the receiver. The power radiation pattern G_R was normalised such that

$$\frac{1}{4\pi} \int_0^{2\pi} \int_0^{\pi} G_R(\gamma_R) \sin\theta d\theta d\phi = 1 \tag{3.45}$$

The directivity gain of the antenna is given by $G_R(0)$. The Gauss shaped radiation pattern is given by:

$$G_R(\gamma_R) = \left(\frac{2}{\Delta\gamma_R}\right)^2 e^{-\left(\frac{\gamma_R}{\Delta\gamma_R}\right)^2} \tag{3.46}$$

where $\Delta\gamma_R$ is the effective beamwidth of the antenna, and its relation with the Half Power Beamwidth of an antenna can be represented as

$$\Delta\gamma_R = 0.6B_{HPBW} \tag{3.47}$$

The specific intensity I expressed by its coherent component I_{ri} and incoherent components I_1 and I_2 is given by Eqs. 3.13, 3.27 and 3.35, respectively. Consequently, P_R relative to the received power at the air-vegetation interface is given by

$$\begin{aligned}\frac{P_R(\tau,\mu_R,\phi_R)}{P_{MAX}} &= e^{-\left(\frac{\gamma_{RP}}{\Delta\gamma_R}\right)^2-\frac{\tau}{\mu_P}} \\ (I_1) &+ \begin{cases}\frac{\Delta\gamma_R^2}{4}\left[e^{-\frac{\hat{\tau}}{\mu_P}}-e^{-\frac{\tau}{\mu_P}}\right]\bar{q}_M(\gamma_{RP}) \\ \frac{\Delta\gamma_R^2}{4}e^{-\frac{\tau}{\mu_P}}\sum_{m=1}^{M}\frac{1}{m!}\left(\frac{\alpha W}{\mu_P}\tau\right)^m\left[\bar{q}_m(\gamma_{RP})-\bar{q}_M(\gamma_{RP})\right]\end{cases} \\ &+ \frac{\Delta\gamma_R^2}{2}\left\{-e^{-\frac{\hat{\tau}}{u_P}}\frac{F_j(\mu_R)}{P_j}+\sum_{k=\frac{N+1}{2}}^{N}\left[A_k e^{-\frac{\hat{\tau}}{S_k}}\sum_{n=0}^{N}\frac{F_n(\mu_R)}{1-\frac{\mu_n}{S_k}}\right]\right\}\end{aligned} \tag{3.48}$$

where

$$\bar{q}_m(\gamma_{RP}) = \frac{4}{\Delta\gamma_R^2+m\beta^2}e^{-\frac{\gamma_{RP}^2}{\Delta\gamma_R^2+m\beta^2}} \tag{3.49}$$

$$\cos(\gamma_{RP}) = \cos(\phi_P-\phi_R)\sqrt{(1-\mu_P^2)(1-\mu_R^2)}+\mu_R\mu_P \tag{3.50}$$

In Eq. 3.48, the received power P_R is normalised with respect to the maximum received power P_{MAX}. The maximum received power P_{MAX} is the consequence of placing the receiver antenna at the air-to-vegetation interface aligned with the direction of the incident wave, so that $\theta_R = \theta_P$, $\phi_R = \phi_P$. θ_P and ϕ_P represent the angles of the direction of the incident radiation direction [16[. P_{MAX} is given by:

$$P_{MAX} = P_R(0,\mu_P,\phi_P) = \frac{\lambda^2}{4\pi}\left(\frac{2}{\Delta\gamma_R}\right)^2 S_P \tag{3.51}$$

The first term on the right hand side of Eq. 3.48 represents the contribution of I_{ri} to the received power; the second and the third terms denote the contribution from

I_1 and I_2 respectively. So that

$$\frac{P_R}{P_{MAX}} = I_{ri} + I_1 + I_2 \tag{3.52}$$

Contributions of normalised received powers from each of the terms I_{ri}, I_1 and I_2 were calculated according to Eq. 3.48. Their effects, combined and individual, are illustrated in Fig. 3.5.

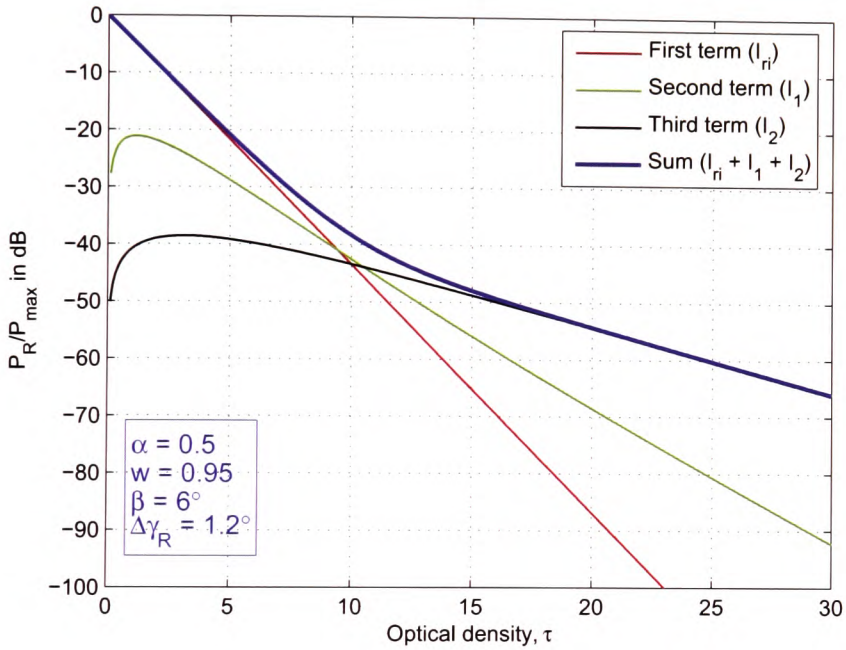

Figure 3.5: Range dependence of received power, contributions of individual terms and sum, under normal incidence ($\theta_p = 0^o$)

Based upon the RET theory, Fig. 3.5 predicts the range dependence of each term as well as the resulting overall attenuation curve as a function of the optical density in a logarithmic scale. The graphs are evaluated for the case corresponding to $\alpha = 0.5$, $W = 0.95$, $\beta = 6^o$ and $\Delta\gamma_R = 1.2^o$. Due to the different physical influences on the three different terms I_{ri}, I_1 and I_2, three distinct areas can be identified [13]:

I The coherent component I_{ri} has a relatively high attenuation rate, corresponding to the extinction coefficient k_e of the vegetation medium. At small distances

$\tau \leq 5$, I_{ri} dominates but declines linearly versus optical density on the decibel scale. I_{ri} falls below about 20 dB of the overall attenuation curve at around $\tau = 17$, which indicates that contribution of I_{ri} can be safely ignored afterwards.

II The incoherent component I_1 increases when $\tau \leq 2$ as the scattering effects just start happening inside the vegetation medium, reaches its maximum at $\tau = 2$ and then decreases afterwards. When $\tau \leq 9$, the value of I_1 is significantly greater than that of I_2; and furthermore I_1 surpasses I_{ri} and becomes the greatest contributor to the overall attenuation curve within the range of $9 \leq \tau \leq 11$. Finally, I_1 decays with a rate slower than that of I_{ri} but faster than that of I_2.

III The incoherent component I_2 takes over the role of the greatest contributor at large distances, more precisely $\tau \geq 11$; and moreover, the I_2 term exhibits a similar slope to the overall attenuation curve after $\tau \geq 17$ due to its slowest attenuation rate. Eventually, I_2 vanishes due to dissipation of the medium but at a much slower decay rate.

Fig. 3.5 shows the range dependence of the received power of each one of the individual terms I_{ri}, I_1 and I_2, as well as their combined behaviour as a function of the optical density. The overall attenuation curve decays linearly at relatively high rate initially as the receiver antenna moves away from the air-to-vegetation interface. As the distance increases, the attenuation rate decreases significantly due to the effect of the scattering in the medium. As the depth increases further, the attenuation rate reduces further as the received signal becomes predominantly affected by the isotropic scattering. Alternatively, the directional dependence of the received power can be investigated. This is done by keeping the parameter of optical density τ constant, and displaying the normalised received power as a function of the rotation angle of the receiver antenna. This plot is called the directional spectrum. An example is shown in Fig. 3.6 for the case corresponding to $\alpha = 0.5$, $W = 0.75$, $\beta = 6^o$, $\Delta\gamma_R = 1.2^o$ and $\theta_p = 0^o$. Fig. 3.6 presents the directional spectrum centred at the rotation angle $= 180^o$. To better observe the characteristics of the directional spec-

trum with varying optical density, Fig. 3.7 presents a plot of the directional spectrum centred at the rotation angle = 0^o for the same case.

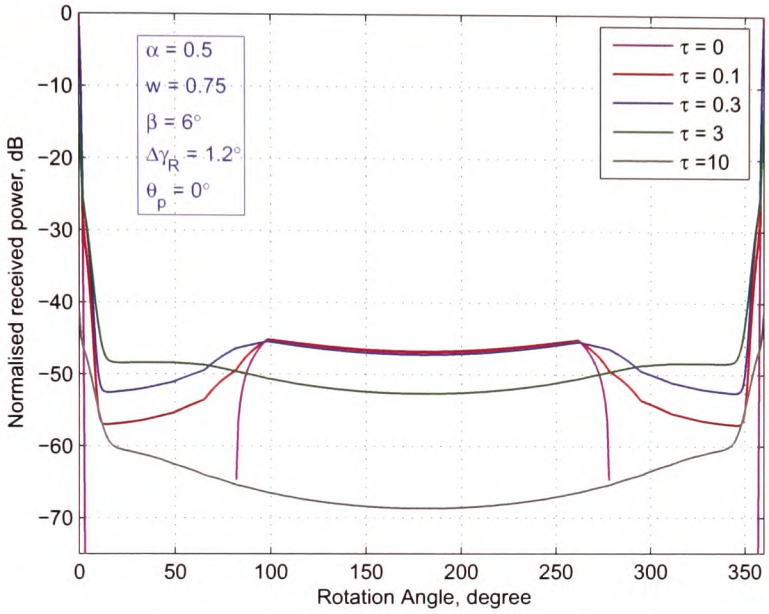

Figure 3.6: Directional spectrum of the received power centred at the rotation angle = 180^o

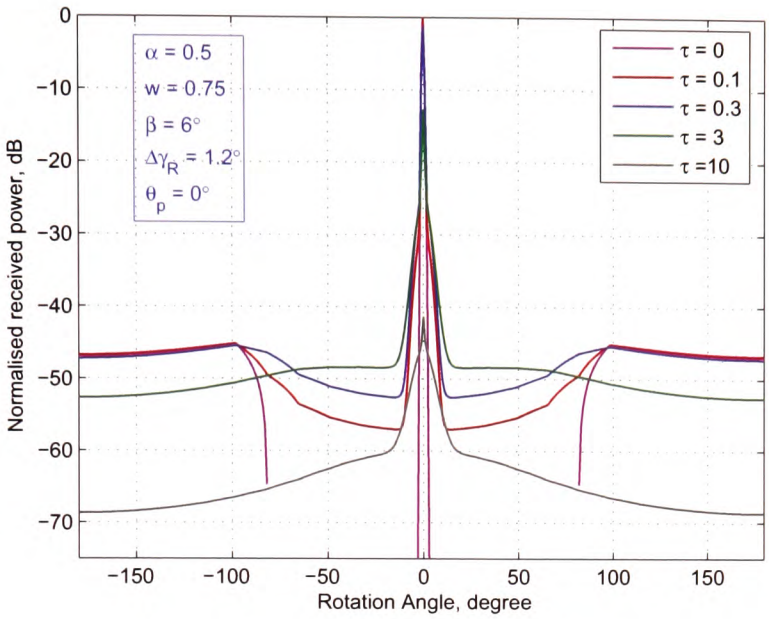

Figure 3.7: Directional spectrum of the received power centred at the rotation angle $= 0^o$

Fig. 3.7 shows that the directional spectrum with $\tau = 0$ resembles more a pulse shaped curve, while as τ increases the peak value of the directional spectrum decreases accompanying noticeable broadening of the beamwidth. At the air-to-vegetation interface, $\tau = 0$, the propagating waves contain coherent components only; and the coherent waves have a well-defined direction. Consequently, the directional spectrum is a pulse shape. While moving into the vegetation, the scattering effect occurs; the incoherent components are generated and increasing; and the peak value of the directional spectrum reduces rapidly in accordance with the decay rate of the coherent component I_{ri}. Moving further into the vegetation the pulse shaped directional spectrum broadens significantly with vegetation depth and will eventually resemble a Gaussian shape.

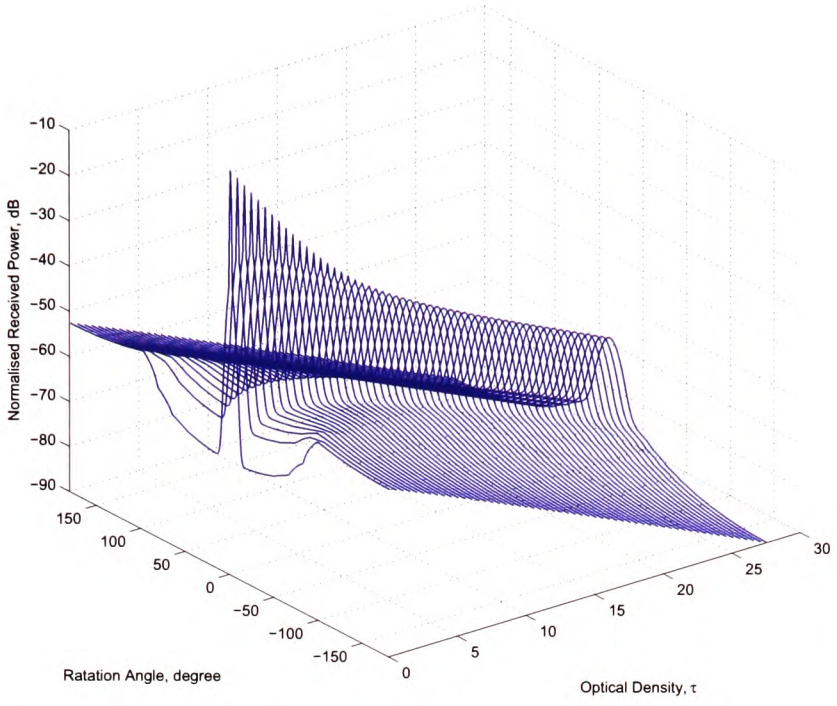

Figure 3.8: 3D demonstration of combined range and directional dependence of the received power

To demonstrate the process of shape-transforming of the directional spectrum profile more intuitively, a three-dimensional figure 3.8 is presented. Tracing the maxima (rotation angle = 0^o) will result in the graph of I, *i.e.* the sum of I_{ri}, I_1 and I_2 in Fig. 3.5. A cross-section of the graph in Fig. 3.8 at a constant optical density will give the function of the normalised received power vs. the rotation angle as shown in Fig. 3.7. Fig. 3.8 clearly indicates both reduction in amplitude and change of the shape of the main lobe of the directional spectrum with increasing optical density.

3.5 Sensitivity of RET excess loss modelling results due to input parameter variation

In this section the sensitivity of the excess loss with vegetation depth prediction of the RET to the variation of the input parameters will be quantified. All examples in this section have been calculated for normal incidence of the transmitted signal with respect to the air-vegetation interface.

In the first 3 examples only one parameter is altered each time the others as well as all conditions are kept constant throughout. The next 2 examples show the cumulative effect of altering several parameters at the same time. All these examples show the excess attenuation as a function of the optical density τ. The influence of varying k_e is also demonstrated, here the excess attenuation is shown as a function of the distance in metres. Finally the influence of the receiver antenna beamwidth on the prediction results is also demonstrated.

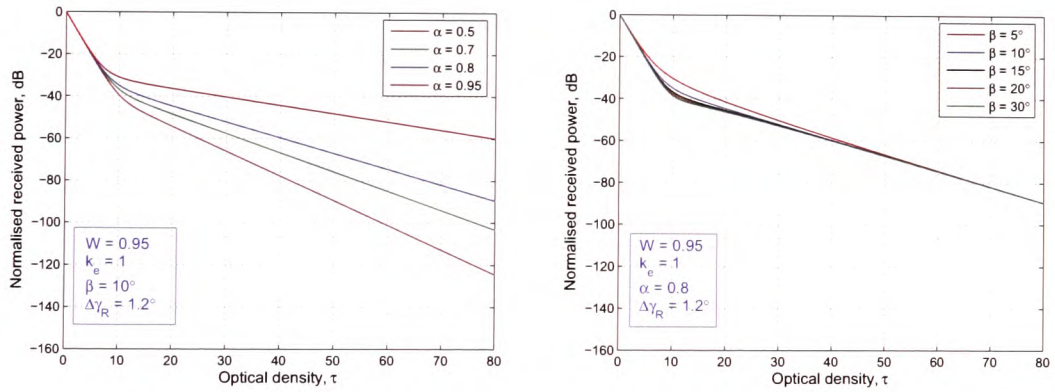

Figure 3.9: Influence of RET input parameters on excess attenuation prediction: (a) α and (b) β

Fig. 3.9 shows the influence of variation of parameters α (a) and β (b) on the excess attenuation prediction. Variation of α has the greater influence on the prediction, both final slope and location of the turnover points are affected. Variation of β mainly changes the location of the turnover points, larger variation can be observed for varying β if the receiver antenna beamwidth is larger.

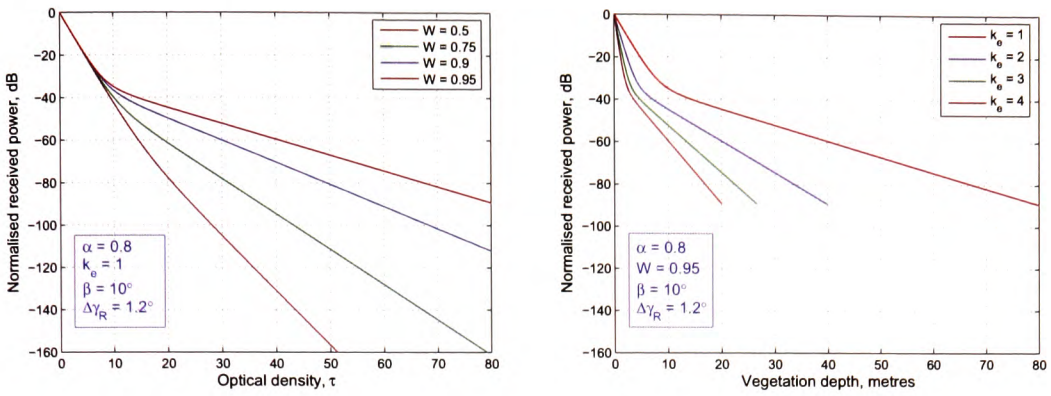

(a) (b)

Figure 3.10: Influence of RET input parameters on excess attenuation prediction: (a) W and (b) k_e

Fig. 3.10a demonstrates that varying albedo (W) mainly influences the final decay rate very significantly. As expected variation of parameter k_e leads to a variation in abscissas scale of the whole graph since $\tau = k_e \cdot d$ (Eq. 3.21).

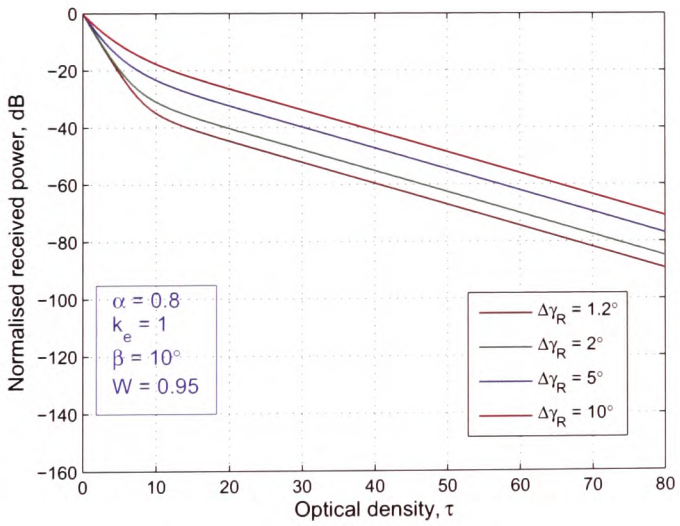

Figure 3.11: Influence of the receiver antenna beamwidths on attenuation curve under normal incidence

Increasing the receiver antenna beamwidth leads to a repositioning of the turnover points towards lower values of τ, hence changing the final excess attenuation level but not the rate of attenuation as shown in Fig. 3.11.

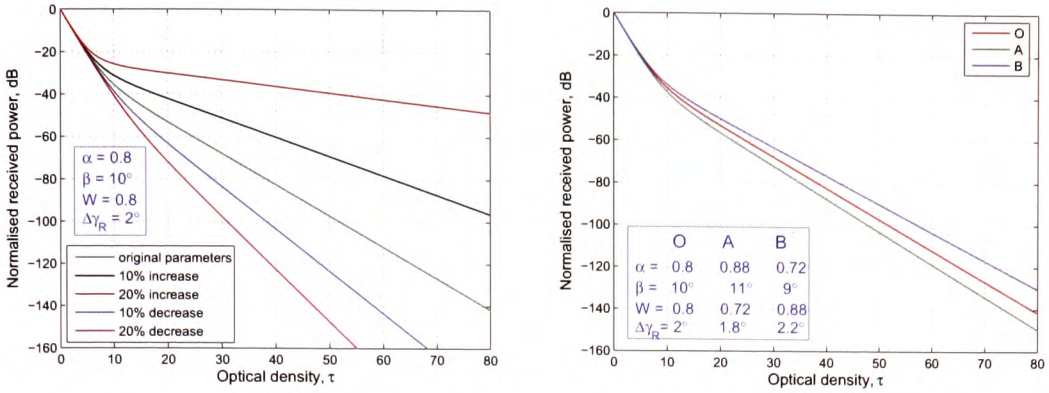

(a) (b)

Figure 3.12: Influence of overall variation of the RET input parameters on attenuation curve under normal incidence

The effect of the variation of all 4 input parameters simultaneously is shown in Fig. 3.12. In Fig. 3.12a the effect of either increasing or decreasing all 4 input parameters by 10% and 20% compared to their original levels is demonstrated. The differences in predicted attenuation rate are obviously very significantly. Part b of Fig. 3.12 shows the effect of either increasing α and β by 10% in value each, while decreasing W and $\Delta\gamma_R$ by 10% at the same time as shown by trace A. Trace B illustrates the prediction result when α and β decreased by 10% each, while W and $\Delta\gamma_R$ are now increased in value by 10%.

The result shows that the input parameters are independent of each other [16,17] and therefore decreasing one set of parameters by a certain value is not necessary compensated by altering the remaining parameters by the same amount in the opposite direction.

		original input parameters values			
		$\alpha = 0.8$	$\beta = 8^o$	$W = 0.8$	$\Delta\gamma_R = 2^o$
Fig. 3.12a	case 1	+10%	+10%	+10%	+10%
	case 2	+20%	+20%	+20%	+20%
	case 3	−10%	−10%	−10%	−10%
	case 4	−20%	−20%	−20%	−20%
Fig. 3.12b	case A	+10%	+10%	−10%	−10%
	case B	−10%	−10%	+10%	+10%

Table 3.1: variation of the RET input parameters in values Fig. 3.12

This subsection clearly indicates that the RET prediction results show significant sensitivity to any input parameter variation. This sensitivity is especially pronounced if all input parameters are varied in the same direction. It is also demonstrated that variation of one subset of parameters cannot be compensated for by altering the value of the other set of parameters in the opposite direction. It is therefore apparent that the prediction accuracy of the RET is highly dependent on the accuracy of the input parameters.

3.6 Influence of antenna radiation pattern

In transport theory, it is assumed the various scattered wave trains are uncorrelated in phase [16]. Hence the power can be added in real quantities at the receiver side. The radiation pattern of a typical antenna, however, is not an ideal pulse but a curve comprised of a mainlobe and significant sidelobes. While placing the receiver inside the vegetation, both the mainlobe and sidelobes are receiving signals from rays both being directly transmitted from the transmitter and scattered from all the trees surrounding the antenna. This can be considered as a multipath situation and the receiver antenna is placed in a combined field arising from the interaction of a continuous distribution of transmitting sources [79].

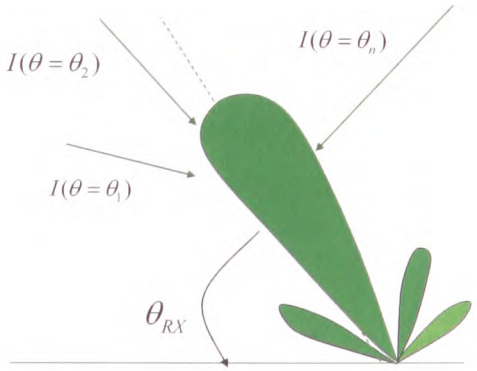

Figure 3.13: Signal distribution at the receiver side

This situation can be geometrically depicted as shown in Fig. 3.13. Its strength can be mathematically calculated as the weighted sum of all directional contributions [14[and represented by:

$$\begin{aligned} p_{RX}(\theta_{RX}) &= i(\theta_1)g_{RX}(\theta_1 - \theta_{RX}) \\ &+ i(\theta_2)g_{RX}(\theta_2 - \theta_{RX}) \\ &+ \cdots \\ &+ i(\theta_n)g_{RX}(\theta_n - \theta_{RX}) \\ &= \sum_{\theta_j} i(\theta_j)g_{RX}(\theta_j - \theta_{RX}) \end{aligned} \tag{3.53}$$

where p_{RX} represents the measured power strength, g_{RX} denotes the receiver antenna radiation pattern. θ_{RX} and θ_j respectively represent the directions of the antenna mainlobe and an individual incident wave j, $j = 1, 2, \cdots n$. Their values are with respect to the same horizontal reference angle. i represents the density of the power being transmitted just before reaching the receiver. Its distribution depends on the vegetation media only [80[, and is therefore not related to the receiver antenna. Here its phase term can be ignored, an assumption can be justified when the receiver is receiving a randomly scattered signal from vegetation surrounding the antenna [79].

As θ_j can be infinitely small approaching a continuous angle, the discrete Eq.3.53 becomes:

$$p_{RX} = \int_{\theta} i(\theta)\, g_{RX}(\theta - \theta_{RX}) \tag{3.54}$$

Eq. 3.54 indicates that the relationship between the phase function, the receiver antenna radiation pattern and the measurement pattern is a convolution product [79, 81, 82] and can be represented by:

$$p_{RX}(\theta) = i(\theta) * g_{RX}(\theta) \tag{3.55}$$

where $*$ denotes the convolution operation. According to convolution theorem, this convolution relationship is equivalent to multiplication in the transform domain after

the Fourier transform [83–85[:

$$P_{RX}(\omega) = I(\omega)G_{RX}(\omega) \tag{3.56}$$

where P_{RX}, I and G_{RX} are the Fourier transform of p_{RX}, i, and g_{RX} respectively; ω is the variable in the transform domain corresponding to θ in the original domain. Eq. 3.56 suggests that a straightforward solution to the process of deconvolution can be achieved by the inverse Fourier Transform of $I(\omega)$, which would be the result of a division of $P_{RX}(\omega)$ over $G_{RX}(\omega)$, *i.e.* $I(\omega) = \frac{P_{RX}(\omega)}{G_{RX}(\omega)}$. However the presence of random noise in the signal and the resolution limits of the computer processing can generate large spike errors in the division. These errors can consequently swamp most of the useful information contained in $i(\theta)$ after the inverse Fourier Transform. This is known as the ill-posed problem [81] and will be discussed further in chapter 6.

3.7 Methods of input parameter optimisation and extraction

In the previous section it was shown that a set of four input parameters k_a, k_s, α and β in the RET model are needed to determine the excess attenuation as a function of vegetation depth. In practice, parameters α, β, $k_e = k_a + k_s$ and $W = \frac{k_s}{k_s+k_a}$ are optimised and extracted. Parameters α and β can be derived from measuring the phase function of the vegetation medium. The extinction coefficient k_s can be obtained by means of calculating the initial slop of the measured attenuation curve with vegetation depth. With parameters α, β and k_s determined, attenuation curves for a range of albedos W are produced and then fitting to the measured pattern, the best fitting curve is chosen through Minimum Mean Square Error (MMSE).

3.7.1 Extraction of parameters α and β

As described above, at microwave and millimeter wave frequency bands, scattering inside the vegetation medium will yield a narrow forward lobe superimposed over an isotropic background. The scattering function, or phase function, can be plotted using Eqs. 3.16 and 3.17. Figures 3.14a) and b) depict the computer-generated phase function for a wide range of α and β parameter values.

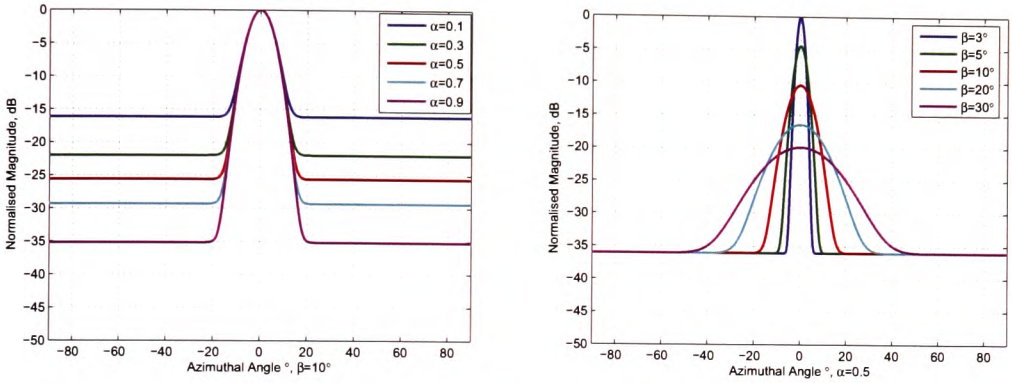

(a) (b)

Figure 3.14: Gaussian shaped phase function for varying α (a) and β (b)

By definition, α is the ratio of the forward scattered signal over the total scattered power, while β represents the width of the forward lobe. It is evident that parameters α and β influence the shape of the computer-generated phase function independently: α regulates the level of the isotropic backscatter without varying the width of the forward lobe, whereas β alone determines the beamwidth of the phase function with no effect on the isotropic background.

Extraction of the parameters α and β is achieved by the following optimisation process: tuning the values of parameters α and β to yield the Gauss-shaped phase function with various beamwidths of the forward lobe and levels of the isotropic backscatter. The window for α and β was chosen large enough to cover all possible values experienced. Fig. 3.15 shows an example of measured data and the best fitting phase function.

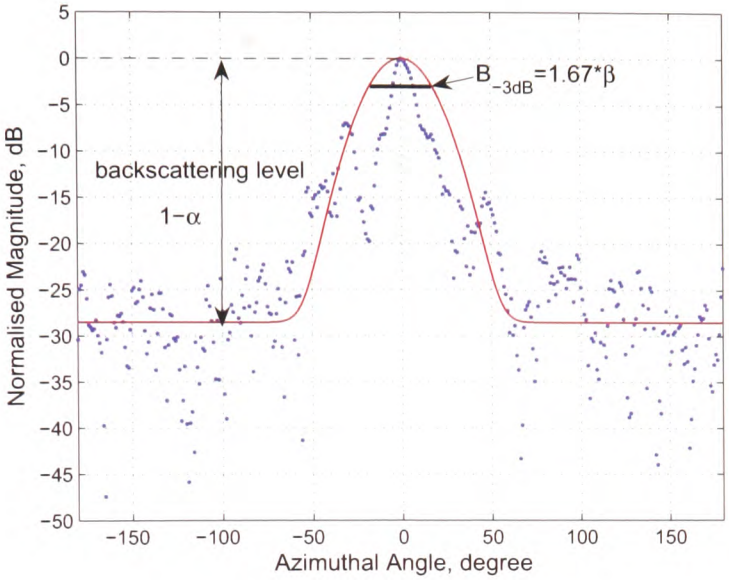

Figure 3.15: Gaussian phase function fitting: $\alpha = 0.96$ $\beta = 0.21$

The extracted parameters resulting from the best MMSE fit to the measured pattern are $\alpha = 0.96$ and $\beta = 21^o$. This measured pattern was obtained using a 20 dBi Gaussian horn as the receiver antenna at 20 GHz. Measurement methods, geometry, setup and results are presented in chapters 4 and 5. Parameters α and β extracted from the straightforwardly measured signal patterns (at Pos. 1 shown in Figs. 5.9 and 5.10) are summarised in Table 3.2.

	Receiver antennas used at 20 GHz				Receiver antennas used at 40 GHz			
	Gauss horn	standard gain horn			Lens horn	standard gain horn		
	20 dBi	20 dBi	15 dBi	10 dBi	29 dBi	20 dBi	15 dBi	10 dBi
α	0.96	0.82	0.53	0.81	0.79	0.85	0.85	0.85
β	21^o	13.5^o	12^o	23.5^o	5.5^o	11.5^o	27.5^o	24.5^o

Table 3.2: Extracted values of parameters α and β from the measured patterns at position 1 at 20 and 40 GHz

In order to obtain accurate results, the effect of the antenna radiation pattern on the directional spectrum measurement has to be reversed by means of applying deconvolution techniques. This is the main concern of this research project and is documented in chapters 6 - 8. Data summarised in Table 3.2 will be used for

comparison with those extracted values of α and β after deconvolution has been applied in chapter 8.

3.7.2 Extraction of the extinction coefficient k_e

The extinction coefficient k_e determines the attenuation rate of the coherent components I_{ri} at small vegetation depth into the medium. The relationship is given by:

$$P_R = P_0 e^{-k_e d} \tag{3.57}$$

where P_R is the received power inside the vegetation medium, P_0 represents the received power at the same location in the absence of vegetation and d denotes the vegetation depth in metres [14, 24, 86]. Rewriting Eq. 3.57 in decibel scale leads to:

$$\log_{10} \frac{P_R}{P_0} = -k_e d \log_{10} e \tag{3.58}$$

$$k_e = -0.23 \frac{10 \log_{10} \frac{P_R}{P_0}}{d} \tag{3.59}$$

The initial slope of the excess attenuation curve is best determined by using the linear region at small vegetation depths, before the first turnover point of the attenuation curve due to I_1 is reached. In many practical forest environments this can be reached after only the first row of trees after the air-to-vegetation interface. The location of the first turnover point depends on the optical density τ and in many cases appears around 3 - 5 τ. The exact location depends on factors such as frequency, leave size, tree size and receiver antenna [13, 14].

3.7.3 Extraction of the albedo, W

In [13], a method using the dependence of the excess attenuation rate of the normalised received power on albedo was proposed to optimise the parameter W. At large vegetation depths, where the incoherent component I_2 is predominant, the excess attenuation rate as a function of the vegetation depth reaches a slow and stable

slope which differs with varying values of albedo W, as shown in Fig. 3.10a.

Fig. 3.10a shows that larger values of albedo W cause a slow rate of decay. This is consistent with large albedo values indicating more scattering and less absorption effects taking place inside the vegetation medium; and that the scatter does not extinguish but redistributes signal energy [18], consequently, leading to a slower attenuation rate. On the other hand, smaller albedo values mean more absorption is present, leading to a faster vanishing received signal power with vegetation depth. With parameters α, β and k_e determined using methods described above, a wide range of values of the parameter W are used to yield the excess attenuation curves. The prediction curve with least squared mean error with the measured data determines the value for albedo.

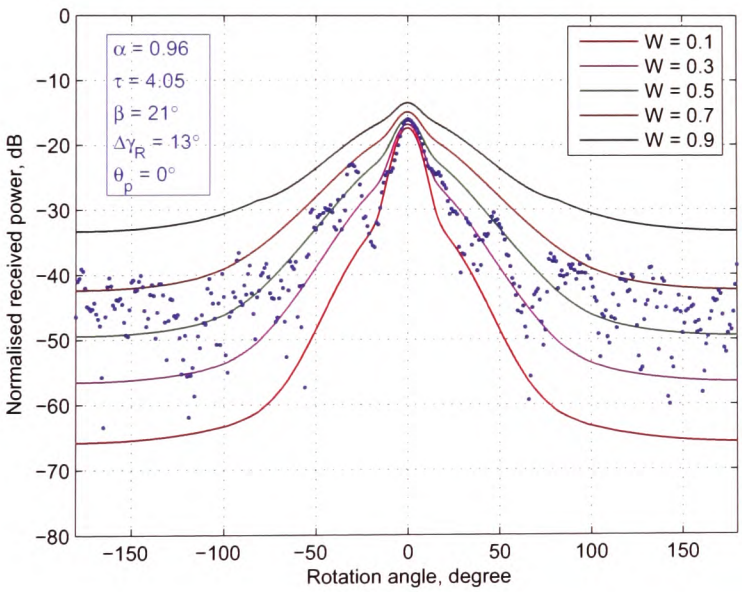

Figure 3.16: Directional spectra for a range of albedo values, overlaid with measured data

In order to obtain an accurate estimate of albedo excess attenuation has to be recorded well into the vegetation medium, since the effect of a change in albedo is most pronounced at larger vegetation depth, where I_2 is the dominant contribution. Dynamic range restrictions of the measurements as well as physical limitations such

as limited forest depth or limited anechoic chamber length can make measurements deep inside the vegetation medium difficult to obtain.

An alternative approach to determine albedo is presented in [14], which uses the directional spectrum instead of the excess attenuation rate with vegetation depth. The directional spectrum can be evaluated using the previously determined parameters α, β and k_e as described in sections 3.7.1 and 3.7.2. The calculated directional spectra will be plotted for a range of albedo values, so that a minimum mean square error fit with measured data can be determined. Fig. 3.16 illustrates this process. The necessary parameters for the simulation data are either hardware determined like the antenna receiver HPBW, resulting in $\Delta\gamma_R = 13^o$, or were previously determined parameters: α, β, k_e and τ. Here an albedo of $W = 0.51$ was obtained.

3.8 Summary and interim conclusion

This chapter presents a sufficiently detailed summary of the theory of the Radiative Energy Transfer (RET). It explains the process involved in obtaining the RET model application to radiowave propagation through vegetation. The importance of the input parameters for accurate RET modelling is highlighted and the sensitivity of the prediction result of the RET to input parameter variation is illustrated. Furthermore, methods for extracting values for these input parameters from measurements are presented. In addition the receiver antenna radiation pattern has a significant influence on the accuracy of the parameter extraction and therefore its influence needs to be compensated for. Chapters 4 and 5 detail the measurement equipment and the experiments carried out in this research project. Chapters 6 and 7 address the antenna radiation pattern compensation.

Chapter 4

Measurement systems

4.1 Introduction

To provide good quality data sets under controlled conditions, a range of experiments were designed and conducted in a controlled indoor environment, *i.e.* the anechoic chamber. These experiments include:

- **Measurements of the radiation patterns of the antennas.** The results obtained yield the radiation patterns of the antennas used during the whole set of measurements.
- **Measurements of the re-radiation function of a single tree.** This kind of measurement investigate the characterisation of the scattering signals from a single tree under consideration, *i.e.* the so called "Stretching Factor". These findings can be used to extract the RET input parameters.
- **Measurements of directional spectra inside a group of trees.** 16 trees of the same species and size are deployed to form an homogeneous small scale forest in order to provide an environment in which the RET parameter extraction can be tested and optimised.
- **Measurements of excess attenuation with vegetation depth.** This measurement focuses on the excess attenuation caused by the presence of veg-

etation with considerable depth placed between transmitter and receiver; up to 8 pairs of trees are used in this measurement.

All experiments performed throughout this project use the 20 GHz and 40 GHz measurement systems described in the following sections. All measurements are narrowband *i.e.* single frequency measurements.

4.2 Prerequisites of the measurement

The indoor measurement is designed to conduct automatically with no need for interventions in order to minimise human influence. The entire experimental room is shielded. All the possible interference sources such as the indexer, the computer, the spectrum analyser and the operator are kept outside except a number of necessary equipment such as the transmitter, the receiver and cables. Therefore, the whole measurement setup is considered as a linear time-invariant system.

4.2.1 The anechoic chamber

All the indoor experiments are performed in a controlled indoor environment, in which the measurement processes are performed automatically without any undesired distribution. This means no presence of persons and any other obstacles in the vicinity, no unexpected electromagnetic interruption. Apart from screening off outside influences the anechoic chamber wall treatment minimises reflections. This anechoic chamber has an interior physical-size of length, $5.60m$, width, $2.25m$, and height $2.40m$. The entire interior is covered with very high performance broadband pyramidal-shape absorbers except the floor. Experimental equipment is situated on the ground, however the rest of the floor is covered as much as possible by pyramidal absorbers available in a variety of size to cover all open space on the floor. Photos can be seen in Figs. 5.11 and 5.17.

4.2.2 The measurement peripherals

Throughout the measurement process, the transmitter is fixed on a tripod and is stationary; and the receiver is mounted on a turn-table which is controlled by computer. The turn-table rotates with precise constant speed with equal steps. The turn-table fitted to a second tripod provides rotation for the receiver antenna in most measurements, apart from the measurement for the re-radiation function of single trees; here a moveable mechanical rig provides the movement. A schematic diagram depicting the arrangement inside the anechoic chamber is shown in Fig. 4.1.

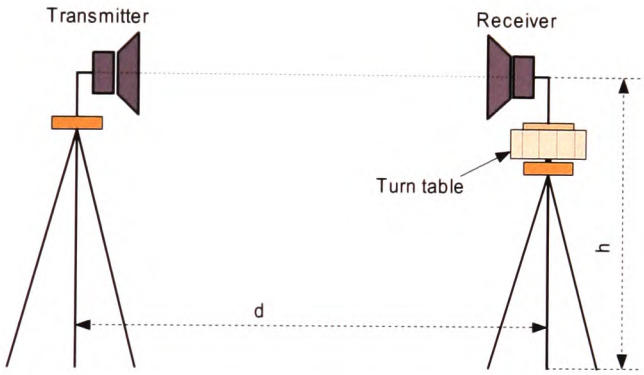

Figure 4.1: Measurement arrangement inside the anechoic chamber

Measurement software developed in house was used to control the movement of the precision "Parker, Inc 200RT" rotary tables, providing an angular accuracy of 0.004^o. The software controls the overall measurement processes. A typical measurement process includes (a) a maximum signal search, ensuring the alignment between the transmitter and the receiver; (b) precise and even moving the receiver from -180^o to $+180^o$ with no intervention needed unless an accident occurs; (c) data acquisition and averaging over a number of independently receiving power strengths at a specified angular position. All the obtained data sets are stored in a pre-designed database structure once the measurement has ended. A spectrum analyser is used to monitor the received power strength in real-time. The spectrum analyser is connected to the computer through a GPIB interface card. A typical measurement

process rotating from -180^o to $+180^o$ at the step of 1^o and taking averaging over 5 independent values at a specific angular position will last 45 minutes and could vary from 30 minute to one hour depending on how many angular positions are accessible and data points are required.

4.2.3 Antennas under test

It is important to accurately characterise the antennas used concerning their radiation patterns, Half Power Beamwidth (HPBW), and far-field distance, even the physical sizes of the antennas used may cause inaccuracies of measured distance between the transmitter and the receiver at the relatively short distances used inside the anechoic chamber. The photos in Fig. 4.2 show all the antenna types used for both 20 GHz and 40 GHz systems, their physical sizes are compared in Table 4.1.

antenna		Length	Width	Height
20GHz standard horn	10 dBi	4.8 cm	1.7 cm	1.2 cm
	15 dBi	5.5 cm	2.9 cm	2.1 cm
	20 dBi	12 cm	5.2 cm	3.8 cm
40 GHz standard horn	10 dBi	2.4 cm	0.7 cm	0.6 cm
	15 dBi	2.0 cm	1.5 cm	1.2 cm
	20 dBi	6.7 cm	2.8 cm	2.0 cm
		Length	Diameter	
20 GHz Gauss horn 20 dBi		12.5 cm	11.7 cm	
40 GHz Lens horn 29 dBi		9.4 cm	6.7 cm	

Table 4.1: Physical sizes of the antennas under test

(a)

(b)

Figure 4.2: Photos of antennas used (a) 20 GHz and (b) 40 GHz systems

The space surrounding an antenna is usually subdivided into three regions: (a) reactive near-field, (b) radiating near-field (*Fresnel*) and (c) far-field (*Fraunhofer*) regions [87] as shown in Fig. 4.3 , where $R_1 = 0.62\sqrt{\frac{D^3}{\lambda}}$ and $R_2 = \frac{2D^2}{\lambda}$, λ is the wavelength and D is the largest dimension of the antenna. R_1 and R_2 are used to separate the three field regions surrounding an antenna.

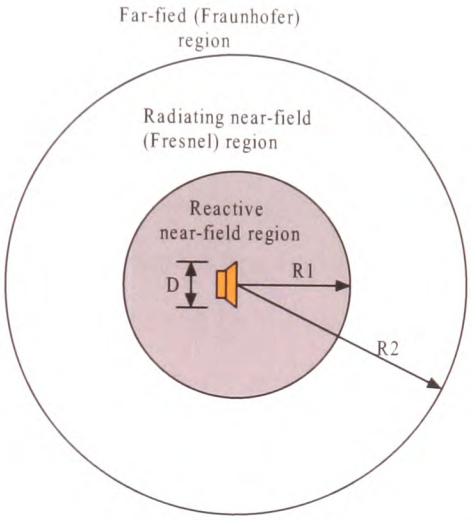

Figure 4.3: Schematic demonstration of an antenna's field regions: $R_1 = 0.62\sqrt{\frac{D^3}{\lambda}}$ and $R_2 = \frac{2D^2}{\lambda}$ [87]

The far-field *(Fraunhofer)* region is defined as the region where the angular field distribution of an antenna is essentially independent of the distance from the antenna. Therefore, the radiation pattern no longer varies with radial distance from the antenna. The range of the far-field region is from the minimum boundary $R_2 = \frac{2D^2}{\lambda}$ to infinity.

The minimum far-field distances of all antennas available for various measurement systems, 20 GHz and 40 GHz, are calculated and presented in Table 4.2. All measurements are conducted in the far-field region of the antennas used. The HPBWs of the antennas used are calculated based on the measured radiation patterns and given in the following sections in this chapter.

Antennas		20 GHz system	40 GHz system
Standard horn	10 dBi	3.7 cm	1.8 cm
	15 dBi	10.8 cm	5.9 cm
	20 dBi	35.7 cm	21.3 cm
Gauss horn	20 dBi	36 cm	--
Lens horn	29 dBi	--	123 cm

Table 4.2: Antennas minimum far-field distances

4.2.4 Dynamic range of the measurement system

The dynamic range of a communication system is defined as the difference between the maximum and the minimum signal levels that it can receive [14], describing the range of signal levels that can be detected by the equipment used. The upper limit is typically constrained by the saturation of active devices in measurements, whereas the lower bound is determined by the receiver's noise floor.

Two main types of loss occur during the process of radiowave propagation through vegetation. One is the Free Space Loss (FSL), which can be calculated by the *Friis* equation [88]

$$\frac{P_R}{P_T} = G_T G_R (\frac{\lambda}{4\pi})^2 \tag{4.1}$$

where P_T, P_R are the transmitted and received powers respectively, G_T, G_R are the gain of the transmitter and receiver antennas relative to an isotropic source, and λ is the wavelength of the radiowave. Hence, the FSL is expressed in logarithmic units, decibels, as

$$FSL(dB) = P_R(dB) - P_T(dB) \tag{4.2}$$

The other is the excess loss caused by the presence of vegetation. This excess attenuation cannot be as easily quantified as the free space loss due to the complex nature of the vegetation itself. The rate of excess attenuation depends on, but is not limited to, the state of foliation, density, and depth of vegetation. The overall dynamic range combined with the rate of attenuation inside the vegetation determines not just measurements, but also the system performance, *i.e.* how far the receiver antenna could be placed into the vegetation before the signal is swamped by the

noise floor.

Attenuators are used to prevent the saturation of the receiver active devices by providing extra attenuation whenever the received power is approaching the saturation threshold of the receiver. The attenuators located at both the transmitter and the receiver sides assist the extension of the overall dynamic range via (a) first, setting the maximum attenuation applicable, which means that the received power is below the saturation threshold when the antenna with maximum gain (20 dBi for 20 GHz and 29 dBi for 40 GHz) is used and above the noise floor of the data acquisition device; (b) the minimum distance available is determined for the far-field criterion to be satisfied. This value is used as the minimum distance between the transmitter and the air-to-vegetation interface, and may be extended to ensure uniform illumination of the interface; (c) once the location of the air-to-vegetation interface is determined, the receiver is moved inside the vegetation, consequently excess loss will increase as a function of the vegetation depth in the presence of vegetation. Adjusting the attenuator to reduce the attenuation ensures the received power is above the noise floor with a safe margin when an antenna with the smallest gain (10 dBi) is used; (d) if the attenuation are set equal to zero on both sides and the received signal level approaches the noise level, the receiver cannot move any further into the vegetation. Therefore, the maximum vegetation depth measurable is determined.

4.3 Characteristics of the measurement systems

Throughout this research project, various types of experiments were carried out using measurement systems at 20 GHz and 40 GHz. Although the two measurement systems have similar architectures, different components, antennas and power supplys *etc.* were used to fabricate the transmitter unit and the receiver unit respectively. Sections 4.3.1 and 4.3.2 give a detailed description of the characteristics of both the transmitter and the receiver as well as the overall dynamic range for both of the measurement systems.

4.3.1 The 20 GHz measurement system

The 20 GHz measurement system consists of a transmitter and a receiver unit. The system allows narrowband continuous wave measurements and its block diagram is presented in Fig. 4.4.

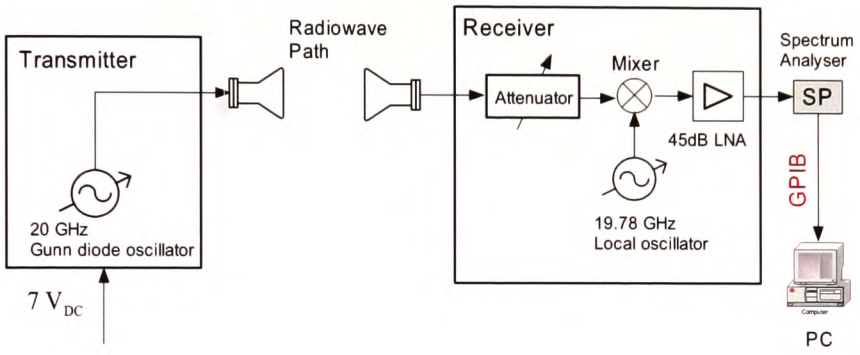

Figure 4.4: Block diagram of the 20 GHz measurement system

4.3.1.1 Transmitter section

The 20 GHz signal is generated by a Gunn diode Voltage Controlled Oscillator (VCO) with a rated output power of 21 dBm (126mW). A heat sink is used to alleviate the effects of increasing temperature of the VCO during the process of measurement. This ensures the stability of the VCO's operational frequency. The $12V - 7V$ converter shown in Fig. 4.5 is used for outdoor measurements and is not necessary for indoor measurements. All necessary components are housed in a metallic box; and the transmitter antenna is fixed on the surface of the box to keep it horizontally steady, as illustrated in the photograph of Fig. 4.5.

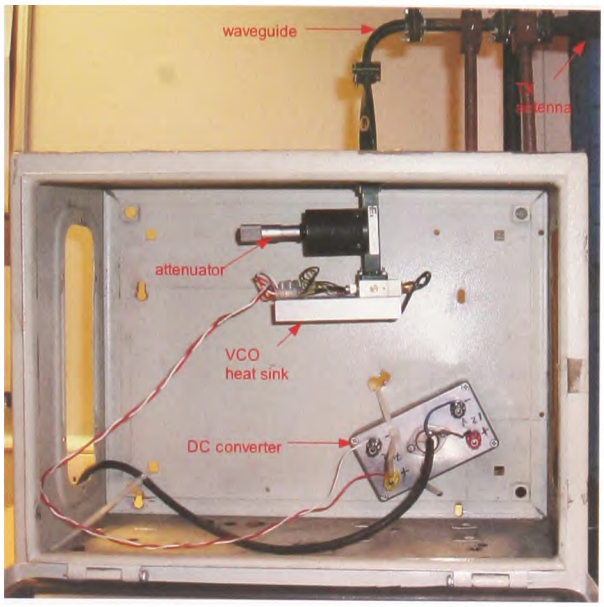

Figure 4.5: Transmitter unit of the 20 GHz measurement system

4.3.1.2 Receiver section

The receiver unit shown in Fig. 4.6 includes the receiver antenna, an attenuator, a local oscillator, a mixer, and a Low Noise Amplifier (LNA). All these components are connected by waveguides to ensure minimum signal losses, and fixed inside and on a metallic box similar to the transmitter section. A local oscillator at a frequency of 19.78 GHz is mixed with the received signal frequency (20 GHz) down to an Immediate Frequency (IF) signal of 220 MHz for the convenience of measurement. The biased mixer has a conversion loss of approximately 4 dB. Mechanical tuning of the mixer allows operators to adjust and maintain the IF as close as possible to 220 MHz. The 220 MHz IF signal was used throughout the measurements.

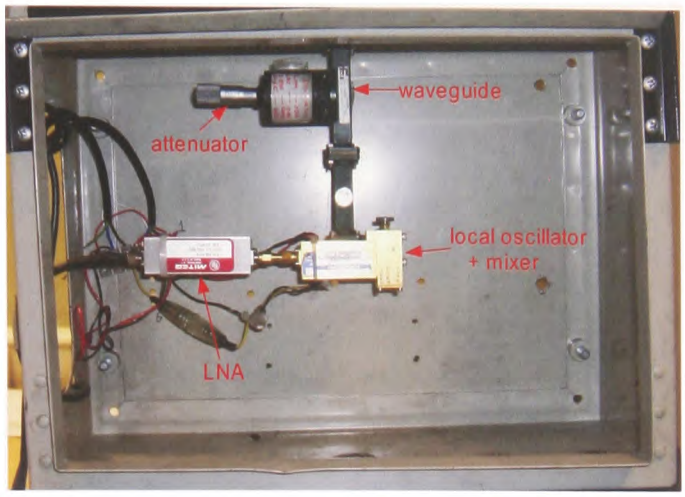

Figure 4.6: Receiver unit of the 20 GHz measurement system

The data acquisition process was achieved using a spectrum analyser, which is connected to a computer through a GPIB interface card. The spectrum analyser was used instead of a logarithmic amplifier for the following reasons:

- The IF signal could be constantly monitored. It may be corrected immediately once a frequency drift occurs.
- Low noise floor and a large overall dynamic range. Using a narrow bandwidth, the spectrum analyser can monitor signals down to levels as low as -90 dBm, which is 30 dBm below that of the logarithmic amplifier, resulting in a large overall dynamic range.
- The spectrum analyser has a wide and adjustable bandwidth. The measurement bandwidth can easily be varied to achieve a balance between a relatively wide bandwidth to accommodate the frequency-drifting and a narrow bandwidth to enlarge the overall dynamic range, depending on which one is more appropriate for each measurement.

The main disadvantage of using a spectrum analyser is its slow acquisition rate, 1 to 10 samples per second depending on the bandwidth used; whereas the data

acquisition speed by using the logarithmic amplifier combined with a data acquisition card (DAQ) can reach up to 100 ksamp/s. Nevertheless, its narrow bandwidth, 50 MHz, and relatively high noise floor, -60 dBm, make it less favorable.

The LNA follows the mixer to amplify the IF signal power, and increase the dynamic range by 45 dB. A 10 m low loss coaxial cable used to supply IF signal from the receiver enclosure to the spectrum analyser with approximately 4 dB extra loss compared to a short, 1m, low loss coaxial cable. The combined losses of cables and connectors between receiver and spectrum analyser amount to around 5 dB. A PC is used to control the measurement and as storage unit for the acquired data. The turn-table is controlled by an indexer, which interfaces with the computer via serial port. The spectrum analyser communicates with the computer via a GPIB card and is also controlled by the measurement software.

4.3.1.3 Link budget of the 20 GHz system

The link budget is determined by the characteristics of both the transmitter and the receiver units. Table 4.3 gives the link budget for the 20 GHz system. The specification is: (a) a 10 dBi standard gain horn is used as a transmitter to provide the broadest illumination of the vegetation interface; (b) a 20 dBi standard gain horn is used as a receiver to provide a larger dynamic range; (c) the distance between the Tx and the Rx is 2.8 metres with no attenuation at either side as shown in Table 4.3. Measured radiation patterns for both the E- and H-plane of all antennas available at 20GHz are illustrated in subsection 4.4.3. Appropriate attenuation may be applied at the receiver side to prevent the received power from approaching the saturation of the active devices.

Component	Associated Loss/Gain	Link Budget
Transmitter Output Power	21 dBm	21 dBm
Gain of Tx antenna	10 dBi	31 dBm
Gain of Rx antenna	20 dBi	51 dBm
Gain of LNA	45 dB	96 dBm
Mixer Inserted Loss	-4 dB	92 dBm
Cable & Connector Loss	-5 dB	87 dBm
Free space loss	-67.4 dB	19.6 dBm

Table 4.3: Link budget for the 20 GHz system

4.3.2 The 40 GHz measurement system

The 40 GHz measurement system has a similar architecture as the 20 GHz system as shown in Fig. 4.7.

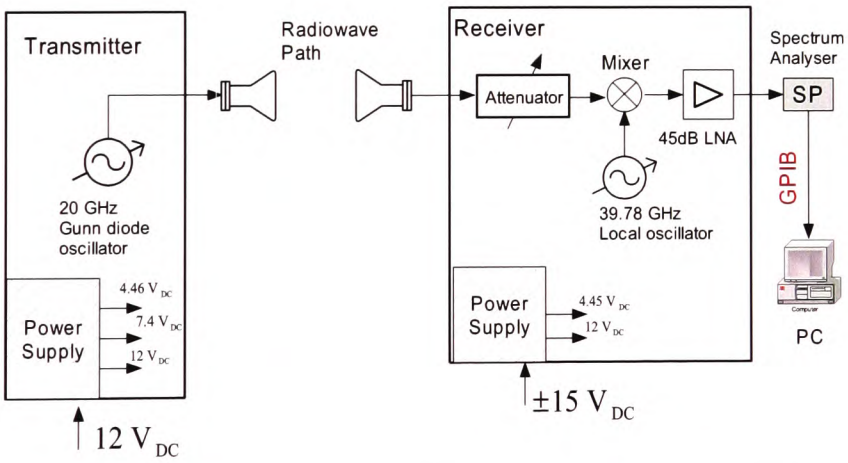

Figure 4.7: Block diagram of the 40 GHz measurement system

4.3.2.1 Transmitter section

The transmitter unit consists of a GV-22 varactor Gunn diode oscillator, an attenuator, and a transmitter antenna. The oscillator provides an output signal rated at 22 dBm (150 mW). A photo of the transmitter unit of the 40 GHz measurement system is shown in Fig. 4.8.

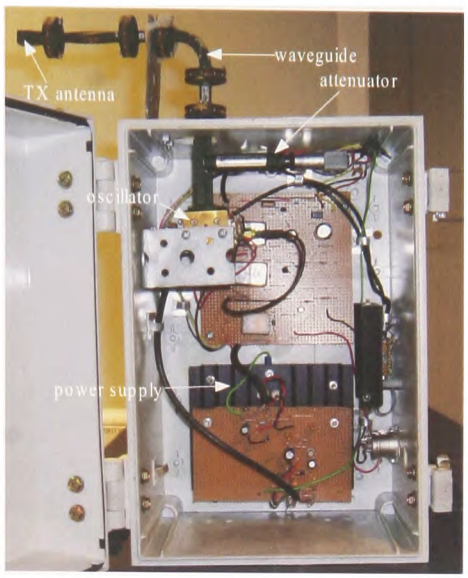

Figure 4.8: Transmitter unit of the 40 GHz measurement system

Both transmitter and receiver Gunn diode oscillators have their own precision power supply with integral transient filters to protect the diodes. The power supplies also include sequencing circuits so that heater, varactor input (transmitter only) and Gunn diode on and off switching is sequenced correctly to protect the diodes from any transients created during switching. Receiver and transmitter Gunn diodes are both heated to provide further frequency stability with temperature. Furthermore both the transmitter local oscillator and the receiver include isolators in the waveguide to protect from RF being fed back into the Gunn oscillator.

4.3.2.2 Receiver section

The receiver unit includes a receiver antenna, an attenuator, the frequency converter which comprises a local oscillator and a mixer, and a low noise amplifier. All elements are connected via waveguides to ensure the minimum of transmission loss. The receiver antenna is fixed on the surface of a box and followed by an attenuator remaining outside to provide adjustment convenience during the course of measurement, whereas the rest of components are housed inside the box offering robustness and portability. A photograph of the 40 GHz receiver unit is illustrated in Fig. 4.9.

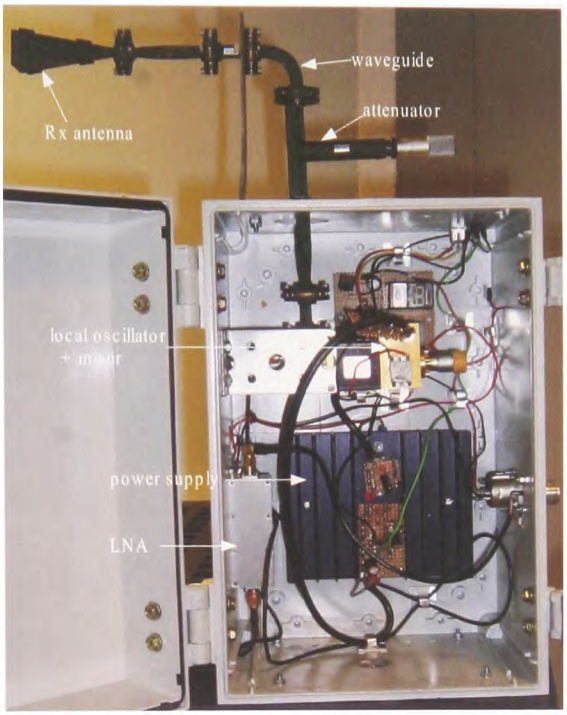

Figure 4.9: Receiver unit of the 40 GHz measurement system

The waveguide attenuator offers a maximum attenuation of 40 dB and can be manually controlled by a micrometer screw. The Local Oscillator (LO) teams up with the mixer to form the frequency conversion section, which converts the input signal at a frequency of 40 GHz down to an IF signal at 220 MHz. This is achieved by feeding the mixer with the local signal at a frequency of 39.78 GHz (generated by the LO). The LO can be manually tuned by a mechanical screw and has a $\pm 2.5\,GHz$ tuning bandwidth, allowing a broad range of choice of IF frequencies. The mixer introduced an inserted loss of 6 dB according to the manufacturer specifications. The mixer has the IF port connected to a low noise amplifier (LNA) which has a gain of 45 dB. The output of the LNA is fed via a 10 m low loss coaxial cable into the data acquisition devices. This cable, combined with the connectors, introduced an extra loss of approximately 5 dB.

Similar to the 20 GHz system, a spectrum analyser is used to acquire the generated signals. Due to the relatively low frequency stability of the 40 GHz system, wider resolution bandwidths compared to the 20 GHz system had to be used dur-

ing measurements. The noise floor increases to a maximum experienced value of approximate -70 dBm due to the frequency high drifting and more noise being generated in the 40 GHz system compared to the 20 GHz one. Again, a computer was controlling the overall measurement processes. The computer connects the indexers through a series RS 232 cable, controlling the rotation of the turn-tables inside the anechoic chamber and in the meantime communicating with the spectrum analyser via a GPIB card.

4.3.2.3 Link budget of the 40 GHz system

The link budget of the 40 GHz system is characterised with specifications: (a) a 10 dBi standard gain horn used as a transmitter to provide a uniform illumination; (b) a 29 dBi Lens horn used as a receiver to yield a larger dynamic range; (c) the distance between the Tx and the Rx is 2.8 metres with no attenuation at either side. The link budget for the 40 GHz system is given in Table 4.4. Measured radiation patterns of both the *E*- and *H*-plane are demonstrated in subsection 4.4.4.

Component	Associated Loss/Gain	Link Budget
Transmitter Output Power	22 dBm	22 dBm
Gain of Tx antenna	10 dBi	32 dBm
Gain of Rx antenna	29 dBi	61 dBm
Gain of LNA	45 dB	106 dBm
Mixer Inserted Loss	-6 dB	100 dBm
Cable & Connector Loss	-5 dB	95 dBm
Free space loss	-74.4 dB	20.6 dBm

Table 4.4: Link budget for the 40 GHz system

4.4 Measurements of radiation patterns of antennas

4.4.1 Definition of the antenna radiation pattern

An antenna radiation pattern or antenna pattern is defined as a mathematical function or a graphical representation of the radiation properties of the antenna as a function of space coordinates [87]. In most cases, the radiation pattern is determined

in the far-field region and represented as a function of the directional coordinates. The radiation property of most concern is the two- or three- dimensional spatial distribution of radiated energy as a function of the observer's position along a path or surface of constant radius. A trace of the received electric or magnetic field at a constant radius is called the amplitude field pattern. On the other hand, a graph of the spatial variation of the power density along a constant radius is called an amplitude power pattern.

Typically, the measured antenna patterns are normalised with respect to their maximum value, yielding normalised patterns. Also, the power pattern is usually plotted on a logarithmic scale in decibels (dB). This scale is desirable because a logarithmic scale can accentuate in more details those parts of the pattern that have very low values, which refer to as minor lobes [87]. For an antenna, the

- *field pattern* (in linear scale) typically represents a plot of the magnitude of the electric or magnetic field as a function of the angular space.
- *power pattern* (in linear scale) typically represents a plot of the square of the magnitude of the electric or magnetic field as a function of the angular space.
- *power pattern* (in a logarithmic scale) represents the magnitude of the electric or magnetic field, in decibels, as a function of the angular space.

All three patterns yield the same angular separation between the two half-power points [87], referred to as Half Power Beam Width (HPBW). In practice, the three-dimensional pattern is measured and recorded in a series of two-dimensional patterns. Hence, two principal planes of the antenna radiation pattern, *i.e.* the E-plane and H-plane were measured and recorded to represent the characteristics of the antennas used.

4.4.2 Radiation pattern measurement setup

For a linearly polarised antenna which is symmetrical about its axis, like the standard gain horn, Lens and Gaussian horn antennas, performance is often de-

scribed in terms of its principal E- and H-plane patterns. The E-plane is defined as "the plane containing the electric-field vector and the direction of maximum radiation," and the H-plane as "the plane containing the magnetic-field vector and the direction of maximum radiation" [87].

To depict an antenna's characteristic quantitatively and graphically, measurements were designed and conducted inside the anechoic chamber. The measurement arrangement is illustrated in Fig. 4.1, where d represents the distance between the transmitter and the receiver. Due to the physical size of the anechoic chamber, the distance was set to 2.8 m for the measurement of antenna radiation patterns, which is sufficient to ensure that the transmitter and the receiver are placed in the far-field region while keeping both of them at minimum distance of 1 m away from the surrounding walls. h represents the height of the transmitter and the receiver, and was adjusted to exactly 1.1 m, which puts the antennas under test just in the middle of the height of the anechoic chamber. Measurements were performed in a two-dimensional plane, the E-plane first. Alternatively, by rotating both the transmitter and the receiver 90 degree along their horizontal axes, radiation pattern in H-plane could be obtained. The measured antenna radiation patterns are presented in following sections.

4.4.3 Results and analysis of the 20 GHz antenna measurements

In the 20 GHz system, the available antennas are 3 types of standard gain horn antennas with gains of 10 dBi, 15 dBi, and 20 dBi and a Gaussian horn antenna with a gain of 20 dBi. The Gaussian horn antenna is of particular interest for this research program as the mathematic equations describing the received power relationships in the RET theory have been derived assuming Gaussian antenna radiation patterns at the receiver side. Hence, a comparison with conventional antennas regarding the effects of the antenna pattern on the parameter estimation for the RET theory should prove interesting.

The radiation patterns were measured by mounting the antenna under test on a rotary turn-table which was remotely controlled by a PC using the specific software application developed in MATLAB. The turn-table was rotated in a circle from -180^o to $+180^o$ in the azimuthal plane with even increment of 0.5^o at each step. At each angular position, five values were recorded and their average was used to depict the radiation pattern. The averaging operation indicates the measured patterns more clearly and alleviates negative effects from random noise significantly over the measurement process.

A 10 dBi standard gain horn antenna is used as the transmitter for the 20 GHz system. As shown in Table 4.5, it has the broadest Half Power Beam Width (HPBW) among all available antennas, hence to ensure the best uniform illumination that can be achieved. The antenna power patterns are measured in both two principal planes, *i.e.* the E-plane and the H-plane radiation patterns.

All measured results are normalised with respective to their respective maxima and presented in dB as shown in Figs 4.10 and 4.11. Fig. 4.10a) shows the E-plane and the H-plane radiation patterns of the 10 dBi standard gain horn antenna. It graphically shows the widest beamwidth, 53^o and 56^o for E-plane and H-plane respectively. Fig. 4.10b) shows the radiation patterns of the 15 dBi standard horn, 33^o and 30.5^o for E- and H-planes respectively. Likewise, Fig. 4.11 a) and b) demonstrate the radiation patterns for the 20 dBi standard gain horn and 20 dBi Gaussian horn respectively, both E- and H-planes are presented. It is evident that the Gaussian horn antenna has the narrowest HPBWs, 13^o in both E and H principal planes. Moreover, the sidelobe values of the Gaussian horn are on average 40 dB below the peak value of the mainlobe. The HPBWs in both E- and H-plane are extracted and summarised in Table 4.5 for all the antennas used in this research project.

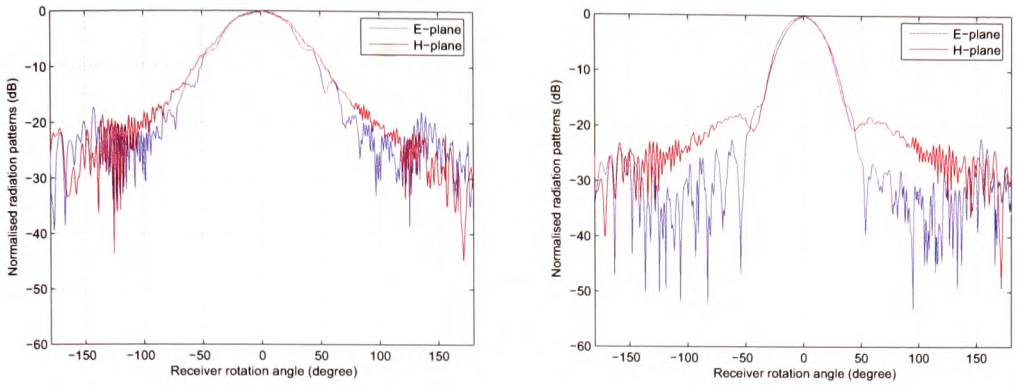

Figure 4.10: Measured radiation patterns of 20 GHz system: a) 10 dBi and b) 15 dBi standard gain horn antennas

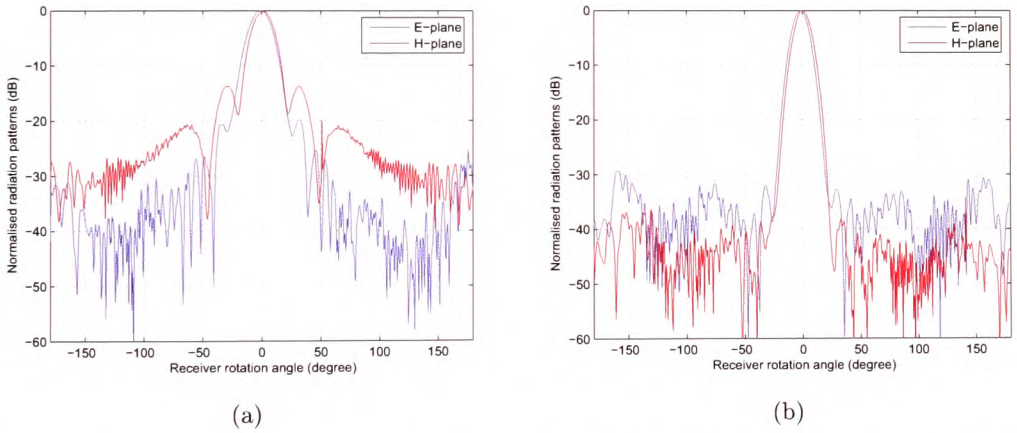

Figure 4.11: Measured radiation patterns of 20 GHz system: a) 20 dBi standard gain and b) 20 dBi Gauss horn antennas

		HPBW	
Antennas	Gain	E-plane	H-plane
standard horn	10 dBi	53^o	56^o
standard horn	15 dBi	33^o	30.5^o
standard horn	20 dBi	18.5^o	17^o
Gauss horn	20 dBi	13^o	13^o

Table 4.5: Measured HPBW of the 20 GHz antennas

4.4.4 Results and analysis of the 40 GHz antenna measurements

In the 40 GHz system, also 3 types of standard gain horn antennas with gains of 10 dBi, 15 dBi and 20 dBi are available, as well as a 29 dBi Lens horn antenna. The 10 dBi standard gain horn is used as the transmitter to provide uniform illumination. Similar to the 20 GHz system setup, the receiver was mounted on a turn-table which rotates automatically under the control of a computer. The turn-table revolves a complete circle of 360^o with precise 0.5^o at each step. At each angular position, five independent values were obtained and averaged to lessen effects of random noise.

Likewise at 20 GHz system, both E- and H- radiation patterns are measured. The results are normalised with respect to their respective maxima, shown as logarithmic scale in Figs. 4.12 and 4.13. Fig. 4.12a) illustrates the E- and H-plane radiation patterns of the 10 dBi standard gain horn, which has the broadest HPBWs of 62^o and 61^o for E- and H-planes respectively. Fig. 4.12b) shows the radiation patterns of the 15 dBi standard gain horn with HPBWs of 39^o and 29.5^o for E- and H-planes respectively. There appears to be a significant difference in beamwidths between the E- and H-plane, this may be due to low frequency noise appearing on the main beam of the measured pattern causing extra error in the beamwidths reading. Fig. 4.13a) and b) present the radiation patterns of both E- and H-planes for the 20 dBi standard gain horn and the 29 dBi Lens horn antennas respectively. The 29 dBi Lens horn has the smallest values of HPBW, which are 7^o and 6^o for E- and H-plane respectively. The Lens horn also shows on average a 35 dB difference between its peak value in the mainlobe and the sidelobe values. For all antennas used in the 40 GHz system, the HPBWs in both E- and H-plane are extracted and summarised in Table 4.6.

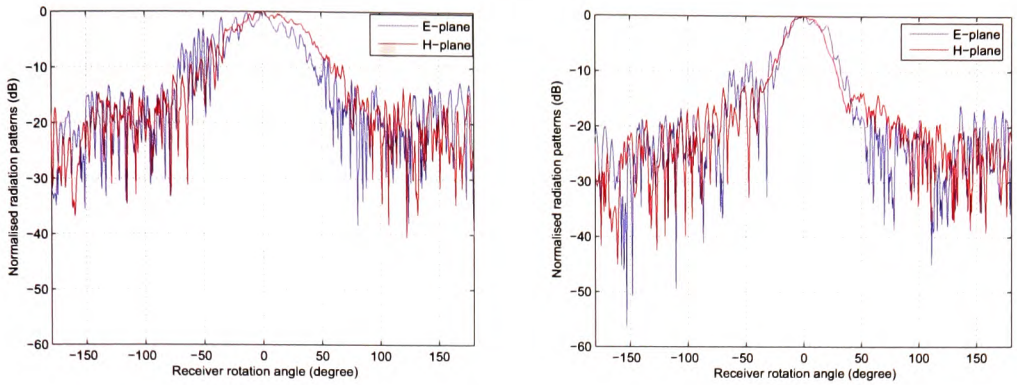

(a) (b)

Figure 4.12: Measured radiation patterns of 40 GHz system: a) 10 dBi and b) 15 dBi standard gain horn antennas

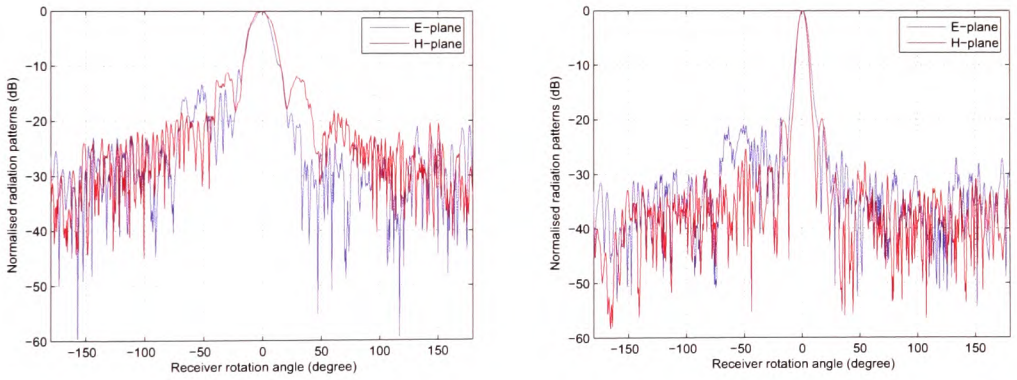

(a) (b)

Figure 4.13: Measured radiation patterns of 40 GHz system: a) 20 dBi standard gain and b) 29 dBi Lens horn antennas

		HPBW	
Antennas	Gain	E-plane	H-plane
standard horn	10 dBi	62^o	61^o
standard horn	15 dBi	39^o	29.5^o
standard horn	20 dBi	17.5^o	19.5^o
Lens horn	29 dBi	7^o	6^o

Table 4.6: Measured HPBW of the 40 GHz antennas

4.5 Measurement error analysis

In general two types of errors occur during a measurement process, namely systematic and random ones. In many cases it may not be possible to avoid systematic errors, however they can be quantified and eliminated using reference measurements with the same equipment under similar conditions. Measurements conducted during this research project are presented with reference to a free space measurement, usually conducted in front of the air-to-vegetation interface for the vegetation loss measurements. Random or non-systematic errors cannot be avoided or calibrated for, these need to quantified.

4.5.1 Non-systematic errors

The main sources for random or non-systematic errors affecting the measurement results are thermal noise generated in components, component manufacturing tolerances, test equipment measurement accuracy and variation of component specification with frequency.

Errors introduced due to thermal noise are easily avoided by not measuring near the noise floor of the measurement set up. Noise floor levels are stated in sections 4.2.4 and 4.3.1; measurements were carried out at more than 10 dB above the noise floor, in most cases well above this level.

4.5.2 Attenuator calibration measurements

The attenuators used in the 20 GHz and 40 GHz systems were both specified in a calibration measurement. To precisely estimate the amount of extra attenuation introduced by an attenuator, all attenuators are need to be carefully calibrated inside the laboratory. Despite these calibrated values, an attenuator may lead to an inaccuracy of ± 0.5 dB in attenuation. The calibration curves of the attenuators at the receiver side for both 20 GHz and 40 GHz systems are shown in Fig. 4.14.

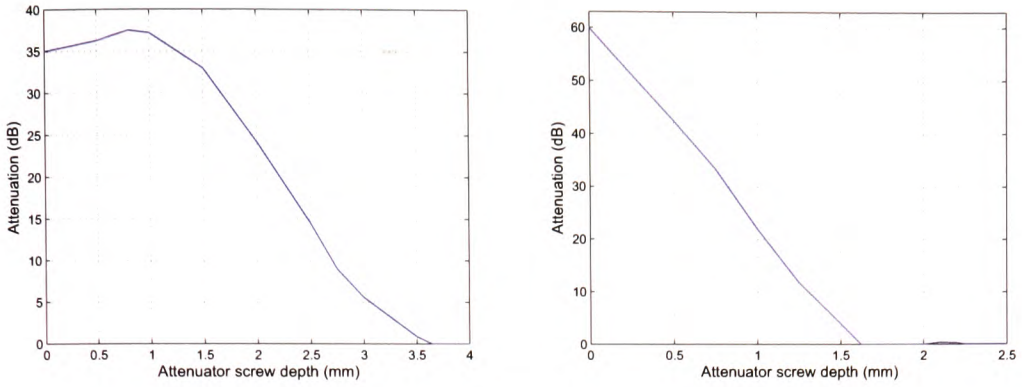

(a) (b)

Figure 4.14: Attenuator calibration curves: a) 20 GHz and b) 40 GHz measurement systems

4.5.3 Estimation of maximum non-systematic errors

Assuming the non-systematic errors generated during the measurements are not related, a worst-case estimation of the overall errors may be obtained by summing individual error contributions. With the same equipment setup and geometry, the maximum possible errors introduced by antennas, attenuators, and the spectrum analyser are evaluated according to their corresponding manufacturer's specifications. The error generated by the IF cable due to frequency deviation was measured using a VNA [14]. Contribution of errors from all components are summarised in Table 4.7.

Maximum possible errors	values
Antennas	±0.5 dB
Spectrum analyser	±0.5 dB
Attenuators	±0.5 dB
Low loss IF cable	±0.2 dB
LNA	±0.2 dB
Overall errors	±1.9 dB

Table 4.7: Maximum possible errors in the measurement systems

The 20 GHz and 40 GHz systems share a similar setup structure and the same IF frequency, therefore may be assumed having alike non-systematic errors. It shows that the maximum possible non-systematic errors is contained in the range of ± 2 dB.

4.5.4 Accuracy analysis of the measured angles

A careful alignment of the equipment setup has to be carried out prior to any measurement. The procedure is: (a) to manually place the transmitter and the receiver at the boresight, and adjust them at the same height level and in the middle of both side-walls, *i.e.* both the Tx and the Rx are pointing to each other through the middle of the vegetation canopy; and their distances to either side-wall are equal. (b) to apply the maximum power searching algorithm. This is done by a developed Graphical User Interface (GUI) software in MATLAB, thus avoiding any random measurement errors. The algorithm allows the receiver antenna to scan in the vicinity of the boresight axis. The scan is performed in a pre-assigned angle range, such as $\pm 10^o$, at a pre-assigned resolution such as 0.5^o or 1^o.

4.6 Summary and interim conclusion

This chapter provides a comprehensive overview of the measurement systems at both 20 GHz and 40 GHz. Measurement equipment is adequately described and illustrated in figures and the measurement procedure was explained. Both measurement systems were characterised in terms of the transmitter and the receiver units, overall dynamic range, and antenna radiation patterns. The underlying techniques used throughout the measurement campaign are presented. Possible causes of measurement errors are analysed, and subsequently evaluated.

In the next chapter, three types of pre-designed measurements will be demonstrated in terms of their geometries and their measured signal patterns. These measurements focus on different aspects when radiowaves propagate through vege-

tation such as re-scattering effects, directional spectra and excess loss as a function of vegetation depth.

Chapter 5

Measurement setups, results and analysis

This chapter describes the measurement setup and presents the results of the experimental programmes undertaken in the presence of vegetation in the radio path. These experiments address 3 different measurement scenarios: (a) measurements of re-radiation function pattern of a single tree in the radio path; (b) measurements of directional spectra of a group of trees while placing the receiver antenna inside the vegetation; (c) measurements of excess loss in the boresight direction as a function of vegetation depth. All measured radiation patterns presented in this chapter were performed in the principal E-plane. This chapter also provides initial analysis of the measurement results. More detailed analysis with respect to parameter extraction from directional spectra is described in section 5.3.2.

5.1 Phase function estimation and parameters extraction

The phase function characterises the directional scattering profile from the radiation impinging on a single specific or group of scatterers. In other words, this function specifies the amount of signal energy transferred from one direction to another due to the scattering process [14]. Furthermore, two out of four input pa-

rameters of the RET, α and β, can be extracted from the phase function pattern. Measurement of the phase function patterns, therefore, play a key role throughout this research project. The measured patterns will be used to extract parameters α and β by minimum squared error curve fitting of the measured re-radiation patterns with Gaussian shaped calculated phase functions.

5.1.1 Single tree measurements

Estimation of phase function patterns is based on measurements of the re-radiation patterns due to re-scattering from a single tree in the radio path. Considering a tree as a group of scatterers, the phase function is measured by rotating the receiver antenna along a circular arc around the tree with the antenna always pointing towards the centre of the tree [12, 13]. The phase function will be given by the received power levels at each angular position. A schematic diagram of the measurement setup is presented in Fig. 5.1.

The phase function measurements were conducted for both a sparsely and a densely foliate Ficus tree, Fig. 5.2 shows the 2 different types used, a) sparse and b) dense. The different densities of scatterers result in different scatter and absorption behaviour of the trees.

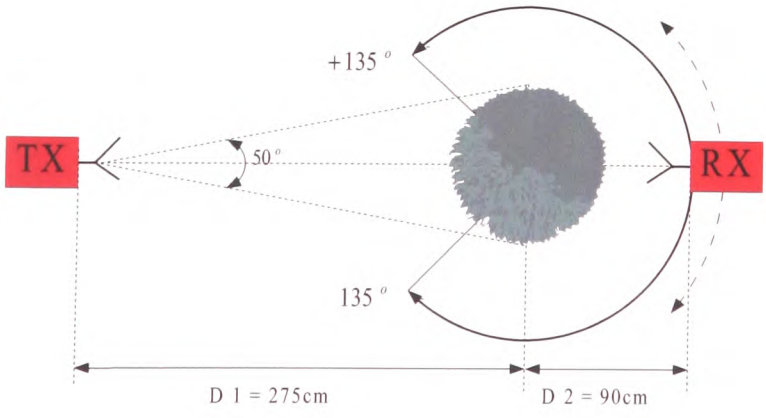

Figure 5.1: Scheme of phase function measurement approach

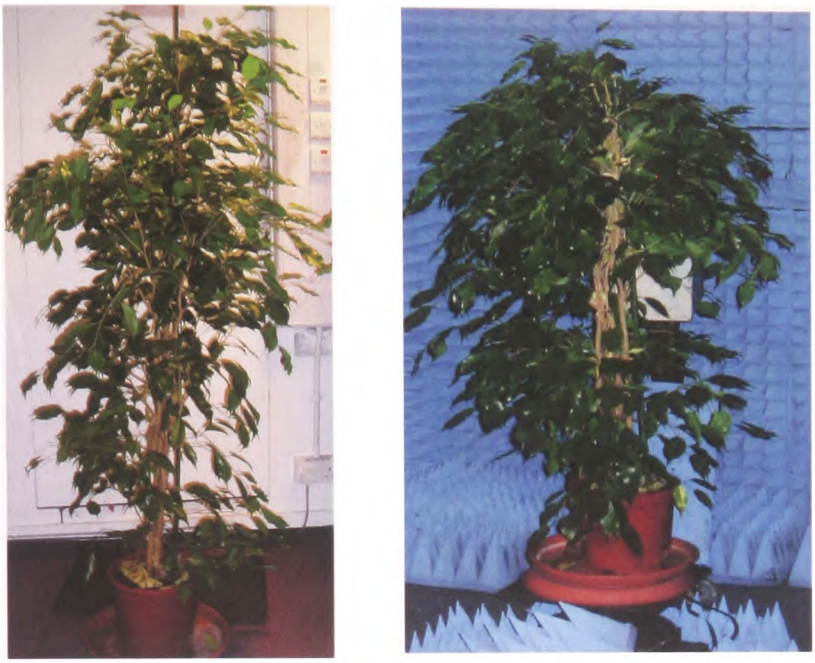

(a) Sparse tree (b) Dense tree

Figure 5.2: Photographs of the Ficus trees used in measurements

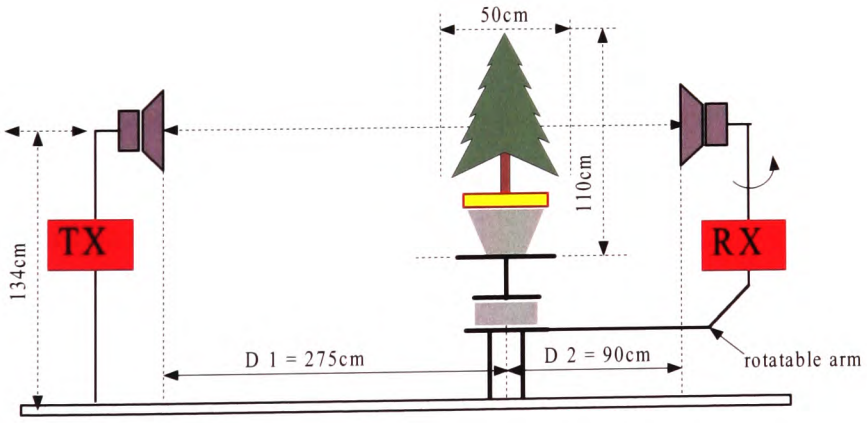

Figure 5.3: Phase function measurement setup: side view

Fig. 5.3 shows the measurement setup as viewed from the side. The transmitter was fixed on a tripod at one end of the chamber. The tree was placed still at the centre of the receiver rotation on top of a turn-table at a distance of 2.75 m from the transmitter. This distance is sufficient to be in the far field of the transmitter

antenna and also ensures that around 90% of the canopy of the tree is illuminated by the transmitter mainlobe. This arrangement minimises any contribution to the received signal due to lateral diffraction modes as well as reflections from walls and floors. The receiver is supported by a moveable rig, which is fixed to the turn-table. The turn-table rotates over an arc of 270^o at exact increments of 0.5^o. The distance between the tree and receiver is given by the length of the rig arm, *i.e.* 0.9 m. The transmitter and the receiver are carefully aligned with the tree under test to insure the illumination pointing is at the centre of the tree's canopy.

5.1.2 Single tree measurement results at 20 GHz

Measurements of phase function patterns were performed for three different sets: (a) free space with no tree present, for comparison purposes; (b) presence of a sparse tree; (c) presence of a dense tree. Standard gain horn antennas of 10 dBi, 15 dBi and 20 dBi were used as receivers respectively. For each antenna type all three sets of measurements are normalised to the free space maximum determined set (a). Fig. 5.4 shows the measured re-radiation patterns at 20 GHz. The measured patterns under set (a) are for comparison. When a tree is present, as expected, an increase of signal level is noticeable compared with its measured pattern under set (a), especially at rotation angles $< -60^o$ or $> +60^o$ which are well outside the main beam of patterns.

The measured 3 dB beamwidths of the re-radiation patterns show a widening with the tree present. The dense tree causes greater widening than the sparse tree. This is explained in section 5.1.5. At the centre of the measured patterns, some measured patterns are blocked very strongly due to presence of the tree. Serious attenuation is observed at the centre of the measured patterns, which is more pronounced when the dense tree is present.

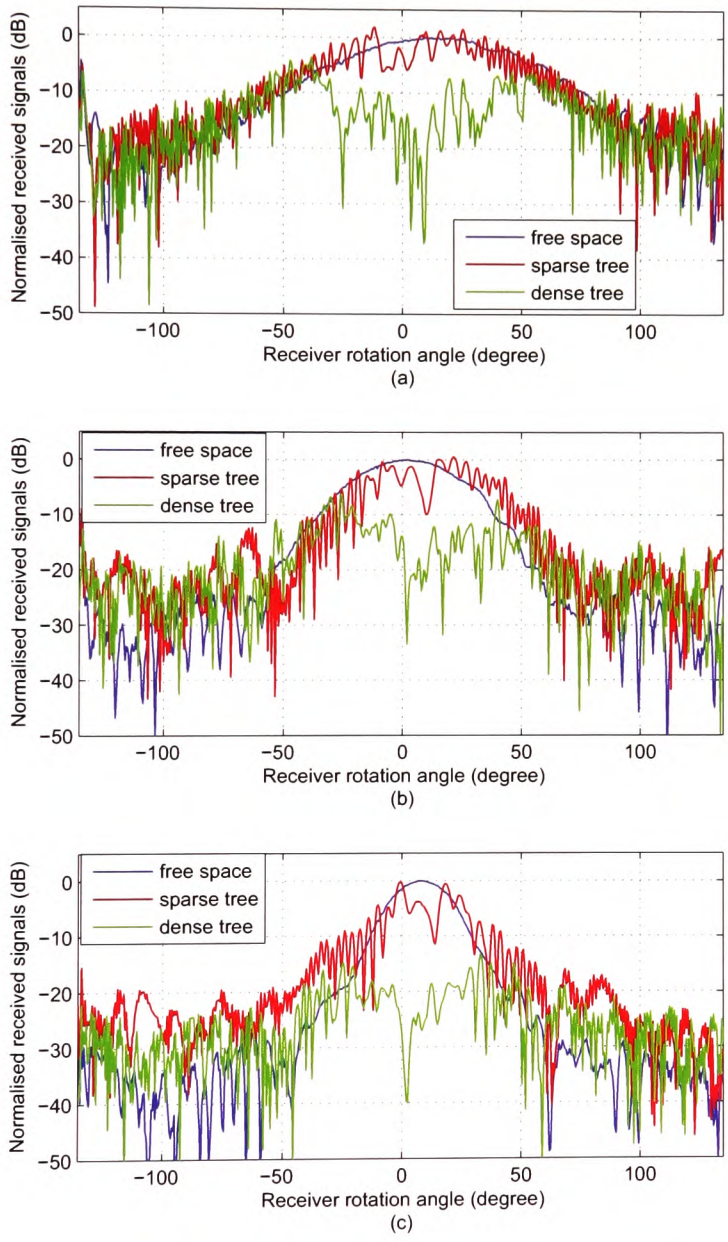

Figure 5.4: Single tree re-radiation measurements at 20 GHz using: (a) 10 dBi, (b) 15 dBi and (c) 20 dBi standard gain horns

5.1.3 Single tree measurement results at 40 GHz

Fig. 5.5 presents the measured re-radiation patterns using antennas at 40 GHz when a single tree is present. In general analysis it can be stated that the results of the re-radiation pattern measurements at 20 GHz and 40 GHz are very similar.

An alike blockage in the mainlobe of the received re-radiation patterns is observed when a tree is present, and it is more pronounced when the tree is dense. It is also observed that more attenuation is generated for the 40 GHz system, compared to the 20 GHz system under the same circumstances. This shows that more loss of signal power happens as the frequency increases.

Table 5.1 presents the calculated HPBW values for the following three cases: free space, a sparse and a dense tree, using standard gain horn antennas of 10, 15, and 20 dBi respectively at both 20 GHz and 40 GHz. For the case using a 20 dBi standard gain horn, when the dense tree was present at 40 GHz, the mainlobe of the received re-radiation pattern was not distinct from the rest of pattern due to a big blockage and severe attenuation. Consequently, its HPBW value is not available, however it can be estimated by the curve fitting approach presented later. Although not consistent in all measurements a general trend towards a widening of the main lobe with increasing vegetation depth is apparent from the results.

		Half power beamwidth (degree)		
Systems	Antennas	Free Space	Sparse Tree	Dense Tree
20 GHz	10 dBi Rx	67	70	111.5
	15 dBi Rx	39	51	74
	20 dBi Rx	24	27.5	80.5
40 GHz	10 dBi Rx	58	55	94
	15 dBi Rx	38.5	41.5	49
	20 dBi Rx	23	29	N/A

Table 5.1: Measured HPBWs of re-radiation patterns at both 20 and 40 GHz systems

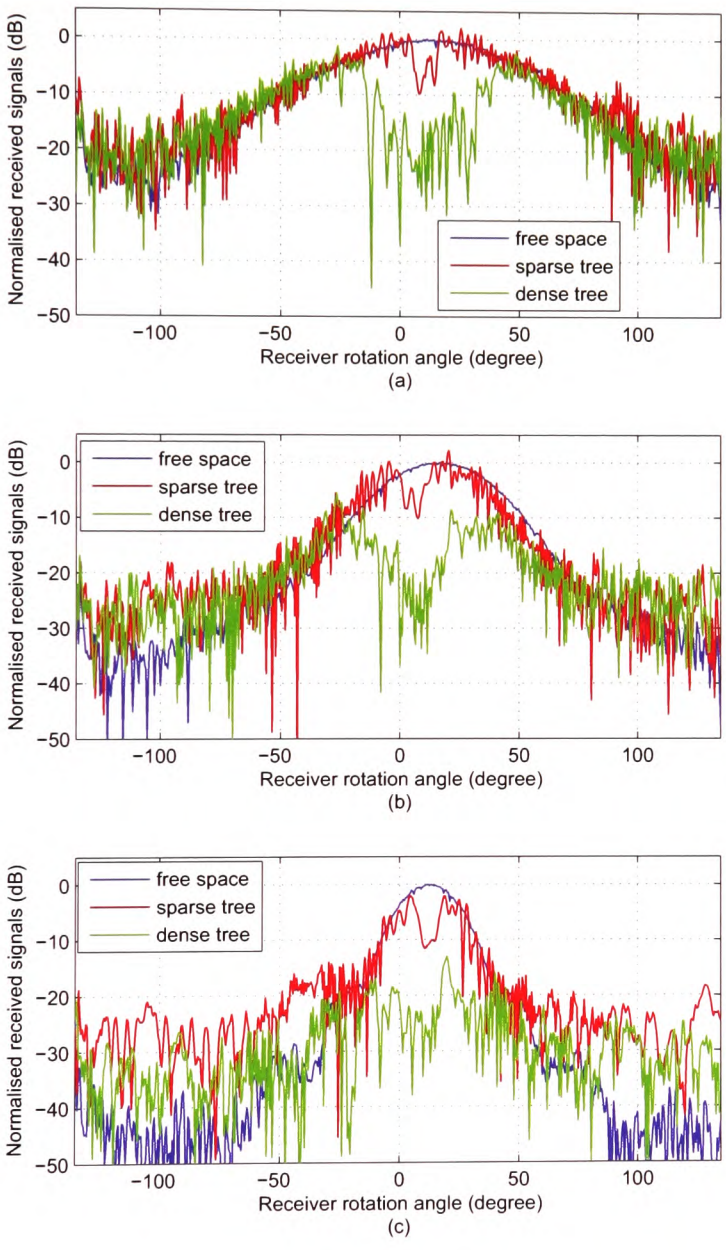

Figure 5.5: Single tree re-radiation measurements at 40 GHz using: (a) 10 dBi, (b) 15 dBi and (c) 20dBi standard gain horns

5.1.4 Phase function parameters extraction

The rationale to extract parameters α, the ratio of the amount of energy in the forward lobe over the total amount of energy, and β, the beamwidth of the forward lobe, is by minimising the rms errors between the measured patterns and the fitting curve in order to find the best fit values for α and β. The fitting curve used is the normalised Gaussian phase function as given by Eq. 5.1:

$$P_n(\phi_{RX}) = \frac{\alpha(\frac{2}{\beta})^2 e^{-(\frac{\phi_{RX}}{\beta})^2} + (1-\alpha)}{\alpha(\frac{2}{\beta})^2 + (1-\alpha)} \tag{5.1}$$

where ϕ_{RX} represents the receiver rotation angle, and P_n denotes the normalised values.

Fig. 5.6 shows two examples to illustrate the curve fitting results graphically. Fig. 5.6a represents the best fit curve of the measured pattern when the receiver antenna is the 15 dBi standard gain horn at 20 GHz (in the presence of a sparse tree). It generated a set of parameters $\alpha = 0.91$ and $\beta = 24^o$. Fig. 5.6b denotes the best fit curve of the measured pattern when the 20 dBi standard gain horn is used as the receiver antenna at 40 GHz (in the presence of a sparse tree). It yielded the extracted parameters $\alpha = 0.88$ and $\beta = 18.5^o$. For all measured patterns, the curve fitting procedures are similar, so are their resultant best fitting curves despite varying values of α and β. All extracted α and β values are presented in Table 5.2. With two examples given in Fig. 5.6, all fit curve graphs are listed in appendix C.

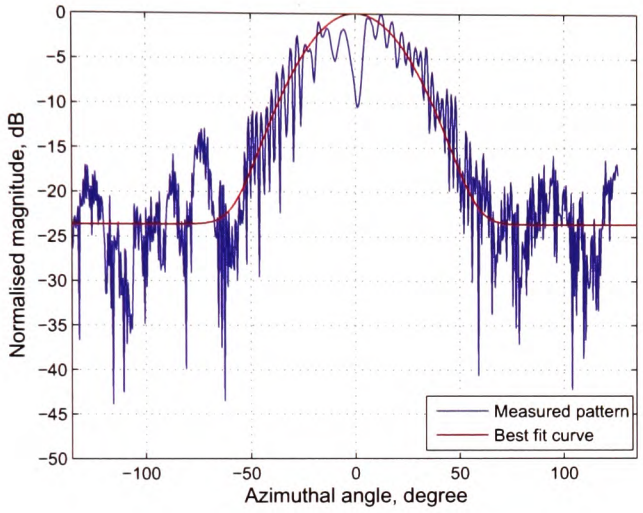

(a)

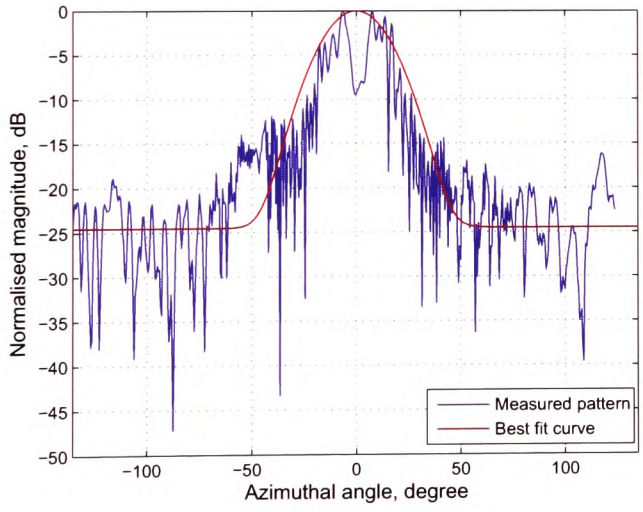

(b)

Figure 5.6: Two examples of curve fitting of the measured re-radiation patterns: (a) sparse tree, Rx antenna 15 dBi standard gain horn, at 20 GHz; and (b) sparse tree, Rx antenna 20 dBi standard gain horn, at 40 GHz.

Standard horn antennas		Measured Patterns	α	β (degree)	$\beta * 1.67$ (degree)
20GHz	10 dBi	free space	0.95	41.5	69
		sparse tree	0.93	37.5	63
		dense tree	0.87	47.5	79
	15 dBi	free space	0.98	24.5	41
		sparse tree	0.91	24	40
		dense tree	0.82	29	48
	20 dBi	free space	0.99	18	30
		sparse tree	0.93	21.5	36
		dense tree	0.66	23.5	39
40GHz	10 dBi	free space	0.96	39.5	66
		sparse tree	0.94	35.5	59
		dense tree	0.91	43.5	73
	15 dBi	free space	0.99	27.5	46
		sparse tree	0.96	22	37
		dense tree	0.88	27.5	46
	20 dBi	free space	0.99	15	25
		sparse tree	0.88	18.5	31
		dense tree	0.62	16	27

Table 5.2: Parameters extraction from the measured re-radiation patterns

In theory, the relationship between the parameter β and its corresponding HPBW is $\beta * 1.67$=HPBW [16[. In general, it shows that the HPBW becomes wider as a tree stands in the boresight direction although some minor exceptions exist. The denser the tree is, the wider the HPBW of the measured pattern. The extracted α values became smaller as the HPBWs are widening due to tree scattering. The results given in Table 5.2 do not consider the influence of the convolution, which happens between the antenna radiation pattern and the re-radiation function during the measurement process. More details regarding this issue will discussed in chapters 6 and 7.

5.1.5 Analysis of beamwidth widening effects

There are two factors contributing to the widening effects: difference of the measurement geometry and scattering of single trees.

5.1.5.1 Widening effect due to measurement setup

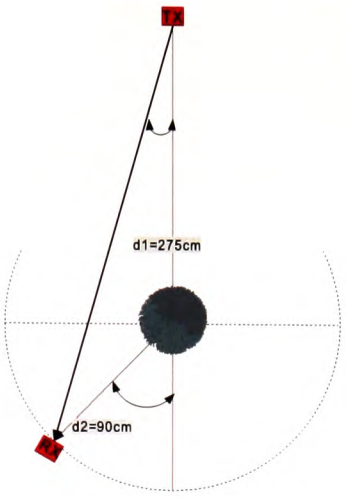

Figure 5.7: "Stretch Factor" demonstration

Fig. 5.7 shows the measurement geometry for the re-radiation functions of single trees. The same setup was used for the free space re-radiation patterns, measurement without a tree present. The resultant patterns are, therefore, different from the measured antenna radiation patterns described in chapter 4. They are apparently wider. The reason is that the difference of the measurement setup causes a widening or "stretching" effect.

In chapter 4, the antenna radiation patterns were measured by placing the receiver on top of the turn-table and rotating itself for a complete circle. While for the measurement setup shown in Fig. 5.7, the receiver antenna was fitted on a mechanical rig and moving along an arc centred at the turn-table. When the radius of the arc (d_2) is significantly smaller than the distance (d_1) of the transmitter to the centre, the received pattern will look similar to the antenna radiation pattern, but not equal to it. Whenever $d_1 \gg d_2$ is not given the antenna beamwidth will increase by what may be termed a "Stretching Factor" SF.

Systems	Antennas	Moving along arc HPBW1 (degree)	Rotating by vertical axis HPBW2 (degree)	Stretch Factor HPBW1/ HPBW2
20 GHz	10 dBi Rx	67	48.5	1.38
	15 dBi Rx	39	28.5	1.37
	20 dBi Rx	24	17	1.41
40 GHz	10 dBi Rx	58	35	1.65
	15 dBi Rx	38.5	29	1.33
	20 dBi Rx	23	16.5	1.39

Table 5.3: Evaluation of the "Stretching factor" of the free space measurements

Evaluation of the SF could be approximated as $SF = \frac{d_1+d_2}{d_1} = \frac{275+90}{275} = 1.33$. It is evident when $d_1 \gg d_2$ the SF will approach 1 and the widening effect would not be noticeable. Table 5.3 quantifies the widening effect based on the measured data and calculated HPBWs. It shows that the calculated values of SF are consistent with the estimation of $SF = \frac{d_1+d_2}{d_1}$, although an exception occurred when using the 10 dBi standard gain horn at 40 GHz.

5.1.5.2 Widening effect due to geometry

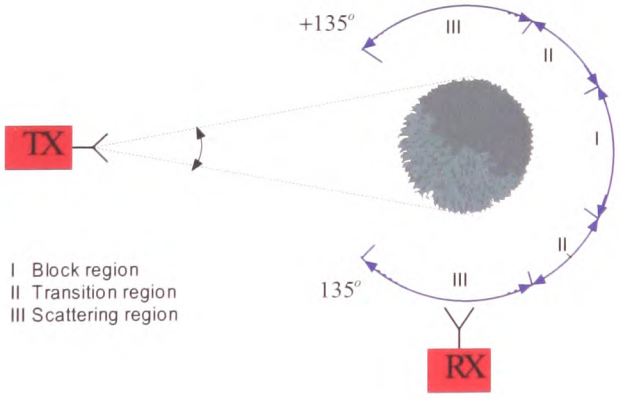

Figure 5.8: Schematic demonstration of three regions of re-radiation patterns

When a tree is present, the widening effect can be explained by partitioning the receiver rotation into three zones (or five parts) as shown in Fig. 5.8:

1. the block zone (I): located behind the canopy. Where the received signal power consists of waves passing straight through the tree canopy and lateral contribution due to partial re-scattering. The lateral contribution, however, is very small, and the tree's blockage causes much severe loss. This explained the blockage occurred at the centre of the measured patterns.

2. two transition zones (II) located between the block region and the scattering region. Where the received power has two sources: one is the signals emanating from the tree due to scattering and the other is being radiated directly from the transmitter and received by the mainlobe of the receiver, the so-called coupling. This may contaminate the received power in these regions and lead to widening beamwidths of the measured re-radiation patterns. Thus, measurements without a tree presence using the same setup were carried out as references.

3. two scattering zones (III): where the principal axis of the receiver mainlobe is pointed away from the transmitter towards the tree. Coupling between the transmitter and the receiver is significantly less than that in the region (II), although partial contribution in much less magnitude may occur through the sidelobes of the receiver. Consequently the received power comprises mainly of the tree's scattering signals. This approach can be used to estimate the scattering coefficient of the vegetation [14[. This also explained the noticeable increase in signal levels in regions (III) with a tree present compared with its counterpart without. The scattering signals contribute to the widening effect of the beamwidth of the measured re-radiation patterns. It can also be observed that an antenna with narrower beamwidth, *i.e.* high directivity, provides an overall higher increase in signal level than that with a wider beamwidth, *i.e.* low directivity.

The two transition and scattering regions are located symmetrically regarding the boresight of the transmitter and the receiver. Division of the three regions may vary due to the diversity of the beamwidths of the receiver antennas.

From the discussions above, the measured re-radiation functions of single trees have been affected by the measurement setup geometry and the mutual coupling between the transmitter and receiver. Therefore, new measurements are designed to avoid such problems. These measurements are conducted using a group of trees to obtain the antenna's directional spectra and are given in section 5.2.

5.2 Group of trees measurements

In this research project, the fundamental of modelling the radiowave propagation through vegetation is the Radiative Energy Transfer theory, in which the vegetation media is simulated as a statistically homogeneous vegetation body. In order to establish a homogeneous vegetation media environment, 16 *Ficus* trees were used to form a downscaled homogeneous forest in a 4×4 configuration as shown in Fig. 5.9. Through such an arrangement, the measurement scenario inside the anechoic chamber could be considered as an ideal forest environment to verify the RET theory despite its limited physical dimension inside the chamber.

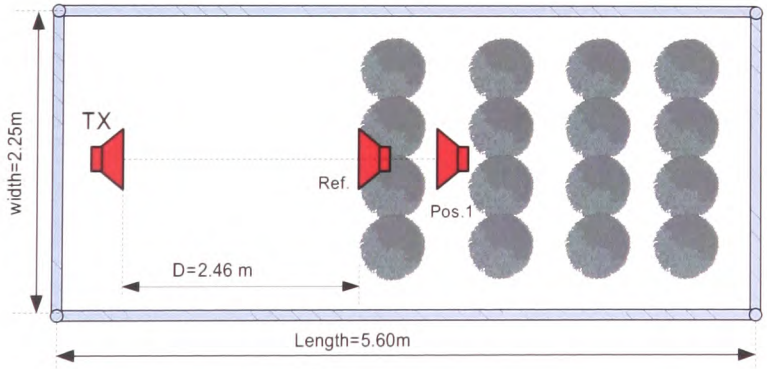

Figure 5.9: Geometry of measurements in a downscaled homogeneous forest

5.2.1 Measurement geometries

Measurements were conducted at four different positions as shown in Figs. 5.9 and 5.10:

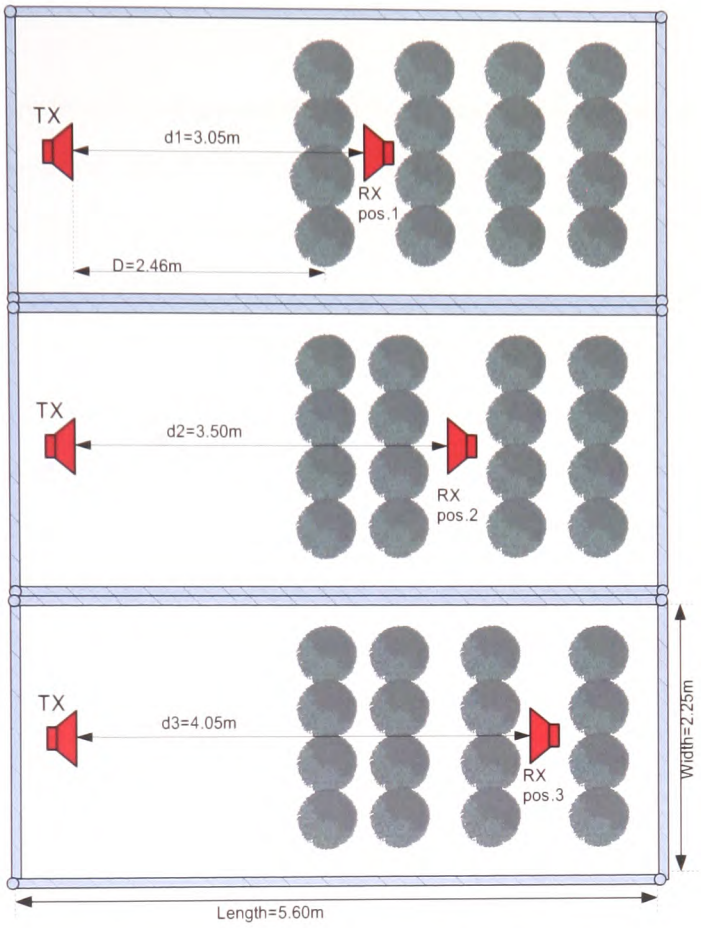

Figure 5.10: Re-radiation measurements in a downscaled forest

1. The position of Ref. indicates the measurement geometry when the receiver antenna is placed at the air-to-vegetation interface. The measured patterns are used as the reference to investigate the excess attenuation caused by the presence of trees. The free space loss can be calculated by the *Friis* equation [88].

2. The location marked as Pos. 1 shows the first available measurement position inside the vegetation, *i.e.* behind the first row of trees. Pos. 1 is considered as the preferred measurement position (where the coherent component I_{ri} dominates) to obtain the extinction coefficient k_s, as described in chapter 3.

3. Receiver Pos. 2 and 3 indicate the second and the last available measurement positions, respectively, inside the vegetation volume.

The distances from the transmitter to the air-to-vegetation interface and to each measurement position are also labeled in Figs. 5.9 and 5.10. The height of the transmitter and the receiver was set to 1.10 metres in order to ensure that the antennas pointed at the middle of canopy, which is also the densest part in the canopy region. The lengths of various receiver antennas under test could vary from 2.0 cm to 12.5 cm, as shown in Table 4.1, which leads to variations in distances between the transmitter and the receiver. Consequently, d_1, d_2 and d_3 could have measured inaccuracies of up to 10 cm.

During measurements, trees were kept still unless necessary movements. The receiver antenna was placed at each position and rotated in a complete circle from -180^o to $+180^o$ in steps of 1^o. The received power consists of radiation impinging from the transmitter through the vegetation, and the re-scattering signals from the trees surrounding the receiver antenna. The measured pattern is known as the directional spectrum.

The term vegetation depth is used to indicate the relative distances inside the vegetation, which is the referenced distance starting at the air-to-vegetation interface. Three measurement positions for depth measurement are used, namely 0.59m, 1.04m and 1.59m. Fig. 5.11 illustrates the views from the transmitter side when the receiver antenna was placed at the air-to-vegetation interface (Fig. 5.11a), and the first position inside the vegetation (Fig. 5.11b). Trees are placed regularly together in order to establish a statistically homogeneous downscaled forest, as illustrated in the photograph shown in Fig. 5.11.

5.2.2 Directional spectra measurement results at 20 GHz

Figs. 5.12 and 5.13 present the measured directional spectrum of the receiver antenna at the four measurement locations described above, *i.e.* the air-to-vegetation interface, the *1st*, *2nd* and *3rd* positions inside the vegetation, using 10 dBi (Fig. 5.12a),

(a)

(b)

Figure 5.11: Photographs of measurement setup with the group of trees: (a) receiver at the air-to-vegetation interface; (b) receiver at position 1 inside the trees

15 dBi (Fig. 5.12b), and 20 dBi (Fig. 5.13a) standard gain horns and 20 dBi (Fig. 5.13b) Gauss horn, respectively, as the receiver antennas at 20 GHz.

	Gauss horn	standard gain horns		
	20 dBi	10 dBi	15 dBi	20 dBi
HPBW at Ref.	13^o	56^o	32.5^o	18^o
HPBW at Pos.1	11^o	69^o	20^o	6^o
HPBW at Pos.2	6^o	30^o	29^o	5^o
HPBW at Pos.3	49^o	37^o	37^o	63^o

Table 5.4: Extracted HPBWs of measured directional spectra at various measurement positions at 20 GHz

As shown in the figures above, all measured values of the directional spectra with appropriate attenuation at the receiver side are well above the maximum experienced values of the noise floor, -70 dBm, and below the saturation threshold of the active devices. The aim of exhibiting four measured patterns with varying vegetation depths in one figure is to demonstrate graphically the widening of the beamwidths of the measured directional spectra as the receiver moves inside the vegetation medium. The extracted HPBWs are presented in Table 5.4.

The HPBW at Ref. in Table 5.4 indicates the extracted Half Power Beam Widths at the measurement location of the air-to-vegetation interface, *e.g.* the reference position. Similarly, HPBWs at Pos.1, 2, and 3 indicate the extracted HPBWs at measurement positions 1, 2, and 3, respectively, as shown in Fig. 5.10. The HPBWs were obtained directly from the measured patterns; however they did not demonstrate rigorously the broadening effect with increasing vegetation depth. The reasons for this are (a) the *Ficus* trees used are relatively dense; (b) the forest was built regularly and thick to make the vegetation medium as homogeneous as possible, and meet the limitation of physical size in the anechoic chamber. These factors expedite the attenuation of the coherent components I_{ri} and the incoherent components I_1, both of which have a well-defined direction along with the incident waves, however they facilitate the incoherent components I_2. This leads to the forward lobe disappearing quickly under current circumstances, and it is not always easy to distinguish it

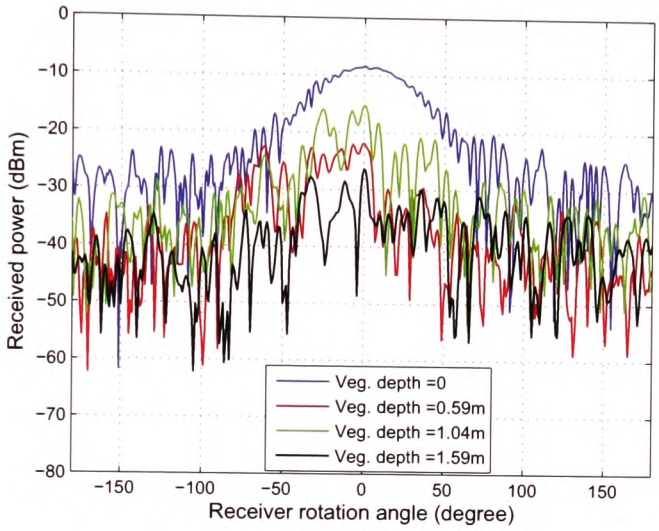

(a)

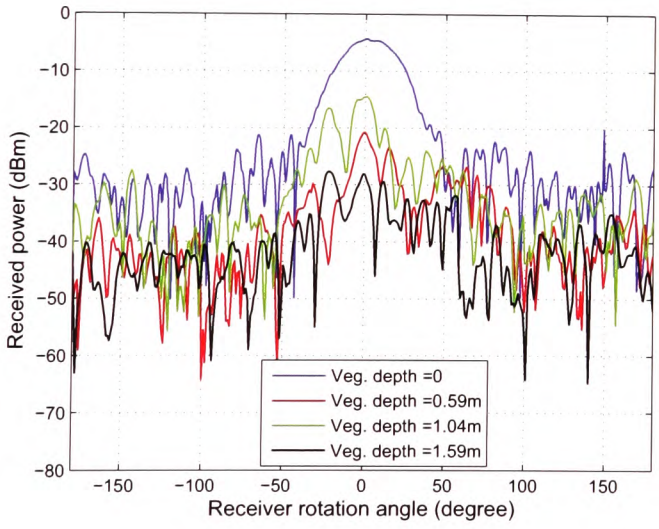

(b)

Figure 5.12: Measured directional spectra at 20 GHz: (a) 10 and (b) 15 dBi standard gain horns

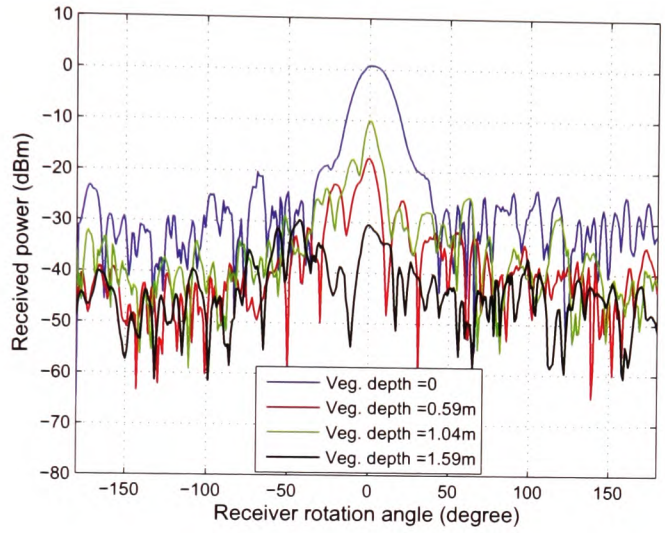

(a)

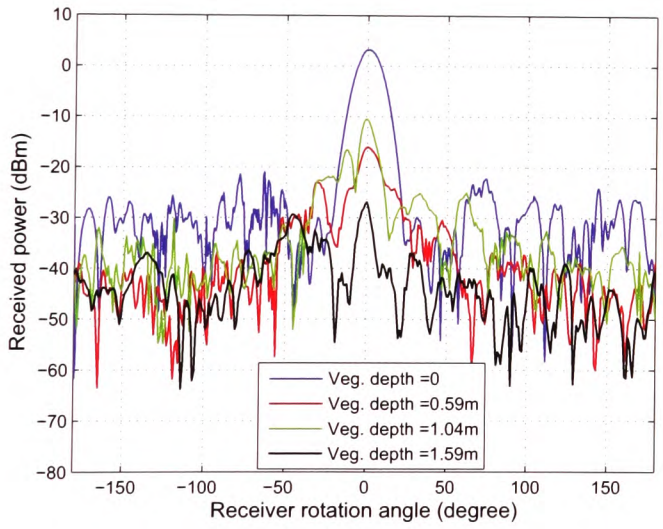

(b)

Figure 5.13: Measured directional spectra at 20 GHz: (a) 20 dBi standard gain and (b) 20 dBi Gaussian horn

from the rest, *e.g.* the sidescatter and backscatter regions. Therefore, the best way to determine the HPBWs need to be determined. In later chapters a pre-filtering technique is introduced to alleviate this problem.

The figures also show that the peak values of the directional spectra, *e.g.* the maximum in Figs. 5.12a), b), and 5.13a), b), respectively, decrease rapidly with increasing vegetation depth. Initially, the forward lobe starts broadening, and decreasing in magnitude; until a certain point where the forward lobe disappears, *e.g.* the incoherent components I_2 prevail. It is evident when using a receiver antenna with a narrow beamwidth that its main beam disappears quicker than that of a wide beamwidth antenna. This partially proves that the radiation pattern of the receiver antenna has influenced the measured patterns. Consequently, to obtain accurate knowledge of the incident wave, it is necessary to remove the influence of the receiver antenna by use of a deconvolution, which is presented in chapters 6 and 7.

5.2.3 Directional spectra measurement results at 40 GHz

Measured directional spectra for all available receiver antennas: 10 dBi, 15 dBi, 20 dBi standard gain horns and a 29 dBi Lens horn at four measurement positions are illustrated in Figs. 5.14a), b), 5.15a) and b), respectively, at 40 GHz. Similar to section 5.2.2, a decrease in the peak values and the disappearance of the forward lobe can easily be observed in each case.

	Lens horn	standard gain horns		
	29 dBi	10 dBi	15 dBi	20 dBi
HPBW at Ref.	7^o	47^o	40^o	12^o
HPBW at Pos.1	6^o	30^o	18^o	11^o
HPBW at Pos.2	5^o	66^o	26^o	29^o
HPBW at Pos.3	81^o	83^o	38^o	81^o

Table 5.5: Extracted HPBWs of measured directional spectra at various measurement positions at 40 GHz

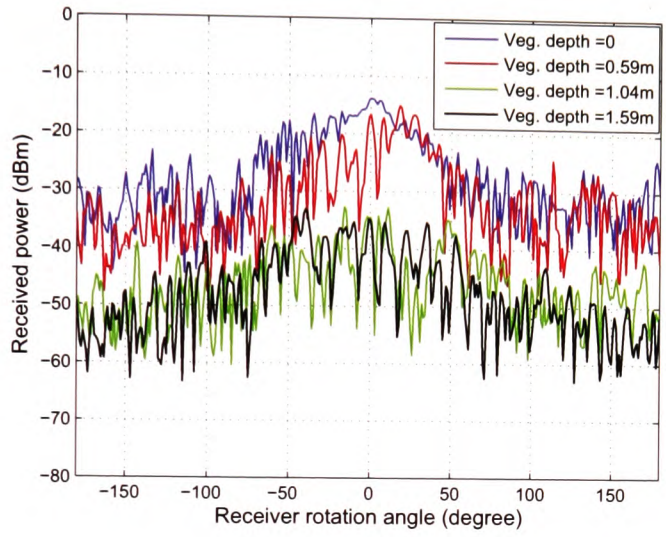

(a)

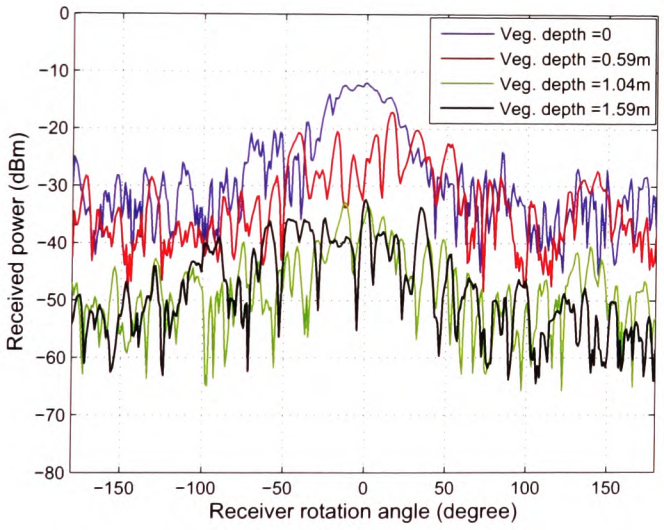

(b)

Figure 5.14: Measured directional spectra at 40 GHz: (a) 10 and (b) 15 dBi standard gain horns

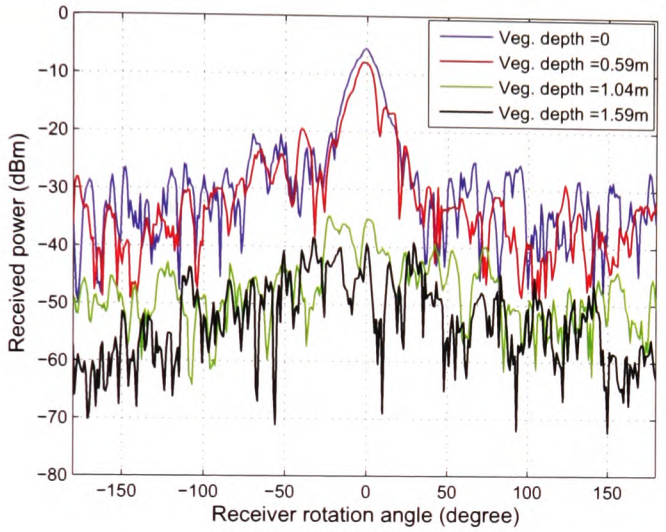

(a)

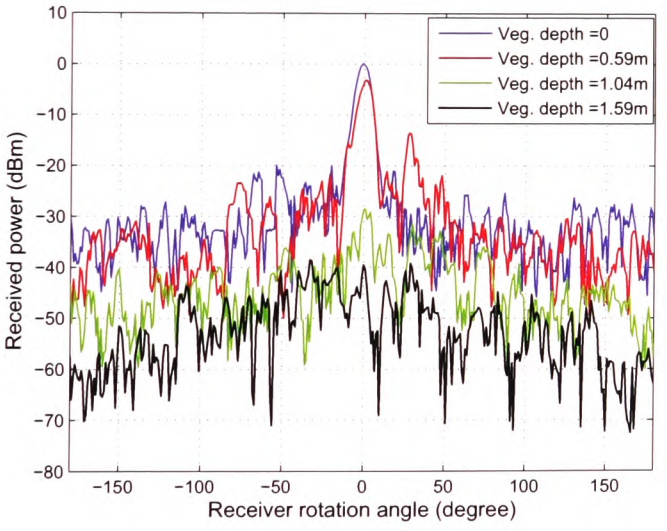

(b)

Figure 5.15: Measured directional spectra at 40 GHz: (a) 20 dBi standard gain and (b) 29 dBi Lens horn

All discussions in subsection 5.2.2 at 20 GHz are also applicable to the 40 GHz system with the exception that the peak values of the measured patterns in magnitude under normal incidence decrease more rapidly; and the forward lobe disappears faster. These are coincident with expectations: radiowaves at higher frequencies decays more rapidly inside the vegetation volume.

The extracted HPBWs for antennas used at each measurement location are given in Table 5.5. It is evident that in Figs. 5.14 and 5.15 the measured patterns at positions 2^{nd} and 3^{rd} are almost indistinguishable. This indicates that the excess attenuation versus the vegetation depth has reached the stable stage and this slows the attenuation rate. The underlying principal of this behaviour has been explained in section 3.4.

5.3 Excess attenuation with vegetation depth measurements

To investigate the excess attenuation as a function of vegetation depth, the vegetation depth measurements were designed and conducted in the anechoic chamber. The measured excess attenuation was utilised for comparison with the prediction of excess attenuation using the RET model.

5.3.1 Schematic measurement geometry

Using the maximum available physical length of the anechoic chamber, the vegetation depth measurements could be performed at up to 8 positions inside the vegetation volume, illustrated in Fig. 5.16. This kind of measurement focuses on the excess attenuation under normal incidence case. Hence, the receiver antenna rotated from -40^o to $+40^o$ only behind the trees as the transmitter and the receiver were coordinated at the boresight, *e.g.* the incident angle = 0^o. The transmitter and the receiver were set to 1.10 m in height in order to point at the middle of the vegetation canopy. The trees were formed in pairs instead of a row of four in the last

section; this makes the maximum vegetation depth possible under current circumstances. All measurement distances were guaranteed on the far-field criterion and are presented in Table 5.6 with correspondingly extra free space loss. Photographs in Fig. 5.17 give an intuitive views of the measurement geometry. Trees were kept still as much as possible during the measurements.

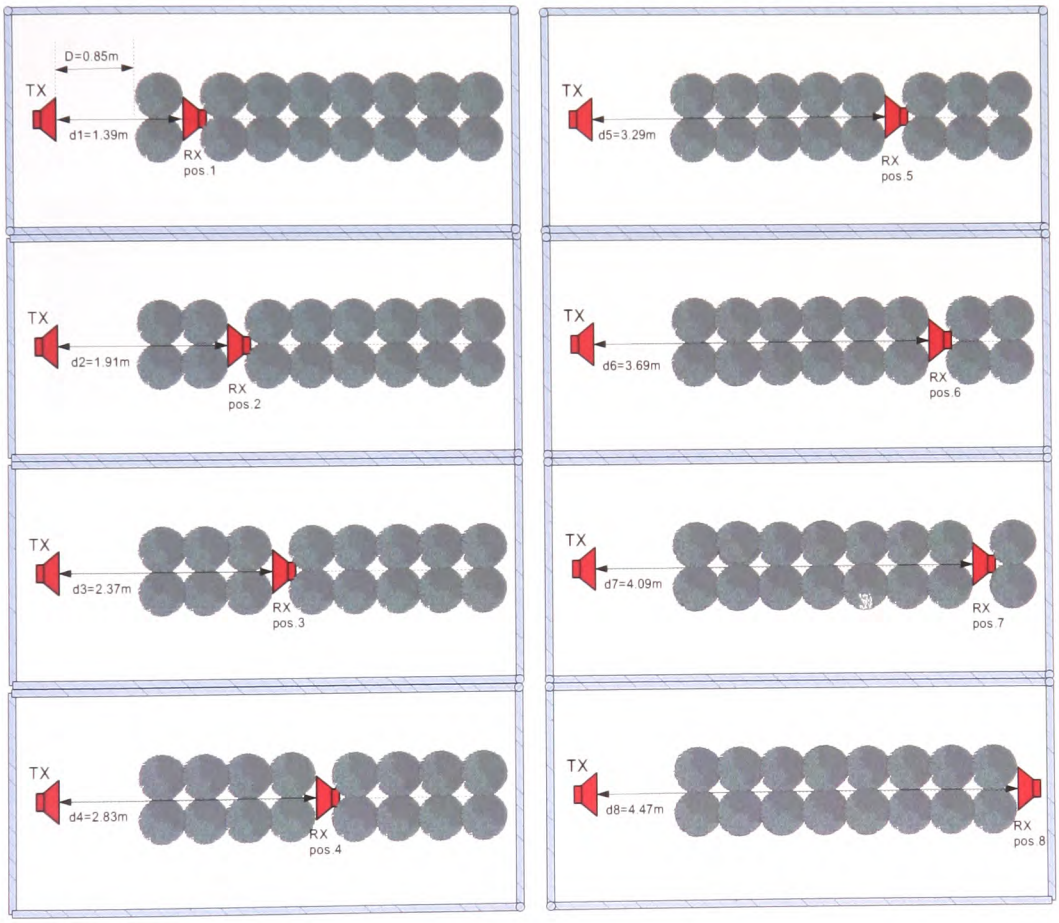

Figure 5.16: Schematic geometry of vegetation-depth measurements

Location	Distances between TX and RX	Vegetation depth	Normalised Excess FSL
Air-to-vegetation interface	0.85 m	0	0 dB
Behind 1*st* line of trees	1.39 m	0.54 m	4.27 dB
Behind 2*nd* line of trees	1.91 m	1.06 m	7.03 dB
Behind 3*rd* line of trees	2.37 m	1.52 m	8.91 dB
Behind 4*th* line of trees	2.83 m	1.98 m	10.45 dB
Behind 5*th* line of trees	3.29 m	2.44 m	11.76 dB
Behind 6*th* line of trees	3.69 m	2.84 m	12.75 dB
Behind 7*th* line of trees	4.09 m	3.24 m	13.65 dB
Behind 8*th* line of trees	4.47 m	3.62 m	14.42 dB

Table 5.6: Parameters of the vegetation depth measurements

(a) (b)

Figure 5.17: Photographs of the vegetation depth measurements: (a) view from the transmitter; (b) view from the receiver

5.3.2 Comparison of the excess attenuation from the measured and the predicted results

In the vegetation depth measurements, antennas with large gain were used so that larger power was provided to ensure that radiowaves transmitted into the vegetation as deep as possible, before the received signals were swamped by the noise floor and hence became undetectable. The antennas used were grouped into four measurement scenarios and presented in table 5.7.

	System	Transmitter	Receiver
scenario A	20 GHz	20 dBi standard gain horn	20 dBi Gauss horn
scenario B	20 GHz	20 dBi standard gain horn	20 dBi standard gain horn
scenario C	40 GHz	20 dBi standard gain horn	20 dBi standard gain horn
scenario D	40 GHz	20 dBi standard gain horn	29 dBi Lens horn

Table 5.7: Antennas under test in the vegetation depth measurements

Prediction of excess attenuation as a function of vegetation depth while the radiowaves propagated through the vegetation was achieved using the RET theory. The input parameters of the RET model were extracted from the measured data using the methods introduced in chapter 3. The relative free space losses were calculated and given in Table 5.6. Their effects are eliminated during the parameter extraction. The extracted input parameters corresponding to the four measurement scenarios are presented in Table 5.8:

	α	β	$k_e\,(^{dB}/_m)$	W	$\Delta\gamma_R$
scenario A	0.39	8^o	7.04	0.3	7.8^o
scenario B	0.45	9^o	5.54	0.15	11^o
scenario C	0.75	12^o	4.19	0.2	10.5^o
scenario D	0.89	7^o	7.11	0.65	4.2^o

Table 5.8: Extracted input parameters of the RET theory for the four measurement scenarios

Figs. 5.18 and present the comparison of excess attenuation between the measured values and the RET prediction curve using the corresponding set of parameters for scenarios A and B, given in Table 5.8. At 20 GHz, the measured patterns show the detectable mainlobe at all eight measurement locations; and the maximum vegetation depth is 3.62 m at the last measurement location. The measured results show a poor overall agreement with the RET prediction curve for both scenarios. The reason for the poor agreement is that all 4 RET input parameters were extracted from one single type of measurement only *i.e.* excess attenuation with vegetation

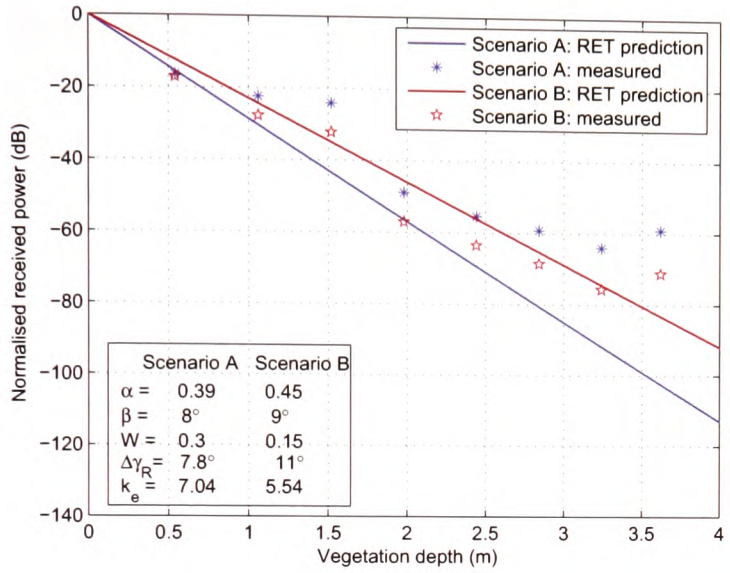

Figure 5.18: Comparison of excess attenuation between the RET prediction and the measured signals at 20 GHz

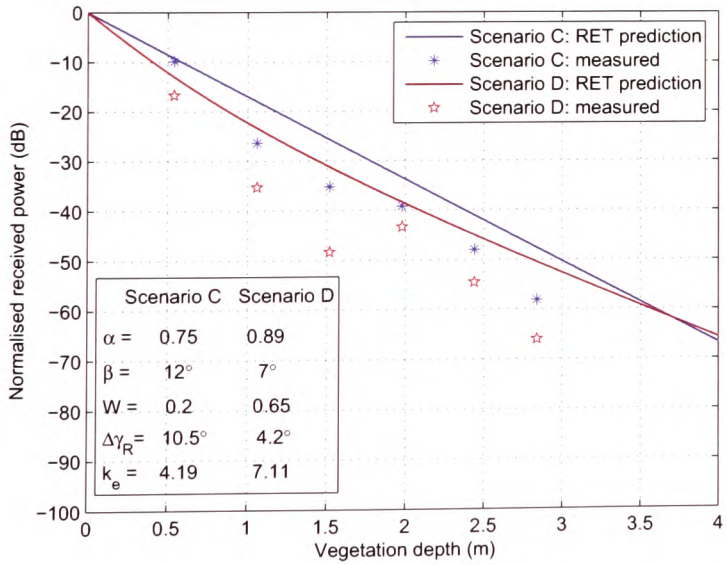

Figure 5.19: Comparison of excess attenuation between the RET prediction and the measured signals at 40 GHz

depth. Neither has any deconvolution process been applied to remove the distortion caused by the receiver antenna radiation pattern. At 40 GHz the agreement between prediction and measurement is similarly poor to the 20 GHz case for the same reason.

5.4 Summary and interim conclusion

This chapter introduced the measurements in three different kinds of tree formation: single tree, groups of trees and paired trees at both 20 GHz and 40 GHz. Measurements with a single tree were conducted to investigate the phase function generated by scattering effects, as well as extracting the parameters α and β. In the measurements with groups of trees, the received signal patterns provided the directional spectra of the incoherent components, which offered an insight into the energy distribution of the signals inside the vegetation volume and partially validated the forward-lobe broadening with increasing vegetation depth. Measurements with pairs of trees had the advantage of enabling on examination of the capability of the RET prediction to model the excess attenuation in the presence of vegetation since the designed measurements provided more vegetation depths than that available in the groups of trees measurements.

Chapter 6

Overview of different deconvolution techniques and implementation difficulties

6.1 Introduction

Over the past few decades, various techniques have been developed to implementing increasingly accurate deconvolution algorithms [27–29[. Generally four different types of deconvolution algorithm can be distinguished. The first type is acquisition averaging, which aims to reduce signal acquisition errors and noise by averaging several acquisitions taken within a short period of time. This technique reduces noise significantly but introduces additional errors to the signal due to time drift [89]. The second type aims at suppressing noise by applying a filter [28[. The filter will modify the deconvolution result as it tries to eliminate the noise, thereby introducing its own errors. The third approach is an iterative operation, in which successive approximations to an estimate are produced in order to minimise the error between the noisy output signal and the estimate at each iterative run. This approach relies on being able to obtain an initial close estimate of the true information to start the iterative process. In addition a correction term needs to be formulated to minimise the errors. The iteration process itself requires a certain amount of repetition

requiring computational time and effort, especially if convergence is slow and high iteration numbers are required. Furthermore as with any iteration method convergence is far from guaranteed and highly depends on the nature of the data that is to be deconvolved. The fourth and final approach is the so called optimal compensation technique [89]. This involves the design of a compensator, which operates on the noisy output signal to yield an estimate to one of the inputs. The design of the compensator involves an iterative process on a single variable.

To provide clarity and consistency the following conventions are observed throughout this chapter as well as chapter 7. The introduction above highlighted what is commonly referred to as "time" and "frequency" domain methods. These are investigated and consequently implemented in chapter 7. However, since the data recorded and intended to be processed by deconvolution represents received and often normalised signal strengths with rotation angle, this cannot be termed "time domain". The domain of the recorded data prior to any transform will therefore be termed the original domain and consequently, after the transform, it will be referred to as the transform domain. For time line data the original domain is the time domain and the transform domain is the frequency domain.

In correspondence with this convolution symbols k, θ and t will appear in the original domain, termed the time domain, when time line data is described. Symbols ω and n are the corresponding variables in the transform domain; these are equivalent to the frequency domain for the time line data. Additionally the symbols t and ω will be used to represent both continuous and discrete data, whereas k, θ and n will only be used for investigations involving discrete data.

6.2 Central-limit theorem and convolution theorem

In general it can be observed that convolving two single-peaked functions yields a much smoother result than either component on its own. For example convolving two rectangle functions yields a triangle; the convolution of two triangle functions (four rectangles) produces a result close to a Gaussian curve, as shown in Fig. 6.1. In fact

a near perfect Gaussian pattern can be obtained by the result of an infinite number of convolution functions with themselves, if they fulfilled the conditions listed below, which when applied rigorously is known as the central-limit theorem [27]. According to Jansson [27], a consequence of the central-limit theorem is that when a function $f(t)$ is convolved with itself n times, in the limit $n \to \infty$, the convolution product is Gaussian with variance n times the variance of $f(t)$, provided that the area, mean, and variance of $f(t)$ are finite. The condition may be stated as:

$$\int_{-\infty}^{+\infty} f(t)dt < \infty \tag{6.1}$$

$$\int_{-\infty}^{+\infty} tf(t)dt < \infty \tag{6.2}$$

$$\int_{-\infty}^{+\infty} t^2 f(t)dt < \infty \tag{6.3}$$

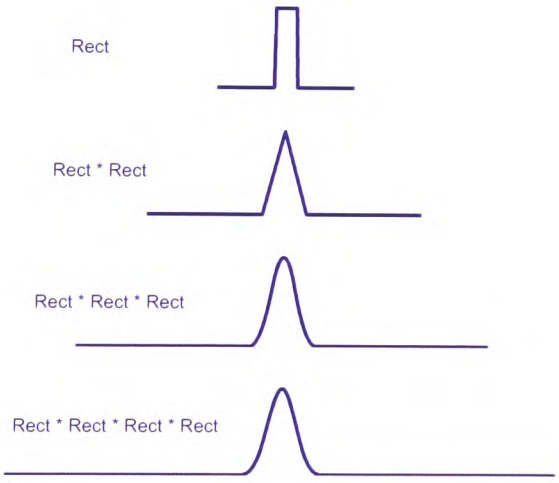

Figure 6.1: Convolution production of rectangles

Convolving non-identical functions, the conditions become somewhat more complex [83]. If two Gaussian functions are convolved, the result is Gaussian with

a variance equal to the sum of the variances of the components. For two non-Gaussian functions, the convolution product will have a variance equal to the sum of the variances of the component functions [27].

The convolution theorem [83] states that convolving two functions is equivalent to finding the product of their Fourier transforms. This can easily be proved using the definition of the Fourier transform:

$$F(\omega) = \frac{1}{\sqrt{2\pi}} \int_{-\infty}^{+\infty} f(t) e^{-j\omega t} dt \tag{6.4}$$

$$f(t) = \frac{1}{\sqrt{2\pi}} \int_{-\infty}^{+\infty} F(\omega) e^{j\omega t} d\omega \tag{6.5}$$

In particular, if random functions $x(t)$, $h(t)$, and $y(t)$ have transform forms $X(\omega)$, $H(\omega)$, and $Y(\omega)$, then

$$y(t) = x(t) * h(t) \tag{6.6}$$

is equivalent to

$$Y(\omega) = X(\omega) H(\omega) \tag{6.7}$$

From the symmetry of Eqs. 6.4 and 6.5, and the relationship of Eqs. 6.6 and 6.7, the pair of relations can be derived as:

$$x * h \leftrightarrow XH \tag{6.8}$$

$$xh \leftrightarrow X * H \tag{6.9}$$

As mentioned above, when two functions are convolved, the variance of the convolution produces the sum of the variances of the individual functions. So if:

$$y = x * h \tag{6.10}$$

holds true, then

$$\sigma_y^2 = \sigma_x^2 + \sigma_h^2 \tag{6.11}$$

This conclusion means that when two Gaussian shaped patterns of equal width are convolved, the result is another Gaussian pattern, which is $\sqrt{2}$ times broader than the original ones. Moreover, it is known that the variance of a Gaussian pattern is the reciprocal of the variance of its Fourier transform [27[. This means the variance of the convolution product in the transform domain is:

$$\sigma_Y^2 = \frac{\sigma_X^2 \cdot \sigma_Y^2}{\sigma_X^2 + \sigma_Y^2} \tag{6.12}$$

This expression indicates that the transform of the convolved Gaussian curve is narrower than either individually transformed Gaussian patterns. Eqs. 6.11 and 6.12 are extremely valuable and can be used to estimate the beamwidth of the restored patterns during the deconvolution process, given the measured patterns and the antenna radiation patterns.

6.3 Loss of information in the convolution process

Generally speaking, the noisy output signals at the receiver side are smoothed to a certain extent and corrupted by random noise over the process of convolving with the antenna radiation pattern. Irregularities along the measured patterns which may contain signal information are difficult to distinguish from the effects of random noise. More importantly, the output noisy signals have to contain a sufficient amount of information which is enough to retrieve the input signal (or the impulse response) [28[. To clarify this point, a general convolution process can be demonstrated in Figs. 6.2 and 6.3. Fig. 6.2 demonstrates an unrecoverable case. Fig. 6.2a) shows the known input signal in the original domain. In this research project, it represents the previously measured radiation pattern of the receiver antenna. Fig. 6.2b) shows the unknown input signal. Here it means the phase function pattern to be restored. Fig. 6.2c) shows the output signal, which represents the measured pattern at the receiver side.

The duration of the unknown signal (Fig. 6.2b) red curve) is smaller than that of the known input (Fig. 6.2a) blue curve). Fig. 6.2c) (green curve) represents the normalised convolution between the two signals, (a) and (b). From the discussion in section 6.3, it is known that the beamwidth of curve (c) is wider than either of (a) and (b). Their corresponding discrete transform domain representations are normalised with respect to their maxima respectively and presented in Fig. 6.2d), e) and f). Evidently, the beamwidth of the signal pattern shown in Fig. 6.2e) is wider than either of the patterns shown in Figs. 6.2d) and f). This means the discrete spectra in Figs. 6.2d) and f) do not contain enough high frequency components to allow a complete description of the unknown signal in Fig. 6.2e). Subsequently it will be impossible to determine the unknown signal unless additional information is provided.

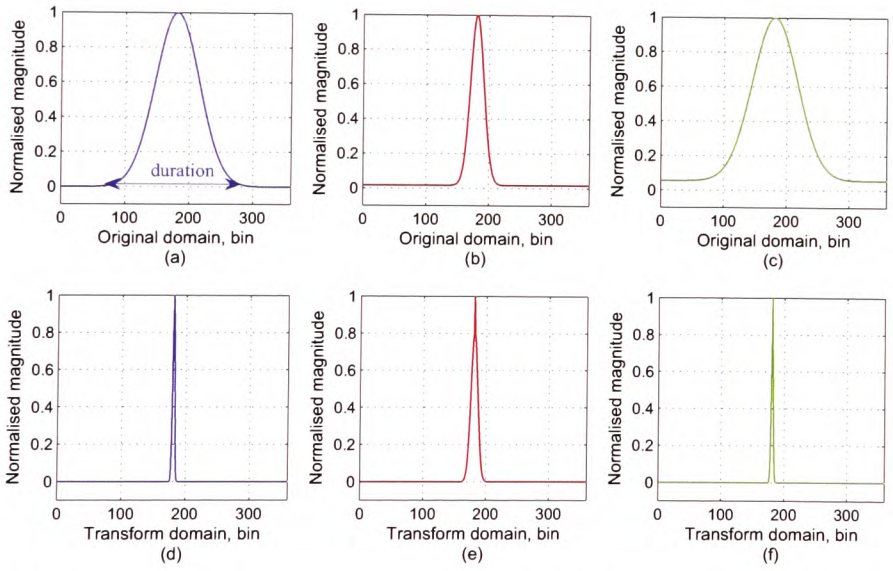

Figure 6.2: Unrecoverable case of signals: (a) known input; (b) unknown to be recovered; (c) convolution between a and b; (d) known signal a in transform domain; (e) unknown signal b in transform domain; (f) convolution in transform domain.

When the duration of the unknown input signal in Fig. 6.3b) is larger than that of the known input signal in Fig. 6.3a) in the original domain. Fig. 6.3c) represents

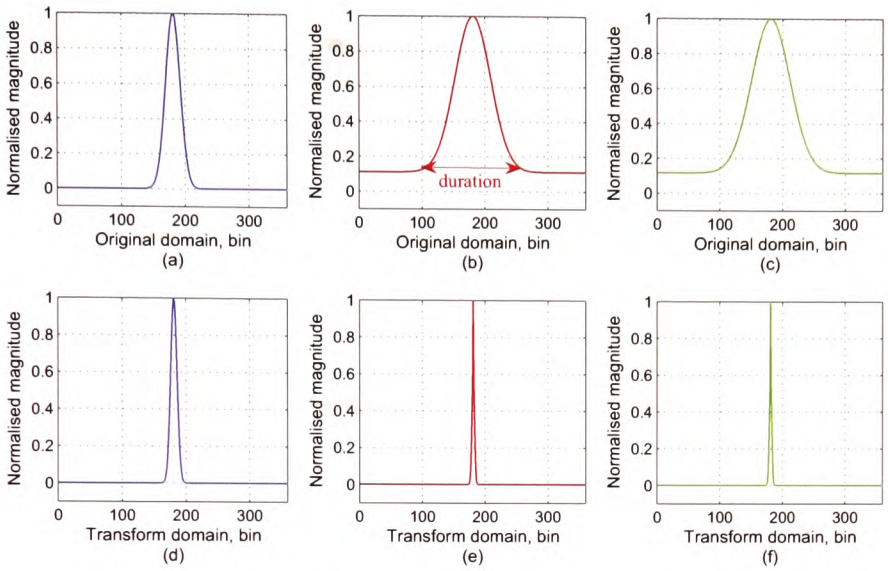

Figure 6.3: Recoverable case of signals: (a) known input; (b) unknown to be recovered; (c) convolution between a and b; (d) known signal a in transform domain; (e) unknown signal b in transform domain; (f) convolution in transform domain.

the normalised convolution between the patterns in Figs. 6.3a) and b). Figs. 6.3d), e) and f) are their corresponding representations in the discrete transform domain and are normalised with respect to their maxima respectively. Obviously, Figs. 6.3a) and c) contain enough information to determine the unknown signal in Fig. 6.3b). Consequently, an effective way to avoid this fundamental difficulty, the loss of information in the process of convolution, is to use a known input signal of less duration.

Applying these findings to the measurements carried out in this project means using a receiver antenna with a narrower beamwidth than that expected for the phase function. This will aid the chance of recovering the phase function by deconvolution. This clearly favours the use of the higher gain antennas in both measurement systems, namely the 20 dBi standard gain and the 20 dBi Gaussian horn antennas at 20 GHz and for the 40 GHz system a 29 dBi Lens horn and also a 20 dBi horn antenna ought to be used.

The discussion above has not considered the effects of random noise yet to simplify the discussion process. In theory information of the phase function pattern can be retrieved completely and successfully once an antenna with a relatively narrow

beamwidth is used as the receiver. However, random noise is always present in the measured data. A rigorously mathematical solution cannot be obtained due to the ever present noise and only a means to manage the effects of noise can be sought. The correlation between the mathematic rigour and the physically measured data must be kept in mind to reach an acceptable estimated solution [90].

6.4 Ill-conditioned systems

6.4.1 Effects of the ill-conditioned system on deconvolution

In practical applications, the deconvolution problem is mathematically classified as an ill-posed problem [81]. According to A. N. Tikhonov in [91] the cause of the "ill-conditioned problem" occurring is that the information represented by the data (sequences), or the equations (continuous functions) are incomplete, which typically holds true when performing any practical deconvolution. The deconvolution operation has no direct mathematical definition, and is only defined as the inverse of the convolution operation [81].

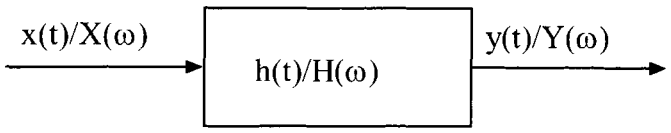

Figure 6.4: Schematic diagram of a linear time-invariant system

The indoor propagation channel inside the anechoic chamber can safely be assumed to be time-invariant if the transmitter and the receiver are still and no motions occur during the measurement [92]. During the measurements conducted in this project the receiver can be perceived as still, since enough time was allowed after each movement to a new measurement location for the whole assembly to settle. Referring to Fig. 6.4, if an input signal $x(t)$ is applied to excite a linear time-invariant system with an impulse response $h(t)$, the system's response $y(t)$ is given by the

convolution [81]. $X(\omega)$, $Y(\omega)$, and $H(\omega)$ are the corresponding transform domain denotations, respectively.

$$y(t) = x(t) * h(t) = \int_{-\infty}^{+\infty} x(\tau) \cdot h(t-\tau) \tag{6.13}$$

where " * " denotes the convolution operation.

Being the inverse process of the convolution operation, deconvolution introduces inaccuracy through adding a constrained term to control the noise below an acceptable level. The inaccuracy cannot be determined due to the lack of knowledge of the true information. In other words, only estimation of filtered results can be obtained. The accuracy of such results can be indicated by an optimal criterion, which needs to be determined. Deconvolution involves the determination of either $x(t)$ or $h(t)$ assuming prior knowledge of the other two functions. The process of determining $h(t)$ knowing both $x(t)$ and $y(t)$ is a system identification one, through which the system's impulse response is determined. The determination of $x(t)$ knowing both $h(t)$ and $y(t)$ is a pulse measurement process, through which the true function $x(t)$ is determined.

According to the Convolution Theorem, a convolution operation in the original domain can be represented as a multiplication in the transform domain, likewise a deconvolution operation in one domain becomes a division in the other. So in the transform domain Eq. 6.13 becomes:

$$Y(\omega) = X(\omega) \cdot H(\omega) \tag{6.14}$$

Derivations of 6.14 are:

$$X(\omega) = Y(\omega)/H(\omega) \tag{6.15}$$

$$H(\omega) = Y(\omega)/X(\omega) \tag{6.16}$$

6.4.2 Effects of ill-conditioning in the transform domain

Ideally, either $x(t)$ or $h(t)$ can be determined with prior knowledge of the other two by applying inverse the Fourier Transform to Eqs. 6.15 and 6.16. In practice the exact knowledge of these time line signals, $x(t)$, $y(t)$ and $h(t)$, may be difficult to obtain due to factors such as:

- Inaccuracy of the sampling or digitization and data acquisition process
- Natural variability of the signal
- Always present random noise

Random noise or errors that occur in measurements cause these signals to be inconsistent in the sense that the input $x(t)$ and output $y(t)$, *i.e.* the two known quantities, are not related to each other through a causal stable impulse response. For example, if for a given causal stable system $x(t)$, $y(t)$, and $h(t)$ are the precise input, output and system impulse response signals respectively, then they are uniquely related by the convolution equation 6.17:

$$y(t) = x(t) * h(t) \tag{6.17}$$

$x(t)$ and $y(t)$ together provide the information to exactly characterise the system impulse response $h(t)$. $x_e(t)$ and $y_e(t)$ are assumed to be independent noise, which corrupt $x(t)$ and $y(t)$ respectively in the process of measurements. Therefore, the measured waveforms, to some extent, are different from that of true signals:

$$x_m(t) = x(t) + x_e(t) \tag{6.18}$$

$$y_m(t) = y(t) + y_e(t) \tag{6.19}$$

Where the measured signals are represented using the index m in $x_m(t)$ and $y_m(t)$; $x_e(t)$ and $y_e(t)$ denote the unknown error components; and their transform domain

counterparts are referred to as $X_m(\omega)$, $Y_m(\omega)$ and $X_e(\omega)$, $Y_e(\omega)$ respectively.

Eq. 6.13 can be rewritten as:

$$[y_m(t) - y_e(t)] = [x_m(t) - x_e(t)] * h(t) \tag{6.20}$$

Its transform domain form as a result of the linearity of the Fourier transform [84] is given as:

$$[Y_m(\omega) - Y_e(\omega)] = [X_m(\omega) - X_e(\omega)] \cdot H(\omega) \tag{6.21}$$

Due to the introduced unknown error quantities $x_e(t)$ and $y_e(t)$, it is not possible to obtain an exact solution of $h(t)$ in Eq. 6.20. Instead, the practically measured function $h_m(t)$ is expressed as follows:

$$y_m(t) = h_m(t) * x_m(t) \tag{6.22}$$

$$Y_m(\omega) = H_m(\omega) \cdot X_m(\omega) \tag{6.23}$$

where $H_m(\omega)$ is the Fourier Transform of $h_m(t)$. The following relations also stand:

$$X_m(\omega) = X(\omega) + X_e(\omega) \tag{6.24}$$

$$Y_m(\omega) = Y(\omega) + Y_e(\omega) \tag{6.25}$$

$$H_m(\omega) = H(\omega) + H_e(\omega) \tag{6.26}$$

$$h_m(t) = h(t) + h_e(t) \tag{6.27}$$

Furthermore, it may be assumed that the values of the error components, $h_e(t)$, $x_e(t)$ and $y_e(t)$ are very small, as are $H_e(\omega)$, $X_e(\omega)$ and $Y_e(\omega)$. Hence,

$$h_m(t) \cong h(t) \tag{6.28}$$

$$H_m(\omega) \cong H(\omega) \tag{6.29}$$

If the approximation holds, then

$$H(\omega) = \frac{Y(\omega)}{X(\omega)} = \frac{Y_m(\omega) - Y_e(\omega)}{X_m(\omega) - X_e(\omega)} \cong \frac{Y_m(\omega)}{X_m(\omega)} = H_m(\omega) \tag{6.30}$$

It appears that this approach yields solutions for $h_m(t)$ and $H_m(\omega)$, which may provide an acceptable approximation to the desired values of $h(t)$ and $H(\omega)$. However significant errors may be encountered due to the neglected error components.

Inside regions, where the value of $X(\omega)$ is fairly small and has the same order as the error component, $X(\omega) \cong X_m(\omega)$ is not a good approximation any more, which could result in considerable mistakes in the final result. Eq. 6.14 implies that the value of $Y(\omega)$ is supposed to be of the same order as $X(\omega)$, whereas Eq. 6.16 would produce spike-like errors around the zeros of $X(\omega)$. The approximation $Y(\omega) \cong Y_m(\omega)$ is, therefore, not accurate. Consequently the result of $H_m(\omega) = Y_m(\omega)/X_m(\omega)$ is expected to be very different from the genuine value, $H(\omega) = Y(\omega)/Y(\omega)$, due to improper approximation.

In practice, $x(t)$ is generally a band-limited signal, so is $X(\omega)$. Therefore there is a region, or regions, in the transform domain where the value of $X(\omega)$ is quite small or even zero. In this particular region, values of $H_m(\omega)$ would consist of large "spikes" due to the division in Eq. 6.16. This explains how the deconvolution errors, or ill-posed problems, occur [81[. As long as the spike-like errors of $H(\omega)$ stay inside regions in which the numerical values of $X(\omega)$ are relatively small, such regions are of little interest to researchers. However if the fault components of $H_m(\omega)$ spread over the entire original domain after the inverse Fourier transform, it may obscure all useful information because the absolute values of errors could be very high. Thus the outcome becomes indeterminable.

Such a direct attack in the transform domain usually does not work. Various problems arise due to small values in the denominator, constraining these small values in particular region or regions, truncating the signals too early, too late, not smoothly enough and so on [93[. The quotient must be modified or regularised by some improvements involving a parameter. Two such techniques, the optimum compensation filter and the automated-regularised filter will be presented in section 6.5.1.

6.4.3 Effects of ill-conditioning in the original domain

According to Jansson, a problem is ill-posed when at least one of three conditions holds: either (1) its solution does not exist, (2) its solution exists but is not unique, or (3) its solution does not depend continuously on the data. Even if a problem passes all three tests for well-posedness, its solution may depend sensitively on small fluctuations in the data. Because all data has uncertainties, such sensitivity limits a solution's value. Problems exhibiting this behavior are said to be ill-conditioned [27].

Assuming x, h and y are discrete sequences and their relation is demonstrated in Fig. 6.4. An approach attempting to solve h in the original domain is:

$$\begin{aligned} y_1 &= x_1 h_1 \\ y_2 &= x_1 h_2 + x_2 h_1 \\ y_3 &= x_1 h_3 + x_2 h_2 + x_3 h_1 \\ &\vdots \\ y_n &= x_1 h_n + \cdots + x_n h_1 \end{aligned} \tag{6.31}$$

The discrete version of Eq. 6.13 may be viewed as numerical integration by approximating the area under the curve $y(t) = x(t')h(t - t' + \Delta t)$ by rectangular pieces [93]. The multiplication factor Δt is suppressed from the equations. Rewriting Eq. 6.31 into a matrix form:

$$\begin{bmatrix} x_1 & 0 & & 0 \\ x_2 & x_1 & & \\ \vdots & & & \\ x_n & & x_2 & x_1 \end{bmatrix} \begin{bmatrix} h_1 \\ \vdots \\ h_n \end{bmatrix} = \begin{bmatrix} y_1 \\ \vdots \\ y_n \end{bmatrix} \tag{6.32}$$

or

$$\bar{X} \cdot \bar{H} = \bar{Y} \tag{6.33}$$

where $\bar{X}$, $\bar{H}$ and $\bar{Y}$ are the notations of matrix in Eq. 6.32 respectively. Since the matrix is in lower triangular form, $\bar{H}$ could be solved by back substitution. That is

$$h_1 = \frac{y_1}{x_1}, \quad h_2 = \frac{y_2 - x_2 h_1}{x_1}, \quad \cdots \tag{6.34}$$

However, attempts to solve Eq. 6.32 using direct back substitution leads to "garbage solutions" [29] as the matrix problem is ill-posed. It is known that it is easy to find a set of numbers $h_1, \cdots, h_n$ which formally solve Eq. 6.32. Slight perturbation in the elements of $\bar{X}$ leads to drastically different numbers $h_1, \cdots, h_n$, which also seem satisfy Eq. 6.32. This is characteristic, in fact essentially the definition, of an ill-conditioned problem [93[.

Direct methods such as back substitution and least square *etc.* lead to "garbage solutions". Typically h_i, h_{i+1}, start to alternate in sign. If x and y were sampled at a certain fixed frequency in measurements, it is highly unlikely that h will oscillate with exactly this sampling frequency, hence h is recognised as "garbage" again. Smoothing the measured data of x and y does not necessary help, and in some cases, smoothing increases the condition number of the matrix $\bar{X}$, which makes circumstances further ill-conditioned.

The formal definition of the condition number of a $n \times n$ matrix $\bar{H}$ is [93[

$$cond(\bar{H}) = \left\|\bar{H}^{-1}\right\| \left\|\bar{H}\right\| \tag{6.35}$$

In solving the linear system $\bar{X} \cdot \bar{H} = \bar{Y}$, if $\bar{Y}$ is perturbed, that is if $\bar{X}$ solves $\bar{X} \cdot \bar{H} = \bar{Y}$ and $\bar{X} + \delta\bar{X}$ solves $\left(\bar{X} + \delta\bar{X}\right) \cdot \bar{H} = \bar{Y} + \delta\bar{Y}$, then

$$\frac{\left\|\delta\bar{X}\right\|}{\left\|\bar{X}\right\|} \leq cond(\bar{H}) \cdot \frac{\left\|\delta\bar{Y}\right\|}{\left\|\bar{Y}\right\|} \tag{6.36}$$

It shows that if a disturbance, $\delta\bar{Y}$, occurred in $\bar{Y}$, a perturbation, $\delta\bar{X}$, subsequently was produced in $\bar{X}$, if a high value of the condition number, $cond(\bar{H})$, is needed to satisfy the inequality 6.36, then the relation $\bar{X} \cdot \bar{H} = \bar{Y}$ is unstable, or ill-conditioned; otherwise, only a small $cond(\bar{H})$ would make the inequality 6.36 hold for most circumstances, then that matrix equation $\bar{X} \cdot \bar{H} = \bar{Y}$ is stable, or well-

conditioned.

6.5 Deconvolution methodology

Numerous approaches to a solution of the deconvolution problem have been reported [27, 28, 94, 95]. The common factor in many approaches is the use of iterations to design an optimum "filter" to reduce the deconvolution noise [96]. The optimum filter interpolates $H(\omega)$ at the zeros of $X(\omega)$, where it is indeterminate, to yield $H_e(\omega)$, the best estimate of $H(\omega)$. In this section, some well proven techniques will be briefly introduced. Notice that categorising a method in the original domain or transform domain depends on its typical employment and limitation such as the computational speed of computer, when the specific method was developed. An approach in one domain can always be used in the other under appropriate circumstances.

6.5.1 Deconvolution approaches in the transform domain

6.5.1.1 Noise reduction filtering

It is proven that the Wiener filter provides the best performance in the sense of white noise reduction [27, 97], its expression in the transform domain is given by:

$$H_e(\omega) = \frac{Y(\omega)}{X(\omega)} \cdot F_{opt}(\omega) = H(\omega) \cdot F_{opt}(\omega) \tag{6.37}$$

$$F_{opt}(\omega) = \frac{|X(\omega)|^2}{|X(\omega)|^2 + \frac{\Phi(\omega)}{|H(\omega)|^2}} \tag{6.38}$$

thus,

$$H_e(\omega) = Y(\omega) \cdot \frac{1}{X(\omega)} \cdot \frac{|X(\omega)|^2}{|X(\omega)|^2 + \frac{\Phi(\omega)}{|H(\omega)|^2}} \tag{6.39}$$

where $F_{opt}(\omega)$ is the optimum filter; and $\Phi(\omega)$ is the noise power density spectrum. According to the Eq. 6.39, the procedure of obtaining the optimum estimate $H_e(\omega)$ can be explained as: the measured data $Y(\omega)$ passed through the ideal inverse filter $\frac{1}{X(\omega)}$, which would cause the ill-conditioned problems without noise reduction.

Subsequently, the filter F_{opt} is performed for noise reduction, and achieves an optimal compromise of signal distortion and noise control.

In practical cases the problem arises that $\Phi(\omega)$ in Eq. 6.39 is unknown. Several solutions have been developed to solve this problem [95, 98[. For instance, the ratio $\frac{\Phi(\omega)}{|H(\omega)|^2}$ may be assumed as a constant factor λ [98[, to eliminate the spike-like noise; or it may be equal to a frequency-dependent term $\gamma\omega^4$ to efficiently reduce the high frequency noise components and ensure the smoothness of the restored signal [28[. Both λ and γ are iteratively determined optimal parameters. λ is called the peak reduction factor and γ the smoothing factor [95[.

6.5.1.2 Optimal compensation deconvolution

Optimal compensation deconvolution involves the design of a transfer function $C(\omega)$, called the compensator [98[. The compensator is to be applied to the response function $Y(\omega)$ to yield an estimate, $H_e(\omega)$, of the ideal transfer function $H(\omega)$:

$$H_e(\omega) = Y(\omega) \cdot C(\omega) = \frac{Y(\omega)}{X(\omega)} \cdot X(\omega) \cdot C(\omega) \tag{6.40}$$

The criteria for designing the optimum compensation filter are as follows:

- Minimising E_e, the discrepancy between the estimate $H_e(\omega)$ and $H(\omega)$:

$$E_e = \int_0^{\Omega} |H_e(\omega) - H(\omega)|^2 \, d\omega \tag{6.41}$$

  where Ω is the frequency band of interest. $H(\omega)$ is used as the reference although it is not the precise representation of the system transfer function due to the presence of random noise.

- Constraining the compensator $C(\omega)$ to be a bounded function in order to limit the magnitude of random noise in the estimate $H_e(\omega)$.

$$E_c = \int_0^{\Omega} |H(\omega) \cdot C(\omega)|^2 \, d\omega \tag{6.42}$$

As $H(\omega)$ is a bounded function, the second criterion will keep the E_c finite.

The two criteria can be grouped into one [98] to minimise the E defined as:

$$E = E_e + \lambda E_c \qquad \lambda \geq 0 \tag{6.43}$$

where λ is an optimisation parameter whose significance could be demonstrated by considering two extreme cases [98]:

- $\lambda = 0$, which results in a minimisation of E_e, consequently the estimate $H_e(\omega)$ is equivalent to $H(\omega) = \frac{Y(\omega)}{X(\omega)}$. This means no noise reduction at all.
- $\lambda = \infty$, which means that the term λE_c plays a more important role whereas the term E_e counts a small part only in Eq. 6.43. This indicates the noise content will be reduced greatly with a large deviation from $\frac{Y(\omega)}{X(\omega)}$.

Both cases are undesirable. The transfer function of the optimum compensation filtering is given by [89]:

$$C(\omega) = \frac{X^*(\omega)}{|X(\omega)|^2 + \lambda} \tag{6.44}$$

where superscript $*$ denotes the complex conjugate. Eq. 6.44 can be obtained by setting its partial derivatives with respect to the real and the imaginary parts being equal to zero respectively. Details of this process will be presented in chapter 7.

6.5.1.3 Automated regularisation deconvolution

The automated regularisation iterative deconvolution is also called the Guillaume-Nahman deconvolution [28], which is also a type of Wiener filter. Its transfer function is given by:

$$F_{opt}(\omega) = \frac{|X(\omega)|^2}{|X(\omega)|^2 + \gamma\omega^4} \tag{6.45}$$

This technique considers the influence of frequency. At low frequency, $\omega \rightarrow 0$, F_{opt} is close to 1, an all-pass filter; while at high frequency its effect increases with

a exponent of 4. It provides an all-stop filter when ω reaches large values. The parameter γ is chosen as the value for which the standard deviation in the imaginary part of the deconvolved impulse response is minimised [96].

6.5.2 Deconvolution approaches in the original domain

6.5.2.1 Van Cittert's method

The separation of two signals combined by convolution is often referred to as deconvolution. The straightforward approach of deconvolution is via the Fourier transform and division in the transform domain. In practice, this technique usually fails due to zeros in the denominator. In 1931, Van Cittert exposed an iterative deconvolution method extended by Bracewell in 1954 [97]. This method converts the division to multiplication in the process of deconvolution. Jansson in 1970 [27] proposed a modified version of this procedure to realise positive reconstruction.

Van Cittert recognised that the measured data $y(t)$ could be considered as a first approximation $h_e^0(t)$. In the context of parameter extraction for the RET, in the absence of deconvolution, the influence of the receiver antenna radiation pattern is often ignored and the measured pattern is used as if it represents the true information of the RET phase function. In some way, the difference $y(t) - x(t) * h_e^0(t)$, which can be easily calculated with measured data, is related to the error in the estimate $h(t) - h_e^0(t)$, and $h(t)$ represents the true information of the RET phase function. Consequently, $y(t) - x(t) * h_e^0(t)$ could be applied as a correction factor to the estimate $h_e^0(t)$ to further yield a new estimate $h_e^1(t)$:

$$h_e^1(t) = h_e^0(t) + \left[y(t) - x(t) * h_e^0(t)\right] \tag{6.46}$$

where the initial estimate $h_e^0(t) = y(t)$. The Van Cittert's method iteratively uses the kth estimate of $h(t)$ as the correction factor to yield the $(k+1)$th estimate. The expression is given by [27, 99]:

$$h_e^{k+1}(t) = h_e^k(t) + b \cdot (y(t) - x(t) * h_e^k(t)) \tag{6.47}$$

where the correction factor is $b \cdot (y(t) - x(t) * h_e^k(t))$; b represents the relaxation factor and is used to damp the noise that grows with each iteration when the method is applied to real data.

6.5.2.2 Constrained Van Cittert's methods

In most of practical cases, the input and output signals and the impulse response of the system have non-negative physical property and physical bound of values [100[such as measured power values at the receiver side. These constraints can be incorporated into the Van Cittert's method to take advantage of such apriori knowledge. This is given by:

$$h_e^{k+1}(t) = ph_e^k(t) + p \cdot (y(t) - x(t) * ph_e^k(t)) \tag{6.48}$$

where

$$p = \begin{cases} 1 & h_e^k > 0 \\ 0 & h_e^k < 0 \end{cases}$$

The effect of the constraint operator p is to truncate the negative artifacts from the estimate during each iteration. The reported results show that this method provides significantly better estimates than Van Cittert's [27[.

Many similar techniques are called the Relaxation-Based iterative method and modify the correction term $(y(t) - x(t) * h_e^k(t))$ using a relaxation function, $r\left\{h_e^k(t)\right\}$, which corrects $h_e^k(t)$ when $h_e^k(t)$ is negative. The relaxation function enables the correction factor to have no negative corrections to the new estimate if the present estimate contains nonphysical values [100[. One form of this method is given by:

$$h_e^{k+1}(t) = h_e^k(t) + r\left\{h_e^k(t)\right\} \cdot (y(t) - x(t) * h_e^k(t)) \tag{6.49}$$

$$r\left\{h_e^k(t)\right\} = \begin{cases} b & h_e^k > 0 \\ 0 & h_e^k < 0 \end{cases}$$

Although the methods represented by Eqs. 6.48 and 6.49 eliminate nonphysical artifacts from the iterative estimates, they are done by truncation. Truncation may cause detrimental effects of removing important information as well [100, 101[.

6.5.2.3 Jansson's method

To avoid the negative effects generated by abruptly truncating the signal, where negative values appear due to additive random noise, Jansson proposed an alternative technique where successive estimates are constrained to occur between upper and lower bounds. The constraining operation is done in a gradual fashion without truncating any information [27[. Jansson's method is given by:

$$h_e^{k+1}(t) = h_e^k(t) + r\left\{h_e^k(t)\right\} \cdot (y(t) - x(t) * h_e^k(t)) \tag{6.50}$$

$$r\left\{h_e^k(t)\right\} = r_o \cdot (1 - 2\left|h_e^k(t) - \frac{1}{2}\right|) \tag{6.51}$$

where the relaxation function $r\left\{h_e^k(t)\right\}$, shown in Fig. 6.5, constrains the estimate between the normalised upper and lower physical bounds [27]. Here r_o is used in the same way as b, damping the iteratively increasing noise. It is generally desirable to choose r_0 large so that large corrections will be made to $h_e^k(t)$, allowing it to approach $h(t)$ with the smallest possible amount of computation. If r_0 is chosen too large some initial estimates will be over-corrected, or worse the method may fail to

converge altogether.

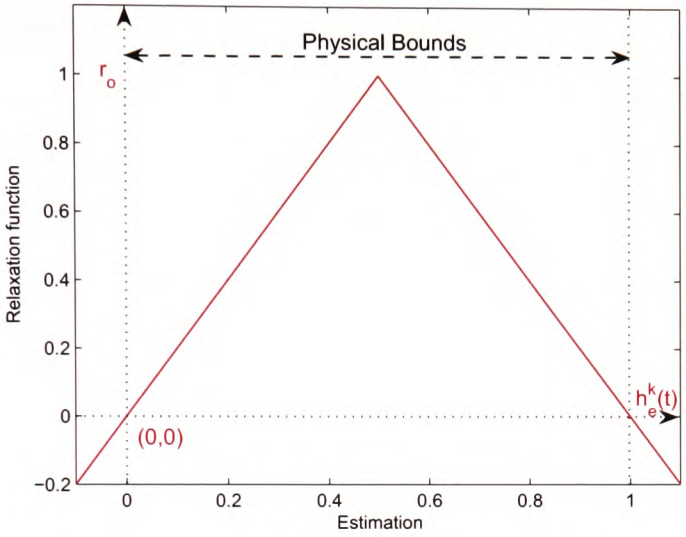

Figure 6.5: Relaxation function of Jansson's deconvolution method

Instead of truncating the correction term, Jansson's method uses the relaxation function, given by Eq. 6.51. The relaxation function $r\left\{h_e^k(t)\right\}$:

- should be positive in the range of $h_e^k(t)$ equal to 0 to 1 shown in Fig. 6.5, in which $h_e^k(t)$ would have a valid solution;
- crosses the $h_e^k(t)$ axis at zero and smoothly continues to negative values in the undesired range;
- gradually corrects $h_e^k(t)$ by first admitting and then suppressing out-of-bounds components as iteration proceeds.

This approach could also be explained as the relaxation function modulates the correction term so that it assumes full value in the center of the physical region and falls to zero at the bounds; and then reverses the sign of the correction term by gently "coaxing" the negative parts back towards the desired range instead of cutting them off. Hard-clipping, *i.e.* setting $r\left\{h_e^k(t)\right\}$ to zero in the undesired range, seriously compromises its value [27]. Truncating the correction term degrades the solution

by removing the possibility of nonvanishing values over much of the $h_e^k(t)$ domain early in the computation, before neighbouring values are refined [27]. In addition, the hard-clipping based methods require excess iterations, because the relaxation constant r_o has to be small for convergence.

An effective relaxation function $r\left\{h_e^k(t)\right\}$ is the essence of this method. Frieden [102] generalises the original relaxation function in Eq. 6.51 to treat the case with arbitrary lower bound c and upper bound a:

$$r\left\{h_e^k(t)\right\} = r_o \cdot (1 - \frac{2}{a-c}\left|h_e^k(t) - \frac{a+c}{2}\right|) \tag{6.52}$$

Another feasible choice for the relaxation function is given by:

$$r\left\{h_e^k(t)\right\} = 4r_o\left[h_e^k(t)\left(1 - h_e^k(t)\right)\right]^n \tag{6.53}$$

A parabolic form satisfying the principal requirements is more readily expressed in Fourier space. Blass and Halsey proposed its generalisation form [103] in Eq. 6.53, n is an integral exponent. This method avoids the awkwardness of dealing with the absolute value in Eqs. 6.51 and 6.52.

It is interesting here to look at the contrast between the Van-Cittert based methods and the typical transform domain iterative techniques. The typical transform domain based iterative techniques start with the accurate but noisy ratio estimate, $H(\omega) = \frac{Y(\omega)}{X(\omega)}$, then use iterative filtering to reduce noise while maintaining the deconvolution accuracy. The Van-Cittert based methods begin with a low-noise but inaccurate estimate, $H_0(\omega) = Y(\omega)$, then use an iterative correction process to improve the accuracy while maintain the noise content at a low level. The ratio estimate, $\frac{Y(\omega)}{X(\omega)}$ is being approached as the number of iterations approaches infinity [104].

It is worth mentioning that in a numerical sense, performing deconvolution in the original domain can be considered very similar to differentiation [81]. As both involve subtraction in both operations, having two values of similar magnitude may lead to large errors. Any small uncertainty in the data will be magnified through multiplications and lead to large errors in the result. So strictly speaking, deconvo-

lution can only be carried out with data that is absolutely accurate, which of course is never the case in practical measurements. Therefore the methods outlined here and detailed in chapter 7 need to be utilised.

6.6 Error analysis

Using matrix notation like in Eqs. 6.32 and 6.33, a convolution process could be modelled as follows:

$$\bar{Y} = \bar{X} \cdot \bar{H} + \bar{N} \tag{6.54}$$

where $\bar{X}$, $\bar{H}$ and $\bar{Y}$ are matrix representation of data sets $x(t)$, $h(t)$ and $y(t)$ respectively, and $\bar{N}$ denotes the additive noise generated in measurements. The landmark of achieving successful deconvolution results or the decision to continue iteration is usually based on achieving a specified minimum error value. In most practical cases, as $\bar{H}$ is unknown a popular residual is calculated [80, 82[:

$$\bar{R} = \bar{Y} - \bar{X} \cdot \bar{H}_e \tag{6.55}$$

where $\bar{H}_e$ represents the deconvolution result, *i.e.* the estimate of the system impulse response $\bar{H}$. Hence, the residual $\bar{R}$ contains not only the additive noise but also the deconvolution error introduced by using $\bar{H}_e$, that is $\bar{H} - \bar{H}_e$. The introduced error may come from computational inaccuracies via Fourier and inverse Fourier transforms, numeric inaccuracy due to limitations of the computer and filtration errors.

In fact, the aim of deconvolution is to yield the best estimate $\bar{H}_e$, as close to $\bar{H}$ as possible, *i.e.* the minimum of $\bar{H} - \bar{H}_e$. Rewriting Eq. 6.54 as:

$$\bar{N} = \bar{Y} - \bar{X} \cdot \bar{H} \tag{6.56}$$

Subtracting Eq. 6.56 from Eq. 6.55:

$$\bar{R} - \bar{N} = \bar{X} \cdot (\bar{H} - \bar{H}_e) \tag{6.57}$$

and

$$\bar{H} - \bar{H}_e = \bar{X}^{-1} \cdot \bar{R} - \bar{X}^{-1} \cdot \bar{N} \tag{6.58}$$

Eq. 6.58 implies that even if the minimum of $\bar{R}$ is achieved in Eq. 6.55 and if $\bar{X}^{-1}$ is ill-conditioned, the error $\bar{H} - \bar{H}_e$ in Eq. 6.58 could be very large. Therefore, a small residual of $\bar{Y} - \bar{X} \cdot \bar{H}_e$ may not imply an accurate solution. Also, Eq. 6.58 indicates that two types of errors arise with any deconvolution process. The first term on the right-hand side of Eq. 6.58 is called the regularisation error [27] caused by the algorithm; the second term of error is generated by the additive noise.

6.7 Summary and interim conclusion

This chapter aims to introduce the principle of deconvolution. It highlights some of the difficulties associated with deconvolution and outlines several approaches found to be applicable methods for this research project. The central-limit theorem and the convolution theorem are introduced. The convolution theorem states that convolution in one domain is equivalent to multiplication in the other. This somewhat simplifies the analysis of the convolution. The next section on possible loss of information during the deconvolution process concludes that for the purpose of phase function retrieval from measurements. The smallest risk of loss of information will be encountered when receiver antennas with narrow beamwidths are used.

Following the problem of ill-posedness or ill-conditioned data is introduced. Its consequences in both the original and transform domain are discussed. This behaviour is referred to again in Appendix B, where it is of great significance for the determination in the first term of the iterative solutions presented. After this, commonly used deconvolution methods in both domains are presented. It is outlined that the optimum compensation and the automated regularisation method can be

successfully implemented to restore the phase function from measured data in this project. This will be documented in detail in chapter 7. A general error analysis of the deconvolution process is presented in this chapter in section 6.6. Additional performance analysis of the chosen deconvolution techniques is undertaken in chapter 8. Here an evaluation on their performance using both measured data and computer generated data with added noise is being presented.

Chapter 7

Deconvolution implementation

7.1 Introduction

Chapter 7 demonstrates implementation of the aforementioned deconvolution methods. Two transform methods, the optimum compensation and automated regularisation, were found to be implemented successfully. Jansson's method is investigated but has not yield any conclusive results. Reasons of its unsuccessful application and possible approaches to conquer it will be discussed under future work in chapter 9.

This chapter aims to demonstrate how the optimum compensation and automated regularisation method can be implemented successfully. In both cases the filter needs to be optimised for an adjustable parameter and their deconvolution products need to be verified. The measured data obtained in this research project is on its own unsuitable to perform the verification since the true information of the phase function pattern, as one of the input signals, is unknown. Therefore, computer generated data is used. This data closely resemble the functions for typical antenna radiation patterns and the expected shape of the phase function with similar quantities of random noise added during measurements. After verification of each method an example of successful deconvolution using measured data will be demonstrated for each method. Chapter 8 presents further evaluation of the two method performance using computer generated data and shows further improvements of these

methods by applying pre-filtering techniques.

7.2 Optimum compensation deconvolution

The development of the optimum compensation method in this project is based on the publications in [81,89,94,98,100,105[by Riad, Bennia and Crilly *etc.* throughout their research spanning more than two decades from 1980 to 2002. As this deconvolution method was originally developed and used in fields like Spectrology and Image Processing, necessary modifications of this method have been developed and applied by the author to suit the nature of the measurement data in this project. The following sections show the modified version of the optimum compensation deconvolution.

7.2.1 Derivation of the optimum compensation filter

As mentioned in chapter 6, the optimal compensation filter is a type of the Wiener filter, which has a general expression $\frac{|X(\omega)|^2}{|X(\omega)|^2+\frac{\Phi(\omega)}{|H(\omega)|^2}}$ and performs best in the sense of white noise reduction [27, 89]. Two criteria, minimum *root mean squared* (RMS) and error-control, are used to develop the formulation of the optimum compensation filter [105[:

$$E = E_e + \lambda E_c \tag{7.1}$$

$$E_e = \int_0^{\Omega} |H_e(\omega) - H(\omega)|^2 \, d\omega \tag{7.2}$$

$$E_c = \int_0^{\Omega} |H(\omega) \cdot C(\omega)|^2 \, d\omega \tag{7.3}$$

where Ω is the band-limit of the frequency of interest; and $\lambda > 0$ is the optimisation parameter, whose significance was described in section 6.5.1. Eqs. 7.2 and 7.3 are the mathematical expression of the terms: RMS and error-control, respectively.

An optimal value of λ to be determined iteratively is expected to achieve the best balance between the noise reduction and filtration errors [105]. Substituting

Eqs. 7.2 and 7.3 into 7.1:

$$E = \int_0^{\Omega} |H_e(\omega) - H(\omega)|^2 \, d\omega + \lambda \int_0^{\Omega} |H(\omega) \cdot C(\omega)|^2 \, d\omega \tag{7.4}$$

where $H_e(\omega)$ is given by Eq. 6.40 $H_e(\omega) = \frac{Y(\omega)}{X(\omega)} X(\omega) C(\omega)$. Replacing $H_e(\omega)$ in Eq. 7.4 with Eq. 6.40 yields:

$$\begin{aligned} E &= \left\{ \int_0^{\Omega} |H(\omega) X(\omega) C(\omega) - H(\omega)|^2 + \lambda \int_0^{\Omega} |H(\omega) \cdot C(\omega)|^2 \right\} d\omega \\ &= \int_0^{\Omega} |H(\omega)|^2 \left\{ |X(\omega) C(\omega) - 1|^2 + \lambda |C(\omega)|^2 \right\} d\omega \\ &= \int_0^{\Omega} |H(\omega)|^2 Q(\omega) d\omega \end{aligned} \tag{7.5}$$

where

$$Q(\omega) = \left\{ |X(\omega) C(\omega) - 1|^2 + \lambda |C(\omega)|^2 \right\} \tag{7.6}$$

To make this filter design a general one, E needs to be minimised for all possible forms of $H(\omega)$. This implies the minimization of $Q(\omega)$. Using the complex forms of $X(\omega)$ and $C(\omega)$ [89[:

$$\begin{cases} X(\omega) = X_R(\omega) + jX_I(\omega) \\ C(\omega) = C_R(\omega) + jC_I(\omega) \end{cases} \tag{7.7}$$

where subscripts R and I denote real and imaginary parts and substituting Eq. 7.7 into Eq. 7.6, leads to:

$$\begin{aligned} Q(\omega) &= [X_R(\omega) C_R(\omega) - X_I(\omega) C_I(\omega) - 1]^2 \\ &+ [X_I(\omega) C_R(\omega) + C_I(\omega) X_R(\omega)]^2 + \lambda [C_R^2(\omega) + C_I^2(\omega)] \end{aligned} \tag{7.8}$$

To minimise $Q(\omega)$, its partial derivatives with respect to the real and imaginary parts of $C(\omega)$ must be equal to zero [89[:

$$\frac{\partial Q(\omega)}{\partial C_R(\omega)} = 2 \left\{ C_R(\omega)(X_R^2(\omega) + X_I^2(\omega)) - X_R(\omega) + \lambda C_R(\omega) \right\} \tag{7.9}$$

$$\frac{\partial Q(\omega)}{\partial C_I(\omega)} = 2\left\{C_I(\omega)(X_R^2(\omega) + X_I^2(\omega)) + X_I(\omega) + \lambda C_I(\omega)\right\} \tag{7.10}$$

$$\frac{\partial Q(\omega)}{\partial C_R(\omega)} = 0 \Rightarrow C_R(\omega) = \frac{X_R(\omega)}{|X(\omega)|^2 + \lambda} \tag{7.11}$$

$$\frac{\partial Q(\omega)}{\partial C_I(\omega)} = 0 \Rightarrow C_I(\omega) = \frac{-X_I(\omega)}{|X(\omega)|^2 + \lambda} \tag{7.12}$$

Combining Eqs. 7.11 and 7.12:

$$C(\omega) = C_R(\omega) + jC_I(\omega) = \frac{X_R(\omega) - jX_I(\omega)}{|X(\omega)|^2 + \lambda} = \frac{X^*(\omega)}{|X(\omega)|^2 + \lambda} \tag{7.13}$$

where the superscript $*$ denotes the complex conjugate.

7.2.2 Verification of the optimum compensation technique

Before a deconvolution technique can be used on measured data obtained in this project, it has to be proven to be able to correctly retrieve information of the phase function pattern from the noisy output obtained at the receiver. To achieve this aim, precise information of the phase function is required for comparison. However this information is not available in reality. In order to verify the optimum compensation filter technique, computer generated data with random noise added are used to simulate the convolution process during measurements. By this means precise information is available for comparison with the restored pattern after applying the deconvolution technique.

Two computer-generated patterns, one representing the phase function pattern and the other representing the radiation pattern of the 20 dBi Gaussian horn antenna at 20 GHz, are used to simulate the values experienced in measurements. The beamwidth of phase function pattern is wider than that of the antenna radiation pattern as shown in Fig. 7.1a). Therefore, it is possible to retrieve the information of the phase function curve successfully according to the discussion in section 6.3. Random mean-zero noise is added to the convolution product as illustrated in

Fig. 7.1b). The Signal-to-Noise ratio (SNR) can be controlled and was set to 20 dB in this example. The noisy convolution curve (Fig. 7.1b) and the antenna radiation pattern (blue curve in Fig. 7.1a)) are the known output and input signals. The phase function pattern (red curve in Fig. 7.1a)) is the one to be restored. The approach of the straightforward deconvolution using division is unsuccessful due to existence of noise. Fig. 7.3a) shows the deconvolution attempts by direct division result in noise only, as expected after the discussion in section 6.4.2.

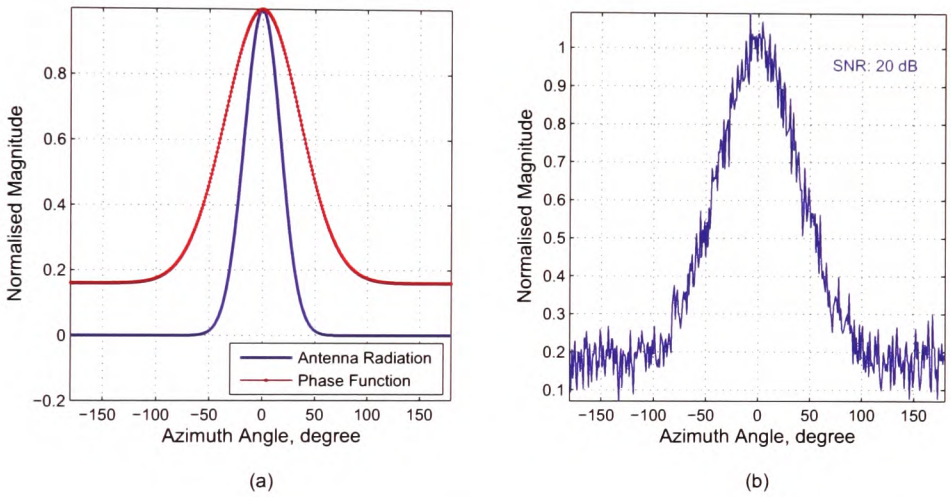

Figure 7.1: (a) Simulated input signals and (b) their convolution with additive random noise

RMS values are calculated between the restored phase function using the optimum compensation filter and the input phase function and normalised with respect to their maximum as shown in Fig. 7.2. The computer generated data allows the RMS values between the restoration and the original to be used as a criterion of success in deconvolution. Here the λ value is consistent with the number of iteration in this iterative filter, varying from 0 to a value of 20000. The variation of this RMS values with filter parameter λ is shown in Fig. 7.2a). An expanded scale at the lower range of iteration conducted (Fig. 7.2b)) shows that a minimum occurs at a value for λ of around 90 in this example, this is the optimal value for λ.

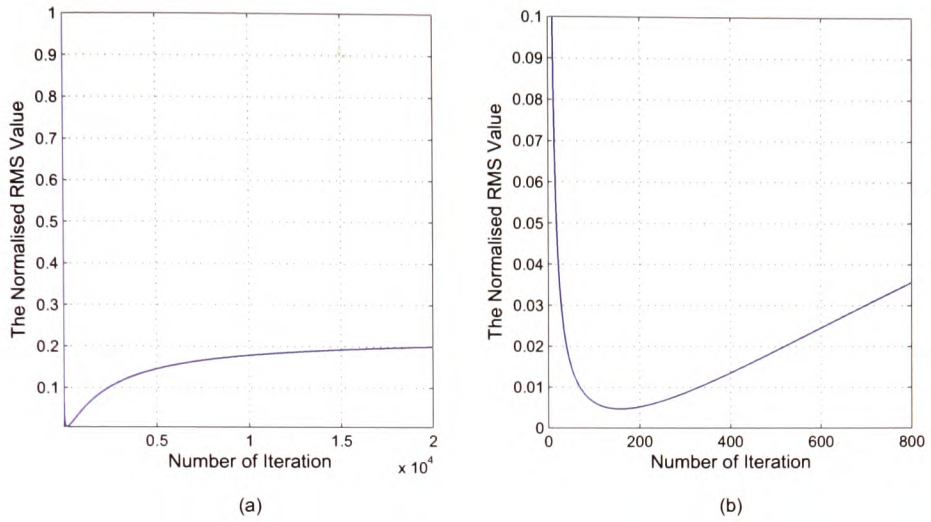

Figure 7.2: (a) The normalised RMS values between the restored pattern and the input phase function pattern and (b) the expanded depiction of the minimum region.

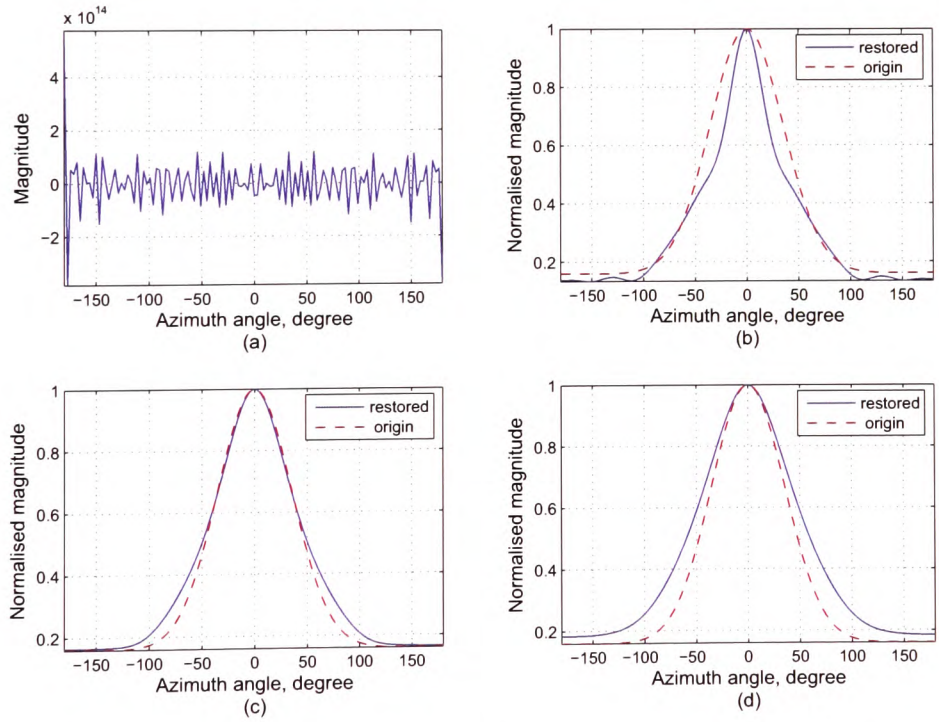

Figure 7.3: Restored signals for the cases: (a) straightforward deconvolution, (b) under-compensation, (c) optimal compensation and (d) over-compensation

Results of restoring the phase function pattern using the optimum compensation technique can be categorised into four: (a) the straightforward division restoration

shown in Fig. 7.3a), in which the true information of signal is completely swamped by noise in original domain; (b) the under-compensated restoration shown in Fig. 7.3b), where the value of λ is chosen too small; (c) the optimal compensation restoration shown in Fig. 7.3c), which indicates the parameter λ is chosen correctly. The input phase function is overlaid for comparison and the two curves show an overall consistency. (d) the over-compensated restoration shown in Fig. 7.3 d), which means the parameter λ is chosen too large.

7.2.3 The Bennia-Riad criterion

Using computer-generated data it is possible to determine the optimal compensation filter parameter λ by minimising the RMS error between the restored pattern and the computer generated phase function. In reality the precise information of the phase function cannot be obtained from measurements other than by deconvolution. Hence, various approaches need to be sought to determine the parameter of the optimal compensation filter. The Bennia-Riad criterion [89] provides a quantitative measure by taking into account the noise reduction and the filtration error. It is achieved by partitioning the transfer function in transform domain into a passband, in which the SNR is large, and a stopband, in which the SNR is small. The partition follows the conventional Half Power criterion shown as in Fig. 7.4. The transfer function of most practical applications is best represented by a low-pass filter [27]. The low-pass filter was designed so that the useful information mainly falls into its passband whereas its stopband contains little information but has high noise content.

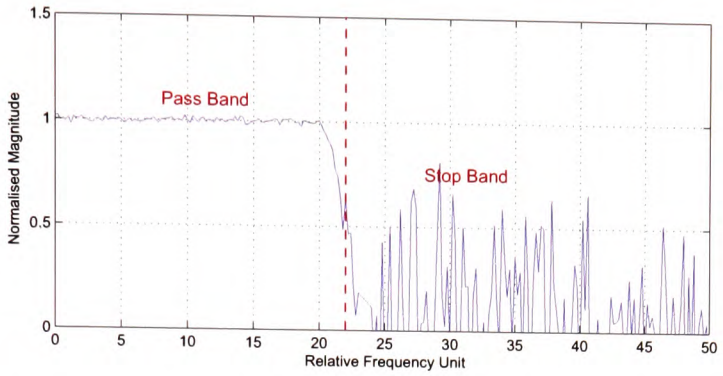

Figure 7.4: Schematic demonstration of divided passband and stopband in a low-pass filter in the presence of noise

The deconvolution is optimal when it manages to restore the useful information while minimising the effects of noise. The Bennia-Riad criterion is used for the iterative deconvolution process. The RMS value between $I(\omega)$ and an iterative estimate $I_e^{\lambda}(\omega)$ was calculated as a function of the parameter λ [105].

$$\sigma_i(\lambda) = rms\left\{\left|I_e^{\lambda}(\omega) - I(\omega)\right|\right\} \tag{7.14}$$

where i represents number of iteration; rms represents the RMS calculation performed on the quantity inside the bracket $\{\}$ over both passband and stopband in transform domain. $I(\omega)$ represents the transfer function obtained by straightforward division $\frac{P_{RX}(\omega)}{G_{RX}(\omega)}$ in the transfer domain, which is the case for $\lambda = 0$. $P_{RX}(\omega)$ and $G_{RX}(\omega)$ are given by Eq. 3.56

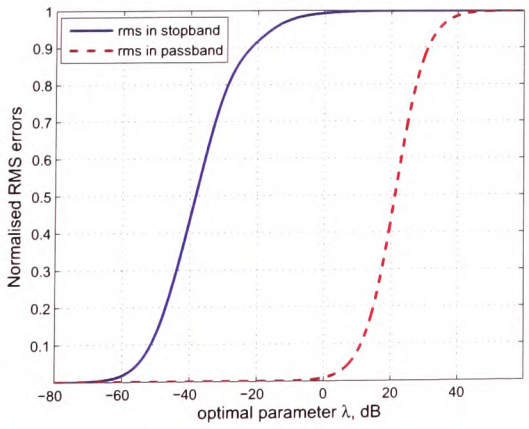

Figure 7.5: the RMS values calculated in the passband and stopband respectively

The optimal values of λ yield such a low-pass filter in which the RMS values are small in the passband ensuring maximised information passing, whereas large in the stopband leading to significant noise reduction. Consequently, the estimate, $I_e^{\lambda}(\omega)$ should be as similar as possible to $I(\omega)$ in the passband, while very different from it in the stopband. Using the measured data with the 20 dBi Gaussian horn as the receiver at 20 GHz, Fig. 7.5 illustrates an example of the RMS values as a function of λ . Here λ is represented on a decibel scale and has a relatively wide range from $-80dB$ to $+60dB$ covering all experienced values. First, Eq. 7.14 is calculated in the stopband and normalised with respect to its maximum. The results are expressed by the blue line in Fig. 7.5. Then, Eq. 7.14 is calculated in the passband, normalised with respect to its own maximum, shown as the red dotted line in Fig. 7.5. The optimal values of λ fall into the range between $-20\,dB$ and $0\,dB$ where the RMS values are close to zero in the passband, which guarantees a high degree of similarity of the estimate $I_e^{\lambda}(\omega)$ and $I(\omega)$; whereas the RMS values approach the maximum in the stopband leading to noise content reduction. Two undesired extremes at either side of the λ range are:

- Under-compensated restoration: the parameter λ is less than $-60\,dB$. This indicates that the estimate $I_e^{\lambda}(\omega)$ is coincident with the $I(\omega)$ in both passband and stopband. The high noise content still remains, therefore this is an ill-posed problem.

- Over-compensated restoration: the parameter λ is greater than $+40\,dB$. This means that too much distortion occurs in both bands. Consequently, most of the useful information is lost after filtering although noise has been greatly reduced.

The Bennia-Riad criterion defines the ranges where the optimal values of the parameter λ are located and where the under- and over-compensated cases take place if λ is chosen inappropriately. To specify the optimal value of λ, the Bennia-Riad

criterion needs to be combined with the error function. This will be detailed in chapter 8.

7.2.4 Implementation of the optimum compensation deconvolution method on measured data

Using the measured data obtained with the 20 dBi Gaussian horn as the receiver at 20 GHz, three restored deconvolution patterns are demonstrated in Fig. 7.6. Fig. 7.6a) represents the optimal restoration by choosing optimal value for the parameter $\lambda = -5\ dB$. The envelop of this graph shows a Gaussian shape, which indicates correct retrieval of the useful information. The curve is smooth, which means sufficient noise reduction. An under-compensated restoration case is illustrated in Fig. 7.6b), in which the value for parameter λ is chosen too small at $-60dB$. The restored pattern still contains a significant amount of noise; and information components appear distorted or swamped. An over-compensation restoration case is presented in Fig. 7.6c), in which λ is chosen too large at $+40\ dB$. The curve is extremely smooth and the noise has been completely eliminated. Nevertheless, considerable information appearing in Fig. 7.6a) has also been removed.

According to the Bennia-Riad, any value in the range between $-20\,dB$ and $0\,dB$ could be used to be optimal value for parameter λ. In this case, choosing parameter $\lambda = -5\ dB$ is based on subjective judgements. In chapter 8, however, it will be shown that when combining the optimum compensation method and error function results it turns out that $\lambda = -5\ dB$ does not quite represent the best value for λ.

7.3 Automated regularisation deconvolution

The automated regularisation deconvolution technique was originally proposed by Nahman and Guillaume [28[. This report dedicates significant amount of discussion to digitisation errors occurring during discrete Fourier transform and its inverse.

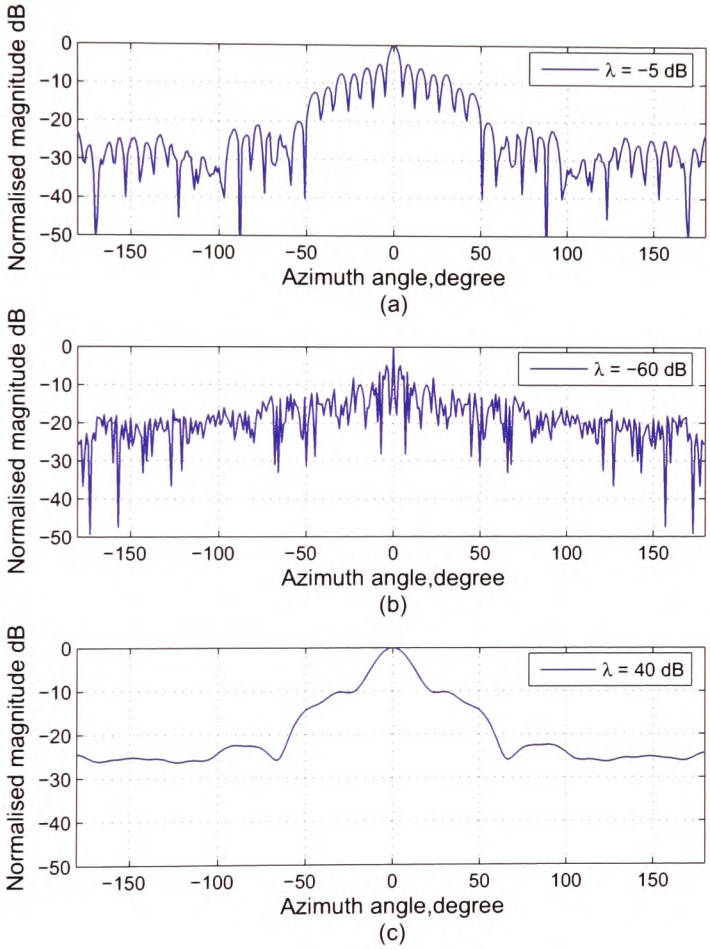

Figure 7.6: The three restored deconvolution patterns: (a) optimal-compensated; (b) under-compensated; (c) over-compensated using the measured data with the 20 dBi Gaussian horn as the receiver at 20 GHz

The principles and findings of that discussion were found to be not applicable to this project. Therefore the development documented in the sections uses the same starting assumptions as [28] and arrives at the same final equations, but uses a slight different approach in the intermediate steps represented in Eqs. 7.30 to 7.40.

7.3.1 Derivation of the automated regularisation filter

The automated regularisation filter is also called the Guillaume-Nahman filter [96]. It is an optimum filter in the sense that it minimises the weighted sum of an error term and a smoothness term [28]. It has only one adjustable parameter and this parameter adjusts the weighting between the error function and the smoothness. Its derivation is demonstrated as following [28[: the error function

$$e(k) = y(k) - x(k) * d(x) \tag{7.15}$$

where $y(k)$ represents the noisy output signal, *i.e.* the measured data, $x(k)$ represents the measured antenna radiation pattern and $d(k)$ denotes the restored pattern, *i.e.* the phase function pattern in this project. In addition to the error constraint $e(k)$, an auxiliary constraint $s(k)$ is defined as [28[:

$$s(k) = c(k) * d(k) \tag{7.16}$$

where $c(k)$ is the discrete function that defines the constraint. Here $c(k)$ is the second-difference operator, which corresponds to the second derivative operator $\frac{d^2}{dt^2}$ if it is a continuous function [28[, thus $s(k)$ depends upon the rate-of-change of the first derivative of $d(k)$, *i.e.* its smoothness. The two criteria defined in Eqs. 7.15 and 7.16 could be integrated into one [28[:

$$P = \bar{E} + \gamma \bar{S} \tag{7.17}$$

where γ represents the weighting parameter, $\bar{E}$ and $\bar{S}$ are given by [28[:

$$\bar{E} = \sum_{k=0}^{N-1} [e(k)]^2 \tag{7.18}$$

$$\bar{S} = \sum_{k=0}^{N-1} [s(k)]^2 \tag{7.19}$$

To obtain an optimum solution, tuning the parameter γ is corresponding to adjusting the automated regularization filter until P is minimised [28]. Here the parameter γ determines the degree of smoothness of the deconvolution pattern. Consequently, the minimisation is obtained when

$$\frac{\partial}{\partial d(k)} \left[\bar{E} + \gamma \bar{S}\right] = 0 \tag{7.20}$$

According to the Parseval's theorem [106]:

$$\sum_{k=0}^{N-1} [e(k)]^2 = \frac{1}{N} \sum_{n=0}^{N-1} [E(n)]^2 \tag{7.21}$$

where $E(n)$ represents the Discrete Fourier Transform (DFT) of $e(k)$, n denotes the discrete variable in transform domain. Consequently, $\bar{E}$ and $\bar{S}$ are equivalent to:

$$\bar{E} = \frac{1}{N} \sum_{n=0}^{N-1} E(n)E^*(n) \tag{7.22}$$

$$\bar{S} = \frac{1}{N} \sum_{n=0}^{N-1} S(n)S^*(n) \tag{7.23}$$

where $E^*(n)$ and $S^*(n)$ denote the complex conjugate of $E(n)$ and $S(n)$ respectively. Eq. 7.17 becomes:

$$P = \bar{E} + \gamma \bar{S} = \frac{1}{N} \sum_{n=0}^{N-1} [E(n)E^*(n) + \gamma S(n)S^*(n)] \tag{7.24}$$

Applying DFT to Eqs. 7.15 and 7.16, $E(n)$ and $S(n)$ become

$$E(n) = Y(n) - X(n)D(n) \tag{7.25}$$

$$S(n) = C(n)D(n) \tag{7.26}$$

where $Y(n)$, $X(n)$, $D(n)$, $E(n)$, $S(n)$ and $C(n)$ are representations of $y(k)$, $x(k)$, $d(k)$, $e(k)$, $s(k)$ and $c(k)$ respectively in the discrete transform domain. Consequently, $E(n)E^*(n)$ and $S(n)S^*(n)$ in Eq. 7.24 become:

$$\begin{aligned} E(n)E^*(n) &= [Y(n) - X(n)D(n)]\,[Y(n) - X(n)D(n)]^* \\ &= |Y(n)|^2 - Y(n)\,(X(n)D(n))^* - (X(n)D(n))\,Y(n)^* + |X(n)D(n)|^2 \end{aligned} \tag{7.27}$$

$$S(n)S^*(n) = C(n)D(n)C^*(n)D^*(n) = |C(n)D(n)|^2 \tag{7.28}$$

Then, $\bar{E} + \gamma\bar{S}$ becomes:

$$\begin{aligned} \bar{E} + \gamma\bar{S} &= \frac{1}{N}\sum_{n=0}^{N-1}\left\{|Y(n)|^2 + |X(n)D(n)|^2 + \gamma\,|C(n)D(n)|^2\right\} \\ &- \frac{1}{N}\sum_{n=0}^{N-1}\left[Y(n)\,(X(n)D(n))^* + (X(n)D(n))\,Y(n)^*\right] \end{aligned} \tag{7.29}$$

Because $D(n)$ is the deconvolution product in the transform domain,

$$D(n) = R(n)\frac{Y(n)}{X(n)} \tag{7.30}$$

where $R(n)$ is the representation of the automated regularisation filter in the transform domain. It is usually complex and can be given by:

$$R(n) = |R(n)|\,\angle\Phi_R \tag{7.31}$$

where $|R(n)|$, $\angle\Phi_R$ represent the magnitude and the phase angle of the automated regularization filter respectively. Inverse transforming Eq. 7.30 back into the original domain:

$$d(k) = r(k) * [y(k)(1/*)x(k)] \tag{7.32}$$

where $(1/*)$ represents the inverse operation of the $*$ convolution. Using Eqs. 7.30 and 7.31 to simplify the second term on the right hand side of Eq. 7.29:

$$Y(n)\left(X(n)D(n)\right)^{*} + \left(X(n)D(n)\right)Y(n)^{*} = 2\left|Y(n)\right|^{2}\left|R(n)\right|\cos\Phi_{R} \tag{7.33}$$

Consequently, Eq. 7.29 becomes:

$$\bar{E} + \gamma\bar{S} = \frac{1}{N}\sum_{n=0}^{N-1}\left|Y(n)\right|^{2}\left\{1 + \left|R(n)\right|^{2} + \gamma\left|\frac{C(n)R(n)}{X(n)}\right|^{2} - 2\left|R(n)\right|\cos\Phi_{R}\right\} \tag{7.34}$$

Representing Eq. 7.20 in transform domain:

$$\frac{\partial}{\partial D\left(n\right)}\left[\bar{E} + \gamma\bar{S}\right] = 0 \tag{7.35}$$

where $D\left(n\right)$ represents the DFT of $d\left(k\right)$. Given Eq. 7.30, the derivative of $D\left(n\right)$ is equal to the derivative of $R\left(n\right)$ [28]:

$$\frac{\partial\left[\bar{E} + \gamma\bar{S}\right]}{\partial D\left(n\right)} = \frac{\partial\left[\bar{E} + \gamma\bar{S}\right]}{\partial R(n)} \tag{7.36}$$

Using Eq. 7.31, Eq. 7.36 becomes:

$$\frac{\partial\left[\bar{E} + \gamma\bar{S}\right]}{\partial R(n)} = \frac{\partial\left[\bar{E} + \gamma\bar{S}\right]}{\partial\left|R(n)\right|} + \frac{\partial\left[\bar{E} + \gamma\bar{S}\right]}{\partial\angle\Phi_{R}} \tag{7.37}$$

Since $\left|Y(n)\right|^{2}$ in Eq. 7.34 is generally not zero, the term in $\{\}$ must be minimised with respect to $R(n)$. In other word, the partial differential of this term with respect to $\left|R(n)\right|$ and $\angle\Phi_{R}$ must be equal to zero.

$$2\left|R(n)\right| + 2\gamma\left|R(n)\right|\left|\frac{C(n)}{X(n)}\right|^{2} - 2\cos\Phi_{R} = 0 \tag{7.38}$$

$$2\left|R(n)\right|\sin\Phi_{R} = 0 \tag{7.39}$$

Since $|R(n)|$ is generally not zero, Eq. 7.39 is equivalent to $\sin\Phi_R = 0$, which leads to $\cos\Phi_R = 1$. This means that the filter expression, $R(n)$, is real:

$$R(n) = \frac{1}{1+\gamma\frac{|C(n)|^2}{|X(n)|^2}} = \frac{|X(n)|^2}{|X(n)|^2+\gamma|C(n)|^2} \tag{7.40}$$

Eq. 7.40 indicates that the automated regularisation filter is a type of Wiener filter.

So far, the derivation proceeded without considering the effects of computation errors. Computation errors mainly involve the round-off error in calculating a specific quantity during Fourier transform and inverse Fourier transform processes and are usually complex and unknown. Optimal results cannot be obtained with the presence of computation errors [28]. In practice the computation errors are very small in values compared with acquisition noise obtained during measurements and can be safely negligible.

As mentioned above, $c(k)$ is defined as the second difference sequence operator and corresponds to the second derivative operator in the continuous case. The first-order difference is [28]:

$$\frac{x(kT) - x[(k-1)T]}{T} \tag{7.41}$$

where T denotes the interval between the kth and $(k-1)$th values in original domain. Eq. 7.41 can be simplified by setting T equal to unity, thus Eq. 7.41 becomes:

$$x(k) - x(k-1) \tag{7.42}$$

Subsequently, the second-order difference is:

$$x(k) - 2x(k-1) + x(k-2) \tag{7.43}$$

Because $c(k)$ is the second operator,

$$c(k) * x(k) = x(k) - 2x(k-1) + x(k-2) \tag{7.44}$$

Apply the DFT to Eq. 7.44,

$$\begin{aligned} X(n)C(n) &= X(n)(1-2e^{-j\frac{2\pi n}{N}}+e^{-j\frac{4\pi n}{N}}) \\ \Rightarrow\ C(n) &= 1-2e^{-j\frac{2\pi n}{N}}+e^{-j\frac{4\pi n}{N}} \end{aligned} \tag{7.45}$$

where $C(n)$ represents the discrete Fourier transform of $c(k)$:

$$C(n)=\sum_{k=0}^{N-1} c(k)e^{-j\Omega Tkn} \tag{7.46}$$

and $\Omega T=\frac{2\pi}{N}$ [83], Ω is the interval in transform domain. N is the total number of discrete points. Hence,

$$\begin{aligned} |C(n)|^2 &= \left[1-2e^{-j\frac{2\pi n}{N}}+e^{-j\frac{4\pi n}{N}}\right]\left[1-2e^{j\frac{2\pi n}{N}}+e^{j\frac{4\pi n}{N}}\right] \\ &= 6-8\cos\frac{2\pi n}{N}+2\cos\frac{4\pi n}{N} \end{aligned} \tag{7.47}$$

Eq. 7.47 can be reduced to [28]:

$$|C(n)|^2=\sin^4(\frac{2\pi n}{N}) \tag{7.48}$$

when N becomes very large, the argument $\frac{2\pi n}{N}$ approaches a continuous variable $2\pi f$ and becomes very small,

$$\lim_{N\to\infty}\frac{2\pi n}{N}\ \to\ 2\pi f=\omega \qquad 0<f<1 \tag{7.49}$$

Since

$$\sin\omega=\omega-\frac{\omega^3}{3!}+\frac{\omega^5}{5!}-\frac{\omega^7}{7!}+\cdots; \qquad \omega^2<\infty \tag{7.50}$$

Consequently,

$$|C(n)|^2=\sin^4\omega=\omega^4 \tag{7.51}$$

Eq. 7.40 becomes:

$$R(n)=\frac{|X(n)|^2}{|X(n)|^2+\gamma\omega^4} \tag{7.52}$$

7.3.2 Error function criterion

Since various approaches may be used for the deconvolution processes, the quality of their corresponding results has to be judged by using a quantitative function. The error function $e(k)$ defined by Eq. 7.15 is used to determine the parameter γ in the automated regularisation filter. The use of the error function can be justified in this way: considering $x(k)$ represents a measured antenna radiation pattern in this project, $h_0(k)$ represents the precise information of the phase function and $y_0(k)$ denotes the precise knowledge of the convolution result between $x\,(k)$ and $h_0\,(k)$ *i.e.* $y_0(k) = x(k) * h_0(k)$. Both $h_0\,(k)$ and $y_0\,(k)$ are unknown in practice.

If the deconvolution implementation is successful, the resultant restored pattern $d(k)$ must accommodate most of useful information of $h_0(k)$ and a convolution relationship still holds among $d\,(k)$, $x\,(k)$ and $y\,(k)$, that is $x(k) * d(k) = y(k)$, where $y\,(k)$ represents a measured output signal with acquisition noise. Although $y(k)$ may not exactly equal to $y_0(k)$, it is considered that $y(k)$ contains most of useful information of $y_0(k)$. In other words, $d(k)$ and $y(k)$ must be very resembling to $h_0(k)$ and $y_0(k)$ respectively. Small variations in $h_0(k)$ or $y_0(k)$ will not undermine their convolution relationship. Otherwise, if $y(k)$ was considered be seriously corrupted and lost significantly useful information of $y_0(k)$ during measurements, information of $h_0(k)$ is impossible to retrieve correctly. Therefore, the measured noisy output $y(k)$ can be used in the error function. Detailed discussion can be referred to [28[.

The error function must be carefully interpreted. Four parameters are used for its characteristics, the mean value $\bar{e}$, the standard deviation σ, the maximum value e_{max} and the minimum value e_{min}. The mean value is given by

$$\bar{e} = \frac{1}{N}\sum_{k=1}^{N} e(k) \tag{7.53}$$

Ideally $\bar{e}$ should be zero, therefore the absolute value of $\bar{e}$ needs to be minimised. The standard deviation is given by

$$\sigma = \left[\frac{1}{N}\sum_{k=1}^{N}[e(k) - \bar{e}]^2\right]^{1/2} \tag{7.54}$$

The standard deviation σ must be small compared to the maximum of the waveform $y(k)$. A typical acceptable value for σ is of the same order of magnitude as the noise on the output $y(k)$ [28]. Also, the magnitude of the maximum and minimum values of the error function, $|e_{max}|$ and $|e_{min}|$ need be of similar order. A well chosen deconvolution result will ensure the parameters $\bar{e}$, σ, e_{max}, and e_{min} are very small compared to the maximum of the waveform $y(k)$.

7.3.3 Verification of the automated regularisation technique

As discussed in section 7.2.2, the automated regularisation deconvolution technique has to be verified before it can be applied on measured data obtained in this project. Similar to section 7.2.2, the verification was achieved by using computer-generated curves, one representing the phase function pattern and the other representing the antenna radiation pattern when the 20 dBi standard gain horn is used as the receiver at 20 GHz.

Fig. 7.7a) shows the measured antenna radiation pattern of a 20 dBi standard gain horn at 20 GHz. This antenna radiation pattern was chosen is due to its relative narrower beamwidth comparing with those using a 10 dBi or a 15 dBi standard gain horn as the receiver. A narrow antenna radiation pattern provides more reliable results as described in section 6.3. The antenna radiation pattern obtained using a Gaussian horn or a Lens horn is similar to a Gaussian shape curve. This has been discussed in section 7.2.2.

To accurately represent this antenna radiation pattern, the effects of its sidelobes have to be considered, although its sidelobe magnitude is not very significant comparing with its mainlobe's as shown in Fig. 7.7a). Two computer-generated curves, a Sinc-squared curve and a Sinc curve with absolute value, are considered possible

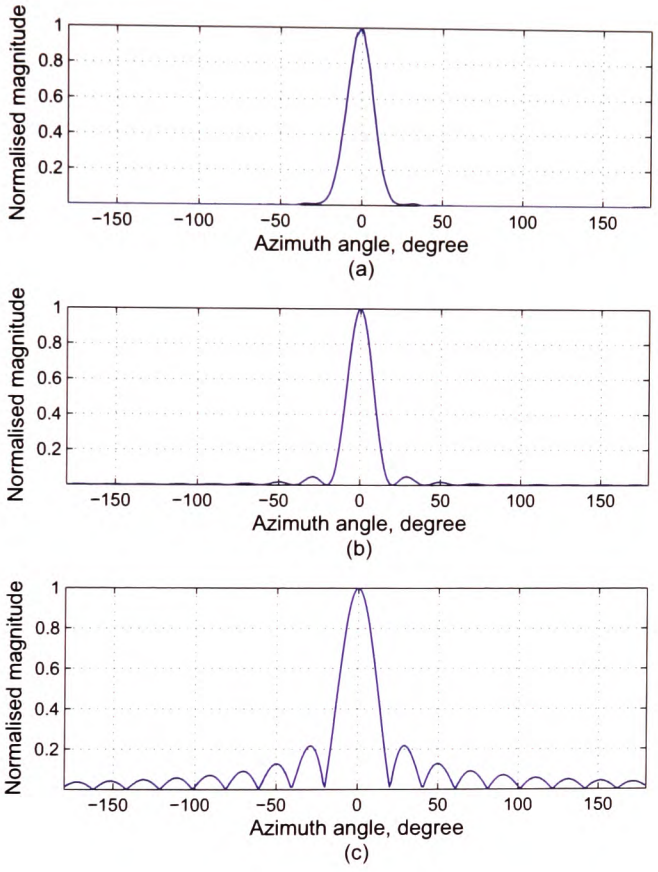

Figure 7.7: Displays of linear signals: (a) the measured antenna radiation pattern; (b) simulation using a Sinc-squared curve; (c) simulation using a Sinc curve with absolute value

choices. Both of them have the sidelobe effects. As shown in Fig. 7.7b) and c), the Sinc-squared curve offers higher similarity than the Sinc curve with absolute value to the pattern represented by Fig. 7.7a). Therefore, the Sinc-squared curve is used to represent the antenna radiation pattern using the 20 dBi standard gain horn as the receiver at 20 GHz.

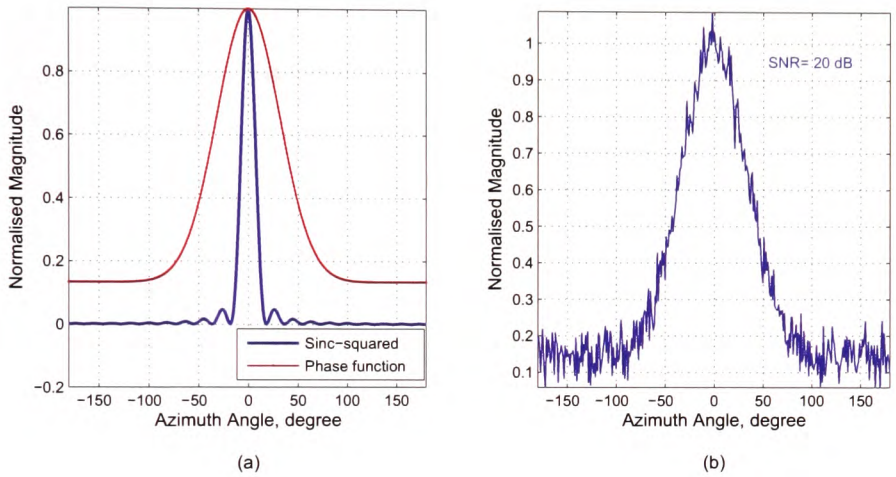

Figure 7.8: (a) computer-generated input signals and (b) their convolution with additive noise

Fig. 7.8a) illustrates the computer-generated input signals: the red curve represents the phase function pattern and the blue one denotes the radiation pattern of the receiver antenna. Fig. 7.8b) shows their convolution product with additive random noise. The noise is assumed to be mean-zero. The SNR is set to be about 20 dB in this example. So far, the noisy output signal (the blue curve in Fig. 7.8b)) and the antenna radiation pattern (the blue curve in Fig. 7.8a)) are known. The red curve in Fig. 7.8a) represents the phase function pattern to be restored.

Fig. 7.9 illustrates a process of restoring the phase function pattern with varying values of the parameter γ from $0\,dB$ to $50\,dB$. The restored patterns are shown as red curves and the original input pattern is overlaid in blue for comparison. In of Figs. 7.9a) and b) values of the parameter γ were chosen too small, which resulted in under restored cases. As shown in Fig. 7.9c) to f), it is evident that the optimal

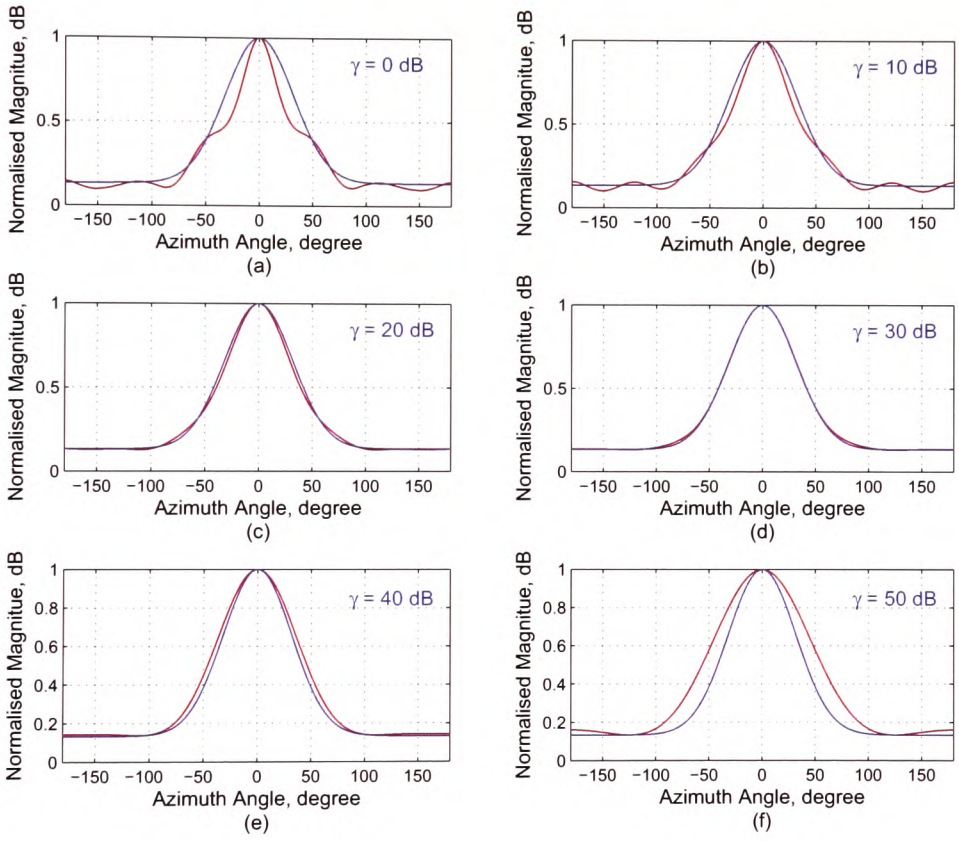

Figure 7.9: Restored phase function patterns with various values of parameter γ

value of the parameter γ will be found within the range of $20\,dB$ to $40\,dB$, which leads to the best restored pattern. Fig. 7.9f) shows an over restored case when the parameter γ was chosen to be $50\,dB$. The parameter γ range, $0\,dB$ to $50\,dB$, under investigation can be estimated using the Bennia-Riad criterion.

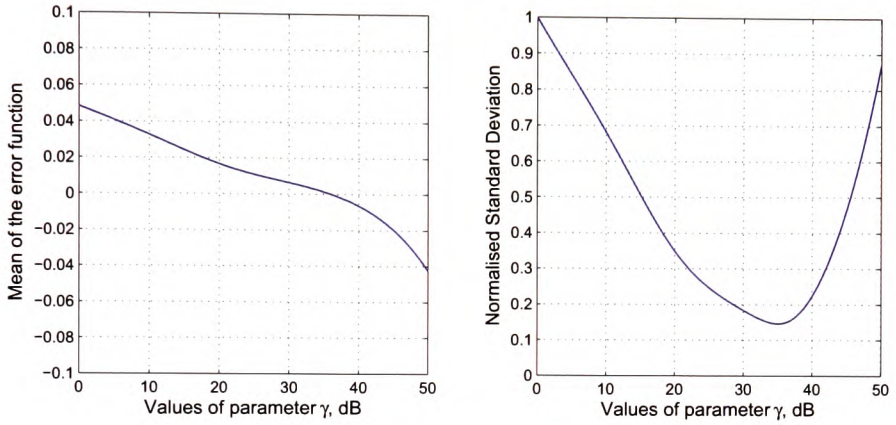

Figure 7.10: Calculated (a) mean and (b) standard deviation of the error function

The error function is used to determine the optimal parameter γ. Fig. 7.10 presents the calculated mean $\bar{e}$ using Eq. 7.53 and standard deviation σ using Eq. 7.54 with parameter γ from $0\,dB$ to $50\,dB$. It shows that the absolute minimum of $\bar{e}$ in Fig. 7.10a) and the minimum of σ in Fig. 7.10b) are consistently corresponding to the abscissa $\gamma = 35\,dB$ and its near neighbours, although the two minima are not leading to the same abscissa. With current computer-generated data, the minima of $|\bar{e}|$ and σ are determined at $\gamma = 36.47\,dB$ and $\gamma = 35.72\,dB$ respectively. Whether the choice of γ depends on the absolute minimum or the minimum of σ will be described in chapter 8.

The restored phase function pattern using the automated regularisation technique with parameter $\gamma = 35.72 dB$ is shown in Fig. 7.11a). The computer-generated input function pattern is also plotted in blue for comparison. The corresponding error function given by Eq. 7.15 is displayed in Fig. 7.11b). Here the error function means the difference between the noisy output and the convolution product of the

restored phase function pattern and the antenna radiation pattern. The restored pattern (the red curve in Fig. 7.11a)) offers a overall high similarity to the computer-generated input phase function pattern (the blue curve in Fig. 7.11a)). The error function shown in Fig. 7.11b) exhibits random and even variation around zero. Magnitudes of its maximum and minimum,$|e_{max}|$ and $|e_{min}|$, have the same order and smaller than 15% comparing with its maximum of the noisy output signal.

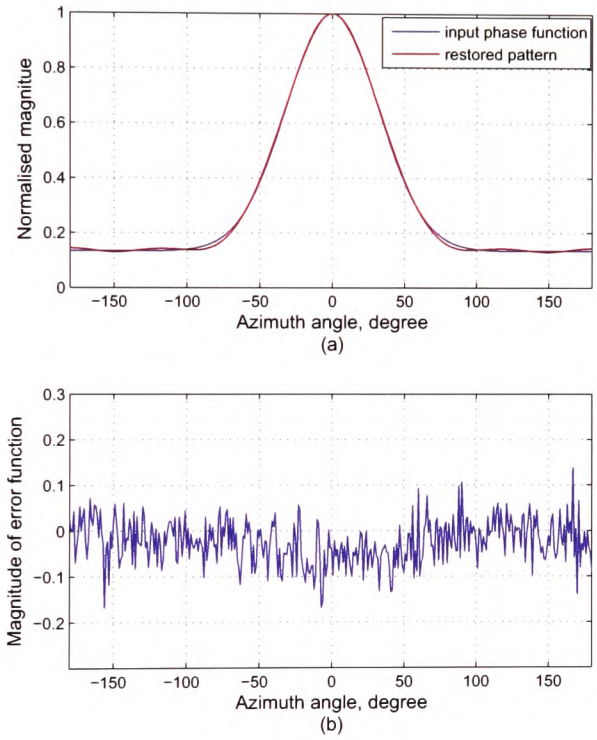

Figure 7.11: (a) the optimal restoration using the automated regularisation filter and (b) the corresponding error function

7.3.4 Implementation of the automated regularisation deconvolution method on measured data

Some measured patterns are restored using the automated regularisation deconvolution technique. As described in section 6.3, those patterns obtained via a narrow beamwidth antenna are favourite, thus measured patterns using the 20 dBi Gaussian

horn and the 20 dBi standard gain horn at 20 GHz, and the 29 dBi Lens horn and 20 dBi standard gain horn at 40 GHz are utilised to demonstrate application of the automated regularisation technique. Figs. 7.12a) and b) present the deconvolution results when the Gaussian and the standard gain horn at 20 GHz were using respectively. For comparison, the actual measured pattern was overlaid in blue. Similarly, the restored patterns with the Lens and standard gain horn at 40 GHz as receiver antenna are illustrated in Figs. 7.13a) and b) respectively.

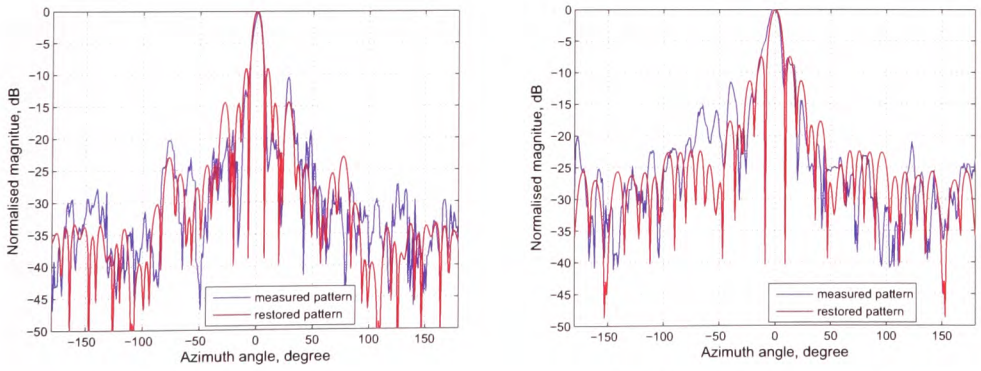

(a) 29 dBi Lens horn (b) 20 dBi standard gain horn

Figure 7.12: Restored patterns using automated regularisation at 20 GHz

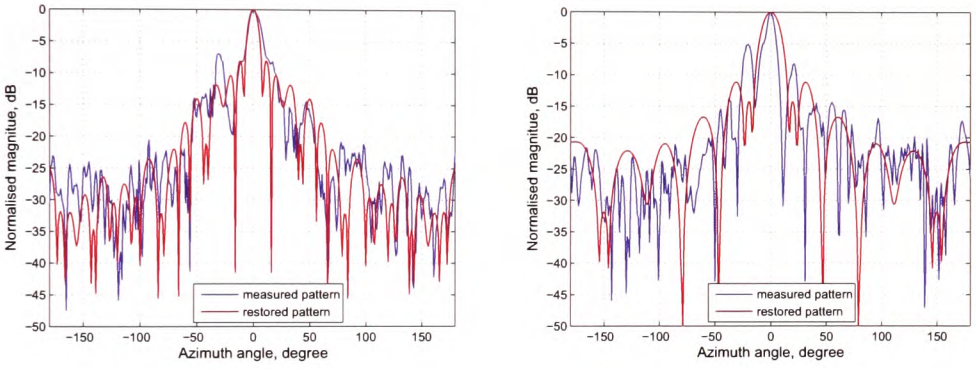

(a) 20 dBi Gaussian horn (b) 20 dBi standard gain horn

Figure 7.13: Restored patterns using automated regularisation at 40 GHz

These restored patterns keep a good similarity to their corresponding measured patterns, in particular at the region of their mainlobes. Those patterns achieve an

acceptable level of smoothness and preserve most of characteristics from the measured patterns. In theory, both the phase function pattern and the antenna radiation pattern are perfectly symmetric. The imperfection demonstrated in the measured patterns was generated by random noise and the nonideal measurement environment such as limited physical dimension of the anechoic chamber and the downsized forest, as well as its inhomogeneity. Nevertheless, the deconvolution techniques, both the optimum compensation and the automated regularisation, and their corresponding algorithms developed via computer programme were implemented in accordance with the assumption that all patterns are symmetric. Consequently, the restored patterns by deconvolution present symmetry. In chapter 8, a pre-filtering technique, auto- and cross-correlation, is used to convert the measured pattern and the antenna radiation pattern into symmetrical patterns without undermining their convolution relationship.

7.4 Summary and interim conclusion

This chapter presents the successful implementation of two iterative deconvolution approaches: the optimum compensation and the automated regularisation methods. First of all, the two methods are introduced via mathematic derivation in detail respectively. Next, both techniques are verified via simulation using computer-generated data. With apriori knowledge of those computer-generated curves, application of both deconvolution techniques are proved successfully.

In reality, due to lack of true information, some criteria have to be utilised to determine the optimal parameter in the deconvolution process, which sometimes involves subjective judgements. Here the Bennia-Riad criterion and the error function are used to identify the optimal values of parameter λ or γ. Then, examples of the deconvolution patterns using both techniques are presented. Some undesired cases resulting from choosing the parameter values too large or too small are also discussed. Finally, a typical deconvolution procedure could be implemented as follows:

1. Offset correction for the known input and output signals, $x(k)$ and $y(k)$. In simulation, the input signal $x(k)$ is noise-free and the SNR of the noisy output $y(k)$ is under control. With measured data, if the quality of the measured patterns is unpredictable or their SNR is very poor, it is better to set $x(0) = x(N-1) = 0$ and $y(0) = y(N-1) = 0$ before the deconvolution, where N represents the number of measured data points. In fact, magnitude of these measured points should be very close to zero, otherwise they were either seriously corrupted by noise or incorrectly truncated.

2. Convert the convolution operation into multiplication in the transform domain by DFT and calculate the ratio $H(\omega) = \frac{Y(\omega)}{X(\omega)}$, where $Y(\omega)$ and $X(\omega)$ are the Fourier transforms of $x(k)$ and $y(k)$ respectively, $H(\omega)$ represents the transfer function.

3. Use the Bennia-Riad criterion to estimate the optimal range of parameter λ or γ, then use the error function to specify the optimal values through spotting the minima of its absolute mean and standard deviation. The identified values for parameter λ or γ should coincide with the optimal range specified by the Bennia-Riad criterion.

4. Use the best chosen parameter, λ in the optimum compensation technique or γ in the automated regularisation technique, to yield the deconvolution result in transform domain and inverse DFT them back into original domain.

5. Display the deconvolution result $h_e(k)$ in decibel scale and the error function $e(k) = y(k) - h_e(k) * x(k)$. The quality of the deconvolution result $h_e(k)$ can be judged graphically and quantitatively via $\bar{e}$, σ, e_{max} and e_{min}.

6. If the result is unsatisfactory, return to step 3 and repeat the process of determining parameters λ and γ.

Chapter 8

RET input parameter extraction using deconvolution

This chapter describes the combination of the RET input parameter extraction with deconvolution techniques. In chapter 3, the methods for extracting the RET input parameters were detailed including the distortion effects caused by the receiver antenna radiation pattern. Two deconvolution techniques, the optimum compensation and the automated regularisation, are applied to remove the distortion and restore the phase function pattern. Consequently the RET input parameters are extracted from the restored patterns.

The performances of both deconvolution techniques are evaluated based on simulations using computer-generated signal patterns. These computer-generated signal patterns represent the characteristics of the phase function pattern and antenna radiation patterns in accordance with previous knowledge of their shapes, beamwidths and SNRs. Pre-filtering techniques using auto- and cross-correlation are also utilised to improve the deconvolution results. Finally, the RET input parameters are also extracted from the pre-filtered and deconvolved patterns. An improvement in the accuracy of the RET parameter extraction is demonstrated.

Chapter 7 explained the optimum compensation and the automated regularisation techniques for deconvolution. Both require the determination of an iterative optimisation parameter, λ for the optimum compensation and γ for the automated

regularisation. The procedures to determine λ and γ can be further improved by applying pre-filtering techniques. Section 8.1 addresses how to selectsuitable values for λ and γ. The addition of the pre-filtering techniques is presented in section 8.3. Results of RET parameter extraction using a combination of the techniques outlined in the previous sections are shown in section 8.4.

8.1 Parameter extraction from restored phase function patterns

The Bennia-Riad criterion [105[is utilised to find the optimal range for λ or γ. The error function, as defined in section 7.3.1, is calculated over this range to obtain its absolute minimum and minimum of the standard deviation and find their corresponding parameter values: λ_{mean}, λ_{std} or γ_{mean}, γ_{std}. The phase function patterns are restored using λ_{mean} or λ_{std} in the optimum compensation technique and γ_{mean} or γ_{std} in the automated regularisation technique. Some degree of subjective judgement is needed to select the parameters λ_{mean} or λ_{std} (γ_{mean} or γ_{std}). Such judgements are based on the knowledge: (a) the central-limit theorem described in section 6.2, which means that the restored phase function pattern should be narrower than the measured pattern; (b) loss of information documented in section 6.3, which indicates that a narrow beamwidth receiver antenna would provide more reliable measured data than its wide beamwidth counterparts. Consequently, narrow beamwidth antennas are selected as the receiver antenna, which in return means that the restored phase function pattern should only be slightly, rather a lot, narrower than the measured pattern.

8.1.1 Parameter extraction from patterns restored using optimum compensation

Optimum compensation deconvolution requires the determination of the optimal value for parameter λ. The process of identifying the best value of λ according to Riad [81[always involves some form of subjective judgement. In the following exam-

ple the measured signal pattern obtained with the 20 dBi Gaussian horn as receiver antenna at 20 GHz is used to demonstrate how the parameter λ is determined. A second criterion is used to reduce the range of possible values for λ. This is found using the error function (Eq. 7.15) between the measured pattern and the convolution product of the restored pattern and the antenna radiation pattern. Determination of λ is achieved by combing the Bennia-Riad criterion and the error function.

Applying the Bennia-Raid criterion results in an approximate optimal range, $-50\,dB$ to $0\,dB$, for parameter λ as shown in Fig. 8.1. However, the Bennia-Raid criterion only gives a scope rather than a specified value for λ. Thus, the error function with its mean value (Eq. 7.53) and standard deviation (Eq. 7.54) are utilised to select the best value for parameter λ.

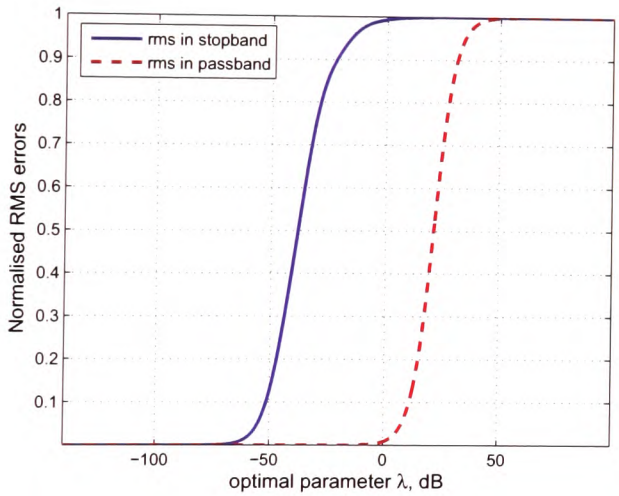

Figure 8.1: Normalised RMS errors using the Bennia-Riad criterion

Fig. 8.2 shows the calculated standard deviation and mean value of the error function using Eqs. 7.15, 7.54 and 7.53 in accordance with the optimal range of λ. The minima of the normalised standard deviation and the absolute mean are found at $\lambda_{std1} = -18.84\,dB$ and $\lambda_{mean1} = 0\,dB$ respectively. Here the subscript 1 denotes that standard deviation and mean value are obtained in the optimal range, $-50\,dB$ to $0\,dB$, indicated by Fig. 8.1.

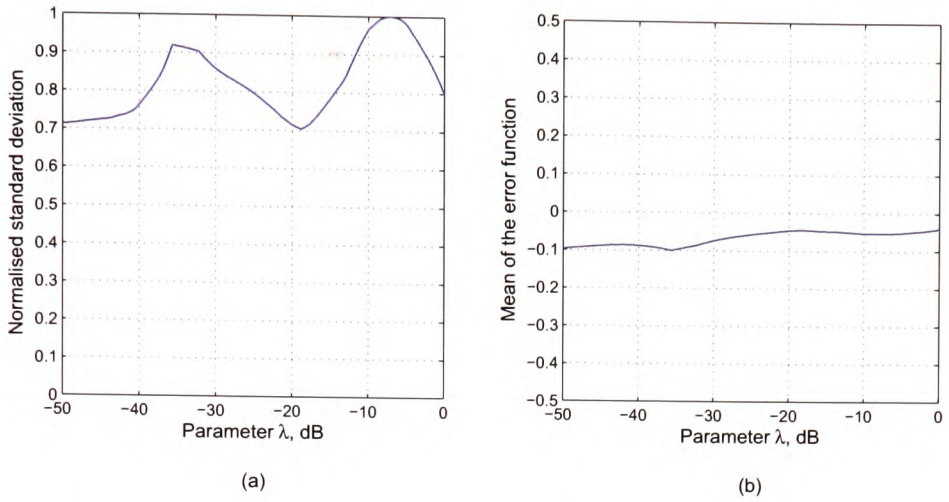

Figure 8.2: Calculated (a) standard deviation and (b) mean of the error function over the optimal range

As a matter of caution, exceptional cases are also being considered where the optimal value of λ may locate outside the indicated range of $-50\,dB$ to $0\,dB$. Thus, the parameter range is extended to $-60\ dB$ to $+10\ dB$. Any value of λ located outside this extended range does not present a reasonable choice for the optimal compensation filter according to the Bennia-Riad criterion. The two extended sub-regions, $-60\,dB$ to $-50\,dB$ and $0\,dB$ to $+10\,dB$, combined with the range, $-50\,dB$ to $0\,dB$, safely cover all possible values for parameter λ in this example.

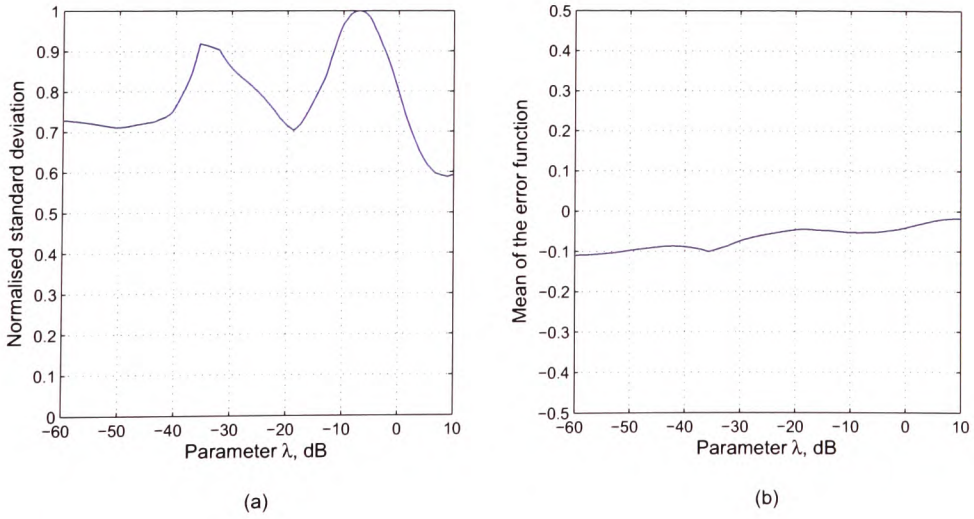

Figure 8.3: Calculated (a) standard deviation and (b) mean of the error function over the extended range

The normalised standard deviation and mean value in the extended range are shown in Figs. 8.3a) and b). Their minima are found at $\lambda_{std2} = 8.97 dB$ and $\lambda_{mean2} = 10 dB$. Subscript 2 denotes that standard deviation and mean value are obtained in the extended range. Once the values for parameter λ determined, the convolution theorem (Eqs. 6.6 to 6.9), Fourier transform (Eq. 6.4) and inverse Fourier transform (Eq. 6.5) and the optimum compensation filter (Eq. 6.44) are used to obtain the corresponding deconvolution patterns. Figs. 8.4a) and b) show the restored patterns achieved with $\lambda_{std1} = -18.84\, dB$ and $\lambda_{std2} = 8.97\, dB$, where the measured pattern is overlaid for comparison.

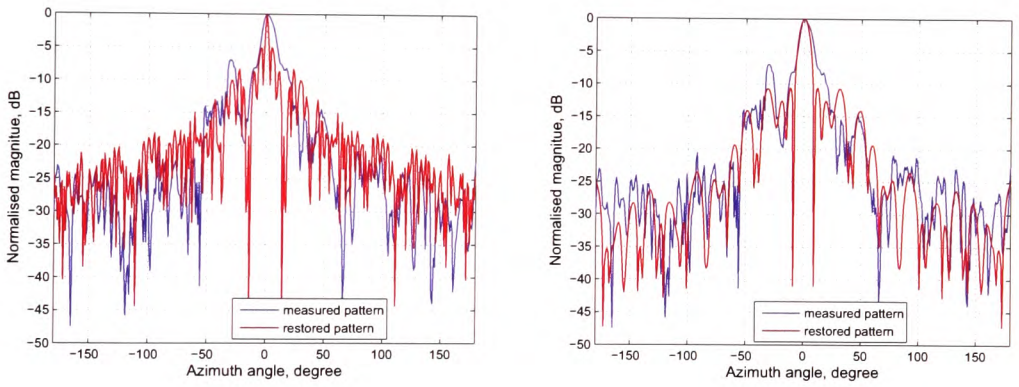

(a) (b)

Figure 8.4: Restored patterns with (a) $\lambda_{std1} = -18.84\, dB$ and (b) $\lambda_{std2} = 8.97\, dB$ overlaid with the measured pattern

Comparing parts a) and b) in Fig. 8.4 it can be seen that the retrieved pattern in b) has a wider $3\, dB$ beamwidth than the one in a), it is however still narrower than the measured pattern. The true phase function is expected to be only slightly narrower than the measurement, since the measured pattern shows the influence of a convolution with a relatively narrow beamwidth antenna radiation pattern of the Gaussian horn used in the example. The deconvolution result shown in Fig. 8.4a) for $\lambda_{std1} = -18.84\, dB$ is considered to be too narrow to have resulted in the measured pattern, when convolved with the Gaussian horn antenna pattern (see also section

6.2). Therefore the deconvolution result based on $\lambda_{std2} = 8.97\,dB$ is chosen for the extraction of the RET input parameters α and β. Fig. 8.5 shows the chosen deconvolution result overlaid with the least rms errors fitted calculated phase function (Eq. 5.1) yielding the extracted parameters α and β.

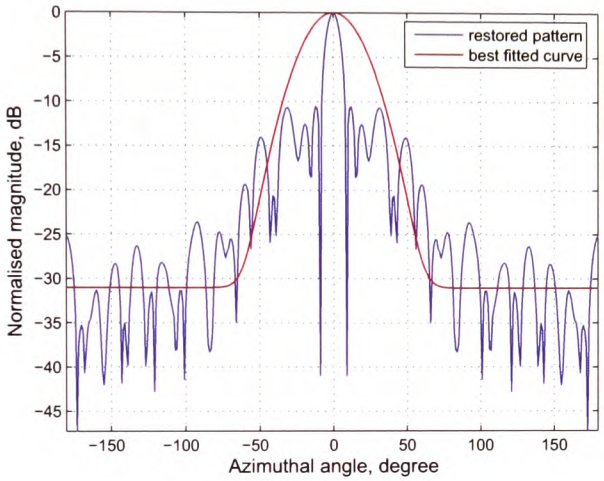

Figure 8.5: Restored pattern with $\lambda_{std2} = 8.97\,dB$ overlaid with best fit phase function curve

Parameter extraction results

The process described above has been applied to all directional spectra measured at both frequencies (20 and 40 GHz) and for all antennas used. The appropriate parameters λ have been determined and the restored patterns have been used to extract the values for the RET input parameters α and β. Table 8.1 summarises the results for the 20 GHz measurements and Table 8.2 for the 40 GHz measurements using the optimum compensation technique.

Receiver antenna	α	β	$\beta * 1.67$
20 dBi Gauss horn	0.98	22.5^o	37.6^o
20 dBi standard gain horn	0.92	26^o	43.4^o
15 dBi standard gain horn	0.38	9^o	15^o
10 dBi standard gain horn	0.16	7^o	11.7^o

Table 8.1: Extraction of parameters α and β from restored patterns for different receiver antennas at 20 GHz

Receiver antenna	α	β	$\beta * 1.67$
29 dBi Lens horn	0.95	12^o	20^o
20 dBi standard gain horn	0.67	9^o	15^o
15 dBi standard gain horn	0.41	13^o	21.7^o
10 dBi standard gain horn	0.66	13.5^o	22.5^o

Table 8.2: Extraction of parameters α and β from restored patterns for different receiver antennas at 40 GHz

8.1.2 Parameter extraction from patterns restored using automated regularisation

To apply the automated regularisation technique it is essential to determine the optimal value for parameter γ. The choice of γ depends on the nature of data [28[and again involves some form of subjective judgement. The measured signal pattern obtained with the 29 dBi Lens horn as receiver antenna at 40 GHz is used on the following example to demonstrate how the parameter γ is determined using the error function.

The mean value and standard deviation of the associated error function are calculated as a function of parameter γ on a dB scale as shown in Figs. 8.6a) and b). The calculation is undertaken over a relatively wide range of $0dB$ to $120dB$, ensuring the optimal value of γ would be found. The optimal value of parameter γ should be found at one of the minima of calculated absolute mean or standard deviation of the associated error function. Their minima are found at $\gamma_{mean} = 22.99\,dB$ and $\gamma_{std} = 4.56\,dB$ for the absolute mean and standard deviation respectively. Once γ is determined, the restored pattern is determined using the transfer function of the automated regularisation Eq. 6.45. Fig. 8.7 shows the resultant restored patterns using $\gamma_{mean} = 22.99\,dB$ (a) and $\gamma_{std} = 4.56\,dB$ (b).

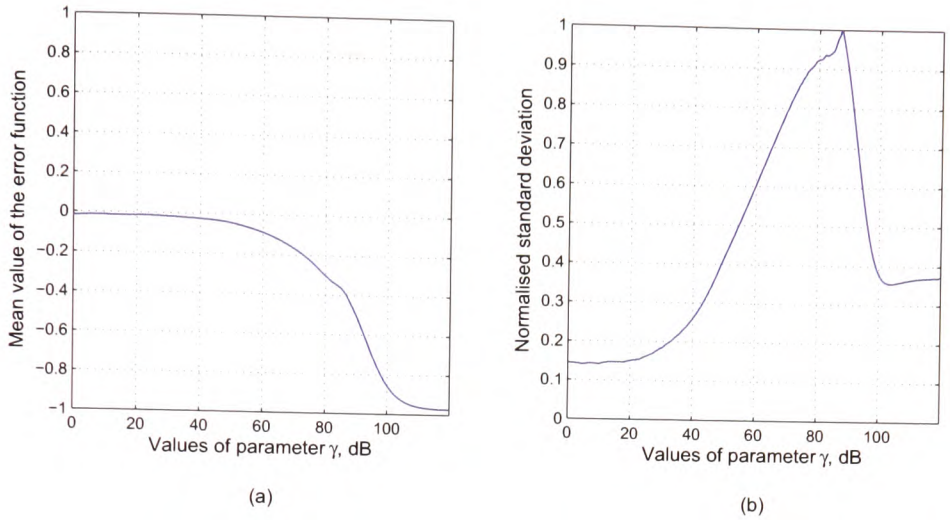

Figure 8.6: Calculated (a) mean and (b) normalised standard deviation of the error function

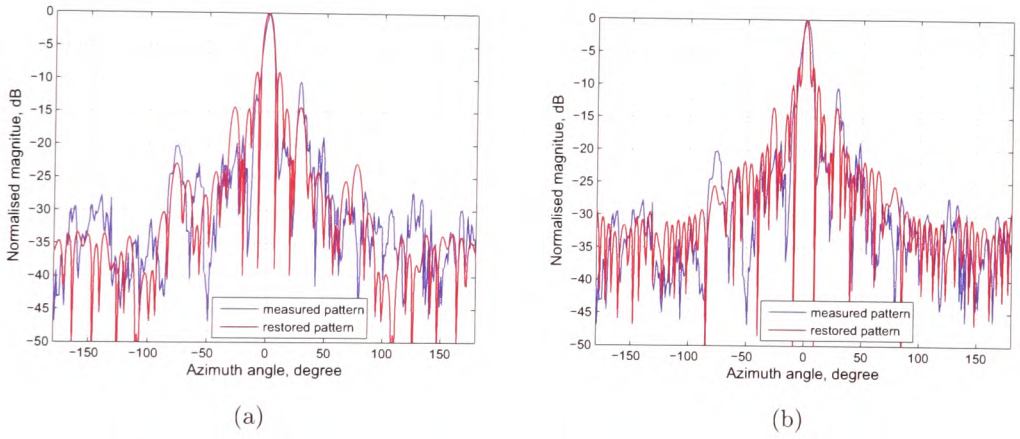

Figure 8.7: Restored patterns with (a) $\gamma_{mean} = 22.99\,dB$ and (b) $\gamma_{std} = 4.56\,dB$ overlaid with the measured pattern

In this example, parameter $\gamma_{std} = 4.56\,dB$ is favourable over $\gamma_{mean} = 22.99\,dB$. Similarly to the example presented in subsection 8.1.1, the phase function is expected to be slightly narrower than its associated measured pattern due to the convolution with the relatively narrow beamwidth radiation pattern of the Lens horn used, as is the case with the restored pattern shown in Fig. 8.7b). The pattern shown in Fig. 8.7a) on the other hand is of the same beamwidth as the original measurement and can therefore not have resulted from a convolution with an antenna radiation

pattern. Fig. 8.8 shows the chosen deconvolution result overlaid with a least rms error fitted calculation phase function, Eq. 5.1. Parameters α and β are again extracted from this result.

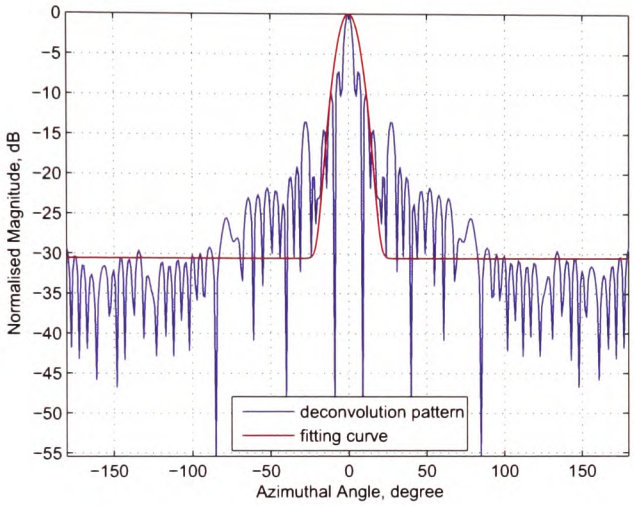

Figure 8.8: Restored pattern $\gamma_{std} = 4.56\,dB$ overlaid with best fit phase function curve

Parameter extraction results

The process described above has been applied to all directional spectra measured in this project at both frequencies, 20 and 40 GHz, and for all antennas used. The optimal values of parameters γ were determined and the restored patterns have been used to extract the values for the RET input parameters α and β. Table 8.3 summarises the results for the 20 GHz measurements and Table 8.4 for the 40 GHz measurements using the automated regularisation technique.

Receiver antenna	α	β	$\beta * 1.67$
20 dBi Gauss horn	0.98	23^o	38.4^o
20 dBi standard gain horn	0.87	16.5^o	27.6^o
15 dBi standard gain horn	0.46	15.5^o	25.9^o
10 dBi standard gain horn	0.86	23^o	38.4^o

Table 8.3: Extraction of parameters α and β from restored patterns for different receiver antennas at 20 GHz

Receiver antenna	α	β	$\beta * 1.67$
29 dBi Lens horn	0.83	7.5^o	12.5^o
20 dBi standard gain horn	0.90	13.5^o	22.6^o
15 dBi standard gain horn	0.38	15^o	25.1^o
10 dBi standard gain horn	0.83	22.5^o	37.6^o

Table 8.4: Extraction of parameters $\alpha$and β from restored patterns for different receiver antennas at 40 GHz

Using the automated regularisation technique it was observed that for the wider beamwidth antenna, 10 and 15 dBi standard gain horns, values for γ_{std} exceed 100 dB. This would lead to extremely wide beamwidth in the restored pattern, therefore when γ_{std} reached these large values it was not used to generate a restored phase function pattern, only γ_{mean} was used. The explanation for these high values is found in the circumstance that wider antenna patterns will lead to curves with very narrow beamwidths in the transform domain. This results in the nonzero values of the term ω^4 being very small. In the transfer function for the automated regularisation technique $F(\omega) = \frac{|X(\omega)|^2}{|X(\omega)|^2+\gamma\omega^4}$, γ needs to assume large values in order to counterbalance the term ω^4 to avoid $F(\omega)$ approaching unity, which would result in an all pass filter. Very narrow beamwidths in the transform domain may also result in a loss of information as described in section 6.3 and are therefore undesirable.

8.2 Performance evaluation of the two implemented deconvolution techniques

Performance of both implemented iterative transform-domain deconvolution techniques is evaluated in this section. A comparison of the two technique's performances is carried out using computer generated signals with different levels of additive white noise at various beamwidths and shapes. Computer generated signals are used since this provides the precise information being available for all the input and the output data throughout the convolution and deconvolution operation. Hence, the information can be used to judge the quality of restored patterns by comparing with them

in graphics and calculating *rms* error between restored patterns and the computer-generated input signal. Moreover, beamwidths, shapes and Signal-to-Noise Ratio of these computer generated signals can be well controlled to closely resemble actually measured patterns in this project in order to better serve this evaluation.

8.2.1 Evaluation with variable additive white noise

Two computer generated signals representing the receiver antenna radiation pattern and phase function pattern are used as the test signals in this evaluation. Effects of random noise are evaluated by adding different levels of computer generated white noise to the convolution product of the two aforementioned signals. The computer generated Gaussian curve has a beamwidth = 14^o as shown in Fig. 8.9a), which is about the same as that of the 20 dBi Gaussian horn antenna at 20 GHz used in this project. The beamwidth of the computer generated phase function is set to 36^o, about two and half times as wide as the computer generated Gaussian curve as shown in Fig. 8.9b). These assigned values for beamwidths are consistent with the assumptions detailed in the RET theory in [16].

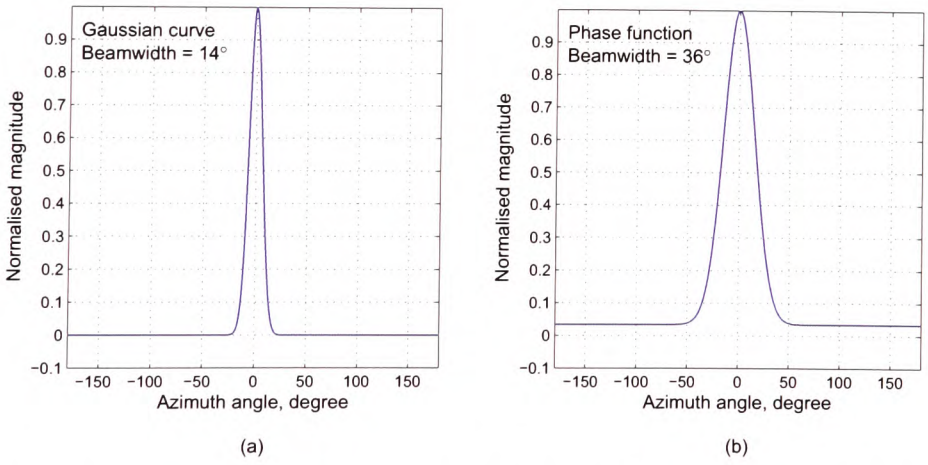

Figure 8.9: Computer-generated input signal patterns: (a) Gaussian antenna radiation pattern and (b) phase function pattern

Two cases are considered here, a signal with relatively high noise level at SNR = 10 dB shown in Fig. 8.10a) and a lower noise level signal at SNR = 30 dB shown in Fig. 8.10b). Both deconvolution techniques were investigated using the computer

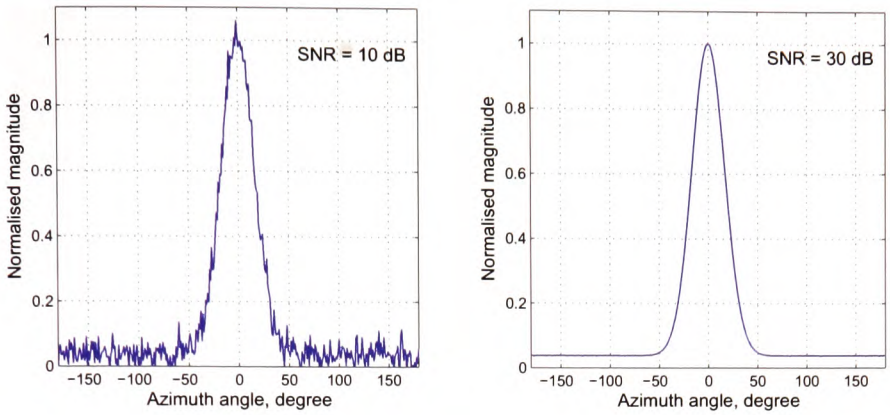

Figure 8.10: Computer-generated noises with (a) SNR = 10 dB and (b) SNR = 30 dB

generated signals with these two levels of added noise, *i.e.* 10 and 30 dB. The procedure applied is as follows:

1. The Bennia-Riad criterion is implemented to yield an approximate optimal range for the filter's parameters λ or γ, for instance, $-10\,dB \sim +50\,dB$.

2. The optimal range is extended to relatively large values up to a range of $-100\,dB \sim +120\,dB$. This ensures the optimal values for parameter λ or γ will never fall outside the extended range.

3. The associated standard deviation or mean value is calculated for the corresponding error function and the minimum is located.

    - Optimum compensation deconvolution application

      The optimum compensation technique requires determination of the optimal value for the parameter λ (section 8.1.1), which occurs at minimum standard deviation of its corresponding error function. This is demonstrated in Fig. 8.11 for an SNR = $10dB$ and Fig. 8.12 for an SNR = $30dB$. For this run λ values are determined as 18.2 dB for SNR = 10 dB and 3.4 dB for SNR = 30 dB. Part b) in both Figs. 8.11 and 8.12 shows an expanded view of the region where the minimum occurs.

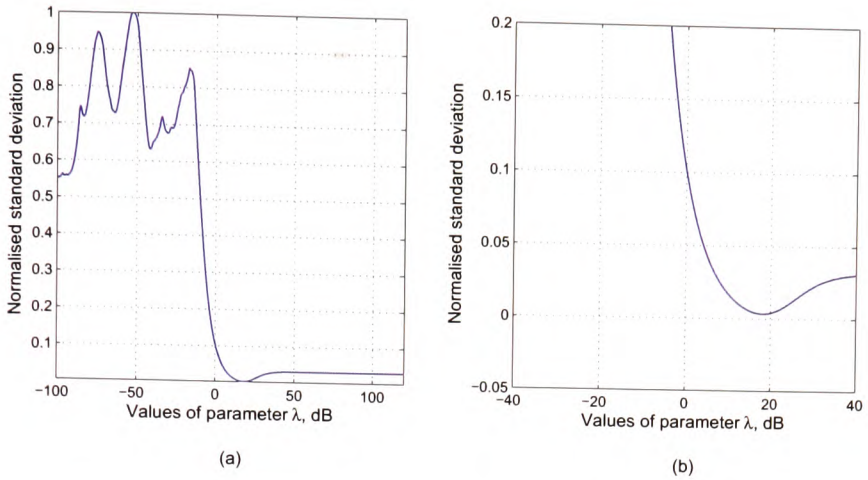

Figure 8.11: Using the optimum compensation technique: (a) calculated standard deviation *versus* λ for SNR $= 10\,dB$ (b) expanded scale around minimum

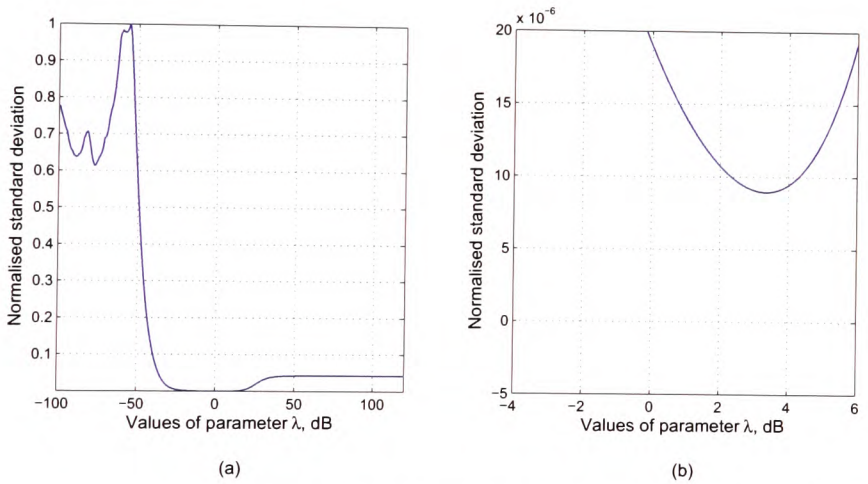

Figure 8.12: Using the optimum compensation technique: (a) calculated standard deviation *versus* λ for SNR $= 30\,dB$ (b) expanded scale around minimum

- Automated regularisation deconvolution application

  The automated regularisation deconvolution also requires a parameter which needs to be optimised, denoted by γ. Meaning and mathematical derivation of this parameter are different to the parameter λ for the optimum compensation as detailed in section 7.3.1, it is however obtained in a similar manner by finding the minimum of the standard deviation of its corresponding error function. Fig. 8.13 shows the variation of the standard deviation with parameter γ for the same signals as before with SNR

$= 10\,dB$, Fig. 8.13b) providing an expanded view of the region around the minimum. Fig. 8.14 shows the result for the same signals with SNR $= 30\,dB$. The values obtained for γ are $46.2\,dB$ at SNR $= 10\,dB$ and $29.3\,dB$ for an SNR $= 30\,dB$ for this example.

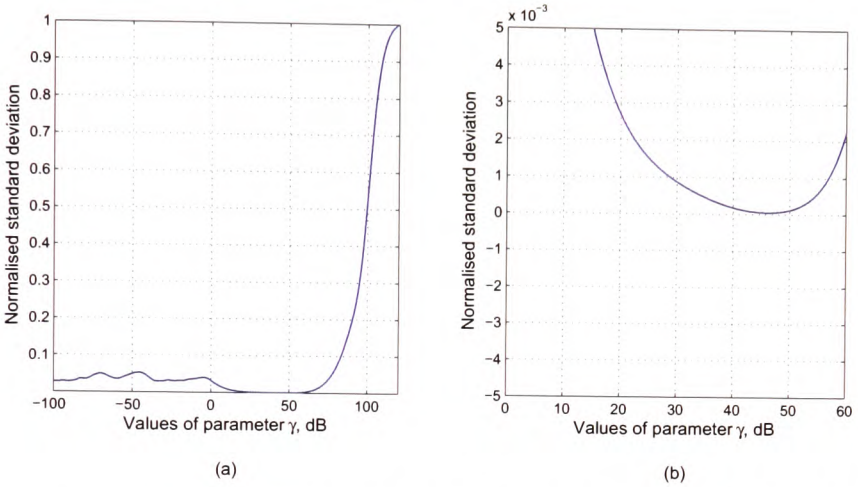

Figure 8.13: Using the automated regularisation technique: (a) calculated standard deviation *versus* γ for SNR $= 10\,dB$ (b) expanded scale around minimum

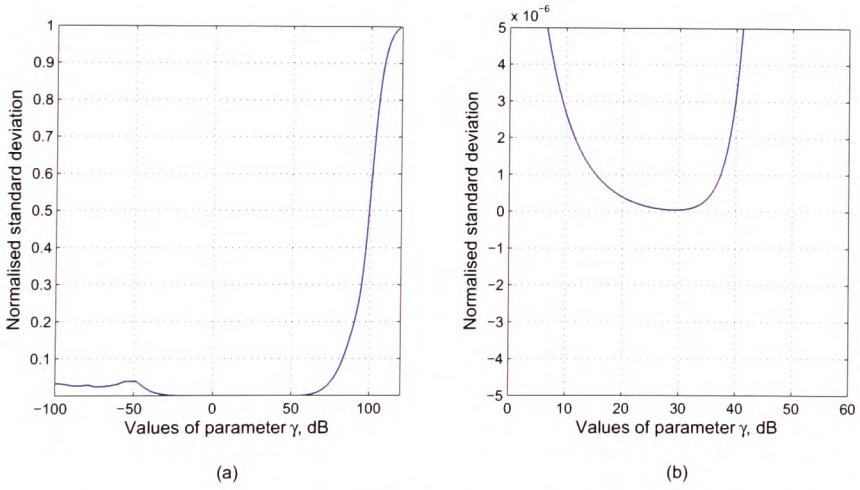

Figure 8.14: Using the automated regularisation technique: (a) calculated standard deviation *versus* γ for SNR $= 30\,dB$ (b) expanded scale around minimum

Using the computer generated antenna radiation pattern and phase function, their convolution provides a pattern similar to the measured phase function, to resemble measured data more closely white noise is added with adjustable SNR. Both the optimum compensation and automated regularisation techniques are applied to the

simulated measurement patterns to restore a phase function from it. This restored phase function is then being compared with the computer generated input phase function. Fig. 8.15 shows the restored phase function compared to the original input for both techniques at 10 dB SNR, Fig. 8.16 compares their errors with the original phase function. Fig. 8.17 and Fig. 8.18 show the respective results for an SNR of 30 dB using the simulated measurement pattern.

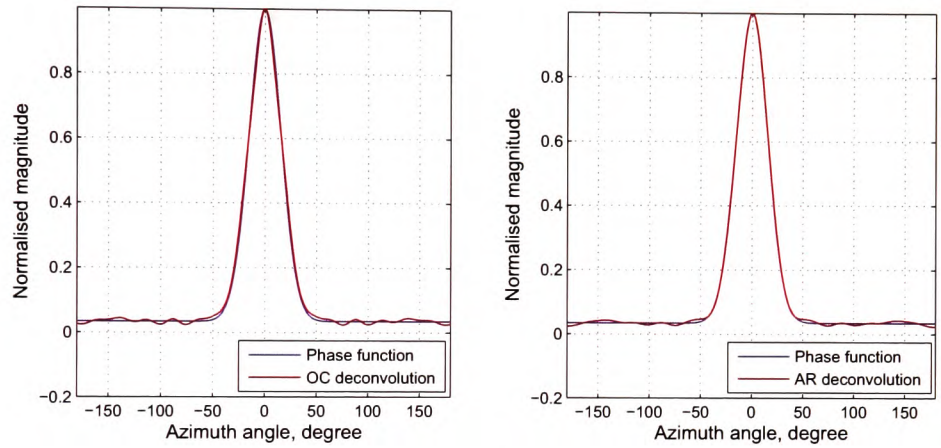

Figure 8.15: Restored phase function patterns at output SNR = 10 dB using: (a) OC and (b) AR overlaid with input phase function for comparison in blue

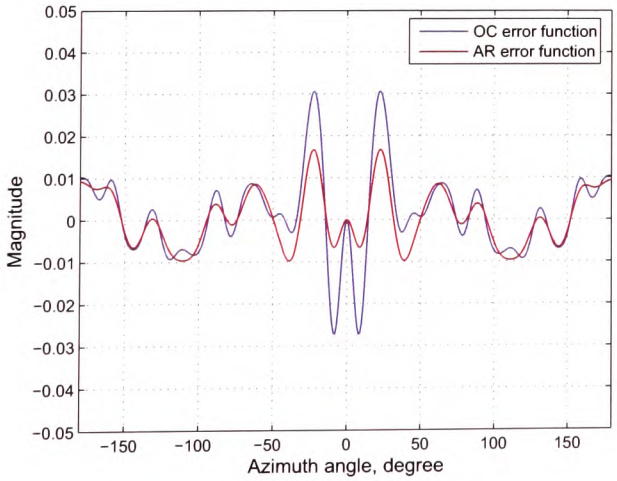

Figure 8.16: Error functions for OC and AR restored phase function at output SNR = 10 dB

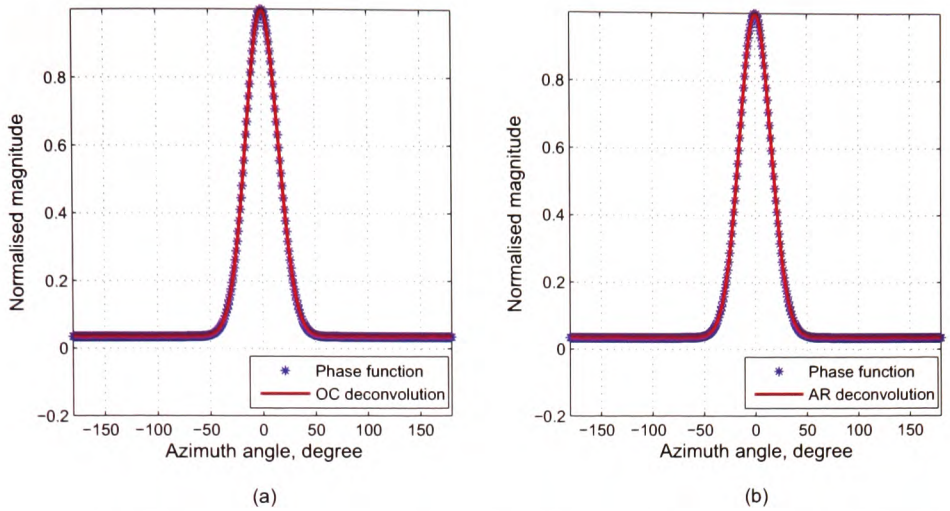

Figure 8.17: Restored phase function patterns at output SNR = 30 dB using: (a) OC and (b) AR overlaid with input phase function for comparison in blue

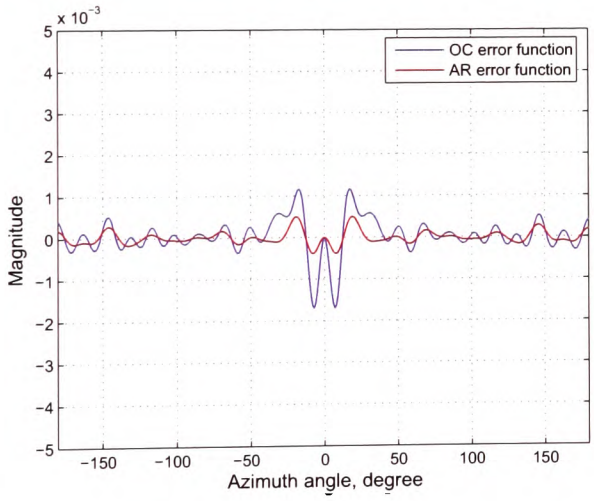

Figure 8.18: Error functions for OC and AR restored phase function at output SNR = 30 dB

The magnitudes in Figs. 8.16 and 8.18 for error functions comparison are normalised values with respect to the maxima in their corresponding convolution patterns with added random noise, *i.e.* they are relative values only. The results show the 'AR' method performed better than the 'OC' method. The maximum magnitude of the error function using optimum compensation can be up to twice as large as the one resulting from using automated regularisation.

8.2.2 Evaluation with various beamwidths and shapes

The previous section illustrated the determination of the parameters λ and γ for the two chosen deconvolution techniques and their performance using a Gaussian signal pattern resembling the 20 dBi Gaussian horn antenna available at 20 GHz. To generalise these findings other signal shapes were also investigated. They were chosen to resemble the antenna radiation patterns of the other antennas used during the experiments. A Gaussian curve with the narrower beamwidth of 8^o resembles the 29 dBi Lens horn antenna radiation patterns used at 40 GHz. Squared Sinc curves were used to resemble the radiation patterns measured for the 20 dBi standard gain horns used in the 20 and 40 GHz measurements. The curves are shown with linear normalised magnitude in Fig. 8.19.

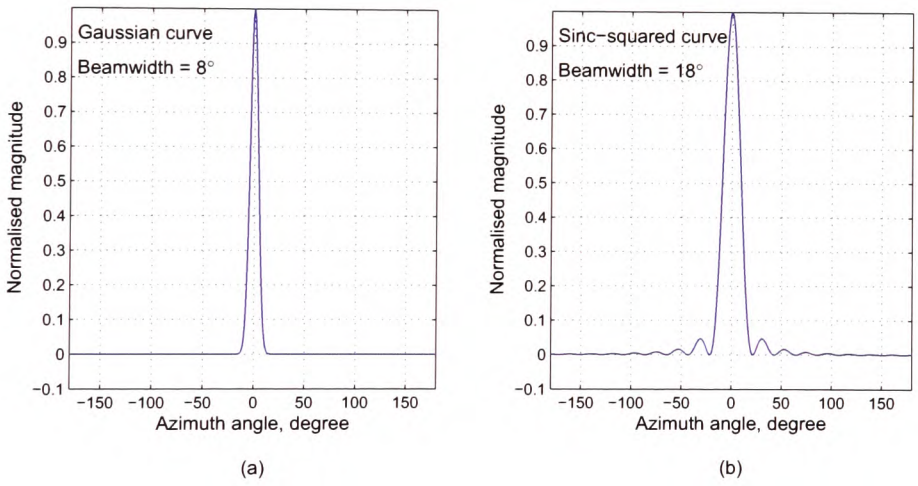

Figure 8.19: (a) Gaussian curve with a beamwidth of 8^o and (b) Squared Sinc curve with a beamwidth of 18^o

This investigation followed the same procedure as detailed in section 8.2.1: optimal values for parameters λ and γ were determined at two different signal to noise ratios (SNR) for three different curve shapes. The values found for λ are summarised in Table 8.5 and for γ in Table 8.6. Again the error functions between the output of each deconvolution method and their input functions were compared. The results are shown in Fig. 8.20 for an SNR $= 10\,dB$ and in Fig. 8.21 for an SNR $= 30\,dB$.

Receiver antenna	Parameter λ for SNR = 10 dB	Parameter λ for SNR = 30 dB
Gaussian curve (beamwidth = 8^o)	21.7 dB	4.2 dB
Gaussian curve (beamwidth = 14^o)	15.0 dB	2.9 dB
Sinc-squared curve (beamwidth = 18^o)	15.7 dB	-3.7 dB

Table 8.5: Determined optimal value for parameter λ in the optimum compensation technique

Receiver antenna	Parameter γ for SNR = 10 dB	Parameter γ for SNR = 30 dB
Gaussian curve (beamwidth = 8^o)	44.7 dB	27.1 dB
Gaussian curve (beamwidth = 14^o)	45.0 dB	29.8 dB
Sinc-squared curve (beamwidth = 18^o)	41.7 dB	20 dB

Table 8.6: Determined optimal value for parameter γ in the automated regularisation technique

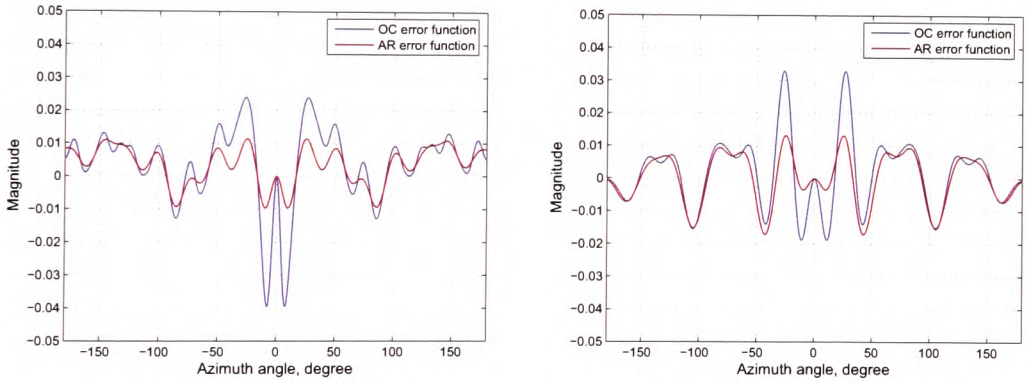

(a) (b)

Figure 8.20: Comparison of the error functions for two deconvolution techniques at SNR = 10 dB. The receiving pattern is: (a) Gaussian curve, beamwidth = 8^o and (b) Squared Sinc curve, beamwidth = 18^o.

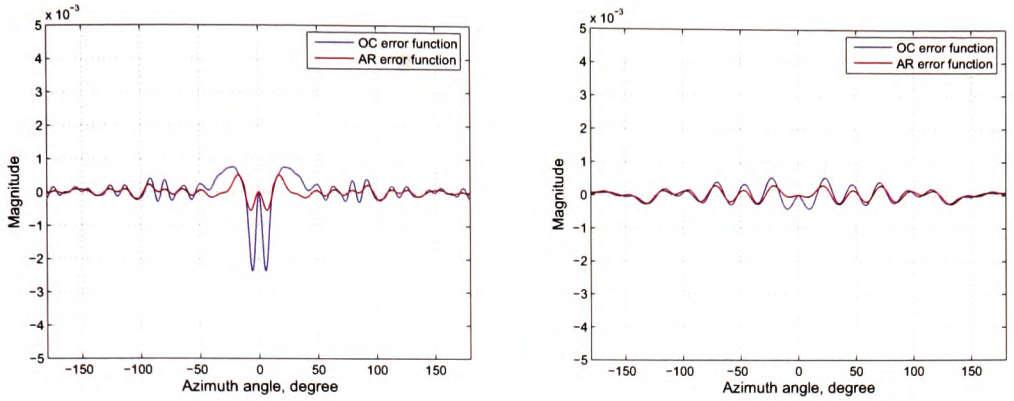

Figure 8.21: Comparison of the error functions for two deconvolution techniques at SNR = 30 dB. The receiving pattern is: (a) Gaussian curve, beamwidth = 8^o and (b) Squared Sinc curve, beamwidth = 18^o.

Summarising the findings of this investigation it is obvious that the automated regularisation technique provides results with smallest errors in all examples chosen, although the difference of the errors between the two methods decreases when the beamwidth increases and when using the squared Sinc function. To explore this further the investigation was expanded to squared Sinc signal patterns with beamwidths of 38^o and 62^o, which resemble the 15 and 10 dBi standard gain horn antenna radiation patterns. The results are again shown for an SNR = 10 dB in Fig. 8.22 and for SNR = 30 dB in Fig. 8.23.

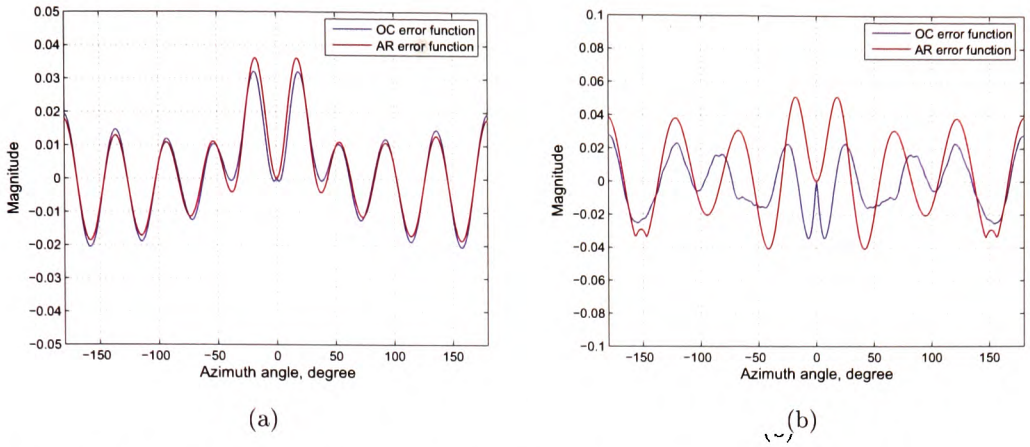

Figure 8.22: Comparison of the error functions for two deconvolution techniques at SNR = 10 dB. The receiving pattern is squared Sinc curve with a beamwidth (a) 38^o and (b) 62^o

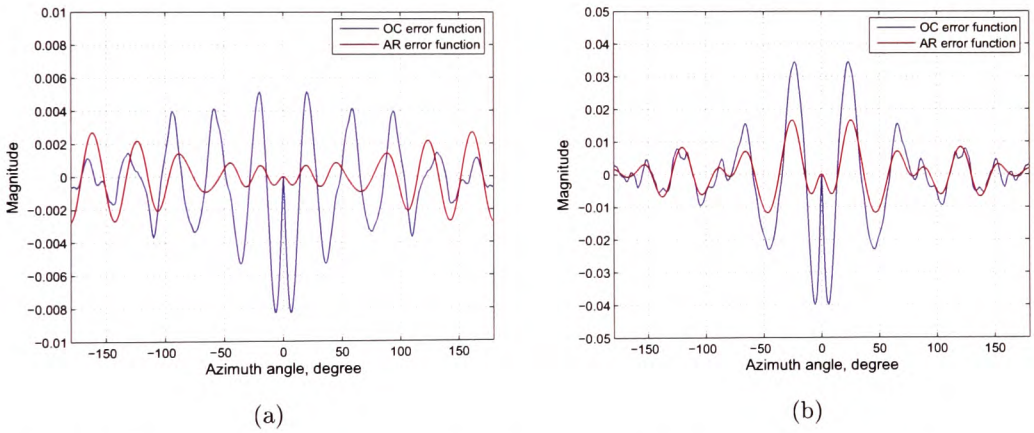

Figure 8.23: Comparison of the error functions for two deconvolution techniques at SNR = 30 dB. The receiving pattern is squared Sinc curve with a beamwidth (a) 38^o and (b) 62^o

Using the wider beamwidths antennas and comparing the results shown in Figs. 8.22 and 8.23 with the previous results it becomes obvious that while the automated regularisation performs generally better than the optimum compensation method this reverses only for wider beamwidth signals with large SNR, since even for wider beamwidth the automated regularisation technique yields better results if the signal to noise ratio is small.

Closer examination of the filtering techniques in accordance with [96] of the two techniques may explain some of the performance behaviour observed above. The

optimum compensation deconvolution technique uses a form of adaptive filtering ensuring the signal content coincides with the passband whereas the noise content of the signal is mainly found in the stopbands of the filter. The automated regularisation technique on the other hand deploys mainly a lowpass filter, which does not adapt to signal shapes. The shortfalls of the automated regularisation technique become obvious by rewriting Eq. 6.45 into the form:

$$F_{opt}(\omega) = \frac{\frac{|X(\omega)|^2}{\gamma\omega^4}}{\frac{|X(\omega)|^2}{\gamma\omega^4} + 1} \tag{8.1}$$

where $|X(\omega)|$ represents the magnitude of the received signal pattern in the transform domain.

Signal patterns with wider beamwidths in the original domain $x(t)$ will show smaller beamwidth once transformed into $X(\omega)$ due to the inverse proportionality between domains. For low frequencies the term ω^4 assumes relatively small values leading to $\frac{|X(\omega)|^2}{\gamma\omega^4} \gg 1$. Consequently $F_{opt}(\omega)$ will approach unity, therefore representing an all pass filter resulting in poor noise reduction.

8.3 Improvements gained using pre-filtering techniques

Examining both the measured antenna radiation patterns and the measured directional spectra curves it is appeared that both are not particularly smooth curves. Their rapid amplitude variation with rotation angle can be considered a form of noise content. Reducing this noise content without losing too much of the overall information in the signal curves prior to deconvolution will therefore be advantageous for the performance of the deconvolution process and the quality of the recovered patterns. The pre-filtering technique found to be useful in this context is the auto/cross-correlation.

To apply pre-filtering both sides of equation 3.55 are convolved with the same expression. The expression used is the antenna radiation pattern, which has been reversed in direction around rotation angle $\theta = 0$, *i.e.* $g_{RX}(-\theta)$. Convolution of both sides of Eq. 3.55 in the original domain with $g_{RX}(-\theta)$ yields:

$$i(\theta) * (g_{RX}(\theta) * g_{RX}(-\theta)) = p_{RX}(\theta) * g_{RX}(-\theta) \tag{8.2}$$

The Left-Hand Side (LHS) contains the auto-correlation $g_{RX}(\theta) * g_{RX}(-\theta)$, whereas the Right-Hand Side (RHS) presents the cross-correlation $p_{RX}(\theta) * g_{RX}(-\theta)$. This operation does not affect the phase function pattern $i(\theta)$, hence there is no loss of information. The Fourier Transform of Eq. 8.2 results in:

$$I(\omega)\,(G_{RX}(\omega)G^*_{RX}(\omega)) = P_{RX}(\omega)G^*_{RX}(\omega) \tag{8.3}$$

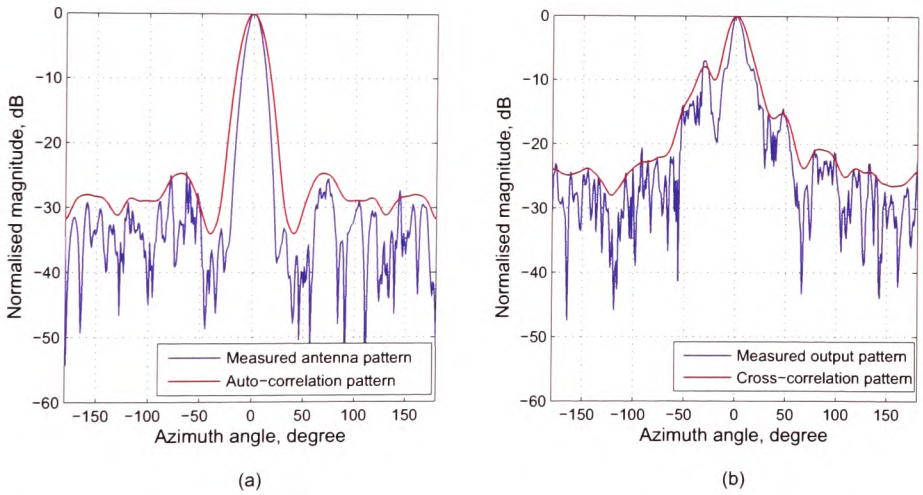

Figure 8.24: Effect of pre-filtering on the measured patterns using (a) auto-correlation of the antenna radiation pattern and (b) cross-correlation of the measured directional spectrum

Fig. 8.24a) shows the application of the auto-correlation pre-filter applied to the measured antenna radiation pattern of the 20 dBi Gaussian horn antenna at 20 GHz. Fig. 8.24b) demonstrates the cross-correlation pre-filter applied to the correspondingly measured directional spectrum recorded at 20 GHz. The new patterns of

$g_{RX}(\theta) * g_{RX}(-\theta)$ and $p_{RX}(\theta) * g_{RX}(-\theta)$ have become much smoother curves, which is advantageous for the deconvolution operation.

In addition the auto/cross-correlation pre-filtering technique helps convergence and provides noise reduction. The expression $G_{RX}(\omega)G^*_{RX}(\omega)$ in Eq. 8.3 will always be positive, this ensures convergence of the iterative transform domain methods while also increasing the rate of convergence [27,94,101,104]. Furthermore, random noise on the measurements will be significantly reduced as demonstrated by the now much smoother patterns in Fig. 8.24. The cross-correlation of $p_{RX}(\theta) * g_{RX}(-\theta)$ will reduce the effect of random signal fluctuations between the two patterns and hence provide a noise reduction yielding better deconvolution results. The auto-correlation of the LHS of Eq. 8.2 will in effect make the resulting pattern from the antenna radiation measurement symmetrical with respect to $\theta = 0^o$, which also improves deconvolution results.

Figs. 8.25 and 8.26 show two examples of restored phase function patterns, comparing the results with and without pre-filtering. Fig. 8.25 compares the influence of pre-filtering, when using optimum compensation deconvolution, whereas Fig. 8.26 illustrates the pre-filtering influence, when using the automated regularisation method. Both examples are for a 20 dBi Gaussian horn antenna at 20 GHz in measurement position 1. Extracted RET input parameters α and β using all 4 methods are summarised in Tables 8.7 and 8.8 in subsection 8.4.1.

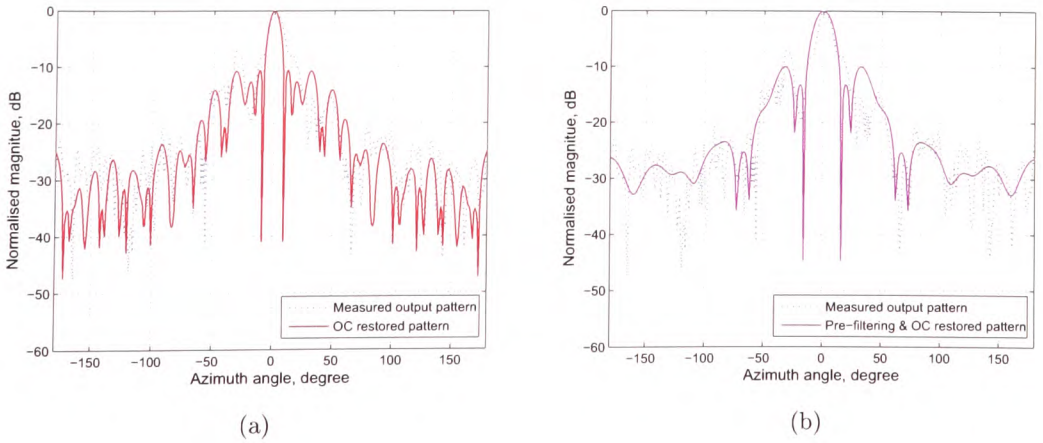

(a) (b)

Figure 8.25: Restored patterns (a) without and (b) with pre-filtering using optimum compensation method

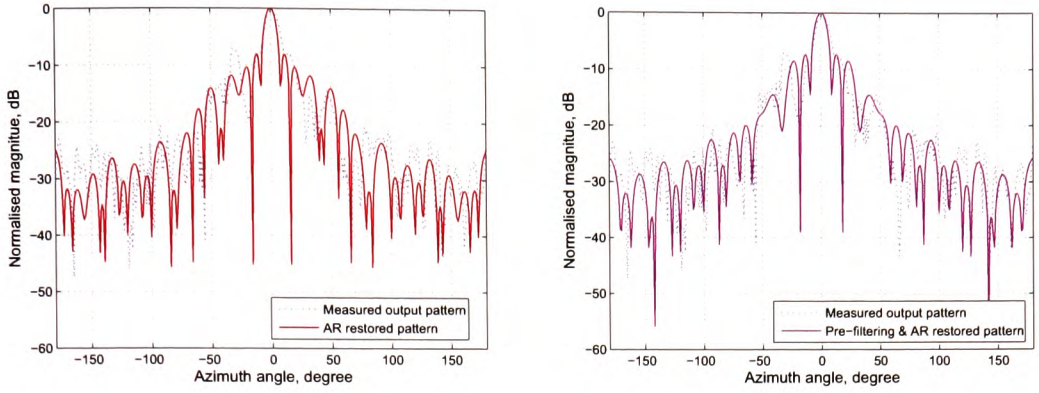

(a) (b)

Figure 8.26: Restored patterns (a) without and (b) with pre-filtering using automated regularisation method

Due to the noise reduction provided by the pre-filtering the ranges for determining the parameter λ or γ using the Bennia-Riad criterion increase compared the non-prefiltered cases. However the decision criteria for determining λ or γ as described in subsections 8.1.1 and 8.1.2 still hold and will provide valid values. The increase in the range for λ or γ may be considered a disadvantage of the pre-filtering, however it is outweighed by the improvements made to the deconvolution results.

8.4 Improvement of RET input parameter extracting using deconvolution

This section will demonstrate how the RET input parameter extraction is improved using deconvolution. It also compares the result between the different methods presented in this thesis as well as comparing them to RET parameters extracted directly from measurement data without any deconvolution. Results for five different cases are demonstrated: RET input parameter extracted from: (a) directly measured patterns; (b) restored patterns using optimum compensation deconvolution; (c) restored patterns using automated regularisation deconvolution; (d) restored patterns using optimum compensation deconvolution with the auto/cross-correlation pre-filtering technique and (e) restored patterns using automated regularisation deconvolution

with the auto/cross-correlation pre-filtering technique.

As outlined in section 3.7 the input parameters α and β can and should be determined from the phase function or a directional spectra measurement avoiding the determination of 4 independent parameters from the same measurement. The remaining parameters k_e and albedo W can then be determined using the excess attenuation with vegetation depth measurements. Section 8.4.1 compares extracted values for α and β using the 5 methods outlined above. Section 8.4.2 lists the results for the extraction of parameters k_e and albedo using the same 5 methods. A comparison of the accuracy of RET prediction results using the parameters extracted with the 5 methods described above is presented in section 8.4.3.

8.4.1 Extraction of the parameters α and β

In subsection 8.4.1, optimal values for parameters α and β are extracted for all available measured data at measurement position 1 at both 20 and 40 GHz. The measurement geometry is illustrated in Figs. 5.9 and 5.10. Successful implementation has been demonstrated for the two iterative deconvolution methods: optimum compensation and automated regularisation. Either has been used to extract values of α and β directly from measured pattern, restored patterns after deconvolution application without and with pre-filtering technique.

Extracted values of parameters α and β are summarised in Table 8.7 for all measured data at both 20 and 40 GHz using the optimum compensation method and in Table 8.8 using the automated regularisation method.

		Direct		OC		Prefilter & OC	
		α	β	α	β	α	β
20 GHz	20 dBi Gauss horn	0.96	21^o	0.98	22.5^o	0.96	22.5^o
	20 dBi standard gain horn	0.82	13.5^o	0.92	26^o	0.89	19.5^o
	15 dBi standard gain horn	0.53	12^o	0.38	9^o	0.49	17^o
	10 dBi standard gain horn	0.81	23.5^o	0.16	7^o	0.9	28.5^o
40 GHz	29 dBi Lens horn	0.79	5.5^o	0.95	12^o	0.9	8^o
	20 dBi standard gain horn	0.85	11.5^o	0.67	9^o	0.92	16^o
	15 dBi standard gain horn	0.85	27.5^o	0.41	13^o	0.9	40.5^o
	10 dBi standard gain horn	0.85	24.5^o	0.66	13.5^o	0.87	27.5^o

Table 8.7: Extracted values of parameters α and β from measurement data directly and using optimum compensation technique without and with prefilter

		Direct		AR		Prefilter & AR	
		α	β	α	β	α	β
20 GHz	20 dBi Gauss horn	0.96	21^o	0.98	23^o	0.83	11.5^o
	20 dBi standard gain horn	0.82	13.5^o	0.87	16.5^o	0.89	20^o
	15 dBi standard gain horn	0.53	12^o	0.46	15.5^o	0.39	17^o
	10 dBi standard gain horn	0.81	23.5^o	0.86	23^o	0.89	34^o
40 GHz	29 dBi Lens horn	0.79	5.5^o	0.83	7.5^o	0.98	16^o
	20 dBi standard gain horn	0.85	11.5^o	0.9	13.5^o	0.79	15^o
	15 dBi standard gain horn	0.85	27.5^o	0.38	15^o	0.86	39^o
	10 dBi standard gain horn	0.85	24.5^o	0.83	22.5^o	0.81	22^o

Table 8.8: Extracted values of parameters α and β from measurement data directly and using automated regularisation technique without and with prefilter

From the RET theory it is expected that the phase function is dependent only on the vegetation medium and independent of the antenna radiation pattern, as opposed to the directional spectrum, which widens for wider antenna beamwidth. Expectation therefore are that after reducing the effects of the antenna radiation pattern from the directional spectra measurements, the extracted values for α and β will be relatively similar for different antenna beamwidth. Tables 8.7 and 8.8 however do still show clear variation in extracted values especially towards the larger beamwidths antennas.

There is also a performance difference between the different deconvolution methods. It has to be considered that there may be a loss of information as described

in section 6.3 when the antenna radiation pattern beamwidth as well as the measured directional spectrum become wider while at the same time the expected phase function beamwidths representing the unknown quantity remains relatively narrow in beamwidth. From a practical perspective, wider beamwidth antennas also result in multipath components arising within the vegetation medium from large branches and trunks as well as possible lateral components and possible contributions from outside the vegetation medium, in this case the anechoic chamber walls, leading to unaccounted contributions being more likely to influence the measurement results. The next section attempts to show the degree of RET prediction improvement gained with the optimised input parameters.

8.4.2 Extraction of the remaining RET input parameters

The remaining RET input parameters, which need to be established from measurement, apart from α and β are the extinction coefficient k_e, measured in $^{dB}/_{m}$, and the albedo, which determines ratio between scattered and absorbed energy inside the vegetation medium. The extraction of the RET parameter is described in subsections 3.7.1 to 3.7.3. The example shown here follows those procedures.

This subsection lists the extracted RET parameters for 2 example cases, these are two measurements undertaken with a 20 dBi Gaussian horn antenna at 20 GHz with beamwidth $\Delta\gamma_R = 7.8^o$ and a 29 dBi Lens horn antenna with $\Delta\gamma_R = 4.2^o$ at 40 GHz. All 4 parameters are extracted using the 5 methods described in section 8.4, where 'Direct' indicates parameter extraction directly from measured data without deconvolution. 'OC' stands for optimum compensation and 'AR' for automated regularisation. The later methods are also used for the parameter extraction after the data has been prefiltered as detailed in section 8.3 and results for those two cases are given in the last two rows of Tables 8.9 and 8.10.

	α	β	$k_e\,(^{dB}/_m)$	W	$\Delta\gamma_R$
Direct	0.96	21^o	6.78	0.46	7.8^o
OC	0.98	22.5^o	6.78	0.45	7.8^o
AR	0.98	23^o	6.78	0.46	7.8^o
Prefilter & OC	0.96	22.5^o	6.78	0.49	7.8^o
Prefilter & AR	0.83	11.5^o	6.78	0.38	7.8^o

Table 8.9: Extraction of the RET input parameters for measurement with 20 dBi Gaussian horn as receiver at 20 GHz using 5 different methods

	α	β	$k_e\,(^{dB}/_m)$	W	$\Delta\gamma_R$
Direct	0.79	5.5^o	5.23	0.41	4.2^o
OC	0.95	12^o	5.23	0.57	4.2^o
AR	0.83	7.5^o	5.23	0.49	4.2^o
Prefilter & OC	0.9	8^o	5.23	0.48	4.2^o
Prefilter & AR	0.98	16^o	5.23	0.64	4.2^o

Table 8.10: Extraction of the RET input parameters for measurement with 29 dBi Lens horn as receiver at 40 GHz using 5 different methods

8.4.3 Evaluation of accuracy of extracted RET parameters

In order to gain information on the accuracy of the extracted RET parameters, results were obtained for RET simulations for the directional spectra at locations equal to those where measured directional spectra were available. The RET was used to calculate directional spectra using the sets of RET parameters extracted with the 5 methods described in section 8.4. The *rms* error between the simulation for each method and the measurement is used to serve as a measure to assess the accuracy of the extracted RET input parameter. Two example figures of the results are presented here, the remaining result graphs are listed in appendixes D and E, Fig. 8.27 shows the directional spectra measurement at position 1 in the measurement geometry outlined in section 5.2. This is compared with simulation using the 5 sets of RET parameter for each of the 5 extraction methods used. The results are for the 20 dBi Gaussian horn antenna at the receiver side at 20 GHz. Fig. 8.28 shows the corresponding graphs at the same position at 40 GHz using the 29 dBi Lens horn antenna.

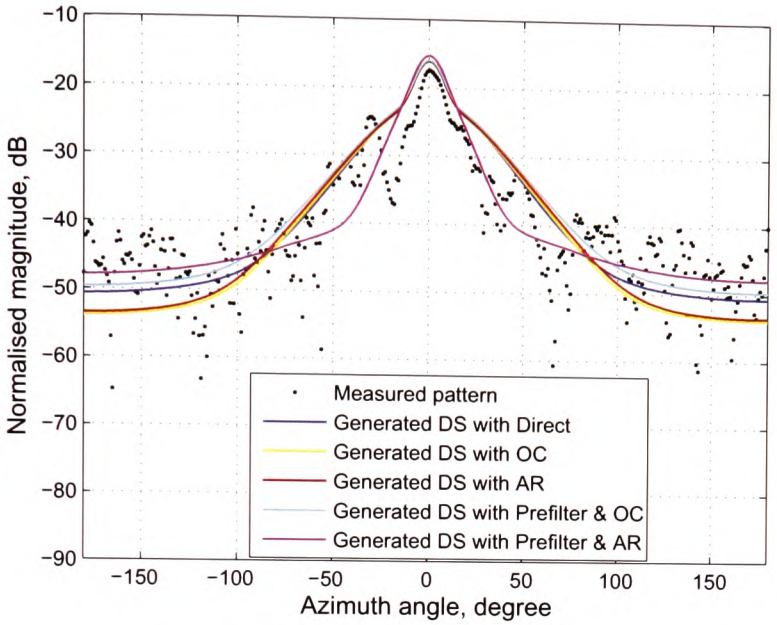

Figure 8.27: Generated directional spectra (DS) using extracted input parameters in accordance with the 5 various cases overlaid with measured directional spectra at measurement Pos. 1, Rx 20 dBi Gaussian horn antenna at 20 GHz

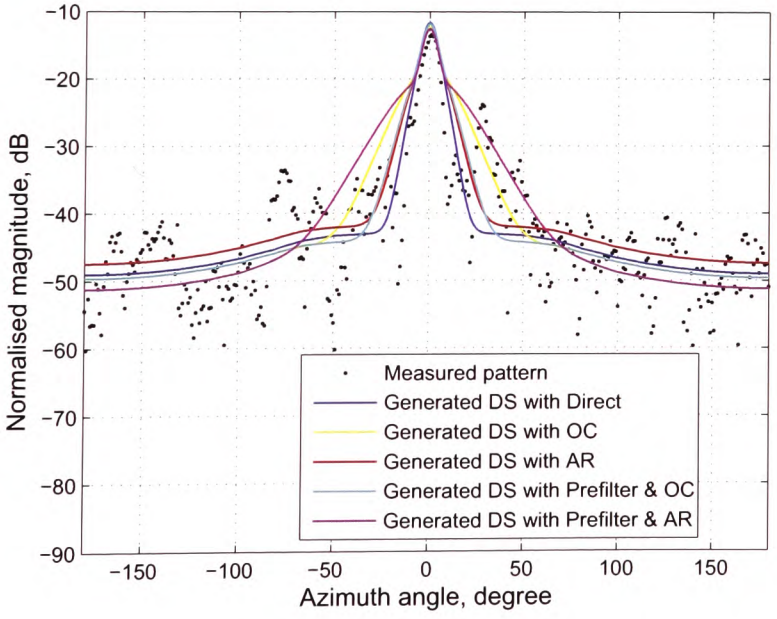

Figure 8.28: Generated directional spectra (DS) using extracted input parameters in accordance with the 5 various cases overlaid with measured directional spectra at measurement Pos. 1, Rx 29 dBi Lens horn antenna at 40 GHz

Rx	20 dBi Gaussian horn, 20 GHz			29 dBi Lens horn, 40 GHz		
	Pos. 1	Pos. 2	Pos. 3	Pos. 1	Pos. 2	Pos. 3
Direct	5.76	7.27	9.13	6.16	10.26	11.84
OC	6.64	7.71	9.61	6.58	9.01	8.38
AR	6.57	7.82	9.58	6.49	11.2	12.57
Prefilter & OC	5.93	7.94	9.45	6.38	9.94	10.18
Prefilter & AR	5.24	5.28	8.86	7.25	9.09	8.22

Table 8.11: Compared RMS errors (dB) from measurements using 5 different methods with receivers: 20 dBi Gauss horn antenna at 20 GHz and 29 dBi Lens horn at 40 GHz

The results summarised in Table 8.11 show deconvolution using the automated regularisation method with pre-filtering provided the minimum RMS error for most of measured patterns except when uses the 29 dBi Lens horn antenna as receiver at 40 GHz and measurement position 1, in which its calculated RMS value indicates the worst case.

	Antennas	Direct	OC	AR	Prefilter & OC	Prefilter & AR
20 GHz	20 dBi Gauss horn	5.76	6.64	6.57	5.93	5.24
	20 dBi standard gain horn	6.49	8.01	6.74	7.03	7.12
	15 dBi standard gain horn	9.04	6.62	7.66	7.06	8.41
	10 dBi standard gain horn	7.79	7.41	7.95	9.15	8.16
40 GHz	29 dBi Lens horn	6.16	6.58	6.49	6.38	7.25
	20 dBi standard gain horn	5.7	5.65	5.97	6.19	6.96
	15 dBi standard gain horn	6.81	6.02	6.6	7.61	7.7
	10 dBi standard gain horn	7.91	7.47	7.83	8.1	7.74

Table 8.12: Compared RMS errors (dB) for all antennas being test at position 1 using 5 different methods

Analysing the results in Table 8.12 it can be observed that the RMS error between measured directional spectra and those calculated with the RET using input parameters extracted using various methods, a reduction in error is not always obvious when using deconvolution compared to the ones using RET parameters extracted without deconvolution (direct). The reason can be found in a principal

difficulty faced when comparing RET prediction results to measurement with real antennas with the accuracy required here. Deconvolution of the antenna pattern for the purpose of the extraction of RET parameters will minimise the effect of the antenna radiation patterns. However the directional spectra prediction using the RET is still based on narrow beamwidth antennas with Gaussian shaped radiation patterns. The measurements of the directional spectra were however conducted using antennas which in the majority do not have Gaussian radiation patterns.

A comparison of measurements conducted with wider beamwidth antennas with non-Gaussian radiation patterns and RET prediction using narrow beam Gaussian antenna patterns will therefore always result in a certain amount of RMS error and can not fully serve to prove the improvement of the prediction due to improved input parameter extraction. However when the Gaussian horn antenna and the Lens horn antenna were used clear improvements in the prediction accuracy using RET parameters extracted after deconvolution and pre-filtering have been applied are demonstrated in Table 8.12. Other factors influencing the RMS error in this comparison are the measurement errors outlined in section 4.5 and the assumption of the RET of an infinite halfspace of homogeneous vegetation (section 3.3), which of course can never be fully provided in a practical measurement set up.

8.5 Summary of final deconvolution procedure

A summary of the final deconvolution procedure based on measured data including pre-filtering is given in the following:

1. The Bennia-Riad criterion is applied to a measured pattern to yield an approximate optimal range for parameter λ or γ. Measured patterns obtained with narrow beamwidth antenna radiation patterns are always favourable. For each specific value of λ or γ in this optimal range, a restored pattern can be generated using the optimum compensation or automated regularisation method.

2. The error function in equation 7.15 serves to determine the optimal values for

λ and γ. Either the minimum standard deviation or the minimum of absolute values of the mean error can be used. This leads to λ_{std} and λ_{mean} as well as γ_{std} and γ_{mean}. The criteria to decide whether to use the minimum standard deviation or absolute minimum of the mean error are given below. It is also useful to point out that the range for possible λ or γ values can be extended at this stage to ensure capture of optimal λ or γ values.

3. With optimal values for λ_{std} and λ_{mean} found, optimum compensation deconvolution can be applied to measured pattern to yield restored patterns. Two restored patterns are generated using λ_{std} and λ_{mean}.

4. The following criteria need to be observed to decide whether to use λ_{std} or λ_{mean} for best results:

   (a) if both restored patterns using λ_{std} or λ_{mean} are wider than the measured pattern, the parameter λ yielding the narrower restored pattern is chosen;

   (b) if one restored pattern is wider than the measured pattern and the other is narrower, the parameter λ yielding the narrower restored pattern is chosen;

   (c) if both restored patterns are narrower than the measured pattern, λ yielding the wider restored pattern is chosen.

5. For the automated regularisation method the statements made in step 3 and 4 apply respectively to determine the optimal values for γ_{std} and γ_{mean}.

6. The deconvolution result can be improved significantly using the pre-filtering technique with auto/cross-correlation. However pre-filtering needs to be applied after step number 2. Steps 3 to 5 are then applied in the same to the prefiltered data resulting in a combination of pre-filtering and deconvolution.

8.6 Chapter summary and interim conclusion

In this chapter performance of both deconvolution methods, optimum compensation and automated regularisation, was evaluated using computer-generated data with added white noise with variable SNR, as well as different signal pattern shapes and beamwidths. Applied to the measured patterns in this project, the automated regularisation method achieved better performance in most cases, in particular when the 20 dBi Gaussian horn of 20 GHz and 29 dBi Lens horn of 40 GHz are used as receiver antennas. Section 8.3 demonstrates the improvement in deconvolution results by pre-filtering based on auto/cross correlation prior to the deconvolution. It is demonstrated that in the majority of cases investigated the automated regularisation deconvolution combined with pre-filtering yield the best results.

The improvement to the RET input parameter extraction using deconvolution will be limited, when the beamwidth of the receiver antenna and consequently that of the directional spectra become very large. The a loss of information as discussed in section 6.3 will occur and additional errors occur in the restoration of the phase function. For very wide beamwidth antennas, the restoration may not be possible at all.

Chapter 9

Conclusion and further work

This chapter has the following purposes: concludes the research work undertaken throughout this project, highlights contributions and proposes possible future work.

9.1 Conclusion of the research work

To effectively predict effects caused by the presence of vegetation in the radio propagation path, accurate models are required. The model used in this research project for the purpose of predicting radiowave propagation through vegetation is the theory of Radiative Energy Transfer. This theory has been developed and investigated by many researchers in the past three decades. The radiowave propagation and system design research unit at the University of Glamorgan has undertaken countless experimental programs to acquire measurements inside and around vegetation that measured results and theoretical prediction could be compared and analysed in order to develop methods to implement the RET in a generic practical prediction model. The measurements showed how important the influence of the receiver antenna radiation pattern on the obtained results is. The RET [16] accounts for the receiver antenna beamwidth, but generalises antennas to have a Gaussian shaped radiation pattern, with very narrow beamwidth. Other antenna pattern than Gaussian shaped one with higher sidelobe levels and wider beamwidths will influence the received signal pattern shape by a convolution of the original shape with that of the antenna radiation pattern. This is particularly important when trying to establish the RET input parameters in experiments, the accuracy of these directly influences any RET

prediction results. Therefore the receiver antenna radiation pattern influence needs to be extracted via a process of deconvolution.

The aim of this research work was to develop deconvolution techniques and implement them on the measured patterns so that true information of the signal patterns can be retrieved. Implementation of various deconvolution techniques has been reported in other fields like Astronomy, Spectrology and Image processing to name only a few. However so far that has been little published on the implementation of deconvolution techniques in the field of radiowave propagation.

9.2 Contributions

9.2.1 Contributions to measurements

This research project concentrated extensively on experimental work. The measured results offer the chance of a closer examination of excess loss with vegetation presence in the radio path. Measurements in the presence of single trees extended results previously obtained at this research unit in the phase function investigation. Measurements in the presence of a downsized forest were designed to investigate directional spectra of the transmitting signal and excess loss versus vegetation depth. Measurements using trees in pairs were designed to study excess loss in the boresight as a function of vegetation depth. All measurements took place in a controlled indoor environment, an anechoic chamber. Great care was taken to obtain good quality measurement data in a time-invariant homogeneous vegetation medium. The measurement geometry for the last two measurements utilised the maximum available physical space of the anechoic chamber.

9.2.2 Contributions to processing of measured signal patterns

Although widely used in other fields, to the author's knowledge, deconvolution techniques have been applied to the area of radiowave propagation in the demonstrated manner for the first time. Deconvolution is a signal processing technique, which in

this context has been utilised to remove signal pattern distortion introduced through antenna radiation pattern characteristics during the measurement. This allows to retrieve information closer to the actual physical signal behaviour of radiowaves influenced by the presence of vegetation in the radio path. The successful implementation of two principal techniques is demonstrated using both computer-generated as well as measured input data. Detailed studies of the implemented techniques are carried out in both the original and the transform domain. The improvement of RET input parameter extraction using deconvolution is clearly demonstrated. Any deconvolution pitfalls and difficulties in the context of this research work are clearly presented in this thesis and will be a vital contribution to any research involving deconvolution. Suggestions for further studies and improvements are listed in section 9.3.

9.2.3 Contributions to literature

It is important to disseminate research finding in the open literature. The author has jointly contributed the following paper to the published literature:

- H. Cui, J. Richter, M. O. Al-Nuaimi, and R. Caldeirinha, "Restoration of the RET Phase Function using Deconvolution," *Proceedings of the 2nd IEEE, NGMAST 2008*, Cardiff, UK, Sept. 2008.

9.3 Recommendation for further studies and future work

This research project has shown successfully how deconvolution techniques can be implemented for the intended purpose of excluding distortion caused by the antenna radiation pattern to measured signal levels. The implemented methods work generally very well, however during the studies areas of further improvement and interest were also discovered, these are:

1. further optimisation of the performance of the two chosen deconvolution techniques in this research project.

2. application of deconvolution to complex input data

3. search for further deconvolution methods including those currently under development.

4. Fourier transform alternatives.

9.3.1 Further optimisation of deconvolution techniques used in this programme

The two deconvolution methods used in this research project both work well in the demonstrated application. However both require an adjustable parameter *i.e.* λ for the optimum compensation and γ for the automated regularisation method. So far the method to determine their values requires some form of decision by an informed user. This process could be automated for a wide range of different input data types in the form of a computer routine. This could also allow users with no or very little knowledge of deconvolution to achieve very good results.

9.3.2 Using complex input data for the deconvolution

The vector form of the RET [18] can describe radiowave propagation through vegetation more accurately than the scalar form although at the cost of far higher complexity. Deconvolution conducted on data that include phase information may also generate more accurate results. The first challenge would be to establish an effective mathematic description of the measurement phase information.

Obtaining measurement data that contain phase information may require the use of a Vector Network Analyser (VNA). Several avenues were investigated during the project to determine suitable measurement set ups [107–109]. Neither of which were found to be immediately applicable to the problem at hand, for the following reasons: [107] requires fixed relationship between measured phase and amplitude, which does

not apply for the vegetation data measurement during this project. [108] presents a complex deconvolution approach for radar pulses, which would need more detailed investigation to assess its applicability to the data in this project, however the author already acknowledge that for increasing amount of sample points the computational effort and the errors raise exponentially. Mu's proposal]109[using the least squares method with point count regularisation claims to be a stable and robust algorithm with excellent results. However Mu indicates possible problems when applying this method to noise RF data. Future studies may be able to find an approval based on a combination of the ones listed above with a particular adaptation to a complex measurement system.

9.3.3 Using alternative deconvolution methods

Many researchers agree that time domain deconvolution promises better results than frequency domain based methods, however that comes at the expense of computational complexity [27, 29, 93, 110]. Jansson reports a time domain based iterative method in [27]. Attempts have been made by the author of this research project to implement the described method. However so far this did not yield generally stable results nor did it provide guaranteed convergence. Convergence would for instance only occur for an even number of iteration but not for odd numbers when Jansson's method was applied to the measurement data obtained during this project. Preliminary analysis suggests that the nature of the measurement data used here is significantly different to the type of data used in Jansson's publication. Some modification to the method or data pre-processing or a combination of both may lead to a successfully generalised implementation of this method.

9.3.4 Fourier Transform alternatives

The deconvolution methods described in this project utilise the Fourier Transform for the transformation between domains. However it may be advantage to investigate deconvolution approaches where other transform methods are being used.

- The measurement data obtained during this research project as well as similar data obtained by other researchers in the field is generally amplitude only information. A transform using real values only such as the Hartley Transform [111[may therefore proof to provide more accurate and faster results when used for deconvolution purposes. Hartley and Fourier Transform can be converted into each other relatively simply [83[.

- Another alternative to Fourier Transform may be the use of Cepstrum analysis [112[. This non-linear technique uses a combination of natural logarithm and Fourier Transform. The well known advantage of using the Convolution Theorem and Fourier Transform is to simplify the convolution operation in the original domain by transforming into a multiplication in the transform domain. Cepstrum analysis takes this advantage further by transforming a convolution operation into a summation.

Bibliography

[1] J. D. Krauss, *Antennas*, 2^{nd} edition, McGraw Hill, 1988.

[2] *Nobel Lectures*, vol. Physics 1901 - 1921, Elsevier Publishing Company, 1976.

[3] C. A. Balanis, *Advanced Engineering Electromagnetics*, John Wiley & Sons, 1989.

[4] J. D. Kraus, *Electromagnetics: with applications*, 5^{th} edition, WCB/McGraw-Hill, 1999.

[5] W. Webb, *Wireless Communications: the future*, John Wiley, 2007.

[6] J. Gozalvez, "HSDPA goes commerical", IEEE Vehicular Technology Magazine, vol. 1, no. 1, pp. 43-53, March 2006.

[7] R. Tafazolli, *Technologies for the Wireless Future: Wireless World Research Forum (WWRF)*, John Wiley & Sons, 2005.

[8] R. Tafazolli, *Technologies for the Wireless Future: Wireless World Research Forum (WWRF)*, volume 2, John Wiley & Sons, 2006.

[9] Spectrum planning for the London 2012 Olympic Games and Paralymic Games, Ofcom, http://www.ofcom.org.uk/consult/condocs/spectrum2012 access, May, 2008.

[10] Satellite Systems Operating Above 10 GHz, Ofcom, http://www.ofcom.org.uk/research/technology/research/ese/above10/, access: May, 2008.

[11] Broadband Fixed Wireless Access in the 28 GHz and 40 GHz Bands, Ofcom, http://www.ofcom.org.uk/static/archive/ra/topics/bfwa/doc28ghz.htm, access: May, 2008.

[12] R. F. S. Caldeirinha, *Radio characterisation of single trees at micro- and millimeter wave frequencies*, PhD thesis, University of Glamorgan, 2001.

[13] N.C. Rogers, A. Seville, J. Richter, D. Ndzi, N. Savage, R. Caldeirinha, A.K. Shukla, M.O. Al-Nuaimi, E. Vilar and J. Austin, "A Generic Model of 1-60 GHz Radio Propagation through Vegetation-Final report", Tech. Rep., Radiocommunications Agency, May 2002.

[14] T. R. C. C. Fernandes, *A Discrete RET Model for Micro- and Millimeter Wave propagation through Vegetation*, PhD thesis, University of Glamorgan, 2007.

[15] H. Bertoni, *Radio Propagation for Modern Wireless Systems*, Prentice Hall, 2000.

[16] R. A. Johnson, and F. K. Schwering, "A Transport Theory of Millimeter Wave Propagation in Woods and Forests", Tech. Rep. CECOM-TR-85-1, Forth Monmouth, 1985.

[17] A. Ishimaru, *Wave Propagation and Scattering in Random Media*, IEEE Press, 1997.

[18] L. Tsang, J. A. Kong, and K. Ding, *Scattering of Electromagnetic Waves: Theories and Applications*, John Wiley & Sons, 2000.

[19] J. Richter, R. Caldeirinha, and M. Al-Nuaimi, "A generic narrow model for radiowave propagation through vegetation", *in Proceedings of the IEEE 61st Vehicular Technology Conference, VTC 2005-Spring*, vol.1, pp.39-43, 2005.

[20] A. K. Shukla, A. Seville, D. Ndzi, J. Richter, and D. Eden, "Description of a Generic Vegetation Attenuation Model for 1-60GHz", COST 280, 1stInternational Workshop, July, 2002.

[21] M. O. Al-Nuaimi and A. M. Hammoudeh, "Attenuation functions of microwave signals propagated through trees", IEE Electronics Letters, vol. 29, no. 14, pp. 1307-1308, July 1993.

[22] M. O. Al-Nuaimi and R. B. L. Stephens, "Measurements and predictions model optimization for signal attenuation in vegetation media at centimeter wave frequencies", *IEE Proceedings - Microwaves, Antennas and Propagation,* vol. 145, pp. 201 -206, June 1998.

[23] M. O. Al-Nuaimi and A. M. Hammoudeh, "Influence of vegetation on attenuation of radiowave signals in the X-band frequency region", COST 235 TD, CP 149, June 1993.

[24] M. O. Al-Nuaimi and A. M. Hammoudeh, "Measurements and predictions of attenuation and scatter of microwave signals by trees", *IEE Proceedings - Microwaves, Antennas and Propagation,* vol. 141, pp.70-76, April 1994.

[25] T. Fernandes, R. F. S. Caldeirinha, M. O. Al-Nuaimi and J. Richter, "A Discrete RET model for millimeter-wave propagation in isolated tree formations", IEICE Transactions on Communications vol. E88-B, no.6, pp. 2411-2418, June 2005.

[26] T. Fernandes, R. F. S. Caldeirinha, M. O. Al-Nuaimi and J. Richter, "A Discrete Model for Radiowave Scattering in Vegetation at Millimetric Wave Frequencies", *Proceeding of IEEE* 15^{th} *International Symposium on Personal, Indoor and Mobile Radio Communications - PIMRC2004,* vol. 1, Barcelona, Spain, September 2004.

[27] P. A. Jansson, *Deconvolution of Images and Spectra,* second edition, Academic Press, 1997.

[28] N. S. Nahman and M. E. Guillaume, "Deconvolution of time domain waveforms in the presence of noise," NBS Tech. note 1047, NBS, Boulder, CO, Oct. 1981.

[29] M. Zhou, *Deconvolution and Signal Recovery,* national defence industry press, Beijing, Mar. 2001.

[30] R. Schmidt, "Multiple emitter location and signal parameters estimation", *IEEE Trans. Antenna Propag.*, AP-34, pp. 276-280, 1986.

[31] R. Roy and T. Kailath "ESPRIT - Estimation of Signal Parameters via Rotational Invariance Techniques", IEEE Trans. Acoustics, Speech, Signal Process., pp. 984-995, 1989.

[32] H. TAKAHIRO, I. KOICHI and A. HIROYUKI, "A Note on the DOA estimation using EM, SAGE algorithm", Institute of Electronics, Information and Communication Engineers, vol. 103, no. 22, pp. 57-62, 2003.

[33] F. de Leon and J. Marciano, "Application of MUSIC, ESPRIT and SAGE Algorithms for Narrowband Signal Detection and Localization", TENCON 2006, IEEE Region 10 Conference, pp. 1-4, Nov. 2006.

[34] M. A. Weissberger, "An Initial Critical Summary of Models for Predicting the Attenuation of Radio Waves by Trees", Tech. Rep. ESD-TR-101, Maryland, 1982.

[35] G. M. Whitman, F. K. Schwering, L. Chen, "A Theory of Millimeter Wave Propagation in Vegetation", Research and Development Technical Report CECOM-TR-84-5, New Jersey, 1984.

[36] L. Tsang, J. A. Kong, K. Ding and C.O. Ao, *Scattering of Electromagnetic Waves: Numerical Simulations,* John Wiley & Sons, 2001.

[37] L. Tsang and J. A. Kong, *Scattering of Electromagnetic Waves: Advanced Topics,* John Wileys & Sons, 2001.

[38] Supplementary Planning Guidance Note 'Telecommunications - A Design Guide', Coventry City Council, Sept. 2005.

[39] Vodafone Comments on Ofcom's Consultation (January 08) on SpectrumUsage Rights (licence verification approaches), Ofcom, Jan.2008.

[40] UK Spectrum Co-ordination Document: Co-ordination of licensed services in the band 3605 to 3689 MHz paired with 3925 to 4009 MHz, OfW188, Ofcom, Jan. 2008.

[41] BT Response to the Ofcom Consultation Document on the Spectrum Framework Review, Ofcom, Feb. 2005.

[42] M. S. Karaliopoulos, and F. N. Pavlidou, "Modelling the land mobile satellite channel: a review", IEE Electronics Communication Engineering Journal vol.11. no.5, Oct. 1999.

[43] M. A. Weissberger, "An initial critical summary of models for predicting the attenuation of radio waves by trees", Tech. Rep. ESD-81-101, Department of Defense, 1982.

[44] R. B. L. Stephens, *A study and modelling of the propagation effects of vegetation on radiowaves at cm-wavelength frequencies*, PhD thesis, University of Glamorgan, 1998.

[45] COST 235, "Radiowave propagation effects on next generation fixed services terrestrial telecommunications systems", Final Report, ISBN 92-827-8023-6, Commission of the European Union, 1996.

[46] R. B. L. Stephens and M. O. Al-Nuaimi, "Attenuation measurements and modelling in vegetation media at 11.2 GHz and 20 GHz", Electron Lett., 31, (20), pp. 1783-1785, 1995.

[47] A. Seville, "Vegetation attenuation: modelling and measurements at millimetric frequencies", in *Proceedings of the 10th International Conference on Antennas and Propagation,* vol. 1, pp. 2.5-2.8, Apr. 1997.

[48] Radiocommunication Assembly, *Recommendation ITU-R P.833-3, Attenuation in vegetation,* ITU-R, 2001.

[49] Radiocommunication Assembly, *Recommendation ITU-R P.526-7, Propagation by diffraction,* ITU-R, 2001.

[50] Radiocommunication Assembly, *Recommendation ITU-R P.833-5, Attenuation in vegetation,* ITU-R, 2005.

[51] CCIR, *CCIR Report 1008-1, Reflection from the surface of ythe earth,* CCIR, 1990.

[52] Radiocommunication Assembly, *Recommendation ITU-R P.527-3, Electrical characteristics of the surface of the earth,* ITU-R, 2000.

[53] F. Schwering, E. Violette, and R. Espeland, "Millimeter-wave propagation in vegetation: experiments and theory", IEEE Transactions on Geoscience and Remote Sensing, vol. 26, no. 3, pp. 355-367, May 1988.

[54] A. K. Fung, *Microwave Scattering and Emission Models and Their Applications,* Artech House, Norwood, Massachusetts, 1994.

[55] F. T. Ulaby and C. Elachi, Eds, *Radar Polarimetry for Geoscience Applications,* Artech House, Norwood, USA, 1990.

[56] D. Didascalou, M. Younis, and W. Wiesbeck, "Millimeter-wave scattering and penetration in isolated vegetation structures", *IEEE Transactions on Geosciemce and Remote Sensing,* vol. 38, pp. 2106-2113, 2000.

[57] B. B. Mandelbrot, *The Fractal Geometry of Nature,* W. H. Freeman & Co., New York, 1983.

[58] P. Prusinkiewicz, and A. Lindenmayer, *The algorithmic beauty of plants,* Springer-Verlag, New YORK, 1990.

[59] A. Lindenmayer, "Mathematical models for cellular interaction in development", parts I and II, Journal of Theoretical Biology, 18, pp. 280-315, 1968.

[60] D. Frijters and A. Lindenmayer, "A model for the growth and flowering of *Aster novae-angliae* on the basis of table (1,0) L-systems" In G. Rozenberg

and A. Salomaa, editors, *L Systems,* Lecture Notes in Computer Science 15, pages 24-52. Springer-Verlag, berlin, 1974.

]61[P. Hogeweg and B. Hesper, "A model study on biomorphological description", *Pattern Recognition,* 6:165-179, 1974.

]62] A. R. Smith, "Plants, fractals, and formal languages". in *Proceedings of SIGGRAPH' 84, Computer Graphics,* 18, 3, pages 1-10, ACM SIGGRAPH, 1984.

[63[H. Abelson and A. A. diSessa, *Turtle geometry,* M.I.T. Press, Cambridge, 1982.

[64] P. Prusinkiewicz, "Graphical applications of L-systems", in *Proceedings of graphics interface' 86 - vision interface'86,* pages 247-253, CIPS, 1986.

[65[G. Cavalcante, and A. Giardola, "Optimisation of radio communications in media with three layers", IEEE Transactions on Antennas and Propagation, vol. AP-31, no.1, pp.141-145, 1983.

[66] S. S. Seker: "Radio pulse transmission along mixed paths in a stratified forest", IEE proceedings, vol. 136, no.1, pp.13-18, February 1989.

[67] L. Li, T. Yeo, P. Kooi, and M, Leong, "Radio wave propagation along mixed paths through a four-layered model of rain forest: an analytic approach", *IEEE Transactions on Antennas and Propagation,* vol. 46, no.7, pp. 1098-1111, 1998.

[68] L. Li, J. Koh, T. Yeo, M. Leong and P. Kooi, "Analysis of radiowave propagation in a four-layered anisotropic forest environment", *IEEE Transactions on Geoscience and Remote Sensing,* vol.37, no.4, pp. 1967-1979, July 1999.

[69[S. A. Torrico and H. L. Bertoni, "Modelling tree effects on path loss in a residential environment", *IEEE Transactions on Antennas and Propagation,* vol. 46, no. 6, pp. 872-880, 1998.

[70] M. Dehmollaian and K. Sarabandi, "A forward scattering model for foliage camouflaged complex targets", in *Proceedings of the IEEE International Geoscience and Remote Sensing Symposium, IGARSS'04,* vol. 1, 2004.

[71] R. Matschek, R. Linot and H. Sizun, "Model for wave propagation in presence of vegetation based on the UTD associating transmitter and lateral waves", in *Proceedings of the IEE National Conference on Antennas and Propagation,* pp.120-123, 1999.

[72] F. Ulaby, K. Mcdonald, K. Sarabandi, and M. Dobson, "Michigan microwave canopy scattering model (MIMICS)", in *Proceedings of the IEEE International Geoscience and Remote Sensing Symposium, IGARSS'88,* IEEE, Ed., vol. 2 pp. 1009-1009, Scotland, September 1988.

[73] P. Liang, L. Pierce , and M. Moghaddam, "Radiative transfer model for microwave bistatic scattering from forest canopies", *IEEE Transactions on Geoscience and Remote Sensing,* vol. 43, no. 11, pp. 2470-2483, November 2005.

[74] P. Liang, M. Moghaddam, and L. Pierce, "Backscattering simulation for nonuniform forest canopies using multi-layer MIMICS", *in Proceedings of the 2004 IEEE International Geoscience and Remote Sensing Symposium, IGARSS'04,* IEEE, Ed., vol. 2, pp. 1021-1024, 2004.

[75] K. Sarabandi and I. Koh, "A complete physics-based channel parameter simulation for wave propagation in a forest environment", *IEEE Transactions on Geoscience and Remote Sensing,* vol. 49, no. 2, pp. 260-271, Feb. 2001.

[76] C. Moss, F. Teixeira, Y. Yang, and J. Kong, "Finite-difference time-domain simulation of scattering from objects in continuous random media", *IEEE Transactions on Geoscience and Remote Sensing,* vol. 40, no.1, pp. 178-186, January 2002.

[77] H. Oraizi and S. Hosseinzadeh, "Determination of the effect of vegetation on radiowave propagation by the parabolic equation method", in Proceedings of

the IST'2003, International Symposium on Telecommunications, vol. 1, pp. 340-344, Iran, August 2003.

[78] G. M. Whitman, F. K. Schwering, L. Chen, "A Theory of Millimeter Wave Propagation in Vegetation", Research and Development Technical Report CECOM-TR-84-5, New Jersey, 1984.

[79] J. Richter, *Resolution of Signal Components of a Resultant Electromagnetic Wave Received in a Multipath Field of Microwave Frequencies*, PhD thesis, University of Glamorgan, 1998.

[80] T. Fernandes, R. F. S. Caldeirinha, M. O. Al-Nuaimi and J. Richter, "RET Scattering Function Optimisation in Vegetation Media using Inverse Convolution", *Proceeding of 2006 IEEE International Geoscience and Remote Sensing Symposium - IGARSS'06*, Vol. 1, Denver CO, USA, June 2006.

[81] S. M. Riad, "The Deconvolution Problem: An Overview," *Proc.* IEEE, vol.74, no. 1, pp. 82-85, Jan. 1986.

[82] J. Li, X. Li, D. Zhou, and E. Zhang, "A Novel Method for Estimating the Power Azimuth Spectrum of the Wireless Channel", IEEE Antennas and Wireless Propagation letters, vol. 5 2006.

[83] R. N. Bracewell, *The Fourier Transform and Its Applications*, Third Edition, McGraw-Hill Higher Education, 2000.

[84] E.O. Brigham, *The Fast Fourier Transform and Its Applications*, Prentice-Hall, 1988.

[85] C. W. Therrien, *Discrete Random Signals and Statistical Signal Processing*, Prentice-Hall, 1992.

[86] F. Ulaby, T. Deventr, J. East, T. Haddock, and M. Coluzzi, "Millimeter-wave bistatic scattering from ground and vegetation targets", *IEEE Transactions on Geoscience and Remote Sensing*, vol. 26, no. 3, pp. 229-243, May 1988.

[87] C. A. Balanis, *Antenna Theory: Analysis and design,* chapter 2, 3^{rd} Edition, John Wiley & Sons, 2005.

[88] J. D. Parsons, *The Mobile Radio Propagation Channel,* 2^{nd} Edition, Chapter 2, John Wiley & Sons, 2001.

[89] S. M. Riad and R. B. Stafford, "Impulse Response Evaluation Using Frequency Domain Optimal Compensation Deconvolution," in *Proc.* 23rd *Midwest Symp. on Circuits and Systems* (Toledo, OH), pp. 521-525, Aug. 1980.

[90] F. Jones and D. L. Misell, "The problem of error in deconvolution". J. Phys. A., Gen. Phys. 3: 462-472; 1970.

[91] A. N. Tikhonov and V. Y. Arsenin, *Solution of Ill-Posed Problems*, New York; Halsted, 1977.

[92] A. Muqaibel, A. Safaai-Jazi, B. Woerner, and S. Riad, "UWB Channel Impulse Response Characterisatization Using Deconvolution Techniques, " Circuits and Systems, MWSCAS-2002. The 2002 45th Midwest Symposium, Aug. 2002.

[93] B. Drachman, "Two Methods to Deconvolve: L_1-Method Using Simplex Algorithm and L_2-Method Using Lease Squares and a Parameter", IEEE Trans. on Antennas and Propagation, vol. AP-32, No.3, Mar. 1984.

[94] P. B. Crilly, A. Bernardi, P. A. Jansson and L. Silva, "Improving the Convergence Rate of Jansson's Deconvolution Method" *IEEE Trans. Instrum. Meas.*, vol.51, pp. 1142-1144, Dec. 2002.

[95] T. Dhaene, L. Martens, and D. D. Zutter, "Extended bennia-Riad Criterion for Iterative Frequency-Domain Deconvolution," IEEE *Trans.* on Instrumentation and measurement, vol.42, no.2, Apr. 1994.

[96] B. Parruck and S. M. Riad, "Study and Performance Evaluation of Two Iterative Frequency-Domain Deconvolution Techniques," IEEE *Trans.* on Instrumenation and measurement, vol. IM-33, No.4, Dec. 1984.

[97] G. Thoms, "An Improvement of the Van-Cittert's method," IEEE International Conference on: Acoustics, Speech, and Signal Processing, vol.6 pp.47-49, Apr. 1981.

[98] B. Parruck and S. M. Riad, "An Optimization Criterion for Iterative Deconvolution," IEEE *Trnas.* on Instrument and measurement, vol. IM-32, no.1, Mar. 1983.

[99] R. B. Whitted and P. B. Crilly, "A VLSI chip for real time iterative deconvolution," IEEE Proceedings of Volume, vol. 1 pp. 70-73, Apr. 1991.

[100] P. B. Crilly, "A Quantitative Evaluation of Various Iterative Deconvolution Algorithms," IEEE *Trans.* on Instrumentation and measurement, vol.40, no.3, Jun. 1991.

[101] N. R. Hill and G. E. Ioup, "Convergence of the Van Cittert iterative method of deconvolution," *J. of Optical Society of America*, vol. 68, no.5, pp.487-489, May 1976.

[102] B. R. Frieden, *Picture Processing and Digital Filtering*, in Top. Appl. Phys., vol. 6, pp. 177-248, Springer-Verlag, New York, 1975.

[103] W. E. Blass, and G. W. Halsey, *Deconvolution of Absorption Spectra*, Academic Press, New York, 1981.

[104] A. Bennia and S. M. Riad, "Filtering Capabilities and Convergence of the Van-Citter Deconvolution Techniaue," IEEE Trans. on Instrumentation and Measurement, vol. 41, no.2, Apr. 1992.

[105] A. Bennia and S. M. Riad, "An Optimization Technique for Iterative Frequency-Domain Deconvolution," *IEEE Trans. Instrum. Meas.*, vol.39, no.2, Apr. 1990.

[106] Parseval's theorem, wikipedia, http://en.wikipedia.org/wiki/Parseval's_theorem, accessed May, 2008.

[107] R. W. Schafer, R. M. Mersereau and M. A. Richards, "Constrained Iterative Deconvolution Algorithm," Proc. IEEE, vol. 69(4), pp. 432 - 450, April, 1981.

[108] K. Yu and M. K. Sistanisadeh, "Complex Deconvolution in Non-Coherent Radar System," *IEEE, ICASSP 86,* pp. 1921 - 1924, Tokyo, 1986.

[109] Z. Mu, R. J. Plemmons and P. Santago II, "Iterative Ultrasonic Signal and Image Deconvolution for Estimation of the Complex Medium Response," International Journal of Imaging System and Technology. vol. 15, Issue 6, pp. 266 - 277, 2005.

[110] T. K. Moon, *Mathematical Methods and Algorithms for Signal Processing,* Prentice Hall, 2000.

[111] Wikipedia, http://en.wikipedia.org/wiki/Hartley_transform, Oct, 2007.

[112] *Singnal Processing Toolbox 6*, MATLAB User's Guide, pp. 4-28 - 4-30, March, 2007.

Appendix A

RMS error calculation

Throughout this research project extraction of the RET input parameters α β and albedo W uses an examination criterion, namely the Root Mean Square (RMS) error. A curve, restored after deconvolution application or predicted using RET theory, in accordance with calculated minimum RMS error between itself and its corresponding measured pattern is believed to provide the optimal result.

This criterion is utilised for extracting optimal values of α and β from re-radiation functions of single trees, measured directional spectra and their correspondingly restored patterns, then using these parameters to find the best fit curves of measured directional spectra in order to obtain albedo W. Furthermore, the RMS error criterion combined with extracted RET input parameters is employed to proof improvement by comparing the calculated RMS errors between the measured patterns and their restored patterns after deconvolution application or predicted curves using the RET theory. The RMS error in dB is given by:

$$E_{RMS}\,(dB) = \sqrt{\frac{\sum_{i=1}^{N} (E_i)^2}{N}} \tag{A.1}$$

$$E_i = D_{restored_i}\,(dB) - D_{measured_i}\,(dB) \tag{A.2}$$

where $D_{restored_i}$and $D_{measured_i}$ are the i^{th} point of restored and measured data sets respectively in dB.

Appendix B

Critical dependence on the first term

In the practical application of classical original (mostly referred to as time) domain methods to deconvolution problems, choice of the first term x_1 in the input sequence is critical. If x_1 is ill chosen the resultant deconvolution will not converge [28]. An understanding of this feature can be gained via investigating the straightforward approach of deconvolution in the original domain.

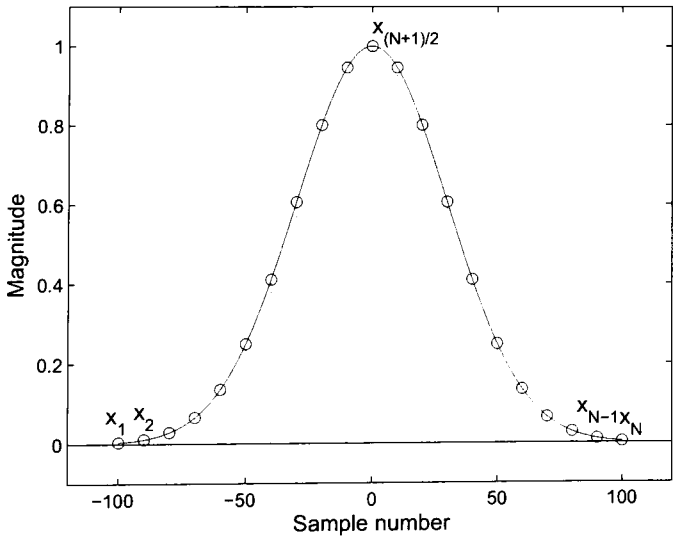

Figure B.1: Example of a discrete sampled sequence

The discrete version of the convolution process is given by:

$$y_m = \sum_k h_{m-k+1} x_k \tag{B.1}$$

for the application presented in this research project y represents the measured data sequence, h represents the RET phase function to be restored, and x the antenna radiation pattern. y_m is the mth element of y, and the same applies to h_{m-k} and x_k.

For convenience, assuming that x has an odd number of nonvanishing points over a finite domain, N, and its peak value at $k = \frac{N+1}{2}$ with $\frac{N-1}{2}$ nonvanishing values on either side of the peak point. A depiction of the sequence x is shown in Fig. B.1. The convolution is given by:

$$y_m = \sum_{i=1}^{N} x_i h_{m-i+1} \tag{B.2}$$

In reality, a noise-free antenna radiation pattern has its maximum value at the middle point, *i.e.* the peak-value point, and is virtually symmetrical regarding this point. Hence the aforementioned assumptions do not damage any generalisation. From Eq. B.2

$$y_1 = h_1 \times x_1 \Rightarrow h_1 = \frac{y_1}{x_1} \tag{B.3}$$

where x_1 denotes the first nonvanishing term in the sequence x, and also x_1 will be the first point to meet the first nonvanishing point h_1 of sequence h in the course of convolution, shown as in Fig. B.2.

$$\begin{array}{rcl} & & 0\ x_1\ x_2 \cdots x_{\frac{N+1}{2}} \cdots x_{N-1}\ x_N\ 0 \\ & \times\ \ \times\ \ \times & \\ \cdots\ h_3\ h_2\ h_1\ \cdots\ 0 \rightarrow & & \end{array}$$

Figure B.2: Demonstration of a convolution process in the original domain

Furthermore,

$$y_2 = h_1 \times x_2 + h_2 \times x_1 \Rightarrow h_2 = \frac{y_2 - h_1 \times x_2}{x_1} = \frac{y_2 - (\frac{y_1}{x_1}) \times x_2}{x_1} \tag{B.4}$$

$$h_3 = \frac{y_3}{x_1} - y_2 \times \frac{x_2}{(x_1)^2} + y_1 \times \left(\frac{(x_2)^2}{(x_1)^3} - \frac{x_3}{(x_1)^2} \right) \tag{B.5}$$

If the first term x_1 is ill sampled and has considerable noise content within it, *i.e.* poor Signal-to-Noise (SNR) ratio, then the noise components in x_1 would be magnified step by step in the process of calculating h_1, h_2, h_3 $\cdots$ because x_1 increases exponentially in the denominator. So far, effects of poor quality of the first term x_1 have been exhibited.

The role of the first term y_1 will be continuously demonstrated as following. The sequence x is assumed to be error-free at this stage. Sequences x and y are normalised with respect to x_1, that is, dividing x and y by x_1, then the ith element in sequence x and the mth component in y are given by:

$$\bar{x}_i = \frac{x_i}{x_1} \qquad i = 1, \cdots N \tag{B.6}$$

$$\bar{y}_m = \frac{y_m}{x_1} \qquad m = 1, \cdots M \tag{B.7}$$

where $M \geq N$. Rewriting Eqs. B.3 to B.5 as below:

$$h_1 = \bar{y}_1 \tag{B.8}$$

$$h_2 = \bar{y}_2 - h_1 \bar{x}_2 \tag{B.9}$$

$$h_3 = \bar{y}_3 - h_1 \bar{x}_3 - h_2 \bar{x}_2 \tag{B.10}$$

Further,

$$h_4 = \bar{y}_4 - h_1\bar{x}_4 - h_2\bar{x}_3 - h_3\bar{x}_2 \tag{B.11}$$

$$h_5 = \bar{y}_5 - h_1\bar{x}_5 - h_2\bar{x}_4 - h_3\bar{x}_3 - h_4\bar{x}_2 \tag{B.12}$$

$$\vdots$$

Consequently, h_k is given by:

$$h_k = \bar{y}_k - \sum_{i=1}^{k-1} h_i\bar{x}_{k+1-i} \tag{B.13}$$

Now y_1 or $\bar{y}_1$, the first term in sequence y, is considered to contain an error e_{y1}, and becomes the erroneous value $\bar{y}_{e1}$:

$$\bar{y}_{e1} = \bar{y}_1 + e_{y1} \tag{B.14}$$

where $\bar{y}_{e1}$ represents the measured value with error, $\bar{y}_1$ denotes the accurate value of the first term in sequence $\bar{y}$. Replacing $\bar{y}_1$ with $\bar{y}_{e1}$ through Eqs. B.8 to B.12, then:

$$h_{e1} = \bar{y}_{e1} = \bar{y}_1 + e_{y1} = h_1 + e_{y1} \tag{B.15}$$

and

$$h_{e2} = \bar{y}_2 - h_{e1}\bar{x}_2 = \bar{y}_2 - (h_1 + e_{y1})\,\bar{x}_2 = h_2 + e_{y1}\,[-\bar{x}_2] \tag{B.16}$$

repeatedly,

$$h_{e3} = h_3 + e_{y1}\left[-\bar{x}_3 + \bar{x}_2^2\right] \tag{B.17}$$

$$h_{e4} = h_4 + e_{y1}\left[-\bar{x}_4 + 2\bar{x}_2\bar{x}_3 - \bar{x}_2^3\right] \tag{B.18}$$

$$h_{e5} = h_5 + e_{y1}\left[-\bar{x}_5 + 2\bar{x}_2\bar{x}_4 + \bar{x}_3^2 - 3\bar{x}_3\bar{x}_2^2 + \bar{x}_2^4\right] \tag{B.19}$$

$$\vdots$$

where h_{ei} represents the corresponding value of h_i with errors. Through Eqs. B.15

to B.19, it is evident that the effect of the error, e_{y1}, is increasing as i increases. The error in h_i is given by:

$$e_i^h = h_{ei} - h_i \tag{B.20}$$

Here, e^h represents the set of errors in the resultant h_e caused by the single error e_{y1} only. In practice, h_e will certainly be affected by the errors in x_1 as well.

Furthermore, errors in x_2, x_3, $\cdots$ and y_2, y_3, $\cdots$ will also cause inaccuracies in the ultimate result. However, they play a less important role than their previous counterparts. In fact, the importance of each individual term is decreasing as moving from either of ends to the middle region, *i.e.* from x_1 or x_N to $x_{N+1/2}$ as illustrated in Fig. B.1. Because of the commutative property of the convolution operation, the influence of the SNR of points x_1 and x_N is of equal importance; and the same applies to x_2 and x_{N-1} and so on. This argument is also true for the output sequence y.

Consequently, the errors in the resultant h_e depend upon the sets of errors from both sequences x and y, and are very sensitive to the points at the end-regions, where the obtained results usually have the poorest SNR throughout measurements. Nevertheless, inaccuracies in the middle part of the measured data, *i.e.* the peak-value region and its near neighbours will not degrade the deconvolution significantly. In fact, the measured data in this region usually has very good SNR values. This finding highlights why deconvolution approaches are very popular where the high-frequency components are cut off or suppressed, as implemented in various types of Wiener filters [27, 28[.

A feasible technique to improve the SNR of the measured signals is averaging. This method independently measures a several values at the same location and then uses their mean value as the sampled result. In measurements conducted in this project, 5 values are independently measured and averaged at each specific angular position. Because the measurement system is considered linear and time-invariant, the inaccuracy introduced by the slight difference of measurement time is negligible.

Appendix C

Measured re-radiation function patterns of single trees

The measured data for the re-radiation function of single trees as concluded here show in some cases very significant signal variation with rotation angles. This can make the curve fitting process somewhat unreliable. When the dense tree is present, a big blockage appeared in the middle of the re-radiation patterns. In particular, when the 10 dBi standard gain horn at 20 GHz, 10 dBi and 20 dBi standard gain horns at 40 GHz were used as the receiver respectively, smoothing algorithms have to be implemented before the curve fitting algorithms applies. The graphs show the re-radiation function of a single tree overlaid with a best fit phase function curve.

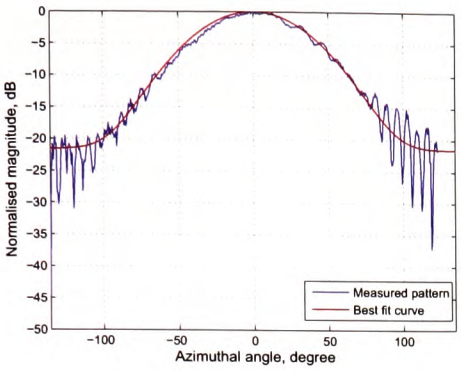

(a) free space, Rx 10 dBi, 20 GHz

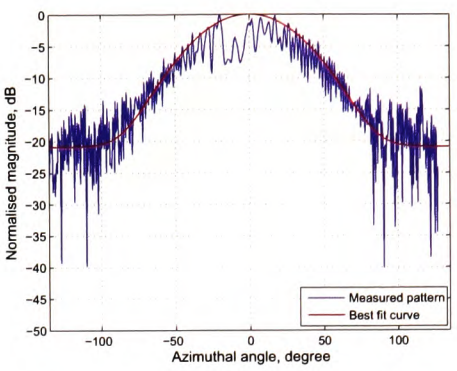

(b) sparse tree, Rx 10 dBi, 20 GHz

Figure C.1: Best fit phase function in curve and the measured re-radiation patterns of single tree, Rx: standard gain horn antenna

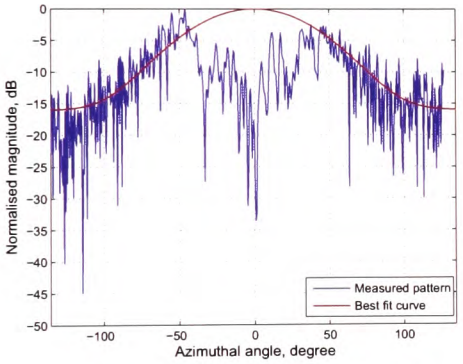

(a) dense tree, Rx 10dBi, 20 GHz

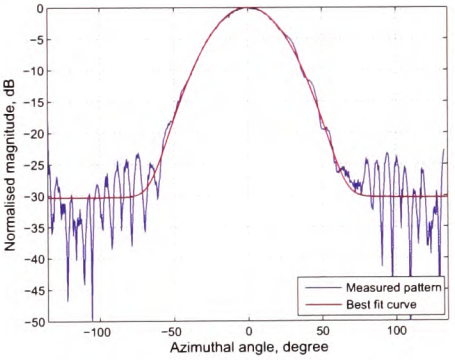

(b) free space, Rx 15dBi, 20 GHz

Figure C.2: Best fit phase function in curve and the measured re-radiation patterns of single tree, Rx: standard gain horn antenna

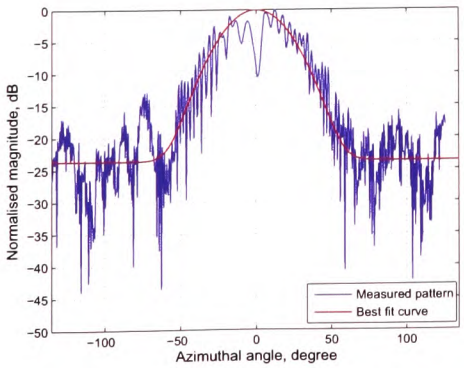

(a) sparse tree, Rx 15 dBi, 20 GHz

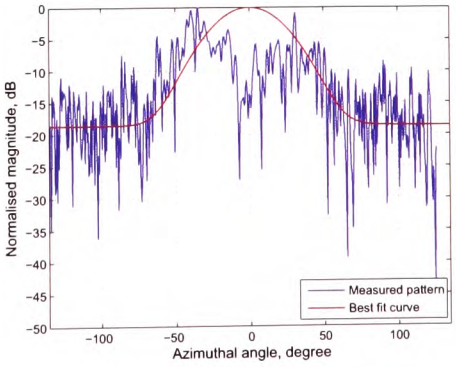

(b) dense tree, Rx 15 dBi, 20 GHz

Figure C.3: Best fit phase function in curve and the measured re-radiation patterns of single tree, Rx: standard gain horn antenna

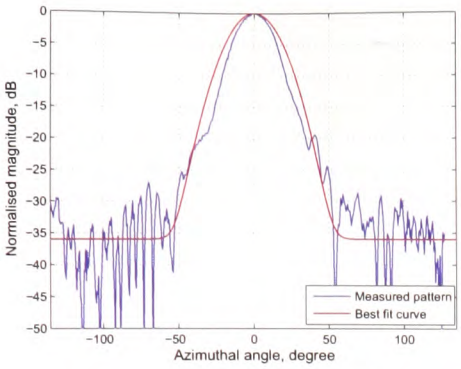

(a) free space, Rx 20 dBi, 20 GHz

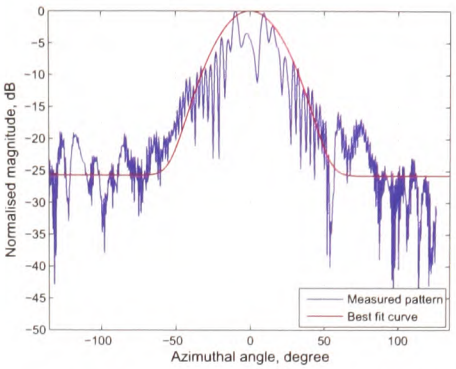

(b) sparse tree, Rx 20 dBi, 20 GHz

Figure C.4: Best fit phase function in curve and the measured re-radiation patterns of single tree, Rx: standard gain horn antenna

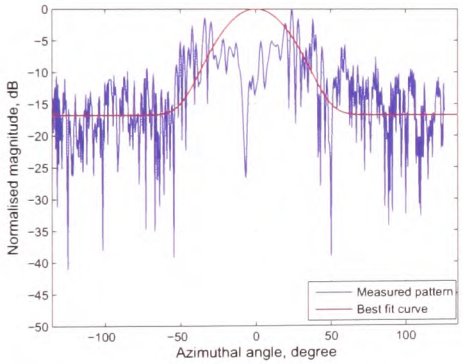

(a) dense tree, Rx 20 dBi, 20 GHz

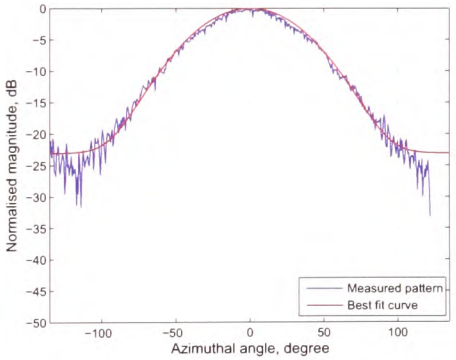

(b) free space, Rx 10 dBi, 40 GHz

Figure C.5: Best fit phase function in curve and the measured re-radiation patterns of single tree, Rx: standard gain horn antenna

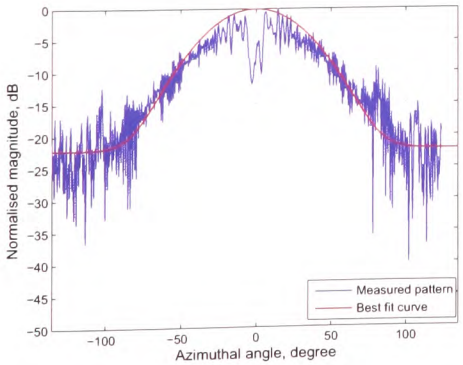

(a) sparse tree, 10 dBi, 40 GHz

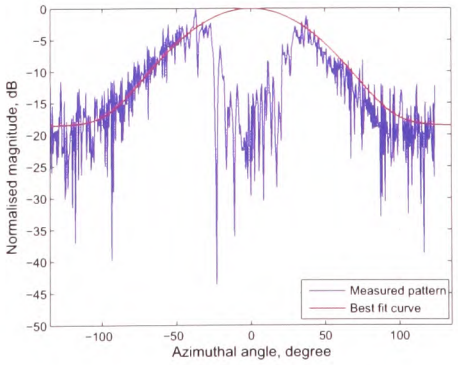

(b) dense tree, 10 dBi, 40 GHz

Figure C.6: Best fit phase function in curve and the measured re-radiation patterns of single tree, Rx: standard gain horn antenna

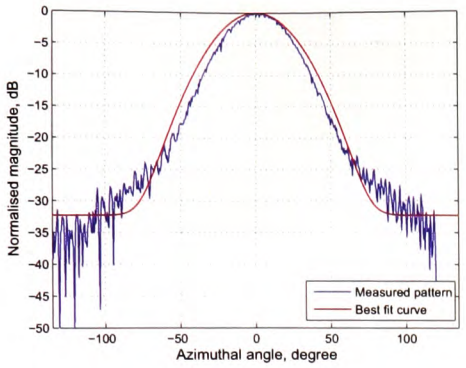

(a) free space, Rx 15 dBi, 40 GHz

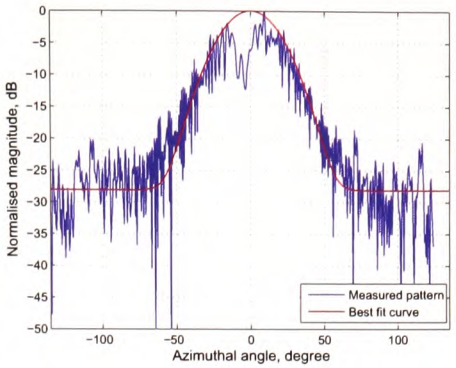

(b) sparse tree, Rx 15 dBi, 40 GHz

Figure C.7: Best fit phase function in curve and the measured re-radiation patterns of single tree, Rx: standard gain horn antenna

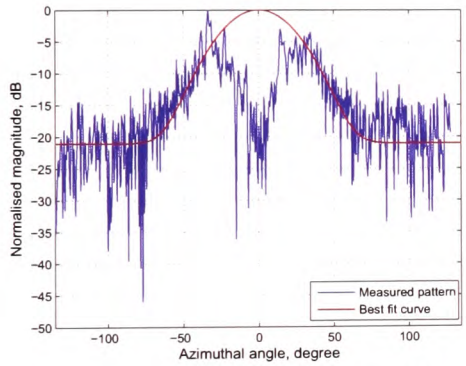

(a) dense tree, Rx 15 dBi, 40 GHz

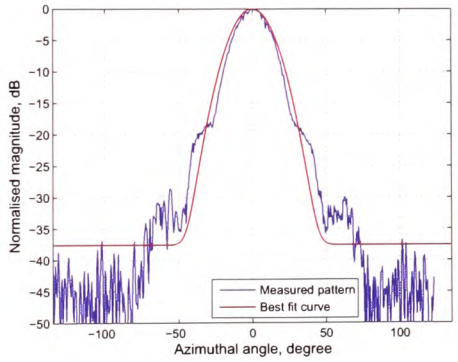

(b) free space, Rx 20 dBi, 40 GHz

Figure C.8: Best fit phase function in curve and the measured re-radiation patterns of single tree, Rx: standard gain horn antenna

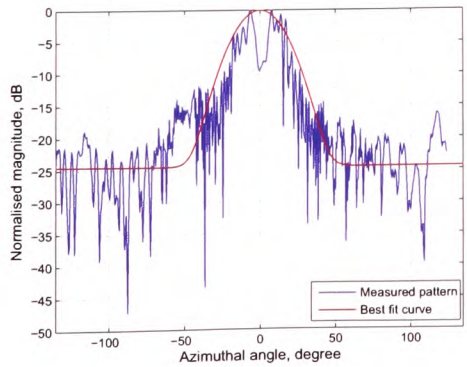

(a) sparse tree, Rx 20 dBi, 40 GHz

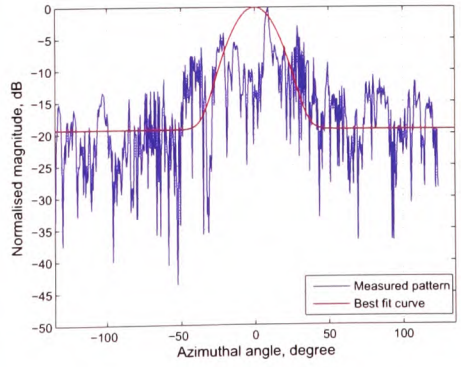

(b) dense tree, Rx 20 dBi, 40 GHz

Figure C.9: Best fit phase function in curve and the measured re-radiation patterns of single tree, Rx: standard gain horn antenna

Appendix D

Restored directional spectra at all positions

Five calculated directional spectra based on the RET theory using extracted input parameters from directly measured patterns, restored patterns using optimum compensation and automated regularisation deconvolution methods and without the auto/cross-correlation pre-filtering technique and with, respectively, are shown in figures as following. Results obtained from the measured data using the 20 dBi Gaussian horn antenna as receiver at 20 GHz are presented in Figs. D.1 to D.3 in accordance with the measurement positions 1, 2 and 3 illustrated in Figs. 5.9 and 5.10. Similarly calculated directional spectra from the measured data using the 29 dBi Lens horn antenna as receiver at 40 GHz are demonstrated in Figs. D.4 to D.6 corresponding to positions 1, 2 and 3. In each case, the measured patterns are overlaid correspondingly for comparison.

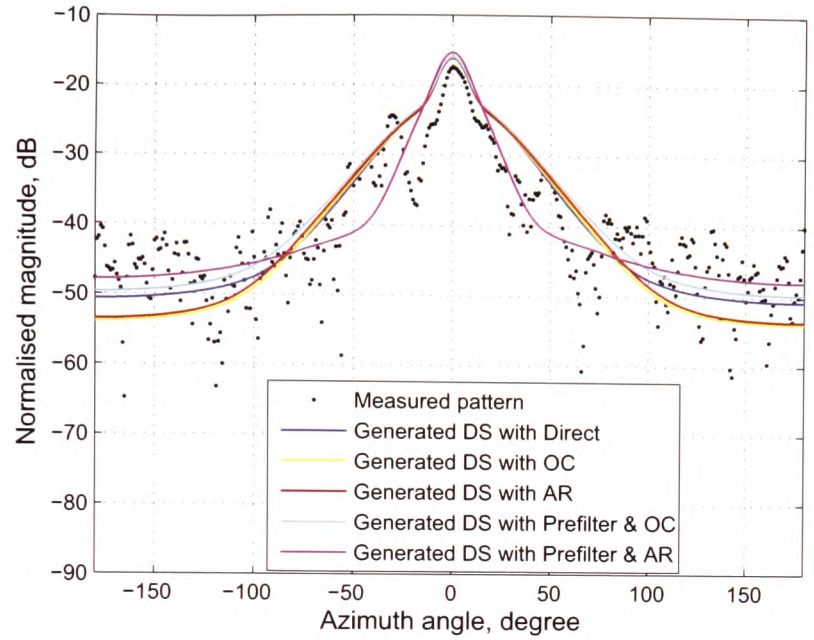

Figure D.1: Measurement at Pos. 1, RX 20 dBi Gaussian horn at 20 GHz

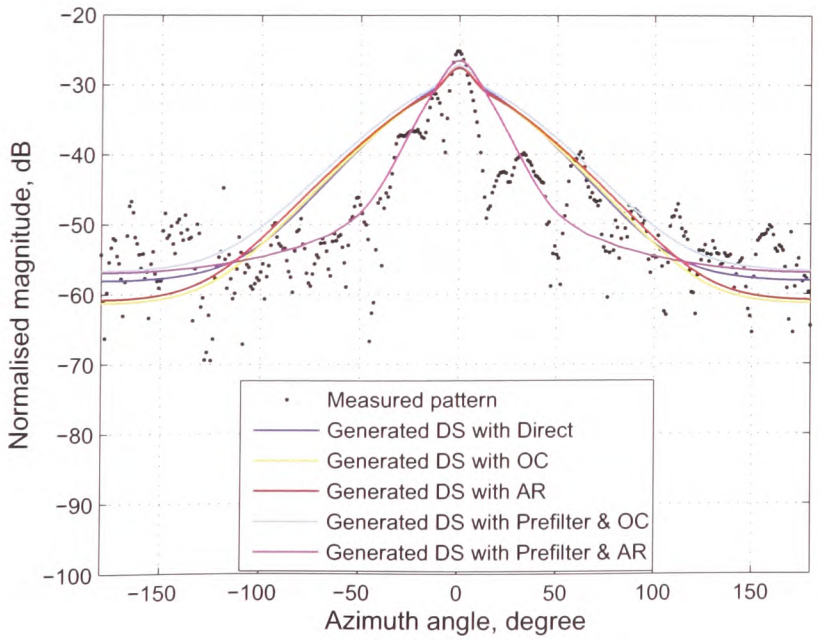

Figure D.2: Measurement at Pos. 2, RX 20 dBi Gaussian horn at 20 GHz

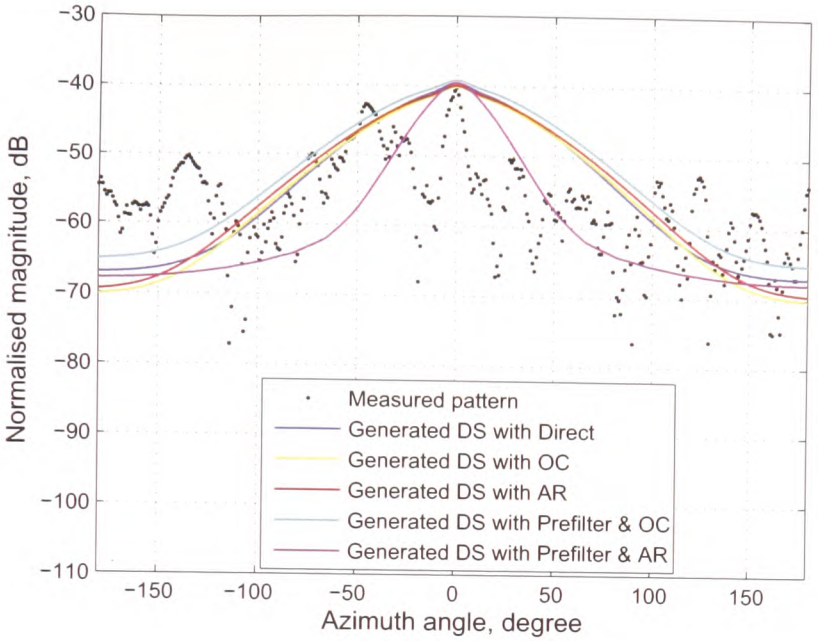

Figure D.3: Measurement at Pos. 3, RX 20 dBi Gaussian horn at 20 GHz

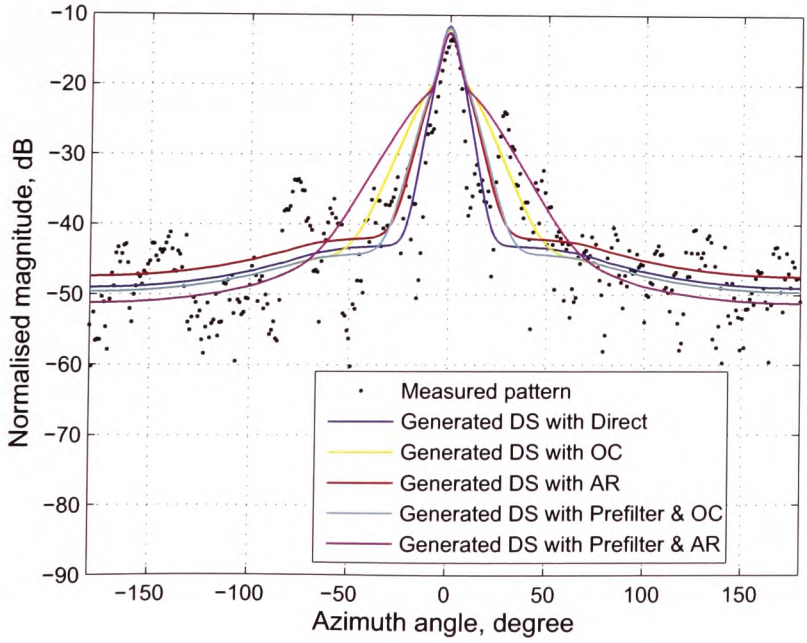

Figure D.4: Measurement at Pos. 1, RX 29 dBi Lens horn at 40 GHz

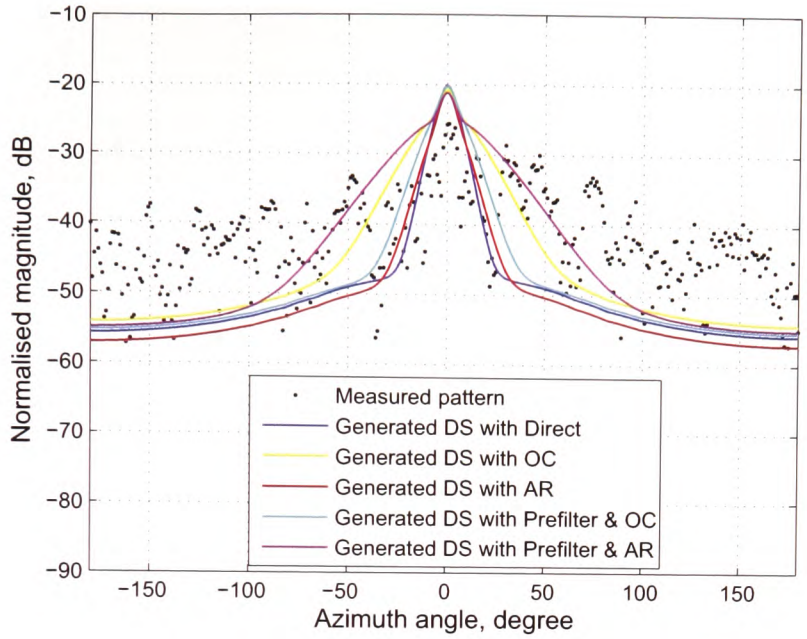

Figure D.5: Measurement at Pos. 2, RX 29 dBi Lens horn at 40 GHz

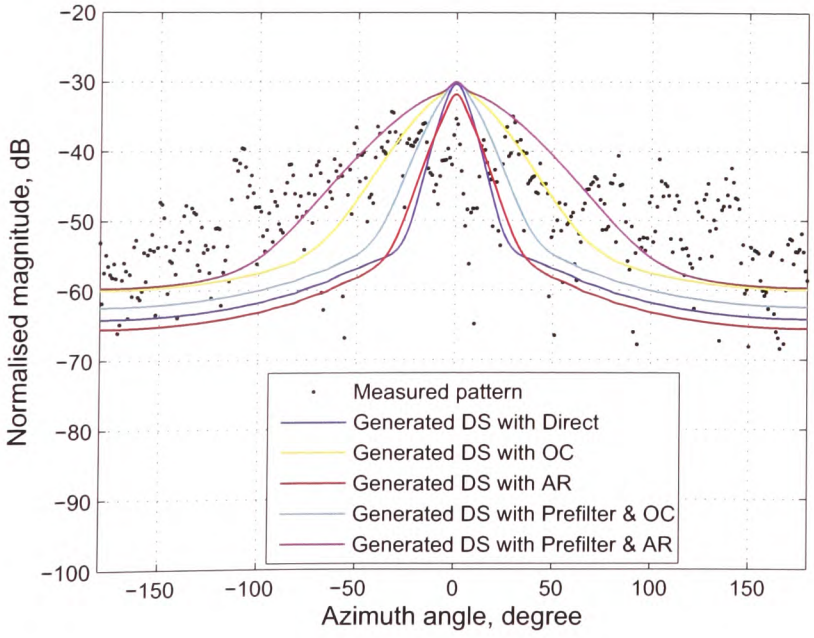

Figure D.6: Measurement at Pos. 3, RX 29 dBi Lens horn at 40 GHz

Appendix E

Restored directional spectra for all antennas under test

RET input parameter are extracted for all antennas available using 5 different methods: (a) directly measured patterns; (b) restored patterns using the optimum compensation deconvolution; (c) the automated regularisation deconvolution; (d) restored patterns using the optimum compensation deconvolution with the auto/cross-correlation pre-filtering technique and (e) restored patterns using the automated regularisation deconvolution with the auto/cross-correlation pre-filtering technique and summarised in Tables1 to 8.

Restored directional spectra are obtained from the measured patterns at position 1, illustrated in Figs. 5.9 and 5.10, with all available antennas under test at both 20 and 40 GHz systems. In each case, the measured patterns are overlaid correspondingly for comparison.

	α	β	$k_e\,(^{dB}/_m)$	W	$\Delta\gamma_R$
Direct	0.96	21^o	6.78	0.46	7.8^o
OC	0.98	22.5^o	6.78	0.45	7.8^o
AR	0.98	23^o	6.78	0.46	7.8^o
Prefilter & OC	0.96	22.5^o	6.78	0.49	7.8^o
Prefilter & AR	0.83	11.5^o	6.78	0.38	7.8^o

Table E.1: Extraction of the RET input parameters for measurement with 20 dBi Gaussian horn as receiver at 20 GHz using 5 different methods

	α	β	$k_e\,(^{dB}/_m)$	W	$\Delta\gamma_R$
Direct	0.82	13.5^o	6.37	0.34	11.1^o
OC	0.92	26^o	6.37	0.48	11.1^o
AR	0.87	16.5^o	6.37	0.38	11.1^o
Prefilter & OC	0.89	19.5^o	6.37	0.41	11.1^o
Prefilter & AR	0.89	20^o	6.37	0.42	11.1^o

Table E.2: Extraction of the RET input parameters for measurement with 20 dBi standard gain horn as receiver at 20 GHz using 5 different methods

	α	β	$k_e\,(^{dB}/_m)$	W	$\Delta\gamma_R$
Direct	0.53	12^o	5.7	0.09	19.8^o
OC	0.38	9^o	5.7	0.25	19.8^o
AR	0.46	15.5^o	5.7	0.4	19.8^o
Prefilter & OC	0.49	17^o	5.7	0.34	19.8^o
Prefilter & AR	0.39	17^o	5.7	0.46	19.8^o

Table E.3: Extraction of the RET input parameters for measurement with 15 dBi standard gain horn as receiver at 20 GHz using 5 different methods

	α	β	$k_e\,(^{dB}/_m)$	W	$\Delta\gamma_R$
Direct	0.81	23.5^o	4.56	0.23	31.8^o
OC	0.16	7^o	4.56	0.16	31.8^o
AR	0.86	23^o	4.56	0.23	31.8^o
Prefilter & OC	0.9	28.5^o	4.56	0.13	31.8^o
Prefilter & AR	0.89	34^o	4.56	0.31	31.8^o

Table E.4: Extraction of the RET input parameters for measurement with 10 dBi standard gain horn as receiver at 20 GHz using 5 different methods

	α	β	$k_e\,(^{dB}/_m)$	W	$\Delta\gamma_R$
Direct	0.79	5.5^o	5.23	0.41	4.2^o
OC	0.95	12^o	5.23	0.57	4.2^o
AR	0.83	7.5^o	5.23	0.49	4.2^o
Prefilter & OC	0.9	8^o	5.23	0.48	4.2^o
Prefilter & AR	0.98	16^o	5.23	0.64	4.2^o

Table E.5: Extraction of the RET input parameters for measurement with 29 dBi Lens horn as receiver at 40 GHz using 5 different methods

	α	β	$k_e\,(^{dB}/_m)$	W	$\Delta\gamma_R$
Direct	0.85	11.5^o	4.9	0.35	10.5^o
OC	0.67	9^o	4.9	0.34	10.5^o
AR	0.9	13.5^o	4.9	0.38	10.5^o
Prefilter & OC	0.92	16^o	4.9	0.42	10.5^o
Prefilter & AR	0.79	15^o	4.9	0.46	10.5^o

Table E.6: Extraction of the RET input parameters for measurement with 20 dBi standard gain horn as receiver at 40 GHz using 5 different methods

	α	β	$k_e\,(^{dB}/_m)$	W	$\Delta\gamma_R$
Direct	0.85	27.5^o	5.96	0.33	23.4^o
OC	0.41	13^o	5.96	0.28	23.4^o
AR	0.38	15^o	5.96	0.37	23.4^o
Prefilter & OC	0.9	40.5^o	5.96	0.41	23.4^o
Prefilter & AR	0.86	39^o	5.96	0.43	23.4^o

Table E.7: Extraction of the RET input parameters for measurement with 15 dBi standard gain horn as receiver at 40 GHz using 5 different methods

	α	β	$k_e\,(^{dB}/_m)$	W	$\Delta\gamma_R$
Direct	0.85	24.5^o	4.43	0.19	37.2^o
OC	0.66	13.5^o	4.43	0.1	37.2^o
AR	0.83	22.5^o	4.43	0.16	37.2^o
Prefilter & OC	0.87	27.5^o	4.43	0.23	37.2^o
Prefilter & AR	0.81	22^o	4.43	0.16	37.2^o

Table E.8: Extraction of the RET input parameters for measurement with 10 dBi standard gain horn as receiver at 40 GHz using 5 different methods

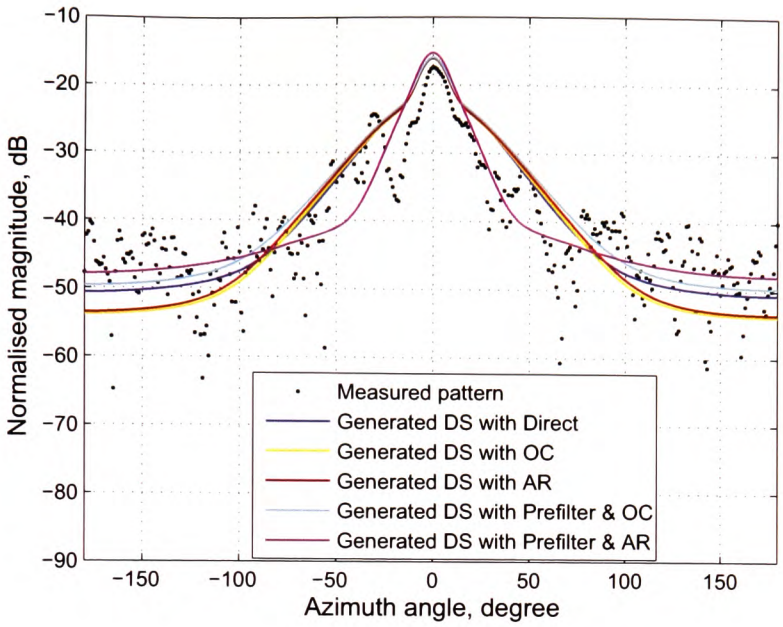

Figure E.1: Measurement at Pos. 1, RX 20 dBi Gaussian horn at 20 GHz

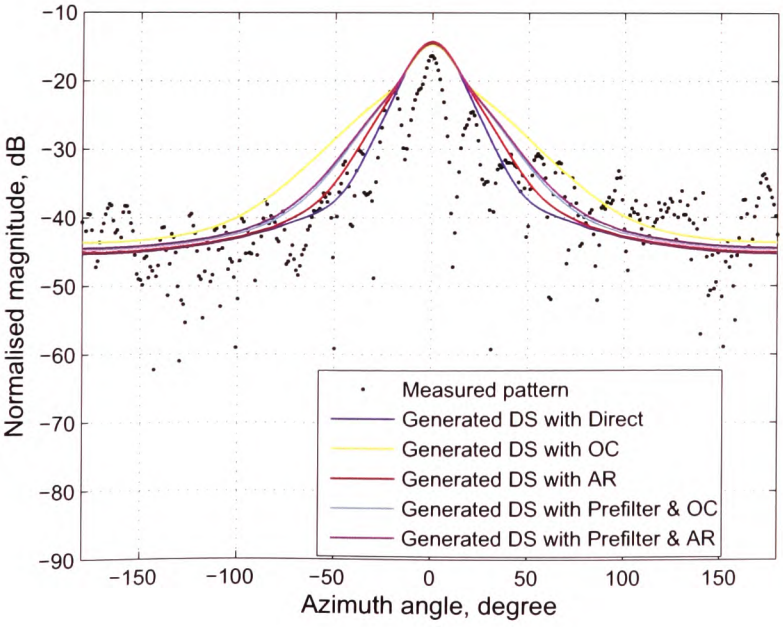

Figure E.2: Measurement at Pos. 1, RX 20 dBi standard gain horn at 20 GHz

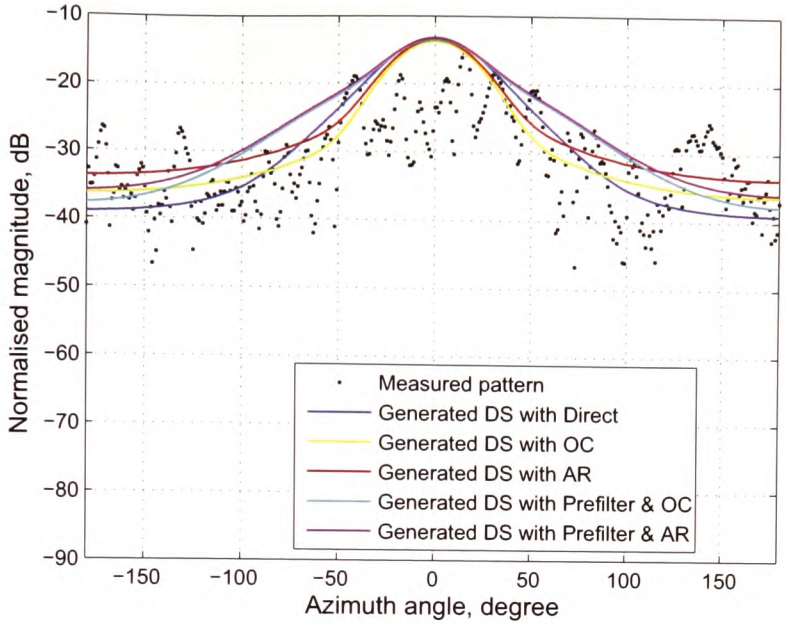

Figure E.3: Measurement at Pos. 1, RX 15 dBi standard gain horn at 20 GHz

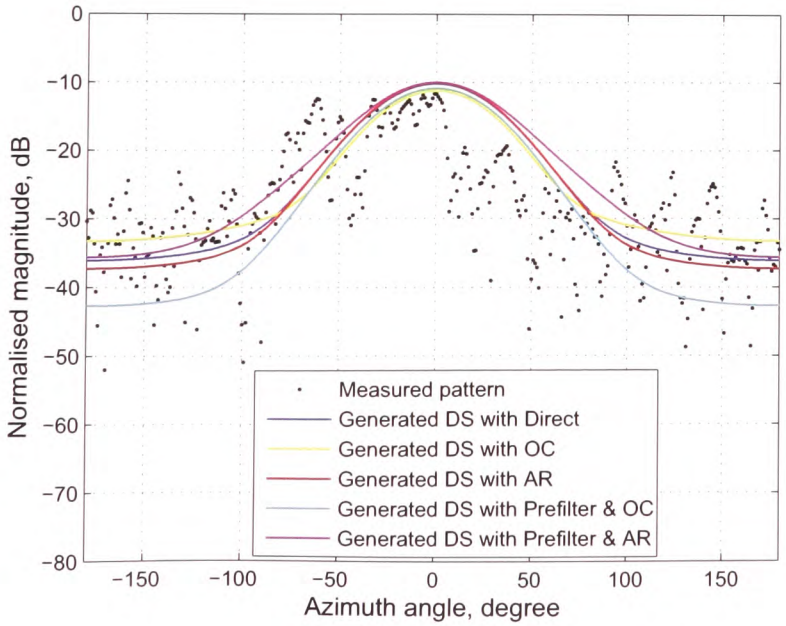

Figure E.4: Measurement at Pos. 1, RX 10 dBi standard gain horn at 20 GHz

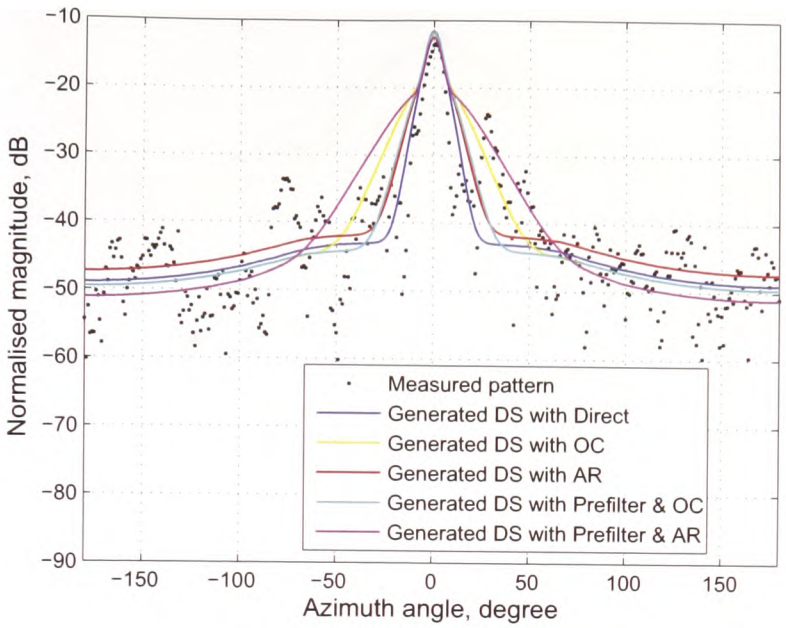

Figure E.5: Measurement at Pos. 1, RX 29 dBi Lens horn at 40 GHz

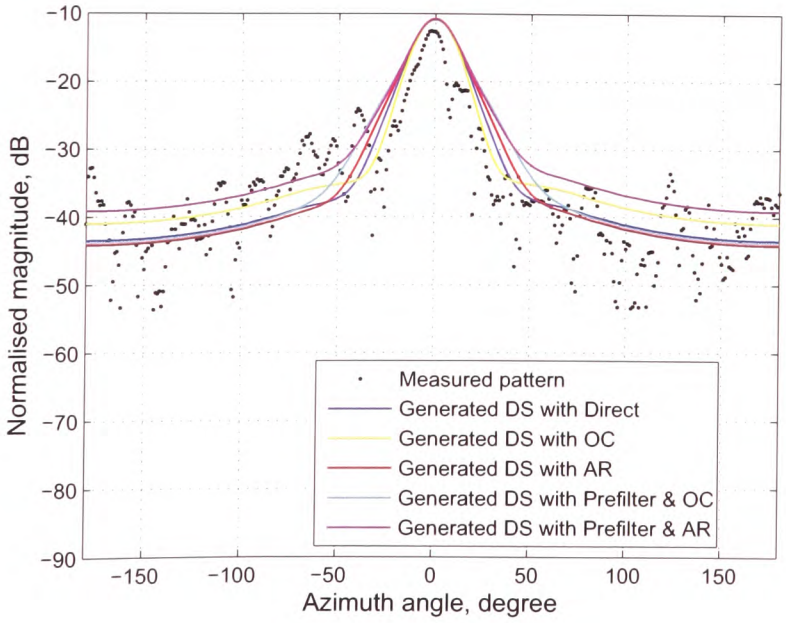

Figure E.6: Measurement at Pos. 1, RX 20 dBi standard gain horn at 40 GHz

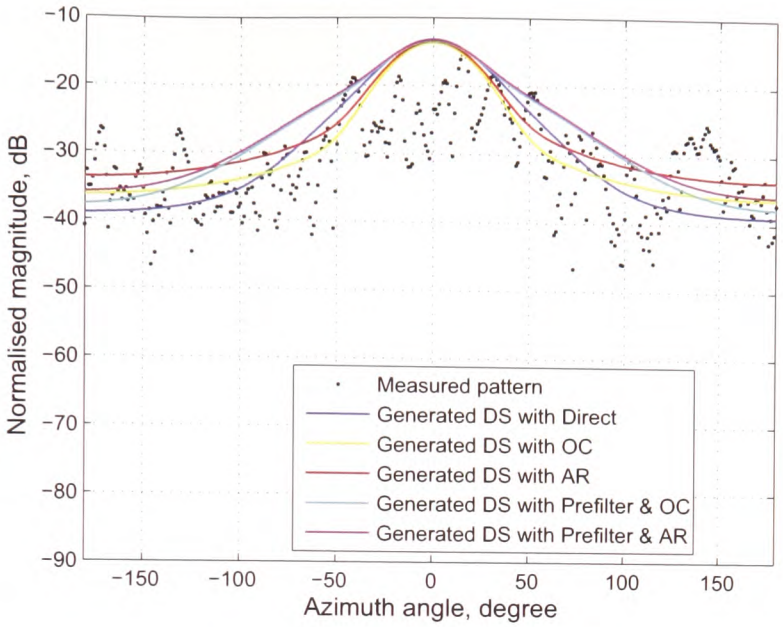

Figure E.7: Measurement at Pos. 1, RX 15 dBi standard gain horn at 40 GHz

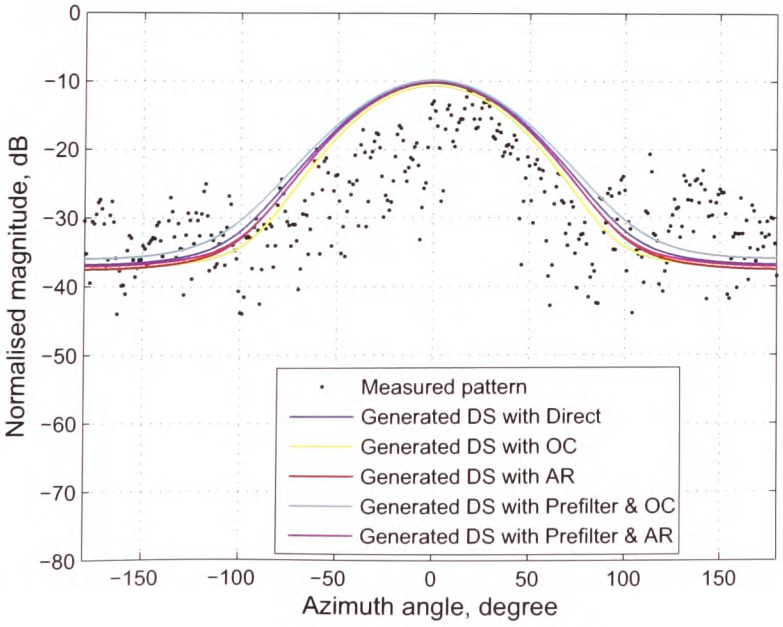

Figure E.8: Measurement at Pos. 1, RX 10 dBi standard gain horn at 40 GHz

Appendix F

Samples of published work

1. H. Cui, J. Richter, M. O. Al-Nuaimi, and R. Caldeirinha, "Restoration of the RET Phase Function using Deconvolution," *Proceedings of the 2nd IEEE, NGMAST 2008,* Cardiff, UK, Sept. 2008.

2. H. Cui, J. Richter, M. O. Al-Nuaimi, and T. Fernandes, "RET Input Parameter Extraction Using Deconvolution from Measurement at 20 GHz," IEEE Transaction on Antennas and Propagation. (submitted)

3. H. Cui, J. Richter, M. O. Al-Nuaimi, and R. Caldeirinha, "RET Phase Function Parameter Extraction using Automated Regularisation Deconvolution based on Measurement at 40 GHz," IET Microwaves, Antennas & Propagation. (submitted)

The Second International Conference on Next Generation Mobile Applications, Services, and Technologies

Restoration of the RET Phase Function using Deconvolution

Huajian Cui*, Jürgen Richter*, Miqdad Al-Nuaimi*, and Rafael Caldeirinha+

***Abstract*—The influence of vegetation has become an important aspect of the design of wireless communication links. In recent years theory of Radiative Energy Transfer (RET) has been adapted as a reliable tool to predict the radiowave propagation through and near vegetation. The developed RET prediction model requires 4 input independent parameters, which so far had to be established from one measurement only, thus limiting their accuracy. An independent measurement which is termed the phase function can readily yield 2 of the 4 input parameters independently, which significantly increases the accuracy of these parameters. However one major factor influencing the phase function measurement is the radiation pattern of the receiving antenna. The measured curve will be the result of the convolution of the antenna radiation pattern and the phase function of the vegetation medium. The measurement curve therefore needs to undergo a deconvolution process before any RET input parameters can be derived from it. This paper presents the deconvolution method developed using optimal compensation deconvolution methods. Deconvolution is demonstrated using both simulation signal shapes and those measured in vegetation set up in the anechoic chamber. This paper discusses different cases of optimal compensation filtering with the relative curves shown.**

***Index Terms*—Optimal Compensation, Deconvolution, RET, Phase Function**

I. Introduction

Accurate prediction models are vital for planning and managing the radio spectrum in the light of a constantly increasing demand for wireless communications services. The influence of vegetation on the radio path has long been recognised as one of the more difficult modelling challenges. The theory of Radiative Energy Transfer (RET) provides a full wave solution for vegetation modelling and has successfully been adapted for modelling of propagation in the presence of vegetation at microwave and millimeter wave frequency [1], [2]. To accurately model radiowave propagation in the presence of vegetation the RET requires a set of 4 input parameters. These depend on factors such as frequency, type of vegetation, state of foliation *etc* and need to be determined experimentally.

In previous implementations of the RET all 4 parameters were determined using one type of measurement only, namely the signal attenuation with vegetation depth [2]. The accuracy that can be achieved by this approach is however limited. Two of the four RET input parameters are also present in the description of the vegetation scatter function in the RET, the so called phase function. Determination of the phase function through a separate set of measurements will yield these 2 input parameters independently and therefore all 4 parameters can be established far more accurately.

However the result of the measurement of the phase function is highly depended on the receiving antenna radiation pattern. The received signal pattern is the result of the convolution of both the phase function and antenna radiation pattern. To determine the phase function with reasonable accuracy a deconvolution therefore has to be undertaken of the received signal pattern and the antenna radiation pattern. Deconvolution is not a linear and not always a straightforward operation. Although deconvolution techniques are widely used in areas like astronomy and image processing [3], they have so far only found limited application in radiowave propagation.

This paper introduces the application of an optimal compensation deconvolution approach for the purpose of restoring the phase function from a measured pattern under consideration of the antenna radiation pattern. The paper is outlined as follows. Section II briefly summarises the relevant parts of the theory of Radiative Energy Transfer. Section III shows how antenna radiation pattern and phase function convolve to produce the measured signal pattern and briefly highlight why straightforward deconvolution may not provide the correct answers. In section IV the optimal compensation filtering is introduced and the derived deconvolution process is demonstrated using computer generated data which includes the influence of white noise. Section V provides a brief description of the measurement scenario for data obtained from vegetation measurements in a controlled indoor environment. Finally section VI details result of the deconvolution of the measured signal pattern using the iteratively optimal compensation technique and shows the introduction of the Bennia-Riad criterion for further optimisation. Concluding remarks are found in section VII.

II. Brief Introduction to the RET and its Phase Function

The RET theory simulates the vegetation medium as a homogeneous environment consisting of randomly distributed scatterers ds. This model can be represented by a set of parameters: σ_a the absorption coefficient, σ_s the scattering coefficient, α the ratio between the forward lobe and the total scattered power, and β the beamwidth of the forward lobe [1], [2]. The scalar form of the fundamental Energy Transfer equation is given by follows:

$$\frac{dI}{ds} = -(\sigma_a + \sigma_s)\cdot I + \sigma_s \int_{4\pi} p(\hat{s}_1, \hat{s}_2')\cdot I \cdot d\Omega \qquad (1)$$

*Radiowave propagation and System design Research Unit, University of Glamorgan, CF37 1DL, UK Email: hcui@glam.ac.uk, jrichter@glam.ac.uk, malnuaim@glam.ac.uk

+Department of Electrical Engineering, Polytechnic Institute of Leiria, ESTG-Leiria, 2401-951 Leiria, Portugal Email: rcaldeirinha@estg.iplei.pt

978-0-7695-3333-9 /08 $25.00 © 2008 IEEE
DOI 10.1109/NGMAST.2008.47

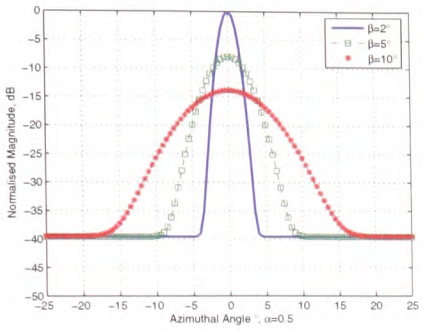

Figure 1. Schematic demonstration of the phase function signal

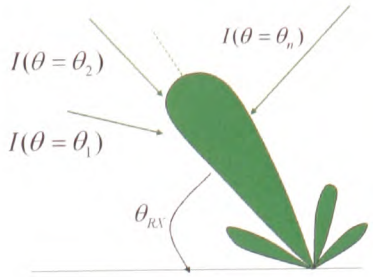

Figure 2. Signal distribution at the receiver side

Where I is the specific signal intensity, and $p(\hat{s}_1, \hat{s}_2')$ is the phase function, with $\hat{s}_1$ and $\hat{s}_2'$ representing the directions of the waves entering and emanating from each other respectively, and Ω is the solid angle over all spatial directions $\hat{s}_2'$. The phase function can be modelled as a Gaussian forward lobe and isotropic back scatter outside the main lobe [1]. Fig. 1 demonstrates the variation of the phase function pattern as varying beamwidths β in 2-dimension, *i.e.* the horizontal plane. The phase function is given by:

$$p(\theta) = \alpha q(\theta) + (1-\alpha) \tag{2}$$

$$q(\theta) = \left(\frac{2}{\beta}\right)^2 e^{-\left(\frac{\theta}{\beta}\right)^2} \tag{3}$$

where θ represents the ratation angle of the receiver antenna in degrees.

In the context it is worth remembering that the beamwidth of a Gaussian antenna pattern and the traditionally used HPBW are related by:

$$\beta = 0.6 \cdot \beta_{-3dB} \tag{4}$$

III. Influence of Antenna Radiation Pattern and Deconvolution Ill-Poseness

In the transport theory, it is assumed the various scattered wave trains are uncorrelated in phase [1]. Hence the power can be added in real quantities at the receiver side. The radiation pattern of a typical antenna, however, is not an ideal pulse but a curve comprised of a mainlobe and a significant amount of sidelobes. While placing the receiver inside the vegetation, both the mainlobe and sidelobes are receiving signals from rays both being directly transmitted from the transmitter and scattered from all the trees surrounding the antenna.

This situation can be geometrically depicted as shown in Fig. 2, and its strength can be mathematically calculated as the weighted sum of all directional contributions [4] and given as:

$$\begin{aligned} p_{RX}(\theta_{RX}) &= i(\theta_1) g_{RX}(\theta_1 - \theta_{RX}) \\ &+ i(\theta_2) g_{RX}(\theta_2 - \theta_{RX}) \\ &+ \cdots \\ &+ i(\theta_n) g_{RX}(\theta_n - \theta_{RX}) \\ &= \sum_{\theta_j} i(\theta_j) g_{RX}(\theta_j - \theta_{RX}) \end{aligned} \tag{5}$$

where p_{RX} is the measured power strength, g_{RX} is the radiation pattern of the receiver antenna. θ_{RX} and θ_j represent the directions of the antenna mainlobe and an individual incident wave, j, respectively, both of their values are with respect to the same horizontal reference angle. i is the density of the transmitted power just before reaching the receiver, its distribution depends on the vegetation media only [4], therefore not related to the receiver antenna.

The discrete expression Eq. 5 shows that the measured power p_{RX} is a convolution relationship between the receiver radiation pattern g_{RX} and the incident wave density, i :

$$p_{RX}(\theta) = i(\theta) * g_{RX}(\theta) \tag{6}$$

According to convolution theorem, convolution in the original domain is equivalent to multiplication in the transform domain:

$$P_{RX}(\omega) = I(\omega) G_{RX}(\omega) \tag{7}$$

where P_{RX}, I and G_{RX} are the Fourier Transform of p_{RX}, i, and g_{RX} respectively; ω is the variable in the transform domain corresponding to θ in the original domain.

Eq. 7 suggests that a straightforward solution of the deconvolution can be achieved by inverse Fourier Transform of $I(\omega)$, which would be the result of division of $P_{RX}(\omega)$ over $G_{RX}(\omega)$, *i.e.* $I(\omega) = \frac{P_{RX}(\omega)}{G_{RX}(\omega)}$. However the presence of random noise in the signal and the resolution limits of the computer processing can generate large spike errors in the division. These errors can consequently swamp most of the useful information contained in $i(\theta)$ after inverse Fourier Transform. This is known as the ill-posed problem [5].

IV. Deconvolution by Optimal Compensation Filtering

Due to the ill-posed problem, accurate deconvolution cannot be undertaken by division in the transform domain. P_{RX} needs

to undergo suitable filtering $F(\omega)$ to produce the optimal estimate $I_e(\omega)$ of the transfer function of the impulse response, $I(\omega)$.

$$I_e(\omega) = P_{RX}(\omega)F(\omega) \tag{8}$$

The optimal compensation filtering deconvolution is documented by S. M. Riad *et.al.* in [6]. In this paper, two criteria are deployed to iteratively determine the optimisation filter.

1) the minimum mean-square-error (MMSE) criterion:

$$E_1 = \int_{-\Omega}^{\Omega} |I_e(\omega) - I(\omega)|^2 d\omega \tag{9}$$

$$I_e(\omega) = \begin{cases} P_{RX}(\omega) \cdot F(\omega) & for\ |\omega| \le B \\ 0 & for\ |\omega| > B \end{cases} \tag{10}$$

where B represents the band limit of the signal in the transform domain. The consistence of $I_e(\omega)$ and $I(\omega)$ is guaranteed when finding the minimum of E_1. The resultant minimum is equivalent to $F(\omega)=\frac{1}{G_{RX}(\omega)}$, but the ill-posed problem still exist in this case.

2) the errors-control criterion:

$$E_2 = \int_{\Omega}^{\Omega} |I(\omega)F(\omega)|^2 d\omega \tag{11}$$

where the function of the filter $F(\omega)$ is used to control the spike-like errors generated by the straightforward division.

The two criteria can be conveniently grouped into one:

$$\begin{aligned} E &= E_1 + \lambda E_2 \\ &= \int_{-\Omega}^{\Omega} |I_e(\omega) - I(\omega)|^2 d\omega + \lambda \int_{\Omega}^{\Omega} |I(\omega)F(\omega)|^2 d\omega \end{aligned} \tag{12}$$

where λ is the optimisation parameter, which is iteratively determined based on a compromise between signal consistency and noise minimisation. The optimal compensation filter $F_{opt}(\omega)$ can be obtained by setting the partial derivatives equal to zero with respect to the real and imaginary parts respectively [7].

$$F(\omega) = \frac{G^*_{RX}(\omega)}{|G_{RX}(\omega)|^2 + \lambda} \tag{13}$$

where in Eq. 13 the superscript $*$ denote conjugate. The optimal compensation filter, $F(\omega)$, represents a form of the Wiener filter.

To develop, optimise and subsequently verify this optimal compensation filter technique, two generated curves, one representing the phase function signal and the other representing the Gaussian radiation pattern of the receiver antenna, are used to generate data similar to the values experienced in measurement data. Random mean-zero noise is added. The Signal-to-Noise ratio (SNR) can be controlled and was set to around 20 dB in the example illustrated in Fig. 3.

Fig. 4 illustrates 4 examples of signal restoration by deconvolution. Fig. 4a) shows the result of the deconvolution by straightforward division in transform domain. The true information of signal in the original domain is entirely swamped by noise. Fig. 4c) depicts deconvolution result of the optimal

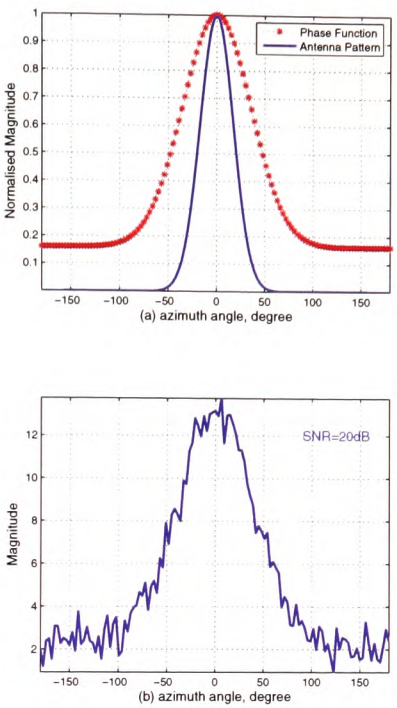

Figure 3. (a) Simulated signals and (b) their convolution plus added noise

filtering, where the parameter λ has been chosen correctly. The original simulated phase function is overlaid for comparison, the two curves are overall coincident. Figure 4b) and d) show the so called under- and over-compensated cases respectively, where the optimal filtering parameter λ has either been chosen too small (Fig. 4b)) or too large (Fig. 4d)).

As the original phase function signal is one of the input signals used to simulate the convolution process, its true information is available and can be used as reference to judge quality of the restoration.

V. ANECHOIC CHAMBER MEASUREMENT

As Eqs. 8 - 13 show, if $P_{RX}(\omega)$ and $G_{RX}(\omega)$ are known, the optimal filter $F_{opt}(\omega)$ will be available by Eq.13, and consequently $I(\omega)$ can be calculated by Eq. 8. Hence, the transform of the radiation pattern of the receiver antenna, $G_{RX}(\omega)$, and the received output pattern, $P_{RX}(\omega)$ need to be known to attain $I(\omega)$. In practice, the non-transformed functions, $g_{RX}(\theta)$ and $p_{RX}(\theta)$, are measured.

Measurements were conducted in a controlled indoor environment (anechoic chamber), which has an interior physical size of $5.60m \times 2.25m \times 2.40m$. The measurement setup is illustrated in Fig. 5. The transmitter uses a $10dBi$ standard gain horn antenna, and at the receiver side a Gaussian horn of

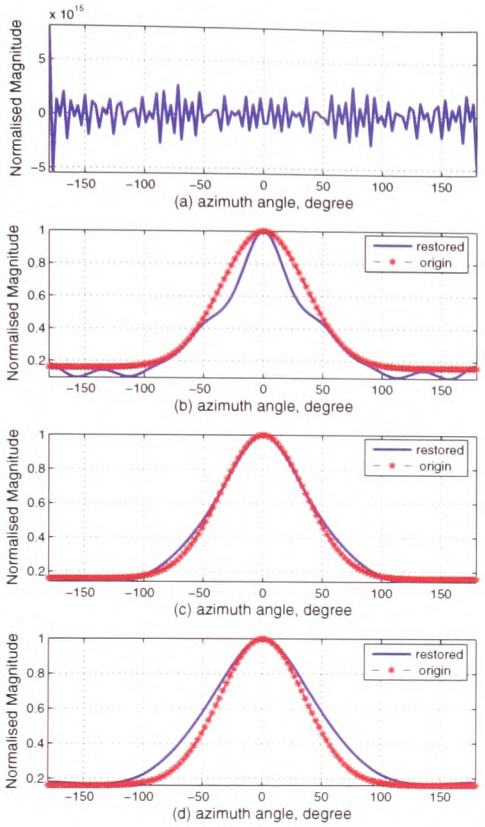

Figure 4. Restored signals under the case of : (a) direct division deconvolution; (b) under-compensated deconvolution; (c) optimal compensation deconvolution; (d) over-compensated deconvolution

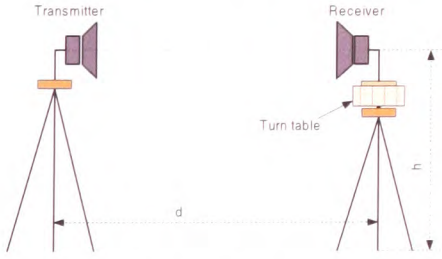

Figure 5. Side view of the measurement setup

$20dBi$ gain at 20GHz . The distance between the transmitter and the receiver is sufficiently large to ensure the far-field conditions.

The phase function measurement was conducted using 16 Ficus trees to form a small scale vegetation body representing a miniature forest. The receiver antenna was placed at different

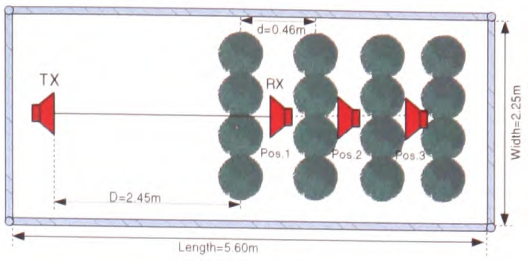

Figure 6. Measurement geometry in the presence of vegetation

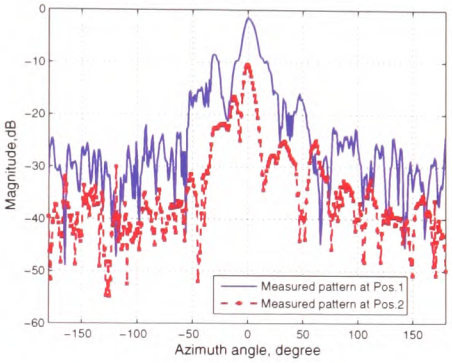

Figure 7. Measured radiation patterns at position 1 and position 2 at 20 GHz

vegetation depths as shown in Fig. 6 and rotated around its own axis at each position. The measured received signal levels at positions 1 and 2 with rotation angle are shown in Fig. 7. The maximum signal occurs when the antennas are boresight (azimuth angle $\theta = 0$). A decrease of signal level of nearly $10dB$ can also be observed between position 1 and 2.

VI. The Deconvolution Result from Measurement

The measured data sets of $p_{RX}(\theta)$ and $g_{RX}(\theta)$ are transformed by Fourier Transform to give $P_{RX}(\omega)$ and $G_{RX}(\omega)$. The measured values of $p_{RX}(\theta)$ and $g_{RX}(\theta)$ are both affected by noise. The noise can reasonably be assumed to be random, mean-zero, white noise.

When using simulated data it is possible to determine the optimal compensation filter parameter λ by minimising the error between the deconvolution result for $p_{RX}(\theta)$ and the original simulated input function as described in section V. Furthermore, unlike in the simulation where both phase function and antenna radiation pattern were readily available due to them being computer generated, the phase function pattern cannot be determined from measurements other than by deconvolution.

Hence a different method needs to be found to yield the parameter for the optimal compensation filter. The Bennia-Riad criterion [6] provides a quantitative measure of the filter taking into account the noise reduction and the filtration error. This is achieved by partitioning the transfer function of the

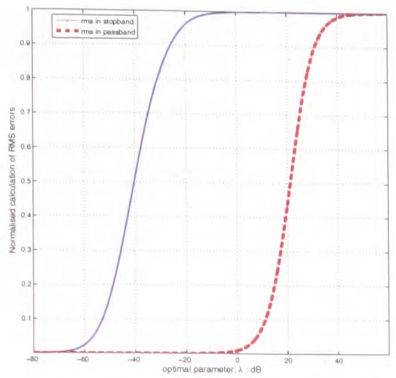

Figure 8. *rms* error values calculated in the passband and stopband respectively

signal in the transform domain into a passband, in which the SNR is large, and a stopband, with small SNR. The partition follows the conventional Half Power criterion. The transfer function of most practical applications is best represented by a low pass filter [3]. The aim is to describe the low pass filter so that the useful information mainly falls into the passband, whereas the stopband contains little information but has high noise content.

The deconvolution is optimal when it manage to restore the useful information in the signal, while minimising the effects of noise. The Bennia-Riad criterion is used for the deconvolution process presented here. It minimises the *rms* error between $I(\omega) = \frac{P_{RX}(\omega)}{G_{RX}(\omega)}$ and iteration $I_e^{\lambda}(\omega)$ as a function of the optimisation parameter λ:

$$\sigma_n(\lambda) = rms\left\{\left|I_e^{\lambda}(\omega) - I(\omega)\right|\right\} \tag{14}$$

where n represents number of iteration; *rms* represents the root mean squared operation performed on the quantity inside the brackets $\{\}$ over both pass- and stop band in the transform domain. $I_e^{\lambda}(\omega)$ represents an estimate of the transfer function in the transform domain after filtering and $I(\omega)$ is the transfer function in the transfer domain obtained by straightforward division $\frac{P_{RX}(\omega)}{G_{RX}(\omega)}$, which is the case when $\lambda = 0$.

To recover useful information, the optimal estimate, $I_e^{\lambda}(\omega)$ in the passband should be as close as possible to the value of $I(\omega)$, while as different as possible in the stopband. Fig. 8 illustrates the calculated *rms* error values in the passband and the stopband. The magnitude of the *rms* error was normalised with respect to its maximum within the corresponding interval band. The abscissa is the value of the optimal parameter λ expressed in dB. The range of λ is chosen to be relatively wide from $-80dB$ to $+60dB$ covering all experienced values.

The chosen optimal parameter λ according to the criterion discussed above falls into the range of $-20dB$ to $0dB$. Here the value of *rms* error in the passband is close to zero, therefore guarantees a high degree of similarity of the optimal estimate $I_e^{\lambda}(\omega)$ and the straightforward division $I(\omega) = \frac{P_{RX}(\omega)}{G_{RX}(\omega)}$ whereas in the stopband the *rms* error approaching the unity, consequently ensuring noise content reduction. The two extremes to either side of the λ range are:

- Under-compensated restoration: value of the optimal parameter λ is less than $-60dB$ in Fig. 8. This indicates the estimate $I_e^{\lambda}(\omega)$ coincides with the division $I(\omega)$ not only in the passband but also in the stopband. Consequently, the high noise contents still remains, this is the ill-poseness.
- Over-compensated restoration: value of the optimal parameter λ is more than $+40dB$. This means that too much distortion occurs in both bands, therefore too much of the useful information is lost after filtering, although noise has been greatly reduced.

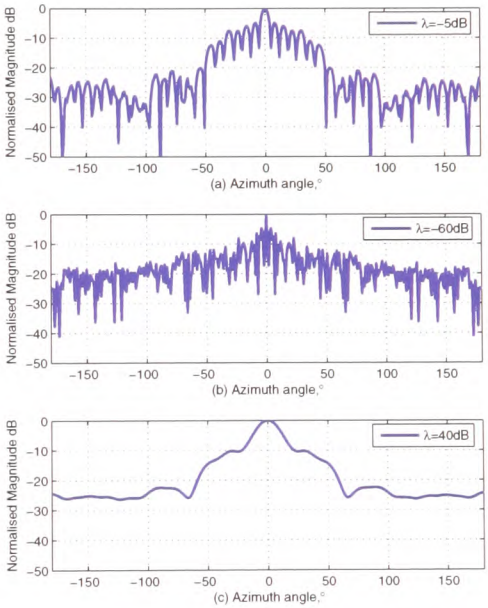

Figure 9. Restored signal patterns under the situations:(a) optimal-compensated restoration; (b) under-compensated restoration; (c) over-compensated restoration

Fig. 9 demonstrates the measurement restoration results in original domain under the three conditions described above: the top curve a) is attained by optimal compensation filtering, where the optimisation parameter λ has been correctly chosen as $-5dB$. The envelop of this graph shows a Gaussian shape, indicating correct retrieval of the useful information. The smoothness of the curve indicates sufficient noise reduction. Fig. 9b) illustrates a case of under-compensated restoration, where the chosen value of optimal parameter λ is too small at $-60dB$. The restored graph still contains a significant amount of noise, and the information part of signal appears distorted. Fig. 9c) depicts the over-compensated case, with the λ value

too large at $+40dB$. It shows that the curve extremely smooth, and the noise has been completely eliminated. However, considerable detailed characteristics of the original signal have also been removed.

VII. Conclusion

This paper demonstrates a feasible technique to restore the phase function of the RET theory from measurement data. To the author's knowledge the paper documents the first implementation of deconvolution techniques on antenna radiation pattern affected amplitude only measurement data. The paper briefly summarised the relevant parts of the RET theory to then concentrate on deconvolution.

Implementation of the iterative optimum compensation deconvolution is first demonstrated with computer generated patterns representing the phase function and simple antenna radiation pattern shapes. Secondly restoration of the phase function from practical measurement data is also shown, including over- and under-compensated cases. Determination of the optimisation parameter λ by the Bennia-Riad criterion is demonstrated.

This paper shows an extension of the application of the optimum compensation filtering technique to case when signal distributions are influenced by the shape of the antenna radiation pattern. This differs significantly from other applications of this deconvolution technique in so far as both input and output of the convolution are affected by noise and neither quantity is known correctly without noise. Successful implementation of this technique to practical measured data was possible since noise effects on the input proved to be less significantly than a noisy output signal [8]. Further improvement are possible using pre-filtering methods such as cross- and auto-correlation filter [9]. This will be presented in the near future.

References

[1] R.A. Johnson, and F. Schwering, "A Transport Theory of Millimeter Wave Propagation in Woods and Forests" New Jersey, Feb. 1985.

[2] N. C. Rogers, A. Seville, J. Richter, D. Ndzi, N. Savage, R. Caldeirinha, A. K. Shukla, M. O. Al-Nuaimi, E. Vilar and J. Austin, "A Generic Model of 1-60 GHz Radio Propagation through Vegetation-Final report", Tech. Rep., Radiocommunications Agency, May 2002.

[3] P. A. Jansson, *Deconvolution of Images and Spectra, Second edition*, Academic Press, 1997.

[4] T. Fernandes, R.F.S. Caldeirinha, M.O. Al-Nuaimi and J. Richter, "RET Scattering Function Optimisation in Vegetation Media using Inverse Convolution," Proceeding of 2006 IEEE International of the incident wave, Geoscience and Remote Sensing Symposium - IGARSS'06, Vol. 1, Denver CO, USA, June 2006.

[5] S. M. Riad, "The Deconvolution Problem: An Overview," *Proc.* IEEE, vol.74, no. 1, pp. 82-85, Jan. 1986.

[6] A. Bennia and S. M. Riad, "An Optimization Technique for Iterative Frequency-Domain Deconvolution," *IEEE Trans. Instrum. Meas.*, vol.39, no.2, Apr. 1990.

[7] S. M. Riad and R. B. Stafford, "Impulse Response Evaluation Using Frequency Domain Optimal Compensation Deconvolution," in *Proc.* 23rd *Midwest Symp. on Circuits and Systems* (Toledo, OH), pp. 521-525, Aug. 1980.

[8] N. S. Nahman and M. E. Guillaume, "Deconvolution of time domain waveforms in the presence of noise," NBS Tech. note 1047, NBS, Boulder, CO, Oct. 1981.

[9] P. B. Crilly, A. Bernardi, P. A. Jansson and L. Silva, "Improving the Convergence Rate of Jansson's Deconvolution Method" *IEEE Trans. Instrum. Meas.*, vol.51, pp. 1142-1144, Dec. 2002.